HAL
open science

Multi-messenger astronomy : from the analysis of transient sources of gravitational waves to electromagnetic counterparts searches

Jean-Grégoire Ducoin

To cite this version:

Jean-Grégoire Ducoin. Multi-messenger astronomy : from the analysis of transient sources of gravitational waves to electromagnetic counterparts searches. Cosmology and Extra-Galactic Astrophysics [astro-ph.CO]. Université Paris-Saclay, 2021. English. NNT : 2021UPASP100 . tel-03514521

HAL Id: tel-03514521

https://theses.hal.science/tel-03514521v1

Submitted on 6 Jan 2022

HAL is a multi-disciplinary open access archive for the deposit and dissemination of scientific research documents, whether they are published or not. The documents may come from teaching and research institutions in France or abroad, or from public or private research centers.

L'archive ouverte pluridisciplinaire **HAL**, est destinée au dépôt et à la diffusion de documents scientifiques de niveau recherche, publiés ou non, émanant des établissements d'enseignement et de recherche français ou étrangers, des laboratoires publics ou privés.

Multi-messenger astronomy: from the analysis of transient sources of gravitational waves to electromagnetic counterparts searches.

Astronomie multi-messagers : de l'analyse des sources transitoires d'ondes gravitationelles à la recherche de contreparties électromagnétiques.

Thèse de doctorat de l'Université Paris-Saclay

École doctorale n° 576, Particules, Hadrons, Énergie, Noyau, Instrumentation, Imagerie, Cosmos et Simulation (PHENIICS)
Spécialité de doctorat: Astroparticules et Cosmologie
Unité de recherche: Université Paris-Saclay, CNRS, IJCLab, 91405, Orsay, France.
Référent: : Faculté des sciences d'Orsay

Thèse présentée et soutenue à Paris-Saclay, le 04/10/2021, par

Jean-Grégoire DUCOIN

Composition du jury:

Sophie HENROT-VERSILLÉ Directrice de recherche, Université Paris-Saclay, Laboratoire de Physique des 2 Infinis Irène Joliot Curie, (UMR9012)	Présidente
Marie-Anne BIZOUARD Directrice de recherche, Observatoire de la Côte d'Azur, (UMR7250)	Rapportrice & Examinatrice
Frederic PIRON Directeur de recherche, Laboratoire univers et particules de Montpellier, (UMR5299)	Rapporteur & Examinateur
Phil EVANS Associé de recherche, University of Leicester	Examinateur
Francesco PANNARALE Professeur associé, Sapienza Università di Roma	Examinateur

Direction de la thèse:

Nicolas LEROY Chargé de Recherche, Université Paris-Saclay, Laboratoire de Physique des 2 Infinis Irène Joliot Curie, (UMR9012)	Directeur de thèse

Thèse de doctorat

NNT: 2021UPASP100

Remerciements

Je tiens tout d'abord à remercier chaleureusement Nicolas pour son encadrement irréprochable et tout ce qu'il m'a apporté pendant ces trois ans. Merci à Patrice, Tito et Florent que j'ai embêté plus d'une fois avec mes questions. Je remercie Angélique, Pierre, Imen et David Cohen de m'avoir accueillit et transmit leurs expériences de thèse. Merci à David Corre pour sa participation à mon travail de thèse et à mon encadrement. Merci à Pierre-Alexandre, Shaymaa et Marion et bon courage pour la suite. Merci à Nicolas Arnaud d'avoir épaulé mon implication dans Virgo. Merci d'une manière générale à l'ensemble du groupe ondes gravitationnelles d'Orsay.

Je remercie également les membres du Jury pour leurs temps, leurs conseils et leurs suggestions.

Je remercie les collaborations GRANDMA, Virgo et SVOM de m'avoir accueillit. Merci à Sarah Antier de m'avoir poussé vers l'avant dès le début de ma thèse.

Je remercie tous les enseignants que j'ai pu rencontrer lors de mes études. Je n'oublie absolument pas qu'une bonne partie de ce travail leurs est due.

Merci à ma famille, ma mère, mon père, mon frère et bien sûr Sarrah.

Contents

Synthèse **1**

Introduction **10**

1 Gravitational wave progenitors **13**
1.1 General Relativity . . . 13
1.2 Linearised General Relativity . . . 18
1.2.1 Weak field approximation . . . 18
1.2.2 Lorenz gauge . . . 19
1.2.3 Gravitational wave propagation . . . 20
1.2.4 Gravitational waves effects on matter . . . 21
1.2.5 Gravitational wave generation . . . 22
1.3 Gravitational wave sources . . . 24
1.3.1 Compact binary coalescence . . . 24
1.3.2 Sources for ground based detectors . . . 28

2 Gravitational wave detection **33**
2.1 Gravitational wave detectors . . . 33
2.1.1 History . . . 33
2.1.2 Detection principle . . . 34
2.1.3 Detector angular response . . . 37
2.1.4 Fundamental noises . . . 39
2.1.5 Virgo design, a few more words . . . 45
2.1.6 Current detector network . . . 47
2.2 Data analysis . . . 54
2.2.1 Calibration . . . 54
2.2.2 Detector characterisation and data quality . . . 56
2.2.3 Transient signal detection . . . 61
2.2.4 Source localisation . . . 63
2.2.5 Parameters estimation . . . 66

3 Gamma-ray bursts **69**
3.1 History . . . 69
3.2 Emission processes . . . 70
3.2.1 From jet properties to emission models . . . 70
3.2.2 GRB progenitors . . . 75

3.3 Gamma-ray burst detectors . . . 77
3.4 Electromagnetic counterparts of gravitational waves . . . 81
3.5 GW170817 and GRB170817A . . . 82
3.5.1 Overview of the detection . . . 82
3.5.2 The scientific outcome of this event . . . 84
3.5.3 Neutrino counterpart . . . 84
3.5.4 GW170817 a very lucky observation . . . 88
3.6 Host galaxies population . . . 89
3.6.1 Long GRB host galaxies . . . 89
3.6.2 Short GRBs host galaxies . . . 92
3.7 Modeling the SED of GRB host galaxies . . . 100

4 Multi-messenger astronomy 101
4.1 Gravitational wave alerts . . . 101
4.1.1 Candidate validation and release . . . 101
4.1.2 RAVEN . . . 104
4.1.3 Channel safety analysis . . . 104
4.2 Search for gravitational waves associated with GRBs . . . 110
4.2.1 GRB sample . . . 110
4.2.2 Modelled search dedicated to compact binary mergers . . . 111
4.2.3 Unmodelled search for generic transients . . . 113
4.2.4 Results . . . 119

5 optimisation of gravitational wave follow-up 123
5.1 Follow-up challenge . . . 123
5.2 Optimisation of the observations . . . 127
5.2.1 GRANDMA: a network to coordinate them all . . . 127
5.2.2 Tiling strategy . . . 130
5.2.3 Galaxy targeting strategy . . . 131
5.3 Mangrove catalog . . . 137
5.3.1 Use of the galaxies for the tiling . . . 144
5.4 GRANDMA and SVOM observations . . . 146
5.5 SVOM follow-up optimisation . . . 150
5.6 Short GRB host galaxies . . . 154
5.6.1 Short GRB sample . . . 154
5.6.2 Association with host . . . 154
5.6.3 GRB host photometry . . . 157
5.6.4 SED fitting procedure . . . 158
5.6.5 Results of the fits . . . 158
5.6.6 Gravitational wave follow-up . . . 159

Synthèse

L'une des premières prédictions de la Relativité Générale, théorie vieille d'un siècle qui réunit la relativité restreinte et la gravitation dans un même cadre géométrique, est l'existence des ondes gravitationnelles. Bien qu'Einstein lui-même, père de la Relativité Générale, doutait de la possibilité de détecter un jour ces perturbations extrêmement faibles de l'espace-temps, les détecteurs actuels ont prouvé leurs efficacités à détecter ces ondes gravitationnelles et à fournir du contenu scientifique à partir de celles-ci. Pour la première fois, le 14 septembre 2015, une onde gravitationnelle est détectée de façon directe à l'aide de détecteurs interférométriques : les détecteurs LIGO. Cette détection a ouvert la voie vers l'observation de l'univers à l'aide des ondes gravitationnelles, nouveau messager qui se propagent sans être dispersées ou absorbées par la matière (contrairement aux ondes électromagnétiques qui constituent la lumière). La détection des ondes gravitationnelles a ouvert une nouvelle porte pour ce domaine très jeune qu'est l'astronomie multi-messager qui consiste à observer un même objet de l'univers à l'aide de plusieurs messagers (ondes gravitationnelles et lumière par exemple).

Cette thèse est dédiée à l'étude multi-messagers des ondes gravitationnelles, de l'analyse de données des détecteurs d'ondes gravitationnelles jusqu'à la recherche de contreparties électromagnétiques. Dans un premier temps, elle porte sur la détection des ondes gravitationnelles et la validation de l'envoi des alertes ondes gravitationnelles. Cette thèse présente ensuite l'analyse de données des détecteurs d'ondes gravitationnelles dédiée à la recherche de contreparties aux sursauts gamma détectés par les satellites Fermi et Swift. Dans un second volet, y est présenté le suivi de ces alertes au sein des collaborations GRANDMA et SVOM, réseaux de télescopes terrestres et/ou spatiaux, afin de rechercher des contreparties électromagnétiques. Enfin, y est présentée l'étude de la population de galaxies hôtes de sursauts gamma court afin d'identifier leurs propriétés et de les utiliser pour optimiser le suivi des ondes gravitationnelles.

Les ondes gravitationnelles

Le formalisme de la Relativité Générale est hérité de la relativité restreinte qui, contrairement à la mécanique galiléenne, regroupe l'espace et le temps en une seule entité appelée "espace-temps". Dans ce formalisme, la géométrie de l'espace-temps est décrite par la métrique, objet définissant la distance entre deux points. En partant du principe d'équivalence d'Einstein, qui peut être décrit comme le fait que l'on peut toujours annuler l'effet de la gravitation par un changement

local de coordonnées, il est possible d'obtenir l'équation d'une géodésique. Cette équation permet de décrire l'effet d'un champ gravitationnel sur une particule et de déterminer l'emplacement de la particule en fonction du temps, à condition de fournir, comme dans la gravité newtonienne, deux conditions initiales (par exemple la position et la vitesse à un certain moment initial). Mais cela nécessite de connaître les composantes du tenseur métrique, or en Relativité Générale l'espace-temps n'est pas nécessairement plat et la métrique est un objet dynamique. Ainsi, en Relativité Générale, la question principale pour résoudre un problème physique consiste à déterminer l'expression de la métrique en prenant en compte la distribution de la masse et de l'énergie dans l'espace-temps. Dans le cas général, on recherche donc une équation fondamentale qui détermine la métrique en fonction de la distribution de la masse et de l'énergie dans l'espace-temps. En imposant de retomber sur les équations Newtoniennes dans le cas de champs de gravitation faible et (quasi-)static pour des objets se déplaçant lentement par rapport à la vitesse de la lumière, il est possible de montrer que les équations recherchées, appelées équations d'Einstein sont :

$$G_{\mu\nu} + \Lambda g_{\mu\nu} = \frac{8\pi G}{c^4} T_{\mu\nu}$$

Ces équations différentielles sont non linéaires à tout ordre et il n'existe pas de solutions générales pour les résoudre. Il est néanmoins possible de s'intéresser aux solutions dans des cas particuliers comme lorsque l'on considère un champ faible, espace-temps dont la métrique est plate avec des perturbations considérées comme petites (ce qui correspond à la linéarisation des équations d'Einstein). Cette étude en particulier est très utile en astrophysique où la métrique peut être souvent considérée comme plate, les importantes déviations étant réservées au voisinage d'objets extrêmes comme les étoiles à neutrons ou les trous noirs. Il est possible dans ce cas d'utiliser l'invariance de jauge, choisir une jauge dite de Lorenz, afin de réduire les équations d'Einstein dans le vide à des équations d'ondes dont les solutions, appelées ondes gravitationnelles, se déplacent à la vitesse de la lumière. Ces ondes gravitationnelles sont décrites par deux degrés liberté ou états de polarisation. Il est possible de caractériser ces deux polarisations en fonction de leurs effets sur un cercle de masses libres dont le plan du cercle est perpendiculaire à la direction de propagation de l'onde. La première polarisation, dite "plus", déforme le cercle en une ellipse qui est périodiquement compressée dans une direction et étirée dans l'autre. La seconde polarisation, dite "croix", a un effet similaire sur le cercle, mais suivant une direction tournée de 45 degrés. Toutes les combinaisons linéaires de ces deux polarisations sont possibles. En résumé, cet exemple du cercle de masses illustre que le passage d'une onde gravitationnelle engendre la variation de distance entre deux points, c'est cette propriété fondamentale qui permet aujourd'hui leur détection directe.

Sachant l'existence des ondes gravitationnelles, l'on peut se poser la question des sources capables de les générer. L'émission des ondes gravitationnelles est décrite, dans les équations d'Einstein, par l'évolution du moment quadripolaire de masses en mouvement. En théorie, toute masse en mouvement qui possède une forme d'asymétrie sphérique est une source d'ondes gravitationnelles. Néanmoins, l'amplitude d'un rayonnement gravitationnel est usuellement très petite et les seules sources que l'on peut espérer détecter sont celles provenant de sources astrophysiques extrêmes présentant des objets compacts, de grandes masses et capables de soutenir de très grandes accélérations. À ce jour, les seules sources d'ondes gravitationnelles détectées sont les binaires d'objets compacts (étoiles à neutrons ou trous noirs), qui émettent quelques instants avant leurs coalescences (de quelques centaines de secondes pour les binaires les plus massives à quelques centaines de secondes pour les moins massives) des ondes gravitationnelles à hautes fréquences (entre 10 Hz et 10^4 Hz) avec des amplitudes suffisamment importantes pour être observé avec les détecteurs actuels. Environ 50 sources de ce type ont été identifiées jusqu'à présent. D'autres types de sources (supernova à effondrement de cœur, instabilité de disque d'accrétion, pulsars, corde cosmique...) sont envisagés, mais l'amplitude de leurs émissions et le nombre de ces sources les rendent moins susceptibles d'être observés.

Détecteurs d'ondes gravitationnelles

Bien qu'il existe de nombreux designs proposés pour les détecteurs d'ondes gravitationnelles seuls sont discutés en détail dans cette thèse les détecteurs au sol reprenant le schéma d'un interféromètre de Michelson. Ce design utilisé par les détecteurs LIGO, Virgo et KAGRA est le seul à ce jour qui, au prix de près d'un demi siècle de développement, a permis la détection directe d'ondes gravitationnelles. Pour un interféromètre de Michelson, la figure d'interférence est induite par la différence de taille entre les deux bras de l'interféromètre. En effet, la figure d'interférence change en fonction de la distance différentielle entre la séparatrice et les miroirs aux extrémités de ses bras orthogonaux. Si l'on place une photodiode sur la position d'une frange sombre de la figure d'interférence, tout changement de distance différentiel sera détecté par la photodiode, car celle-ci sera temporairement décalée de la frange sombre. Ce design est donc particulièrement efficace pour mesurer des effets différentiels, or comme nous l'avons vue précédemment, les ondes gravitationnelles produisent justement des modifications de distance différentielles sur un ensemble de masses en chute libre. Dans ce design, les masses en chute libre utilisées dans la pratique sont les miroirs de l'interféromètre qui sont suspendus à des fils et isolés des bruits sismiques par des atténuateurs. Pour Virgo, les bras de l'interféromètre font 3 km de long ce qui produit un mouvement relatif suffisament important pour rendre le signal détectable. Un détecteur in-

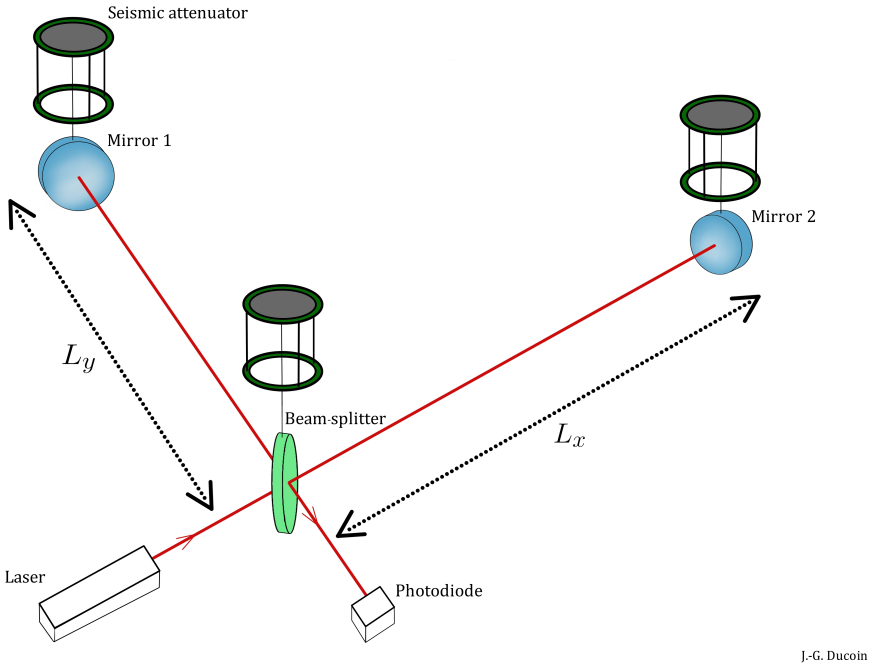

Figure 1: schéma simplifié d'un détecteur d'ondes gravitationnelles reprennant le principe d'un interféromètre de Michelson. Les miroirs aux extrémités des bras sont présentés en bleu, la séparatrice est présentée en vert. Tous deux sont suspendus à des atténuateurs de bruit sismique.

terférométrique peut être assimilé à une antenne possédant une réponse angulaire différente pour chaque point du ciel et pour chaque polarisation. La réponse angulaire totale, que l'on appelle le facteur d'antenne, prenant en compte la réponse aux deux polarisations possible de l'onde gravitationnelle se présente comme étant presque uniforme dans le ciel, mais avec quatre points aveugles. En bref, lorsqu'il est en fonctionnement, un détecteur interférométrique est capable de détecter des sources provenant de la quasi-totalité du ciel, mis à part quatre régions précise où la sensibilité du détecteur devient nulle. Malheureusement, cet avantage est également un inconvénient, car il signifie qu'un interféromètre seul ne dispose pas d'un moyen robuste de localiser une source d'onde gravitationnelle dans le ciel. Bien que le design général d'un détecteur reprenant le schéma d'un interféromètre de Michelson soit particulièrement bien adapté à la détection des ondes gravitationnelles, celui-ci est confronté à de grands nombres de limitations pratiques et confronté à de nombreuses sources de bruits qu'il a fallu réduire au maximum au cours du développement des détecteurs afin de réussir à obtenir les sensibilités actuelles. Parmi les sources de bruits fondamentaux, on peut citer le bruit sismique. Important à basse fréquence, il est néanmoins supprimé au-dessus de 10 Hz dans le design actuel par les atténuateurs sismiques. On peut également citer le bruit thermique résultant de la dissipation à l'intérieur des miroirs et de leurs revêtement, provocant une déformation de leur surface, de la dissipation dans les câbles de suspension et l'excitation du mouvement pendulaire. Dans le design actuel, le bruit thermique est réduit à l'aide de l'utilisation de matériaux tels que la silice fondue, le saphir ou le silicium pour les miroirs et le pendule, afin de réduire le niveau de bruit à large bande. Enfin le bruit le plus limitant dans les détecteurs actuels est le bruit quantique qui est décrit comme la somme du bruit de grenaille et de bruit lié à la pression de radiation. Alors que le bruit lié à la pression de radiation peut être réduit en limitant la puissance du laser, le bruit de grenaille quant à lui peut être limité en augmentant la puissance du laser. Il existe donc un compromis à choisir pour optimiser la sensibilité du détecteur.

Le réseau actuel de détecteurs est composé de l'interféromètre Virgo situé à Cascina en Italy, de deux Laser Interferometer Gravitational-Wave Observatory (LIGO) situés aux États-Unis d'Amérique et du Kamioka Gravitational Wave Detector (KAGRA) au Japon. Juste avant le début officiel de la première prise de donnée d'Advanced LIGO, le 14 septembre 2015, la première onde gravitationnelle (GW150914) issue de la coalescence de deux trous noirs a été détectée par les détecteurs LIGOs. La première prise de donnée (O1) a duré 5 mois avec seulement les deux LIGOs et a mené à la détection de deux autre ondes gravitationnelles issue de la coalescence de deux trous noirs. La seconde prise de donnée (O2) a duré 9 mois et le détecteur Virgo a rejoint cette prise de donnée pour le dernier mois. En plus de la détection de sept ondes gravitationnelles issues de la coales-

cence de deux trous noirs, cette seconde prise de donnée a permis la détection de la première onde gravitationnelle issue de la coalescence de deux étoiles à neutrons (GW170817). Enfin la troisième prise de donnée (séparée en deux avec O3a et O3b) a durée 11 mois et a été rejoint par KAGRA à sa toute fin. La deuxième partie de cette dernière prise de donnée est encore en cours d'analyse, mais sa première partie a déjà fournie de nombreuses détections (toutes issues de coalescence d'objets compacts) avec par exemple la première onde gravitationnelle issue de la coalescence d'une binaire étoile à neutrons trou noir (GW190426).

Les données des détecteurs d'ondes gravitationnelles sont non stationnaires et non gaussiennes. Elles sont largement contaminées par des bruits transitoires, appelés "glitches", qui rendent compliqué la recherche de signaux astrophysiques. Avec un réseau de détecteurs, sachant qu'une onde gravitationnelle est censée être visible dans tous les détecteurs (en prenant en compte les différences de sensibilité et de facteur d'antenne) toute techniques de coïncidence et/ou de cohérence multi-détecteurs permettent de réduire le nombre signaux intéressants. Mais en pratique ceci n'est pas suffisant pour effectuer une détection statistiquement significative et il est nécessaire d'effectuer un travail conséquent de nettoyage des données. Cela passe principalement par la suppression de périodes connues pour être altérées par des perturbations environnementales. Ces périodes sont essentiellement identifiées à l'aide de détecteurs joins aux interféromètres qui mesurent tout un tas de propriétés liées à leur fonctionnement et à leur environnement (sondes magnétiques, sondes sismiques, microphones, détecteurs radio, mesure de la stabilité du laser...).

Sursauts gamma

Les sursauts gamma sont des émissions électromagnétiques transitoires, très brillantes dans la gamme des rayons gammas. Observés par hasard pour la première fois par les satellites Vela dans les années 70, ils représentent l'une des sources les plus énergétiques de l'univers. La condition initiale de production d'un sursaut gamma est le dépôt d'une quantité très importante d'énergie dans une région de petite taille. Ainsi, un jet de matière à une vitesse proche de celle de la lumière est émis. Les ondes de choc au sein de cette matière émettent alors des radiations dans la gamme des rayons gammas. Les sursauts gamma sont usuellement séparés en deux classes différentes.

Les sursauts dit long, dont l'émission dure typiquement entre 2 secondes et plusieurs minutes, identifiés comme étant la résultante du collapse d'une étoile massive. Leur population de galaxie hôte présente, des galaxies à haut taux de formation stellaire et des redshifts allant jusqu'à $\sim 8 - 10$. Ces sursauts représentent donc une opportunité pour sonder l'univers jusqu'à de très grandes distances.

Les sursauts dit courts, dont l'émission dure typiquement moins de 2 secondes, identifiés comme étant la résultante de la coalescence de binaire d'étoile à

neutrons. Ils jouent donc un rôle primordial dans l'astronomie multi-messager en lien avec les ondes gravitationnelles. Leur population de galaxie hôte présente en moyenne des galaxies à plus petit redshift que les sursauts long (avec un redshift médian de ~ 0.5), des galaxies plus massives et avec un taux de formation stellaire significativement moins important.

Le 17 août 2017, la collaboration LIGO-Virgo a rapporté la détection de la première onde gravitationnelle issue de la coalescence de deux étoiles à neutrons (GW170817). Cette détection a été identifiée comme étant coïncidente avec la détection d'un sursaut gamma court (GRB170817A) détecté par le satellite Fermi et le satellite INTEGRAL. Près de 11 heures après la détection par LIGO-Virgo, la collaboration One-Meter Two-Hemisphere (1M2H) identifie la kilonovae associée à l'événement. Cette kilonova, visible pendant quelques jours des bandes ultraviolettes aux bandes infrarouges est la résultante de la matière fraîchement éjectée par la coalescence et chauffée par sa propre radioactivité. Cette combinaison de détection sans précédent a permis d'améliorer notre compréhension de la physique en champs de gravités forts et a imposé des contraintes aux modèles astrophysiques liés à la matière pendant la phase de fusion et post-fusion (telles que sur l'équation d'état des étoiles à neutrons, l'énergie et la géométrie de l'éjecta, le rémanent de la fusion et le milieu environnant).

Astronomie multi-messager avec les ondes gravitationnelles

Au sein de la collaboration LIGO-Virgo-KAGRA, j'ai participé à l'implémentation de tests dédiés à: l'étude du comportement du détecteur aux moments des alertes (permettant de valider ou d'invalider celles-ci), l'étude des canaux auxiliaires du détecteur (canaux parallèles au signal principal du détecteur, contrôlant son statut et son environnement) et l'identification de bruits dans le détecteur. Parmi mes contributions, j'ai développé, implémenté et utilisé l'analyse des canaux auxiliaires de O3b permettant de savoir s'ils sont sensibles au passage d'une onde gravitationnelle. En effet, afin d'éliminer des données des région temporelles pour lesquelles les détecteurs peuvent être affectés par des perturbations environnementales, les canaux auxiliaires sont utilisés pour identifier les perturbations. Or le couplage entre le détecteur et les cannaux auxiliaires ne sont pas tous identifiés et on ne sait pas à priori si certains de ces canaux ne peuvent pas capter d'une quelconque manière les perturbations induites dans le détecteur par les ondes gravitationnelles. L'analyse que j'ai fournie permet d'identifier et d'utiliser les canaux qui sont en pratique insensibles au passage d'une onde gravitationnelle à travers le détecteur. Pour effectuer cette analyse, j'ai utilisé des injections manuelles qui miment l'effet d'une onde gravitationnelle sur le détecteur et j'ai identifié parmi les ~ 2500 canaux auxiliaires ceux qui sont statistiquement sensibles à ces injections. Il en résulte 69 canaux auxiliaires considérés comme trop sensibles aux injections et qui donc sont

mis de côté pour l'identification de périodes bruitées dans le détecteur. Cette analyse a été développé de sorte à être utilisée de manière répétée lors de la prochaine prise de donnée (O4). J'ai également participé au développement d'outils permettant l'automatisation de l'envoi des alertes ondes gravitationnelles et j'ai participé à la validation des alertes en temps réel nécessaire pour chacune d'entre elle afin de confirmer le comportement des détecteurs et la fiabilité de la détection.

Toujours au sein de la collaboration LIGO-Virgo-KAGRA, j'ai participé à l'analyse de données dédiée à la recherche de contreparties aux sursauts gamma détectés par les satellites Fermi et Swift pendant O3a. Cette analyse est divisée en deux parties. La première est dédiée à la recherche de signaux gravitationnels en contrepartie de coalescence de binaire d'objets compacts contenant au moins une étoile à neutrons. Cette première recherche est donc spécifiquement utilisée pour rechercher des contreparties aux sursauts gammas courts et bénéficie de la modélisation des signaux attendu pour ce type de source. Cette analyse, contrairement à une recherche standard de signal dans les données des détecteurs, bénéficie de la localisation spatiale (localisation de la source du sursaut gamma dans le ciel) et temporelle (temps de la détection du sursaut gamma) de la source en plus de la modélisation de la forme du signal attendu, ce qui la rend particulièrement efficace. Afin de ne pas se limiter à une recherche sur les sursauts gamma court avec un seul type de signal, la seconde analyse, dite non modélisée, recherche de manière générique des signaux transitoires en coïncidence avec les sursauts gamma (courts et longs). Cette seconde analyse bénéficie également de la localisation spatiale et temporelle de la source fournie par la détection du sursaut gamma et recherche un excès de puissance cohérent dans le réseau de détecteurs d'ondes gravitationnelles. Cette recherche est donc limitée aux cas où au moins deux détecteurs sont en observation au moment de la détection du sursaut gamma. Les résultats de ces analyses pour O3a ne présentent aucune évidence d'un signal significatif. En l'absence de détection, des limites ont été posées sur la distance de la source du sursaut gamma. Ces limites s'appuient sur les modèles de coalescence de binaire d'objets compacts pour la première analyse. Pour la seconde, ces limites s'appuient également sur deux autres familles de modèles : les sino-Gaussienne circulaires, représentant les ondes gravitationnelles provenant des effondrements stellaires ; les modèles d'instabilité des disques, représentant des formes d'onde de longue durée qui sont dues aux instabilités du tore magnétiquement suspendu autour d'un trou noir en rotation rapide. Les limites obtenues pour O3a sont meilleures que celles obtenues pendant les analyses des précédentes prises de donnée. Ceci est essentiellement dû à l'amélioration de la sensibilité des détecteurs.

Optimisation du suivi des ondes gravitationnelles gravitationnelles

Pendant ma thèse, j'ai travaillé sur l'optimisation des stratégies de suivi des ondes gravitationnelles à l'aide de réseaux de télescopes terrestres et/ou spatiaux. Ce suivi est particulièrement difficile, car, les localisations des sources par les détecteurs d'ondes gravitationnelles sont très peu précises (avec une boîte d'erreur allant de plusieurs dizaines à plusieurs milliers de degrés carré). De plus, les contreparties optiques recherchées (kilonovae et rémanent du sursaut gamma court) sont relativement peu lumineuses. Pour espérer détecter une contrepartie, il est donc primordial d'utiliser des stratégies d'observation robuste permettant d'optimiser les chances de détection. Pour répondre à ces difficultés, les réseaux de télescopes GRANDMA et SVOM ont choisi développer des stratégies d'observation qui coordonne les observations entre différents télescopes afin de tirer parti au mieux des observations.

La stratégie d'observation des collaborations GRANDMA et SVOM utilise deux approches différentes en fonction du champ de vue des télescopes. La première stratégie, dite de tuilage, usuellement utiliser pour les télescopes à grand champ de vue ($\gtrsim 1$ degré carré) consiste en la construction d'un pavage optimisé du ciel où la programmation de l'observation est définie en utilisant la distribution de probabilité 2D de la carte du ciel des ondes gravitationnelles. J'ai participé au développement de cette stratégie afin d'optimiser une couverture simultanée du ciel par un réseau de télescopes en prenant en compte la sensibilité des détecteurs la possibilité de défaillances dans l'observation (météorologiques ou techniques) et en garantissant que les régions les plus intéressantes de la carte du ciel sont explorées plusieurs fois par le réseau. La seconde stratégie, dite de ciblage de galaxies, usuellement utiliser pour les télescopes à petit champ de vue ($\lesssim 1$ degré carré) consiste à tirer parti des catalogues de galaxies pour cibler les observations sur les galaxies intéressantes dans l'horizon d'intérêt pour une alerte donnée. Les développements de cette stratégie, auxquels j'ai participé, s'appuient en grande partie sur la production d'un catalogue de galaxies dédié au suivi des ondes gravitationnelles nommé Mangrove qui est entièrement public (tout comme les méthodes de production de plans d'observation qui lui sont associées).

Ces stratégies et leurs développements ont été utilisés par les collaborations SVOM et GRANDMA pendant le suivi de toute la troisième prise de donnée O3. Ces deux collaborations ont montré leurs efficacité à suivre les alertes ondes gravitationnelles en réalisant des suivis d'une grande quantité de ces alertes avec des observations sur des grandes régions du ciel. Cependant, aucun candidat transitoire intéressant n'a été trouvé pendant ces suivis.

Enfin, cette thèse présente l'étude de la population de galaxies hôtes de sursauts gammas courts. Cette étude vise à mettre à jour les résultats précédents disponibles dans la littérature, la dernière compilation datant de presque dix ans.

La sélection de l'échantillon de sursauts gammas courts est basée sur un critère de haute énergie et l'identification de la galaxie hôte est basée sur un nouveau code d'association que j'ai développé. Les propriétés des galaxies, telles que la masse stellaire et le taux de formation stellaire, sont déduits par l'algorithme CIGALE ajustant la distribution spectrale d'énergie sur les données photométriques pour l'ensemble de l'échantillon (conduisant à une détermination homogène des propriétés). Les données photométriques ont été collectées une à une dans la littérature ainsi que les catalogues de galaxies disponibles publiquement, ce qui représente un travail long et fastidieux. Afin de s'assurer de la bonne détermination des propriété physiques à l'aide de CIGALE, la distribution spectrale d'énergie n'est déterminée que l'orsque l'on dispose de suffisament de donnée photomètrique (~ 4 en optique et au moins une en (proche-)infrarouge). Cela représente un échantillon de 37 galaxies. Les propriétés physiques déterminées sont comparées aux résultats de la littérature et leur utilisation pour le suivi des ondes gravitationnelles es discutée.

Introduction

Predicted by Albert Einstein in 1916 on the basis of his general theory of relativity, gravitational waves are disturbances in spacetime curvature propagating in a wave like matter. Einstein himself had doubt about the detectability of those extremely faint and weakly interacting signals. About one century after their prediction, the direct detection of gravitational waves with ground-based interferometric detectors, has provided lot of scientific material and opened a new area for astronomical observations. The identification of a binary neutron star merger event coincident with a gamma-ray burst the 17th August 2017 provided a real breakthrough for multi-messenger astronomy. This thesis is dedicated to multi-messenger astronomy related to the detection of gravitational waves with ground-based interferometric detectors. From the analysis of transient sources of gravitational waves to electromagnetic counterparts searches.

The basic of the gravitational waves properties and their astronomical sources will be presented in chapter 1. In chapter 2 I will give an overview on detecting gravitational waves, from the design of current ground-based interferometric detectors to the various steps required to achieve a signal detection. Then, in chapter 3 I will present the basics of the gamma-ray burst physics and their detection. The event of the 17th August 2017 will be discussed in detail in this chapter as an illustration of what can be expected for multi-messenger astronomy with gravitational waves. Chapter 4 will present the involvement I had during my thesis within the LIGO-Virgo-KAGRA collaboration for the detection of gravitational wave sources and the production of gravitational wave alerts, along with the search for gravitational waves associated to gamma-ray bursts. Finally chapter 5 will present my participation in the optimisation of the follow up of gravitational wave events with ground based telescopes and satellite telescopes for the GRANDMA and SVOM collaborations.

Chapter 1

Gravitational wave progenitors

General Relativity is a geometric framework which brings together special relativity and gravitation. It predict that in some circumstances, described in this chapter, accelerating objects can produce gravitational waves. In the following sections I give a rapid overview of the General Relativity formalism and the main steps of the derivation of gravitational waves from this theory focusing on results relevant for this thesis, mainly following the results given by [1] and [2] with inputs from other sources [3, 4, 5].

1.1 General Relativity

From Special Relativity...

The formalism of General Relativity is inherited from Special Relativity. It merges space and time in a single entity, so called "space-time". In this formalism, time becomes a coordinate such as spacial coordinates. However, moving in time is not identical to move in space, one can go back in space while the causality prevents to go back in time. The non Euclidean metric maintains the fundamental distinction between space and time, indeed the Minkowski space-time is based on a four dimension vector space $\mathbb{R}^4$ with a (pseudo-)scalar product, i.e. with signature $\{-,+,+,+\}$. If one choses local coordinates like

$$\{x^\mu\} = \{x^0, x^1, x^2, x^3\} = \{ct, x, y, z\} \tag{1.1}$$

The scalar product between $\boldsymbol{X} = x^\mu e_\mu$ and $\boldsymbol{Y} = y^\mu e_\mu$ (e_μ being the basis vectors) is defined as

$$\boldsymbol{g}(\boldsymbol{X}, \boldsymbol{Y}) = g_{\mu\nu} x^\mu y^\nu \tag{1.2}$$

where the Einstein summation convention is used and $g_{\mu\nu}$ is the metric equal here to the Minkowski metric given by

$$\eta_{\mu\nu} = \begin{pmatrix} -1 & 0 & 0 & 0 \\ 0 & 1 & 0 & 0 \\ 0 & 0 & 1 & 0 \\ 0 & 0 & 0 & 1 \end{pmatrix} \tag{1.3}$$

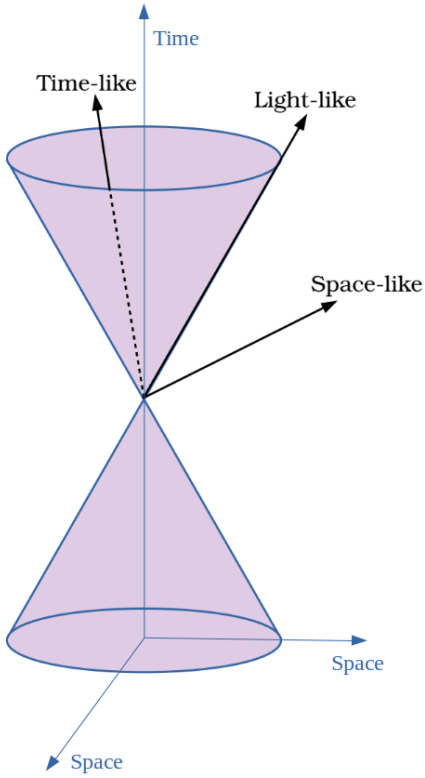

Figure 1.1: Light-cone with 3 vector, respectively time-like, light-like and space-like.

In Special Relativity, like in General Relativity, the lorentzian signature allows to classify any non nul vector in three classes

- time-like vectors: $\boldsymbol{g}(\boldsymbol{X}, \boldsymbol{X}) < 0$
- light-like vectors: $\boldsymbol{g}(\boldsymbol{X}, \boldsymbol{X}) = 0$
- space-like vectors: $\boldsymbol{g}(\boldsymbol{X}, \boldsymbol{X}) > 0$

Those three classes are usually represented in the so called light-cone visualisation (figure 1.1) where the hypersurface $\boldsymbol{g}(\boldsymbol{X}, \boldsymbol{X}) = 0$ draw a cone splitting the different categories.

In one hand, in the first class, one can check that if we have $x^0 > 0$ (or $x^0 < 0$) then any change of reference frame will give $x'^0 > 0$ (or $x'^0 < 0$), i.e that an event in the future (or the past) of the origin in any reference frame will still be in the future (or in the past) after any change of reference frame. In this case the distance between the event and the origin is intrinsically temporal, hence the name time-like.

On the other hand, in the third class, while we can always find a new reference frame where the sign of x^0 is different from the sign of x'^0 it is impossible to find one where the event have the same spacial position in both reference frame. In this case the distance between the event and the origin is intrinsically spacial, hence the name space-like.

Despite the relativity of simultaneity the causality is conserved if we impose that the physical object travel through the space-time with time-like trajectory (or light-like for massless particles).

... To General Relativity

Still in Special Relativity, taking the coordinates expression from 1.1 one can express the infinitesimal length element ds (and the proper time infinitesimal element $d\tau$) as a function of the infinitesimal changes in coordinates dx^μ like

$$ds^2 = g_{\mu\nu} dx^\mu dx^\nu = -c^2 d\tau^2 \tag{1.4}$$

In order to introduce the General Relativity we can start by assuming the Einstein equivalence principle which can be expressed as the fact that one can always locally cancel the effect of a gravitational field by a change of coordinates. This is equivalent to say that one can find a change of coordinate $x^\mu \to \xi^\mu$ where locally the physics is described by the Special Relativity equations. By hypothesis, in absence of other forces, in this new frame we have

$$\frac{d^2\xi^\mu}{d\tau^2} = 0 \tag{1.5}$$

Note that in a sense the effect of the gravitational field is hidden in the expression of the functions $\xi^\mu(x)$. In order to get the effect of the gravitational field on the system of coordinate x^μ one can introduce the following expression in 1.5

$$\frac{d\xi^\mu}{d\tau} = \frac{\partial \xi^\mu}{\partial x^\alpha} \frac{dx^\alpha}{d\tau} \tag{1.6}$$

This leads to the geodesic equation

$$\frac{d^2 x^\nu}{d\tau^2} + \frac{\partial x^\nu}{\partial \xi^\alpha} \frac{\partial^2 \xi^\alpha}{\partial x^\mu \partial x^\sigma} \frac{dx^\mu}{d\tau} \frac{dx^\sigma}{d\tau} = 0 \tag{1.7}$$

Which can be re-expressed as

$$\frac{d^2 x^\nu}{d\tau^2} + \Gamma^\nu_{\mu\sigma} \frac{dx^\mu}{d\tau} \frac{dx^\sigma}{d\tau} = 0 \tag{1.8}$$

Introducing the Christoffel symbols

$$\Gamma^{\nu}_{\mu\sigma} = \frac{\partial x^{\nu}}{\partial \xi^{\alpha}} \frac{\partial^2 \xi^{\alpha}}{\partial x^{\mu} \partial x^{\sigma}} \tag{1.9}$$

These Christoffel symbols allow us to define for any vector A^{μ} the covariant derivative operation that keeps the same form when using any coordinate system

$$\bigtriangledown_{\alpha} A^{\mu} = \frac{\partial A^{\mu}}{\partial x^{\alpha}} \Gamma^{\mu}_{\alpha\sigma} A^{\sigma} \tag{1.10}$$

Knowing that, like in the Newtonian case, acceleration four-vector of a massive particle can be defined as

$$a^{\mu} = \frac{dx^{\nu}}{d\tau} \bigtriangledown_{\nu} \frac{dx^{\mu}}{d\tau} \tag{1.11}$$

one can identify in (1.8) the acceleration four-vector components. This lead us to the conclusion that a massive particle follow a space-like geodesic trajectory in space-time[1]. From this observation we generally refer to the geodesic equation to designate the equation of the motion of a particle. Furthermore one can show that the Christoffel symbols can be re-expressed as

$$\Gamma^{\nu}_{\mu\sigma} = \frac{1}{2} g^{\nu\alpha} (\partial_{\mu} g_{\sigma\alpha} + \partial_{\sigma} g_{\alpha\mu} - \partial_{\alpha} g_{\mu\sigma}) \tag{1.12}$$

Where $g^{\nu\alpha}$ is the inverse metric tensor, defined with $g^{\nu\alpha} g_{\alpha\sigma} = \delta^{\nu}_{\sigma}$, $\delta^{\nu}_{\sigma} = 1$ if $\nu = \sigma$ and $\delta^{\nu}_{\sigma} = 0$ if $\nu \neq \sigma$. As a result, the geodesic expression (1.8) can be rewritten only with the metric and its derivatives. In conclusion, with the geodesic equation one can find the location of the particle as a function of time providing, like in Newtonian gravity, two initial conditions (for instance location and velocity at some initial time). But this requires to know the metric tensor components. With General Relativity the space-time is not necessarily flat and the metric is a dynamical object which can significantly differ from the Minkowski metric. The major question in General Relativity then becomes how to derive the metric for a given physical problem taking into account the mass and energy distribution in the space-time.

Einstein equations

In the general case we are looking for a fundamental equation which determines the metric in function of the mass and energy distribution in space-time, something like

$$G_{\mu\nu} = \kappa T_{\mu\nu} \tag{1.13}$$

[1]For massless particle the geodesic expression take the same form but with a generic parameter along the trajectory instead of τ which cannot be defined

In this expression, $T_{\mu\nu}$ is the stress-energy tensor accounting the mass and energy distribution, κ is a constant and $G_{\mu\nu}$ is the tensor that describes space-time curvature and should be expressed using $g_{\mu\nu}$ and its derivatives. The $T_{\mu\nu}$ expression can be found knowing that this equation has to be independent of the coordinate system (i.e $T_{\mu\nu}$ is a tensor) and that this form generalises the Poisson equation

$$\Delta U = 4\pi G \rho_m \tag{1.14}$$

Which links the Newtonian gravitational potential U and the mass density ρ_m. Of course the equation (1.13) should become the equation (1.14) in the Newtonian limit. In order to find the complete expression of $G_{\mu\nu}$, one has to solve some mathematical problem to find a tensor expression constructed with $g_{\mu\nu}$ and its derivatives. Note that, knowing the conservation equation $\Delta_\mu T^{\mu\nu} = 0$, the solution should also satisfies $\Delta_\mu G^\mu_{\ \nu} = 0$. Finally the $G_{\mu\nu}$ can be expressed as

$$G_{\mu\nu} = R_{\mu\nu} - \frac{1}{2} R g_{\mu\nu} \tag{1.15}$$

Where $R_{\mu\nu}$ is the Ricci tensor expressed as[2]

$$R_{\mu\nu} = \partial_\rho \Gamma^\rho_{\mu\nu} - \partial_\mu \Gamma^\rho_{\rho\nu} + \Gamma^\sigma_{\mu\nu}\Gamma^\rho_{\sigma\rho} + \Gamma^\rho_{\mu\sigma}\Gamma^\sigma_{\nu\rho} \tag{1.16}$$

And $R = g^{\mu\nu} R_{\mu\nu}$ is the Ricci scalar. At the end the Einstein equations becomes

$$R_{\mu\nu} - \frac{1}{2} R g_{\mu\nu} = \frac{8\pi G}{c^4} T_{\mu\nu} \tag{1.17}$$

While Einstein firstly proposed to introduce a new term using a cosmological constant Λ allowing a model of static universe

$$G_{\mu\nu} + \Lambda g_{\mu\nu} = \frac{8\pi G}{c^4} T_{\mu\nu} \tag{1.18}$$

It was rapidly discarded once observations showed that the universe is expanding, however later observations of distant supernova [6, 7] and cosmic microwave background [8, 9, 10, 11] suggested to reintroduce the cosmological constant to account for the acceleration of the universe expansion. This cosmological constant is interpreted as an hypothetical unknown mass–energy density, the *dark energy*. One can re-express this new term as an effective stress-energy tensor

$$T^\Lambda_{\mu\nu} = -\frac{\Lambda c^4}{8\pi G} g_{\mu\nu} \tag{1.19}$$

[2]The Ricci tensor is a contraction of the Riemann tensor $R^\rho_{\lambda\mu\nu} = \partial_\lambda \Gamma^\rho_{\mu\nu} - \partial_\mu \Gamma^\rho_{\lambda\nu} + \Gamma^\sigma_{\mu\nu}\Gamma^\rho_{\sigma\lambda} - \Gamma^\sigma_{\lambda\nu}\Gamma^\rho_{\sigma\mu}$ which expresses the curvature of the space-time.

1.2 Linearised General Relativity

The Einstein equations presented above are partial differential equations for metric components $g_{\mu\nu}$. They are non linear at all orders and no general solutions exist. However linearise these equations allow to study solutions sufficiently close to exact solution in the case of perturbation of the Minkowski metric. This analysis is very useful for astrophysics since the deformation of the metric compare to the Minkowski's metric are generally very small, important deviation being limited to the neighborhood of extreme objects like neutrons star and black holes.

1.2.1 Weak field approximation

In this section we consider space-time where the geometry is the slightly deformed Minkowski metric[3] meaning that the metric $g_{\mu\nu}$ can be written in the form

$$g_{\mu\nu} = \eta_{\mu\nu} + h_{\mu\nu}, \quad |h_{\mu\nu}| \ll 1 \tag{1.20}$$

where $h_{\mu\nu}$ is the metric perturbation. The derivatives of $h_{\mu\nu}$ are also supposed to be small. As a first step we can express the Christoffel symboles by substituting (1.20) in (1.12)

$$\begin{aligned} {}^{(0)}\Gamma^{\lambda}_{\mu\nu} &= 0, \\ {}^{(1)}\Gamma^{\lambda}_{\mu\nu} &= \frac{1}{2}\eta^{\lambda\sigma}(\partial_\mu h_{\sigma\nu} + \partial_\nu h_{\mu\sigma} - \partial_\sigma h_{\mu\nu}) \end{aligned} \tag{1.21}$$

where the top left index indicates the order. We deduce the Ricci tensor component at the first order

$${}^{(1)}R_{\mu\nu} = \partial^{(1)}_{\rho}\Gamma^{\rho}_{\mu\nu} - \partial^{(1)}_{\mu}\Gamma^{\rho}_{\rho\nu} \tag{1.22}$$

which gives the Einstein tensor component, using (1.21) and (1.15)

$${}^{(1)}G_{\mu\nu} = \frac{1}{2}\left[\partial_\mu\partial^\alpha\bar{h}_{\alpha\nu} + \partial_\nu\partial^\alpha\bar{h}_{\alpha\mu} - \partial^\beta\partial_\beta\bar{h}_{\mu\nu} - \eta_{\mu\nu}\partial^\alpha\partial^\beta\bar{h}_{\alpha\beta}\right] \tag{1.23}$$

defining

$$\bar{h}_{\mu\nu} = h_{\mu\nu} - \frac{1}{2}h\,\eta_{\mu\nu}, \quad h = \eta^{\alpha\beta}h_{\alpha\beta} \tag{1.24}$$

we obtained the expression of Einstein's tensor in the linear order, which depends on the second derivatives of the perturbations $h_{\mu\nu}$.

[3]It is of course possible to consider the linear perturbations of the metric with respect to other reference geometries. An important example is the consideration of cosmological metric $\widetilde{g} = a^2(\tau)(\eta_{\mu\nu} + h_{\mu\nu})dx^\mu dx^\nu$, where $a(\tau)$ is the scale factor.

1.2.2 Lorenz gauge

In order to continue to simplify the linearised Einstein equations it is useful to choose a specific gauge, or in other words to choose a new coordinate system. While changing the coordinates the $g_{\mu\nu}$ components and therefore the perturbations $h_{\mu\nu}$ change. I will restrict myself here to changes in coordinates such that the new perturbations $h'_{\mu\nu}$ also checks the condition $\|h'_{\mu\nu}\| \ll 1$. In practice, this leads to consider the changes in infinitesimal coordinates

$$x^\mu \to x'^\mu = x^\mu + \xi^\mu(x) \tag{1.25}$$

where ξ^μ is treated as a perturbation quantity of the same order as the perturbations $h_{\mu\nu}$. Noticing that $h'_{\mu\nu}(x')$ can be replaced by $h'_{\mu\nu}(x)$ at the first order, we end up with the perturbation metric transformation[4]

$$h_{\mu\nu} \to h'_{\mu\nu} = h_{\mu\nu} - \partial_\mu \xi_\nu - \partial_\nu \xi_\mu \tag{1.26}$$

One can notice that the perturbation $\bar{h}_{\mu\nu}$, defined in (1.24), are transformed according to

$$\bar{h}_{\mu\nu} \to \bar{h}'_{\mu\nu} = \bar{h}_{\mu\nu} - \partial_\mu \xi_\nu - \partial_\nu \xi_\mu - \partial_\lambda \xi^\lambda \eta_{\mu\nu} \tag{1.27}$$

and so

$$\partial^\mu \bar{h}_{\mu\nu} \to \partial^\mu \bar{h}'_{\mu\nu} = \partial^\mu \bar{h}_{\mu\nu} - \partial^\mu \partial_\mu \xi_\nu \tag{1.28}$$

We can then use the freedom in the choice of coordinates to impose the following condition on the metric perturbations

$$\partial^\mu \bar{h}_{\mu\nu} = 0 \tag{1.29}$$

Indeed we can always find a new coordinate system x'^μ where the condition (1.29) is satisfied looking for a vector field ξ_ν with $\partial^\mu \partial_\mu \xi_\nu = \partial^\mu \bar{h}_{\mu\nu}$. The main interest of the gauge condition (1.29), called Lorenz gauge, is to simplify the linearised Einstein equations since the expression (1.23) is reduced in this gauge to

$${}^{(1)}G_{\mu\nu} = -\frac{1}{2} \partial^\sigma \partial_\sigma \bar{h}_{\mu\nu} \tag{1.30}$$

[4]This transformation is analogous to the gauge transformation for the quadri-potential A_μ in electromagnetism

1.2.3 Gravitational wave propagation

In the absence of matter, $T_{\mu\nu} = 0$ the linearised Einstein equations are therefore reduced to

$$\partial^\sigma \partial_\sigma \bar{h}_{\mu\nu} = 0 \tag{1.31}$$

The general solutions of this equation are linear combinations of plane waves, so called gravitational waves, which propagate at the speed of light. Like for the electromagnetism equations, we need to determine the number of degrees of freedom. One can show that an adequate choice of function ξ_μ allow to get

$$h = 0, \quad h_{0i} = 0 \tag{1.32}$$

These relations implies that $h_{\mu\nu} = \bar{h}_{\mu\nu}$ and we can resume the restrictions imposed to

$$h^{TT} = 0, \quad \partial^\mu h^{TT}_{\mu\nu} = 0, h^{TT}_{0i} = 0 \tag{1.33}$$

defining the transverse and traceless gauge where in the gauge, $h^{TT}_{\mu\nu}$ is the metric perturbation. In order to resolve the equation

$$\partial^\sigma \partial_\sigma h^{TT}_{\mu\nu} = 0 \tag{1.34}$$

I will consider the solution as monochromatic plane waves superposition

$$h^{TT}_{\mu\nu} = H_{\mu\nu} e^{ik_\sigma x^\sigma} \tag{1.35}$$

The wave equation (1.34) implies that the wave vector k_σ is light-like, i.e. $\eta_{\mu\nu} k^\mu k^\nu = 0$. Again we can choose a coordinate system which fit with our needs, to unveil the gravitational waves properties I will choose here one such that the propagation direction is parallel to the z axis. The wave vector is then expressed as

$$k^\mu = (\omega, 0, 0, \frac{\omega}{c}) \tag{1.36}$$

The gauge condition (1.33) imposes

$$H = 0, \quad k^\mu H_{\mu\nu}, \quad \omega(H_{0\nu} + H_{z\nu}), \quad H_{0i} = 0 \tag{1.37}$$

This leads to the conclusion that most of the components are null and among them only two are independent, for instance H_{xx} and H_{xy}. Finally, we have

$$H_{\mu\nu} = \begin{pmatrix} 0 & 0 & 0 & 0 \\ 0 & H_{xx} & H_{xy} & 0 \\ 0 & H_{xy} & -H_{xx} & 0 \\ 0 & 0 & 0 & 0 \end{pmatrix} \tag{1.38}$$

In conclusion gravitational waves present only two independent degrees of freedom. The H_{xx} mode is generally called + polarisation and noted H_+ and the mode H_{xy} is generally called $\times$ polarisation and noted $H_\times$. The final solutions takes the form

$$h^{TT}_{\mu\nu} = \begin{cases} h_+ = H_+ e^{iw(t-\frac{z}{c})} \\ h_\times = H_\times e^{iw(t-\frac{z}{c})} \end{cases} = \begin{pmatrix} 0 & 0 & 0 & 0 \\ 0 & H_+ & H_\times & 0 \\ 0 & H_\times & -H_+ & 0 \\ 0 & 0 & 0 & 0 \end{pmatrix} e^{i\omega(\frac{z}{c}-t)} \tag{1.39}$$

1.2.4 Gravitational waves effects on matter

Now that we know that gravitational waves exist, we can ask ourselves what an observer will observe if a gravitational wave passes through its environment. Let's imagine a test particle moving freely, which is to say it is not subject to any force but the gravity, and let's investigate how its spatial position varies in the presence of a gravitational wave. As I described in section 1.1 this particle will follow a trajectory described by a geodesic equation in a space-time characterised by the metric

$$\boldsymbol{g} = -dt^2 + (\delta_{ij} + h^{TT}_{ij})dx^i dx^j \tag{1.40}$$

At the first perturbation order the spatial components of this equation are

$$\frac{d^2x^i}{d\tau^2} = -\Gamma^i_{\mu\nu}u^\mu u^\nu = -{}^{(1)}\Gamma^i_{00} \tag{1.41}$$

Injecting the metric (1.40) in the expression (1.21), we get

$${}^{(1)}\Gamma^i_{00} = 0 \tag{1.42}$$

where the top left index indicate the order. This means that the particle is at rest in the chosen coordinate system. If we inspect now the distance between two free particles A and B[5], within the transverse and traceless gauge we have

$$L = \sqrt{g_{ij}\Delta x^i \Delta x^j}, \quad \Delta x^i = x^i_B - x^i_A \tag{1.43}$$

We introduce the unitary vector n^i that joins A and B and therefore

$$\begin{cases} \Delta x^i = L_0 \\ L_0 = \sqrt{\delta_{ij}\Delta x^i \Delta x^j} \end{cases} \tag{1.44}$$

Using the unitary property, we can express L as

[5]The distance L is defined as half of the proper time (of A) that elapses between an emission of a light beam from A, its reflection on B and its reception again on A, $L = \frac{1}{2}c(\tau^{rec}_A - \tau^{em}_A)$.

$$L = L_0[1 + h_{ij}^{TT} n^j n^j]^{1/2} \tag{1.45}$$

At first order in h this expression becomes

$$L = L_0[1 + \frac{1}{2} h_{ij}^{TT} n^j n^j] \tag{1.46}$$

Thus, the relative variation of the distance L to the passage of a gravitational wave is given by

$$\frac{\delta L}{L_0} = \frac{1}{2} h_{ij}^{TT} n^i n^j \tag{1.47}$$

This expression shows that the relative change in distance is proportional to the amplitude of the wave h, also called *strain amplitude*. To visualize the impact of the gravitational wave, it is convenient to introduce new coordinates

$$\begin{cases} \widehat{x}^0 = x^0 \\ \widehat{x}^i(t) = x^i + \frac{1}{2} h_{ij}(t, 0, 0, 0) x^j \end{cases} \tag{1.48}$$

Let's take the example of a monochromatic gravitational wave propagating along the z-axis. As we saw in equation (1.38) we have only two non null components, representing two polarisations and we finally have

$$\begin{aligned} \widehat{x}(t) &= x_0 + \frac{1}{2}[H_+ x_0 + H_\times y_0] e^{i\omega t} \\ \widehat{y}(t) &= y_0 + \frac{1}{2}[H_\times x_0 - H_+ y_0] e^{i\omega t} \\ \widehat{z}(t) &= z_0 \end{aligned} \tag{1.49}$$

The deformation, differential effect, obtained in equation (1.49) is presented for a ring of test particles in the plan $z = 0$ in the figure (1.2).

1.2.5 Gravitational wave generation

General solution

Now that we have seen how gravitational waves propagate in the vacuum, we can wonder how they can be produced in the presence of matter. One can look at general solution for the linearised Einstein equations

$$\partial_\sigma \partial^\sigma \bar{h}_{\mu\nu} = -16\pi G \, T_{\mu\nu} \tag{1.50}$$

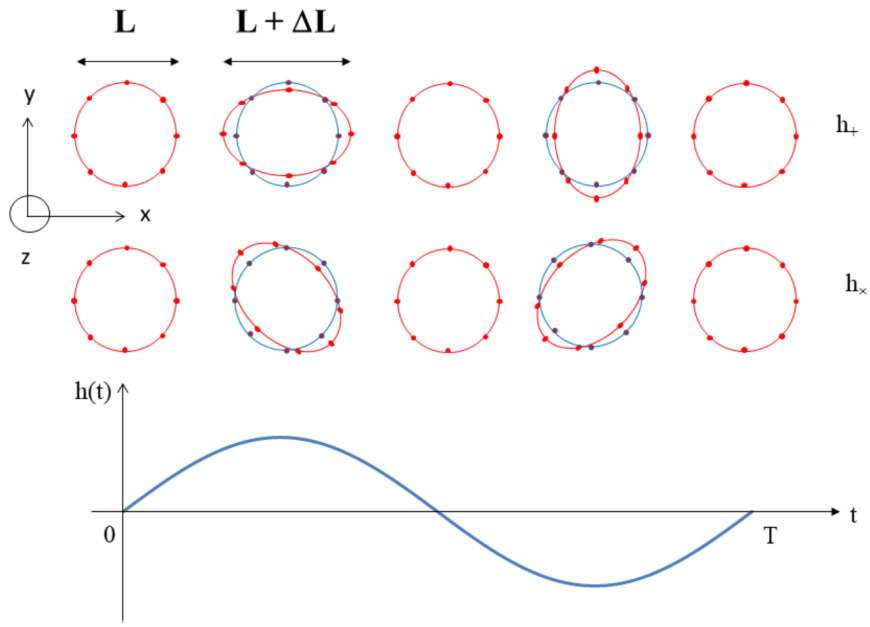

Figure 1.2: Effect of the h_+ and $h_\times$ polarizations of a gravitational wave propagating along the z-axis on a ring of free test masses according to the evolution with time of the amplitude of the gravitational wave h. Figure from [12].

Without going into details here [2], it will lead to the conclusion that the expression of gravitational waves emitted by a matter distribution is

$$\bar{h}_{ij}(t,\vec{x}) = \frac{2G}{r}\left(\frac{d^2}{dt^2}I_{ij}\right), \quad I^{ij} = \int d^3\, y\, \rho\, y^i\, y^j \tag{1.51}$$

where I^{ij} is called the quadrupole moment of the source[6] and ρ is the mass density. Such as electromagnetic waves, gravitational waves carry the energy emitted away from their sources. Predicting the long-term behavior of the source therefore involves estimating the energy loss in the form of a gravitational wave. Without demonstration, the flux of energy and the power emitted or luminosity are given by [2]

[6]This expression is still true when the movement of masses, and thus the stress-energy tensor, is determined by the deformation of space-time generated by the masses.

$$F = \frac{\langle \dot{h}_+ \dot{h}_+ + \dot{h}_\times \dot{h}_\times \rangle}{16\pi G}$$
$$L_G = \frac{G}{5} \langle \dddot{Q}_{ij} \dddot{Q}^{ij} \rangle \tag{1.52}$$

where the brackets $\langle\rangle$ signify an average over many wavelengths, $\dot{h}$ represents the time derivative of the gravitational wave and $\dddot{Q}_{ij}$ is the third time derivative of the reduced quadrupole moment defined as

$$Q_{ij} = I_{ij} - \frac{1}{3}\delta_{ij}\delta^{kl} I_{kl} \tag{1.53}$$

L_G expresses the total amount of energy, per unit of time, emitted by the source in the form of a gravitational wave. These expression are essential to estimate the amplitude of gravitational waves that can be generated by a source.

1.3 Gravitational wave sources

1.3.1 Compact binary coalescence

To illustrate the results of the previous parts, I propose here to describe in more detail an example of an astrophysical system producing gravitational waves, a binary system. Compact binary systems consist of compact bodies (neutron stars or black holes) orbiting around the common center of gravity. This type of system represents the most promising source of gravitational waves for current detectors (and the only one detected to date). The importance of this type of system for multi-messenger astronomy and their association with short gamma ray bursts will be discussed in the chapters 3 and 4.

Movement of the two bodies

I choose here to treat the motion in the Newtonian approximation. The equations of motion for each of the bodies, with mass M_1 and M_2 respectively, impose that the separation vector $\vec{d} = \vec{x_1} - \vec{x_2}$ satisfies the equation

$$\ddot{\vec{d}} = -\frac{GM_{tot}}{d^3}\vec{d} \tag{1.54}$$

where $M_{tot} = M_1 + M_2$ is the total mass of the system. Choosing x and y coordinates in the plane of the binary system, the origin being placed at the

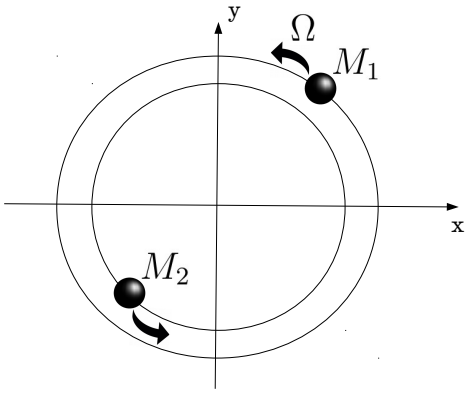

Figure 1.3: binary system in the reference frame of the barycenter of the two bodies

barycenter of the system and assuming circular motion with angular velocity Ω, i.e $\vec{d} = \{d\ \cos(\Omega t),\ d\ \sin(\Omega t)\}$, it implies the Newtonian form of Kepler's third law

$$\Omega = \frac{(GM_{tot})^{1/2}}{d^{3/2}} \tag{1.55}$$

It is common to treat the total energy of such system as the total energy of a fictive particle of mass $\mu = M_1 M_2 / M_{tot}$ moving in the potential $V(d) = -GM_{tot}\mu/d$, In this case the total energy of the system can be written as

$$E = \frac{1}{2}\mu\,\Omega^2 d^2 - \frac{G\mu M_{tot}}{d} = -\frac{G\mu M_{tot}}{2d} \tag{1.56}$$

Finally the coordinates of the two bodies are

$$\begin{aligned} x_1 &= \frac{M_2}{M_{tot}} d\cos(\Omega t) \qquad & x_2 &= \frac{M_1}{M_{tot}} d\cos(\Omega t) \\ y_1 &= \frac{M_2}{M_{tot}} d\sin(\Omega t) \qquad & y_2 &= \frac{M_1}{M_{tot}} d\sin(\Omega t) \end{aligned} \tag{1.57}$$

Gravitational wave emission

The two bodies are considered as punctual, consequently the quadrupole moment of the system is

$$I_{ij} = \int d^3x \rho x_i x_j = M_1 (x_1)_i (x_1)_j + M_2 (x_2)_i (x_2)_j \tag{1.58}$$

Substituting in the equation (1.51) we can deduce the emitted gravitational wave form

$$\bar{h}_{ij}(t,\vec{x}) = \frac{4G^2\mu M_{tot}}{rd}\begin{pmatrix} -\cos 2\Omega t & -\sin 2\Omega t & 0 \\ -\sin 2\Omega t & \cos 2\Omega t & 0 \\ 0 & 0 & 0 \end{pmatrix} \tag{1.59}$$

Assuming that the two bodies have the same mass we can estimate the amplitude of the emitted gravitational waves as

$$h \sim \frac{(GM)^2}{rd} \sim \frac{r_s^2}{rd} \tag{1.60}$$

where r_s is the Schwarzschild radius associated to the mass M. This will be the measured quantity (see equation 2.8) and only decreases as $1/r$. For compact object like neutrons stars or black holes $r_s \sim 10$ km and supposing that the two bodies are very close, i.e. $d \sim 10r_s \sim 100$ km, we get for a distance of $r \sim 100$ Mpc an amplitude of $h \sim 10^{-21}$. In order to directly detect such gravitational waves it is mandatory to reach a length variation measurement sensitivity of the order of 10^{-21}. This number may seem at first sight inaccessible, but to date dozens of systems of this type have been detected directly. I will come back to the considerable efforts put in place to complete such a detection in chapter 2.

System evolution, energy loss

For a monochromatic wave of amplitude h and frequency f and substituting (1.59) in the expression (1.52) we can show that of the flux emitted and the luminosity are reduced to

$$\begin{aligned} F &= \frac{\pi c^3}{4G} f^2 h^2 \\ L_G &= \frac{32}{5}\frac{G^4\mu^2 M_{tot}^3}{c^5 d^5} \end{aligned} \tag{1.61}$$

where the c factors are explicitly displayed. Taking $f = 100$Hz and $h \sim 10^{-21}$ we find an estimation of $F \sim 0.003\, W.m^{-2}$. So a gravitational wave of very small amplitude still carries an appreciable amount of energy.

The emission of gravitational waves results in a loss of system total energy

$$\dot{E} = -L_G \tag{1.62}$$

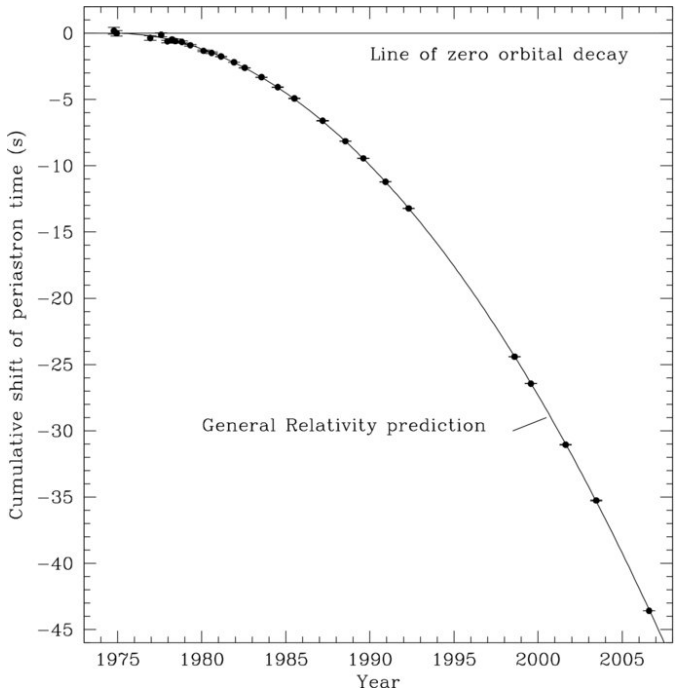

Figure 1.4: Cumulative shift of the periastron time caused by the loss of energy by gravitational radiation. Data points represent measurements, with error bars mostly too small to see. Solid line represent the General Relativity prediction. Figure from [13].

this implies a gradual approximation of the two bodies and a decrease in the period $P = \frac{2\pi}{\Omega}$ of the binary system. Indeed from (1.55) and (1.56) we know that P, d, and E variation are connected by

$$\frac{\dot{E}}{E} = -\frac{\dot{d}}{d} = -\frac{2\dot{P}}{3P} \tag{1.63}$$

we can deduce

$$\dot{P} = \frac{3P}{2E} L_G = -\frac{96}{5}(2\pi)^{8/3} G^{5/3} \mu M_{tot}^{2/3} P^{-5/3} \tag{1.64}$$

If one knows the bodies mass, observing the system period allows to predict the period diminution. This strategy was the first one used to provide an evidence of the existence of gravitational waves. Indeed, observing the same radio binary pulsar PSR B1913+16 for three decades people managed to observe an orbital period decay in perfect agreement with one caused by the loss of energy by gravitational radiation [13].

Frequency variation of gravitational waves

The evolution of the distance between the two bodies is determined by the relation

$$\dot{d} = -\frac{64}{5}\frac{G^3 \mu M_{tot}^2}{d^3} \tag{1.65}$$

which is obtained by combining (1.63) and (1.64). By integrating, we find

$$d^4 = \frac{256}{5} G^3 \mu M_{tot}^2 (t_c - t) \tag{1.66}$$

where t_c corresponds to the (theoretical) instant of collision. The evolution of the binary system has consequences on the frequency of gravitational waves. Since

$$f = \frac{2\Omega}{2\pi} = \frac{2}{P} \tag{1.67}$$

we have

$$\frac{\dot{f}}{f} = -\frac{\dot{P}}{P} \quad \Rightarrow \quad \dot{f} = \frac{96}{5}\pi^{8/3} G^{5/3} \mu M_{tot}^{2/3} f^{11/3} \tag{1.68}$$

The evolution over time of the frequency and amplitude are therefore

$$\begin{aligned} f &\sim (t_c - t)^{-3/8} \\ h \sim \frac{1}{d} &\sim (t_c - t)^{-1/4} \end{aligned} \tag{1.69}$$

We can thus see that the coalescence of a binary system emits a very specific gravitational signal with a frequency and an amplitude that increases over time (figure 1.5), this signal is called "chirp".

1.3.2 Sources for ground based detectors

As we have seen the efficiency in converting mechanical energy in a system into gravitational radiation is very low, leading to very weak signal. In practice, for observation, this means that scientists seeking to detect gravitational waves must focus on sources with extreme properties (compact and relativistic). Therefore the sources that are likely to be detected will originate from astrophysical objects. I propose in this section to focus on sources detectable by ground-based interferometric detectors as Virgo and LIGO, i.e. sources which are expected to emit gravitational waves powerful enough in the high frequency band between 10 Hz and 10^4 Hz (see chapter 2).

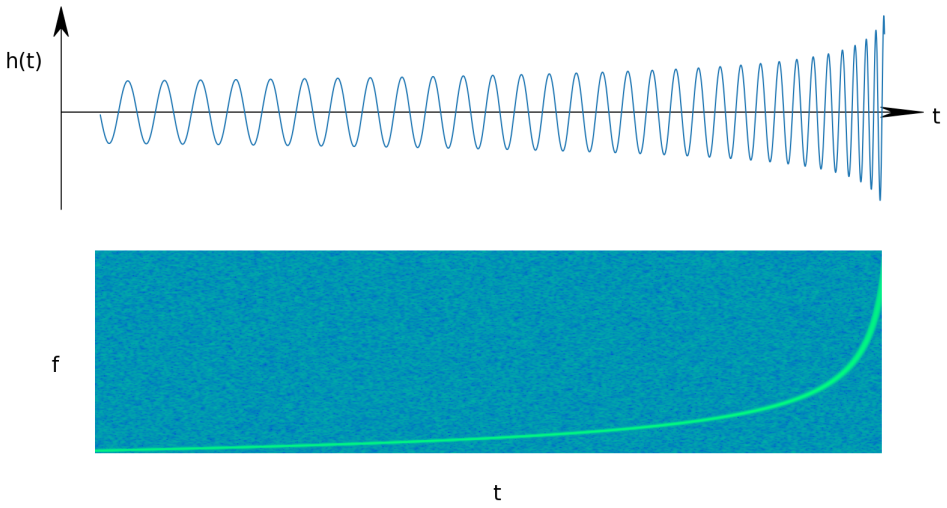

Figure 1.5: Top: Shape of the gravitational signal emitted during the coalescence of a binary system, equation (1.69). Bottom: Spectrogram of the top signal.

Gravitational wave bursts

To date, the only population of signal detected with ground-based detectors are the gravitational waves transients, or burst, emissions that have only a short duration compared to the observation time. The category of systems producing this type of gravitational wave is varied and the final signal shape is expected to be very different. In any case, the detection of this type of signal is highly affected by the presence of transient noise (named glitches) in ground-based detectors that can mimic a true signal, this will be discussed in the chapter 2.

One of the important sources of burst signal for ground-based detectors are compact binary system, i.e. binary black holes (BBH), binary neutrons stars (BNS) or neutrons star black hole binary (NSBH). We discussed in the previous section a simple model of the emission from such sources, but the whole inspiral phase can be retrieved using analytical post-Newtonian theory. The total inspiral signal depends on the physical parameters of the binary system: masses, spins and eccentricity. But accurate waveforms can be constructed and thus matched filtering based searches are possible. While binary systems are expected to spiral inwards over billions of years, only the signal from their last instants is detectable by the ground based detectors, when the gravitational waves frequency is sufficiently high to fall in the detectors observational bandwidth. This represents between ~ 0.1s for the heaviest BBH and hundreds of seconds for lowest-mass BNS. To date ~ 50

of this kind has been detected [14, 15].

Apart from compact binary coalescence, without being exhaustive, we can mention core-collapse supernovae, considered as one of the most promising sources for ground based detectors. While the massive star core-collapse mechanisms has been studied for half a century, and knowing that gravitational wave emission is now predicted in different phases of the collapse [16, 17, 18], theoretical models and simulations need to be improved on several fronts to have a complete catalogue of all possible waveforms. For instance currents waveforms templates do not take (much) into account non aligned spins, radiation modes beyond the quadrupole, precessing spins, orbital eccentricity [19]. This kind of source may produce gravitational waves lasting up to few tens of seconds in the observational bandwidth of ground based detectors. But the amplitude of the signal produced is much smaller than for compact binary, with the current detectors sensitivity, the signal may be marginally visible for a source within our galaxy.

Others sources of gravitational wave bursts emitting in the ground-based detector sensitivity range are proposed (accretion disk instabilities, rotational instabilities, cosmics strings, pulsar glitches...), see [5] and references within, but their estimated amplitude and rate makes them less likely to be observed with current detectors.

Continuous waves

The sources of continuous gravitational waves are sources considered to be constantly emitting quasi-monochromatic gravitational waves. The primary expected sources for ground-based detectors are rotating neutron stars (or pulsar) with some asymmetric distortion in its shape that is not along its rotation axis. These distortions could be produced and maintained through extremely large internal magnetic fields or could be "frozen" into the crust or core of the star after it was born [20]. The search for continuous wave signals from pulsars is divided into two populations, according to whether the pulsar has already been observed or not. There are hundreds of known pulsars [21][7] spinning fast enough so that their gravitational wave emission fall in the detection band of the current ground-based detectors. For such objects already observed with electromagnetic detectors we have access to several information (frequency of rotation, sky position, ...) hence the gravitational waveform is well modelled. While the searches are able to put deep limits on gravitational-wave emission, especially for some of the nearby known pulsars, no direct detection has been observed [22, 23].

[7]For updated catalog see https://www.atnf.csiro.au/people/pulsar/psrcat/

Stochastic gravitational wave background

The incoherent superposition of weak individually unresolvable cosmological and astrophysical sources is expected to produce stochastic background of gravitational waves (SGWB). While astrophysical sources are typically the sources discussed before, the cosmological ones include amplification of quantum vacuum fluctuations during inflation [24], electro-weak phase transitions [25], pre Big Bang models [26, 27] and cosmics (super-)strings [28, 29, 30]. The stochastic gravitational-wave background is described by the gravitational-wave energy density defined as

$$\Omega_{GW}(f) = \frac{f}{\rho_c}\frac{d_{\rho GW}}{df} \tag{1.70}$$

where ρ_c is the critical energy density of the universe and $d_{\rho GW}$ is the gravitational wave energy density contained in the frequency range $[f, f + df]$ [31]. While no signal was detected, upper limits have been placed on the energy density of the background from 10 Hz to 1000 Hz [32].

Chapter 2

Gravitational wave detection

2.1 Gravitational wave detectors

In this section, I will shortly review the fundamental principle, detector concept and data analysis achieved to detect gravitational waves focusing on the ground based interferometric detectors. Please note that only a short part of the physics developments, and so the scientists, that have contributed to the research of gravitational waves are mentioned here.

2.1.1 History

As seen in the chapter 1 gravitational waves are one of the early prediction of General Relativity theory firstly published in November 1915 by Einstein. However for several decades the debate about the existence and detectability of gravitational waves has remained open. The Chapel Hill conference in 1957 is known to leave a significant impact on the vision of the scientific community on gravitational waves [33]. In this conference discussions on the effect a gravitational pulse would have on a particle when passing by, whether or not the wave transmits energy to the particle (i.e. can gravitational waves do work?), provided a required boost to gravitational research. Indeed a description of a thought experiment (the so-called sticky bead argument) that shows that gravitational waves contain energy and could be detected was discussed [33, 34, 5]. Among the Chapel Hill audience, Joseph Weber was present, fascinated by discussions about gravitational waves and device that could detect them, he chose to work on this topic and proposed few years later the design of a detector of gravitational waves measuring vibrations induced in a mechanical system [35]. After several years of trying to fix the many experimental issues related to his gravitational wave detector he finally claimed the detection of gravitational waves [36, 37]. Unfortunately, after years of excitement, from attempted replication and controversy emerged the consensus that Weber's results could not be duplicated by other workers and thus that they were most likely incorrect [34]. Later, studies showed that the Weber's detector design was affected by quantum fluctuations with an amplitude greater than the expected gravitational waves [38]. Despite the non detection, Weber's efforts remain to be mentioned as they have strongly encouraged the scientific community to develop

today's useful data detection and analysis techniques.

2.1.2 Detection principle

Using an interferometric detector shaped like a Michelson interferometer to detect gravitational waves is an idea almost as old as Weber's bars [39]. Without going into details about the historical development of the ideas and concepts necessary for the realization of the current design of gravitational wave detectors, I will focus in this section on the general principle of detection of the existing network. The story of the Virgo and LIGO projects development is nicely and concisely presented in [5].

For an Michelson interferometer the interference pattern induced by difference in arm length consists of interference fringes. The idea of the detection is to put a photon detector (photodiode) at one of the dark fringe of the initial interference pattern and to register the detected signal of this photon detector over time. The interference pattern will change according to any change in the differential length between the beam-splitter and the mirror at the ends of its orthogonal arms. This change will be detected by the photon detector as it will be temporally out of the dark fringe, thus this design is well suited to measure time dependent differential effects. The essential idea of using interferometric detector is, in fact, the ability to detect a differential signal from a set of free falling test masses. Like presented in chapter 1, from these test masses we can directly infer the characteristics of the Riemann tensor. If one consider that the beam-splitter and the mirrors can be treated as free-falling masses, a gravitational wave passing though the detector will then induce a space-time deformation which will result in a change in the differential length and so a signal in the photon detector. The basic configuration of a Michelson interferometer is shown in figure 2.1 . Note that with this design, there is no need to connect the test masses so they can be put very far apart (by enlarging the size of the arms), this produce a much larger relative motion making the signal easier to detect.

In order to detail why this measure of the photon detector signal, i.e. the optical path difference, is a direct measure of the gravitational wave strain amplitude one can imagine the following highlighting. We choose the coordinates origin to be on the beam-splitter and the x and y axis along the two arms. Assuming a plus polarized gravitational wave incoming from the z direction (normal incidence), the metric at any time t is, as described in chapter 1, given by (1.39) which yields the equation for light propagation

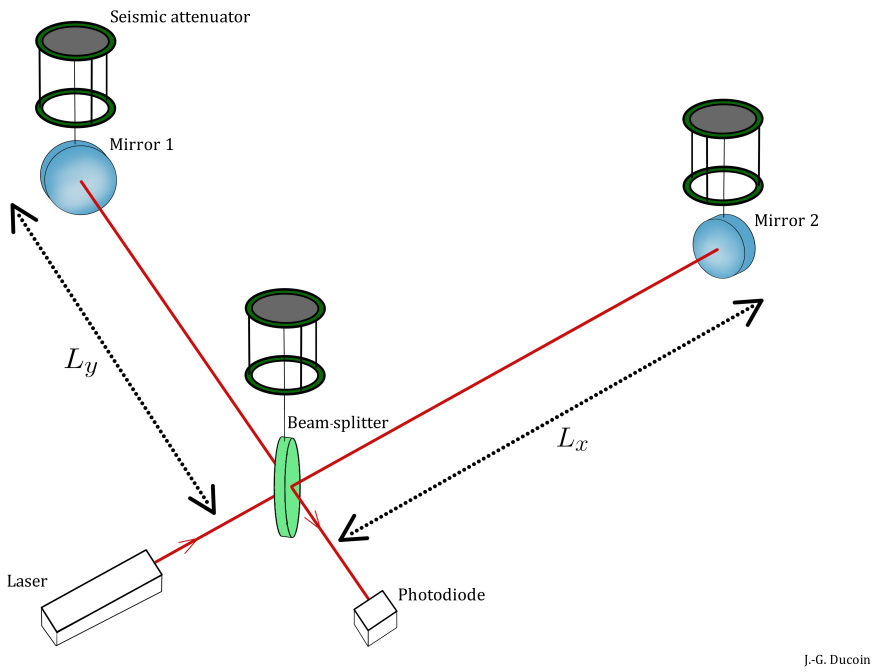

Figure 2.1: Scheme of the basic of a Michelson Interferometer gravitational wave detector. In blue the arm end mirrors, in green the beam-splitter. Mirrors are suspended with seismic attenuators. The role of these seismic attenuators (called superattenuators for Virgo) is discussed in section 2.1.5.

$$\begin{aligned} 0 = ds^2 &= (\eta_{\mu\nu} + h_{\mu\nu})dx^\mu dx^\nu \\ &= -dt^2 + (1 + h_+(t))dx^2 \quad \text{for the arm along the } x \text{ axis,} \\ &= -dt^2 + (1 - h_+(t))dy^2 \quad \text{for the arm along the } y \text{ axis.} \end{aligned} \tag{2.1}$$

Calling L_0 the arm length, supposed identical for both arms, we can now integrate these relations:

$$\begin{aligned} L_x &= \int dt = \int_0^{L_0} \sqrt{1 + h_+(t - x)}dx \\ L_y &= \int dt = \int_0^{L_0} \sqrt{1 - h_+(t - y)}dy \end{aligned} \tag{2.2}$$

L_x and L_y being the optical path in the arm along the x and y axis respectively. since we are working in the weak-field limit ($h \ll 1$) we get:

$$\begin{aligned} L_x &\sim \int_0^{L_0} [1 + \frac{1}{2}h_+(t - x)]dx \\ L_y &\sim \int_0^{L_0} [1 - \frac{1}{2}h_+(t - y)]dy \end{aligned} \tag{2.3}$$

In our particular case L_0 is much shorter than the typical wavelength of our gravitational waves signal in the sensitive band (10 to 10^4 Hz), Hence we can consider the long wavelength approximation $h_+(t + x) \sim h_+(t)$ and obtain

$$\begin{aligned} L_x &\sim L_0 + \frac{1}{2}L_0 h_+(t) \\ L_y &\sim L_0 - \frac{1}{2}L_0 h_+(t) \end{aligned} \tag{2.4}$$

This expression highlights the fact that the distance between two free falling test masses (in our case the beam splitter and the end mirror) will vary when a gravitational waves is passing by and this modification is proportional to the amplitude of the gravitational waves:

$$\frac{\Delta L}{L_0} \propto h_+(t) \tag{2.5}$$

As the design mimics a Michelson interferometer the field at the photon detector, which can be, as we saw, determined by the optical path difference ΔL at the photon detector, can be re-expressed as a phase difference with

$$\Delta\phi = \frac{2\pi}{\lambda}\Delta L \tag{2.6}$$

leading to

$$\begin{aligned} \Delta\phi(t) &= \frac{2\pi}{\lambda}(2L_x - 2L_y) \\ &\sim \frac{2\pi}{\lambda}(2L_0 h_+(t)) \\ \Rightarrow h_+(t) &= \frac{\lambda}{4\pi L_0}\Delta\phi(t) \end{aligned} \tag{2.7}$$

For such interferometer the power arriving to the photon detector, P_{out}, considering perfectly reflecting mirrors can be expressed as [40]

$$P_{out} \sim \frac{1}{2}P_{in}[1 - \cos(\alpha + \Delta\phi)] \tag{2.8}$$

where α is the static tuning of the interferometer, phase difference at the beam-splitter between the two reflected beams [40]. Thus with this interferometer design a gravitational wave induces and is detected as a power change in the photon detector signal over time, proportional to a variation in the phase-shift $\Delta\phi$ (or equivalent ΔL), which gives a direct measure of the the gravitational wave strain amplitude $h(t)$.

2.1.3 Detector angular response

So far we have only considered the case of a linearly polarized gravitational wave ($h = h_+$ and $h_\times = 0$) that propagates perpendiculary to the detector plan. If we consider now, in the transverse and traceless gauge, a plane gravitational wave coming from an arbitrary direction $\hat{n}$ on the sky we have

$$h_{ij}(t, \vec{x}) = h_+(t, \vec{x})e^+_{ij}(\hat{n}) + h_\times(t, \vec{x})e^\times_{ij}(\hat{n}) \tag{2.9}$$

where $(e^+_{ij}, e^\times_{ij})$ are the polarisation tensors [41]. If we now consider the unit vectors $\hat{a}$ and $\hat{b}$ aligned with the detector arms, in the long wavelength approximation and assuming that the detector, localised at $\vec{x} = \vec{0}$, has a negligible size compare to the wavelength we can write the signal as

$$s(t) = F_+(\hat{n})h_+(t) + F_\times(\hat{n})h_\times(t) \tag{2.10}$$

where

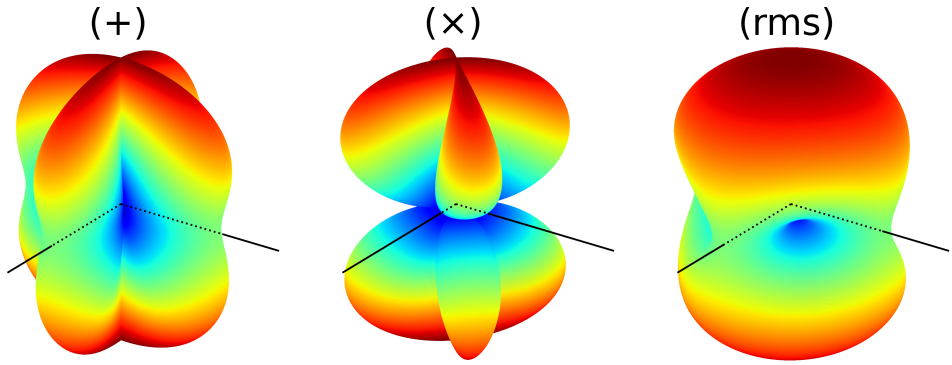

Figure 2.2: From left to right, F_+, $F_\times$ and F_{rms} antenna pattern function of sky direction. Redder colors represent best responses and bluer colors worst responses. The interferometer is located at the center of each pattern and the black lines indicate the orientation of the interferometer arms.

$$\begin{aligned} F_+(\hat{n}) &= \frac{1}{2}(a_i a_j - b_i b_j) e_+^{ij}(\hat{n}) \\ F_\times(\hat{n}) &= \frac{1}{2}(a_i a_j - b_i b_j) e_\times^{ij}(\hat{n}) \end{aligned} \tag{2.11}$$

are the interferometer responses to the two independent polarisations of the gravitational waves. In the frequency domain the equation (2.10) becomes

$$\tilde{s}(t) = F_+(\hat{n})\tilde{h}_+(f) + F_\times(\hat{n})\tilde{h}_\times(f) \tag{2.12}$$

Traditionally, the three dimensional representations of the absolute value of $F_{+,\times}$ as a function of $\hat{n}$ are called *antenna patterns*. Usually we represent this antenna patterns in the coordinate system where $\hat{n} = (\sin\theta\cos\phi, \sin\theta\sin\phi, \cos\theta)$ with $\theta \in [0, \pi]$ and $\phi \in [0, 2\pi]$ corresponding to the spherical coordinates. The figure 2.2 shows the antenna patterns in this coordinate system with x and y aligned with the interferometer arms.

The directional function for unpolarized gravitational waves F_{rms} can be found by taking the quadratic sum of antenna pattern functions for the two polarizations:

$$F_{rms} = \sqrt{F_+^2 + F_\times^2} \tag{2.13}$$

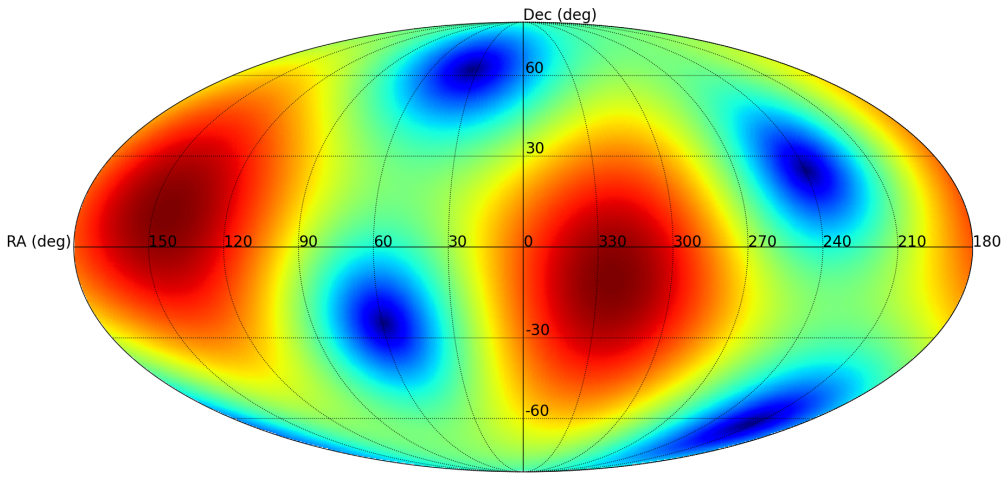

Figure 2.3: Mollview projection of the F_{rms} antenna pattern function of the Virgo interferometer computed for the 01/01/2021 at 00:00. Colors are the same as for figure 2.2.

This results for an angular response almost uniform for all sky direction but for four "blind spots". The figure 2.3 shows a projection of this antenna pattern over the sky, it highlights one of the advantages of this detector: it is sensitive to almost the entire sky (except so for the "blind spots"). Unfortunately this also means that the sensor does not have a robust way of locating the source of the gravitational wave in the sky and that only this antenna factor can be used as prior. More details about the source localisation and the importance of a network of gravitational wave detector for such uses is discussed in section 2.2.4.

Note that the exact computation of the detector angular response (taking into account the finite size of the interferometer), presented in more details in [42, 43, 41], can change significantly the antenna patterns as the frequency of the gravitational wave increases. Nevertheless, for a kilometer long interferometer with sensitive band between 10 and 10^4 Hz the effects are relatively small and can be corrected as the exact formula is available [42, 43, 41].

2.1.4 Fundamental noises

As seen in the previous section the detector output signal $s(t)$ is a single time serie which includes the interferometer responses the two independent polarisations of the gravitational waves $h(t)$. Practically this signal will also include the detector noise $n(t)$:

$$s(t) = h(t) + n(t) \tag{2.14}$$

Ideally, the noise time series n(t) is well defined by a sum of contributions described by a random process for which the contribution can be, in most cases, considered as independent. The quantity usually used to characterise the noise of the detector is the amplitude spectral density $A_s(f)$, defined as the square root of the power spectral density $P_s(f)$ and expressed in $\frac{1}{\sqrt{\mathrm{Hz}}}$:

$$A_s(f) = \sqrt{|P_s(f)|} \tag{2.15}$$

where

$$P_s(f) = \int_{-\infty}^{+\infty} (n \star n)(t)\, e^{-2i\pi f t} dt \tag{2.16}$$

and

$$(n \star n)(\tau) = \int_{-\infty}^{+\infty} n(t)\, n(t+\tau) dt \tag{2.17}$$

The amplitude spectral density is linear in the amplitude of the noise and is a good way of describing the sensitivity of a detector to gravitational waves as discussed in section 2.2.1. In the following sections I focus on the presentation of the principal contributions to the fundamental noise. The transient source noise will be discussed in section 2.2.2.

Seismic noise

As the detector is a ground-based interferometer, it is sensible to ground motion. In order to understand the ground motion effects on the detector one should understand how optics are isolated to the ground, and, above all, why can they be treated as free falling masses.

If we consider a mass m suspended at the end of a string of stiffness constant k attached to the ground. Looking at the one dimensional problem with x_g being the position of the ground and x the position of the mass one can get the following equation of motion:

$$m\ddot{x} = -k(x - x_g) + F \tag{2.18}$$

where F is the sum of the external forces. Note that we have neglected the fluid friction or the damping from internal friction. In the frequency domain, introducing $\omega_0^2 = \frac{k}{m}$ the resonant angular frequency, the equation of motion becomes

$$\left(\omega_0^2 - \omega^2\right) x(\omega) = \frac{F(\omega)}{m} + \omega_0^2 x_g(\omega) \tag{2.19}$$

If we consider only the external forces term we find at high frequencies ($\omega \gg \omega_0$)

$$\frac{F(\omega)}{m} \sim -\omega^2 x(\omega) \tag{2.20}$$

which is simply the equation of a mass subject only to the external force F , this is the starting point in explaining why our optical elements are free-falling masses. If we now only consider ground motion (i.e. $F = 0$), the amplitude transfer function is :

$$\left|\frac{x(\omega)}{x_g(\omega)}\right| = \frac{\omega_0^2}{|(\omega_0^2 - \omega^2)|}$$

$$\begin{aligned} &\to 1 && \text{for} \quad \omega \ll \omega_0 \\ &\to +\infty && \text{for} \quad \omega = \omega_0 \\ &\sim \frac{\omega_0^2}{\omega^2} \to 0 && \text{for} \quad \omega \gg \omega_0 \end{aligned} \tag{2.21}$$

Hence the ground motion is amplified at the resonant frequency ω_0 and is suppressed at high frequencies. We will see in section 2.1.5 how, in the light of these results, this principle is used in practice in current Virgo detector with the so called *superattenuators* suppressing the seismic noise above 10Hz.

Thermal noise

The main expected contributions of thermal noise are the thermal dissipation inside the test masses themselves (resulting in a deformation of the mirror surface), the suspension wires thermal noise and excitation of the pendular motion. The thermal noise randomly excites resonant frequency of the system like coating vibration modes or vibration modes of the suspension wires (violin modes). These fluctuations are well modelled by an internally damped oscillation excited by a Brownian force.

The use of the fluctuation-dissipation theorem encourages the use of high mechanical quality factor (which describe the internal losses in a system or how long it takes a resonator to decay in amplitude) materials, like fused silica, sapphire or silicon for the mirrors and the pendulum in order to lower the wide band noise level [3]. As shown in the figure 2.4 those noises are the main contribution of the detector fundamental noise in the mid frequency range of the detection band.

Quantum noise

Paradoxically, although the design of the detector features arms several kilometers long, one of the most important noises of the detector originates at the quantum

scale. The quantum noise plays an important role over the whole bandwidth and it is even a limiting noise at high frequency. The quantum noise is described as the sum of the shot noise and the radiation pressure noise both inherent to the quantum nature of the laser light.

shot noise

We saw that what is measured by the photodiode is the output light power P_{out} and a gravitational waves induce a phase difference $\Delta\phi$ which can be determined by a careful measurement of the output light power. A first limit originates from the precision with which we can measure this power.

Modelling the light flux as a set of discrete photons whose arrival times are statistically independent, the measure of the power P_{out}, with a photodiode, is equivalent to determining the number of photons of a certain energy arriving during a time interval. From the Planck–Einstein relation we know that each photon carries an energy proportional to its frequency ν, then the mean number of photons $\langle N \rangle$ arriving during a time period τ is given by:

$$\langle N \rangle = \frac{P_{out}\tau}{h\nu} \tag{2.22}$$

where h is the Planck constant. The mean number of photons $\langle N \rangle$ is described by a Poisson distribution, which implies the uncertainty $\sigma_N = \sqrt{N}$. Thus the power measured is a random variable described by its mean $\langle P \rangle = P_{out}$ and by its standard deviation:

$$\sigma_p = \sigma_N \frac{h\nu}{\tau} = \sigma_N \frac{P_{out}}{\langle N \rangle} \tag{2.23}$$

This power fluctuation can be re-expressed as a phase shift fluctuation:

$$\begin{aligned} \sigma_\phi &= \frac{2\sigma_P}{P_{in}\ \sin(\alpha)} \\ &= \frac{1}{\cos(\frac{\alpha}{2})}\sqrt{\frac{h\nu}{\tau P_{in}}} \end{aligned} \tag{2.24}$$

where we used (2.8) with no gravitational waves signal ($\Delta\phi = 0$). As the phase fluctuation is inversely proportional to $\cos(\frac{\alpha}{2})$, choosing $\alpha = 0$ we minimize the phase fluctuation. It is then more convenient to work on the dark fringe. Using $\Delta\phi = \frac{4\pi L_0 \nu}{c} s(t)$, we can rewrite the phase noise as a contribution to the amplitude spectral density [44]

$$n_{shot} = \frac{1}{L_0}\sqrt{\frac{c^2 h}{8\pi^2 \nu P_{in}}} \tag{2.25}$$

For a 3 kilometer long Michelson interferometer with a 50 Watt laser of wavelength $\lambda = 1.064\ \mu$m we find

$$n_{shot} \sim 2.5 \times 10^{-21} \mathrm{Hz}^{-\frac{1}{2}} \tag{2.26}$$

which is of the same order of magnitude as the amplitude expected for a gravitational wave. The frequency dependence of the shot noise is found considering the Fabry-Perot cavity which acts like a low-pass filter with a frequency cut-off [3].

Radiation pressure noise

Like all science experiment that rely heavily on lasers, radiation pressure occurs in interferometers because photons transfer momentum to the end of arms mirrors when they are reflected. This radiation pressure induces changes in phase, adding non negligible noise in the photodiode data. One can obtain the following expression for the radiation pressure noise [44, 45]:

$$n_{rp}(f) = \frac{4\mathcal{F}}{Mf^2}\sqrt{\frac{h\nu P_{in} G_{pr}}{2\pi^6 c^2 (1 + 16 f^2 \mathcal{F}^2 L_0^2 c^{-2})}} \tag{2.27}$$

where M is the mass of the end mirrors, $\mathcal{F}$ is the arm cavity finesse and G_{pr} is the power recycling cavity gain (see section 2.1.5 for the presentation of both cavity). This noise is reduced by increasing the mirror mass. The radiation pressure noise dominates at low frequencies.

Standard quantum limit

Finally, the total quantum noise can be simply expressed as the sum of the shot noise and the radiation pressure noise:

$$n_{qn}(f) = n_{shot}(f) + n_{rp}(f) \tag{2.28}$$

As we can see in equations (2.25) and (2.27) if we increase the laser power, we will reduce the shot noise but increase the radiation pressure noise. Reversely if we reduce the laser power, we will reduce the radiation pressure noise while increasing the shot noise. This trade-off leads to the definition of the standard quantum limit which can be approximated considering a P_{in} such that $n_{shot} = n_{rp}$ [12].

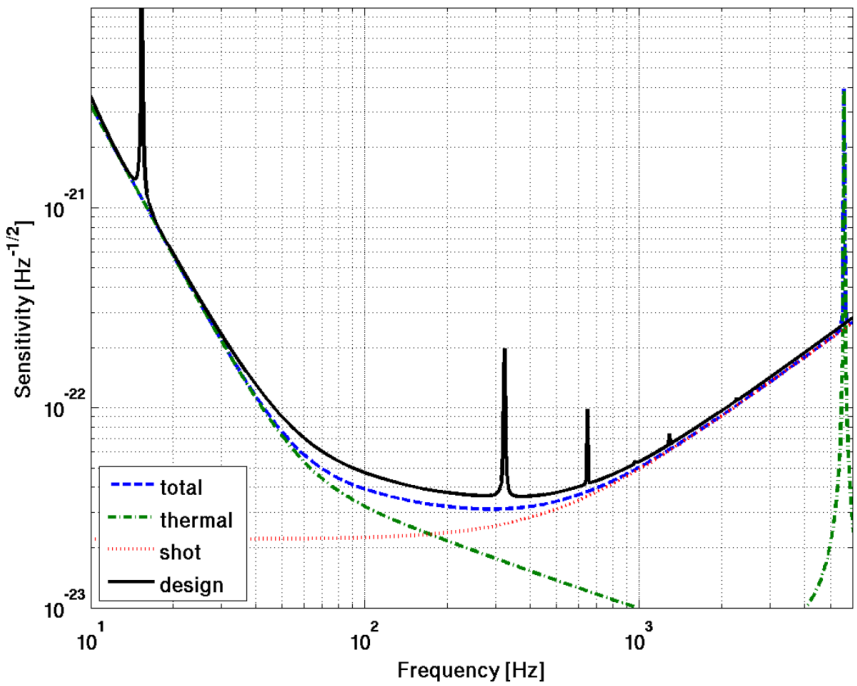

Figure 2.4: Simplified noise budget (blue dashed line) as a quadratic sum of simplified thermal (green dot-dashed line) and shot noise (red dotted line), and Virgo design noise budget for summer 2009 (black solid line). Figure from [3].

2.1.5 Virgo design, a few more words

I presented in the previous sections the general design of Virgo interferometer, as this thesis is not detector oriented, I will not go into deep details on the Virgo design. Nevertheless, I want to add in this section a few words about some of the important features implemented from the simple interferometer scheme to achieve the current sensitivity.

The starting point is the **laser**[1] source, an ultra-stable single-mode high power laser with wavelength of $\lambda = 1064$nm, wavelength mainly chosen because of the research and development available to date for such laser and surface treatment (essential for mirrors). In order to send the laser beam through the interferometer, we use an in-vacuum suspended bench which has two purposes: to clean spectrally and spatially the laser beam by means of a suspended triangular cavity, called the **input mode cleaner**, and to adapt the laser beam size to the interferometer to maximize the coupling efficiency [46]. The laser is then injected to into the interferometer, the current power achieved as this step is 19 W [15]. The entire interferometer, including the input mode cleaner, is set in an adequate **vacuum** in order to avoid fluctuations in gas density that would cause changes in the index of refraction and hence modification of the optical path length [47]. This vacuum tank is one of the main reason why we cannot endlessly extend the interferometer arms length (alongside with the earth curvature and the difficulty to find available sites for such a large device), the arm cavity length is 3 km for a diameter of 1.2 m, note that this makes Virgo the largest ultra-high vacuum installation in Europe.

After being splitted by the **beam-splitter**, the laser light enter in the arms of the interferometer. Unlike the simple Michelson interferometer scheme presented in figure (2.1) the Virgo detector have **Fabry-Perot cavities** on the arms. The main goal of these cavities is to increase the optical path travelled by the light that resonates inside them. While the increase of the optical path is maximized at the resonance position, the challenge is to achieve the lock of this position with such kilometer long cavity, especially knowing that the mirrors are suspended [48]. The Virgo interferometer Fabry-Perot cavity finesse is $\mathcal{F} \sim 450$ leading to an equivalent arm length of $L_{eq} \sim 860$km [12]. With this in mind, the expression of n_{shot} has to take into account the Fabry-Perot cavity which acts as a low-pass filter of high frequency cut-off f_c. Then the expression of the shot noise n_{shot} is multiplied by a factor $\sqrt{1 + \left(\frac{f_{GW}}{f_c}\right)^2}$ making it the dominant noise contribution at high frequency [3].

Leaving the Fabry-Perot cavities, the light is sent back to the beam-splitter. Here comes into play the **power recycling mirror**. This new mirror takes advantage of the dark fringe working point of the interferometer, indeed added between

[1] In bold are the components that are visible in the figure 2.6

the laser source and the beam-splitter it allows to reflects most of the input power in the laser direction thus enhance the circulating power inside the interferometer (i.e. increase the P_{in}). As shown in section 2.1.4 this lead to reduce the shot noise, but will increase the radiation pressure noise, we are limited here by the standard quantum limit. However, with the implementation of squeezing the standard quantum limit can be outperformed. The squeezing of trying to take advantage of the Heisenberg uncertainty to optimise the error on the phase/amplitude (see for instance [12]). The current squeezing used in Virgo is frequency independent, reducing the phase uncertainty it decreases the shot noise (i.e. increasing the sensitivity at high frequency). In the future, frequency dependent squeezing will be implemented allowing to increase the sensitivity in all the frequency range [12].

The Virgo detector **mirrors** has be chosen to be heavy enough ($m \sim 42$ kg) to counterbalance the radiation pressure noise and large enough to reduce the thermal noise and fit with the laser beam size. A special attention has been paid to the polishing in order to reduce the scattering of light, the RMS flatness is inferior to 0.5nm (i.e.$\sim \frac{\lambda}{2000}$) [49]. Furthermore a coating of the mirrors has been implemented to limit as far as possible the mechanical losses that limit the sensitivity of the detector due to the associated mirror thermal noise [5].

In order to lower the seismic noise the principle presented in section 2.1.4 is used in the Virgo **superattenuator**. Composed of an inverted pendulum fixed to the ground and a series of seven wires and mechanical filters attached to the top of the inverted pendulum it isolates the suspended mirror from the ground motion. The Virgo superattenuator cuts all the seismic noise above 10 Hz [50] with an attenuation factor of $\sim 10^{14}$. All the Virgo mirrors and the beam-splitter are suspended to a superattenuator. A scheme of the Virgo superattenuator is presented in figure (2.5).

Finally the light that is reflected by the beam-splitter in direction of the photodiode passes through the **output mode cleaner**, which is a non-degenerate optical cavity that, like the input mode cleaner, transmits only the fundamental Gaussian mode at the carrier frequency. The purpose is to keep only light which leaves the interferometer due to a gravitational wave signal and remove higher order modes caused by interferometer mirror defects and radio-frequency sidebands used for the control of auxiliary degrees of freedom [51].

In the near future to increase the sensitivity an extra mirror will be implemented in the detector between the beam splitter and the photodiode to recycle the signal light, so called **signal recycling mirror**. With the current used tuning this has the advantage to increase the detector bandwidth, reduces the finesse of the cavity and so reduces the shot noise. Different tuning could be used to influence the detector bandwidth in order to optimize its response to expected astrophysical signals, indeed the position of this mirror changes the frequency of the maximal

sensitivity. Well tuned this allows to alter the resonance of the interferometer to boost signals from, for instance, coalescing black hole and neutron star systems [12][2].

2.1.6 Current detector network

On this section I will focus on the LIGO-Virgo-KAGRA collaboration. Note that with the various development and technological implementation of the detector design the exact name of the detector is changing from Virgo to Advanced Virgo and then Advanced Virgo+ (same for LIGO, Enhanced LIGO, Advanced LIGO and Advanced LIGO+), for the sake of clarity of this thesis I will simply refer to Virgo and LIGO. The Virgo interferometer, whose design is presented in the previous sections, is located in Cascina in Italy. The Laser Interferometer Gravitational-Wave Observatory (LIGO) detectors are located in United States of America, LIGO Hanford is located in the Columbia Basin region of Eastern Washington near the Tri-Cities of Richeland, Kennewick and Pasco, LIGO Livingston is located in Livingston Louisiana. The main differences between the Virgo design and the LIGO's one is the arm length being 4 km (instead of 3km for Virgo). The signal recycling mirror is already implemented in the LIGO detectors. The Japanese Kamioka Gravitational Wave Detector (KAGRA) is located in the Kamioka mine in the Gifu Prefecture, this is the first gravitational wave detector built underground, and the first whose uses cryogenic mirrors.

The detector development can be illustrated using the so called *BNS range*, one possible metric used to represent the detectors sensitivity. It gives the distance at which a single detector could observe a pair of 1.4 $M_\odot$ neutron stars, with a signal-to-noise ratio (see section 2.2.1) of 8 (sky-averaged and inclination/orientation averaged).

Mainly because of the noise variation, within the same observing run the range of each detector varies significantly on hourly time-scales. Figure 2.7 presents the achieved and expected value of the BNS range for each given run of the detectors. In a few words, on September 14, 2015 at 09:50:45 UTC (just before the O1 observing run) the first direct detection of a gravitational wave occurred. The two LIGO running at the time detected the so called GW150914, signal produced by the inspiral, merger and ringdown of a black hole binary system with masses of respectively $36^{+5}_{-4}M_\odot$ and $29^{+4}_{-4}M_\odot$ [52]. The signal lasted for a few tens of milliseconds and had a typical chirp waveform as presented in 1.3 (see figure 2.8). which, in this case, increases in frequency from 35-250 Hz and reaches a maximum strain amplitude of 10^{-21}. The detected signal is in agreement with the General Relativity prediction [53]. The O1 observing run lasting five months, with the two

[2]Such uses would however lead to an increase of the difficulty to lock the detector cavity

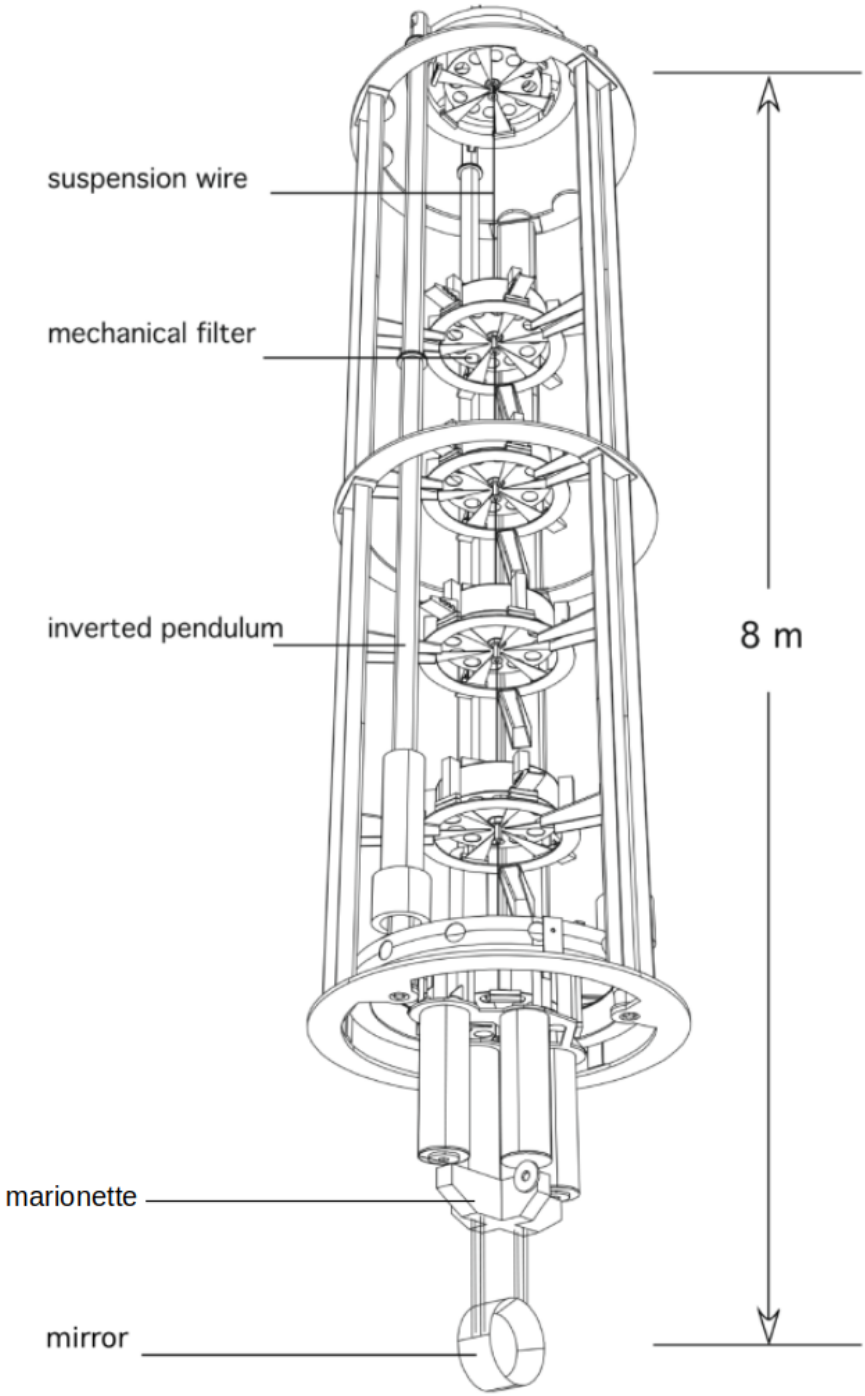

Figure 2.5: Scheme of the Virgo Superattenuator [50].

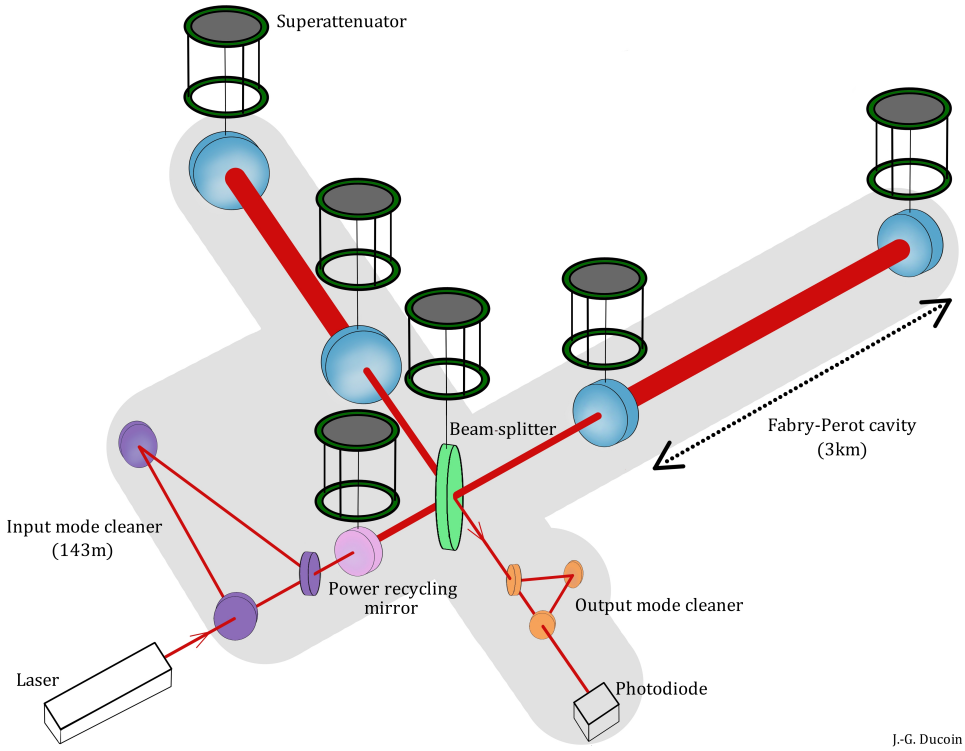

Figure 2.6: Scheme of the Virgo detector. Update of the figure 2.1 with the systems discussed in section 2.1.5. The beam size reflects its power (not to scale). Grey background indicates in vacuum systems.

LIGOs detectors observing, leaded to two other BBH merger detection [54]. The O2 observing run lasting nine months started with the two LIGO detectors with improved sensitivity compared to O1, and the Virgo detector joined the observation for the last month. This run saw the first detection of gravitational waves from a binary neutron star inspiral, named GW170817 (see 5.3 for details), in addition to the observation of gravitational waves from a total of seven binary black hole mergers [14]. Finally the O3 run (split in two with respectively O3a and O3b), lasted 11 months (interrupted prematurely because of the covid epidemic). This last run shared is load of very interesting events among which: GW190521 a merger of remarkably massive black holes, GW190426 the first observed Neutron star black hole (NSBH) merger, GW190412 a merger of unequal-mass black holes, GW190425 a merger involving massive Neutron stars [15]. Despite few BNS merger detections, no multi-messenger event occurred (see 5.1 for discussions). At the very end of the O3 run, the KAGRA detector started taking data in science mode. Figure 2.9 shows the number of gravitational wave event per run. During a given observation run the duty cycle, amount of science quality data taken over a period of observing time, is not 100%. There is various reasons which can lead to the loss of observing time like the need for maintenance handling, interferometer control loss, environmental perturbation... To give an idea of what can be typically achieved, in figure 2.10 the duty cycle for the whole network and Virgo detector alone for O3a and O3b observing run are presented.

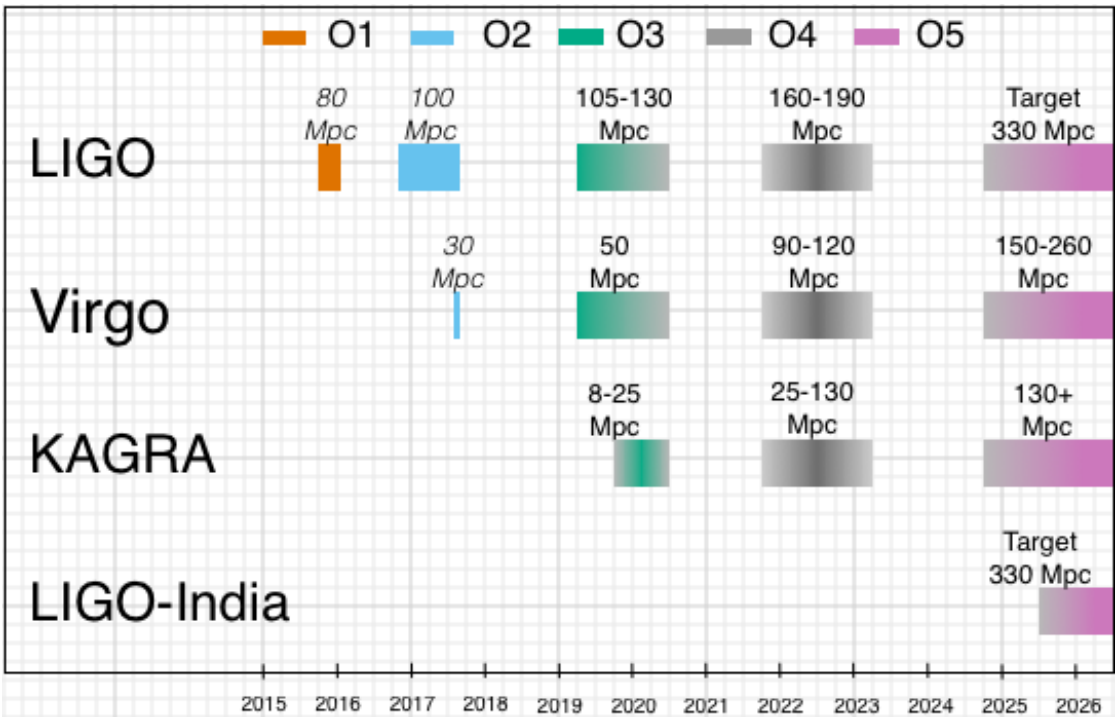

Figure 2.7: The expected BNS range evolution and observing runs of the gravitational waves detectors over the coming years. The colored bars show the observing runs,with achieved sensitivities in O1 and in O2, and the expected sensitivities for future runs. There is significant uncertainty in the start and end times of the planned observing runs, especially for those further in the future, and these could move forward or backward relative to what is shown above. Uncertainty in start or finish dates is represented by shading.

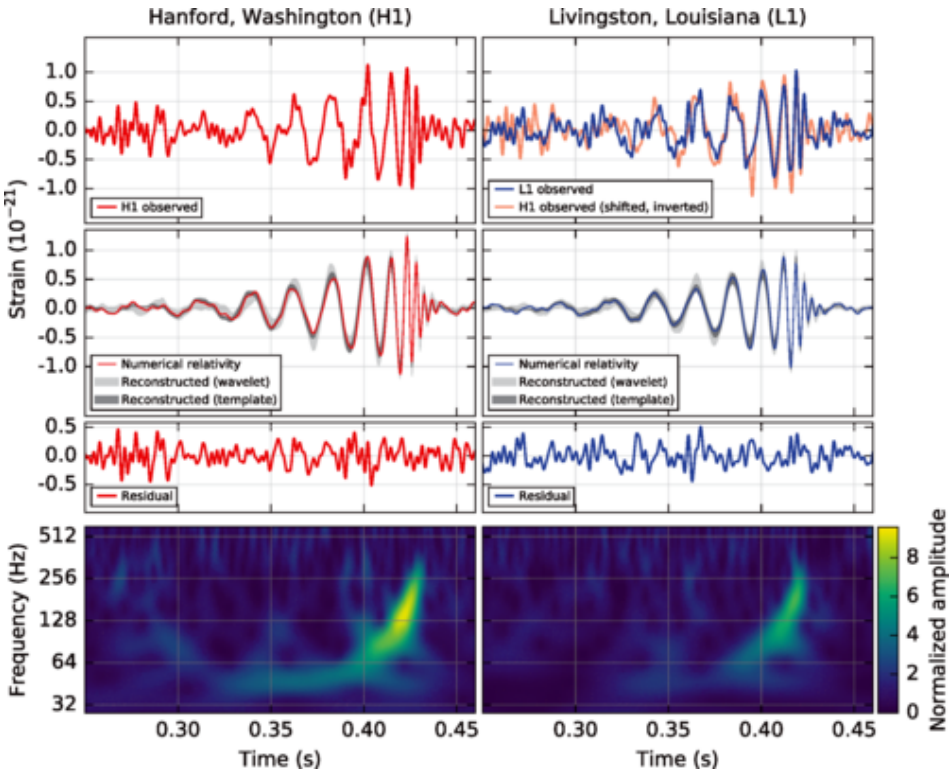

Figure 2.8: The gravitational-wave event GW150914 observed by the LIGO Hanford (H1, left column panels) and Livingston (L1, right column panels) detectors. Times are shown relative to September 14, 2015 at 09:50:45 UTC. *Top row, left*: H1 strain. *Top row, right*: L1 strain. GW150914 was detected first at L1 and $6.9^{+0.5}_{-0.4}$ ms later at H1; for a visual comparison, the H1 data are also shown, shifted in time by this amount and inverted (to account for the detectors'relative orientations). *Second row*: Gravitational-wave strain projected onto each detector in the 35–350 Hz band. Solid lines show a numerical relativity waveform for a system with parameters consistent with those recovered from GW150914. *Third row*: Residuals after subtracting the filtered numerical relativity waveform from the filtered detector time series. *Bottom row*: A time-frequency representation of the strain data, showing the signal frequency increasing over time. Figure from [14].

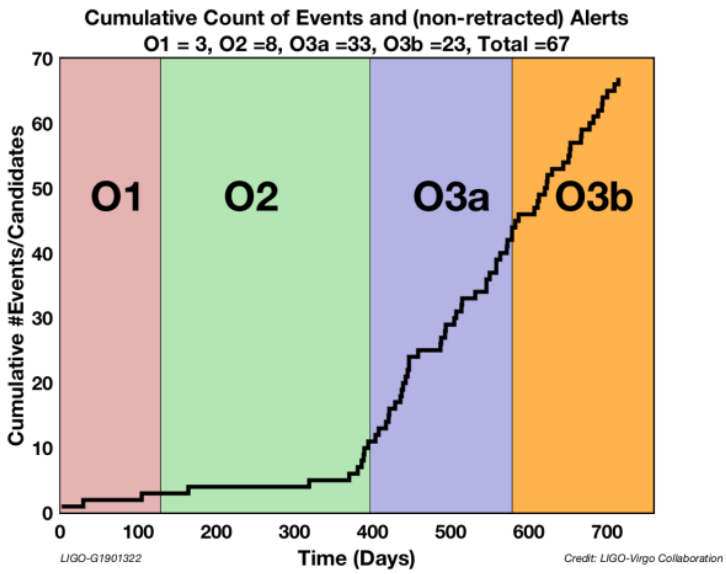

Figure 2.9: Cumulative count of events per runs. Figure from LIGO-Virgo-KAGRA collaboration.

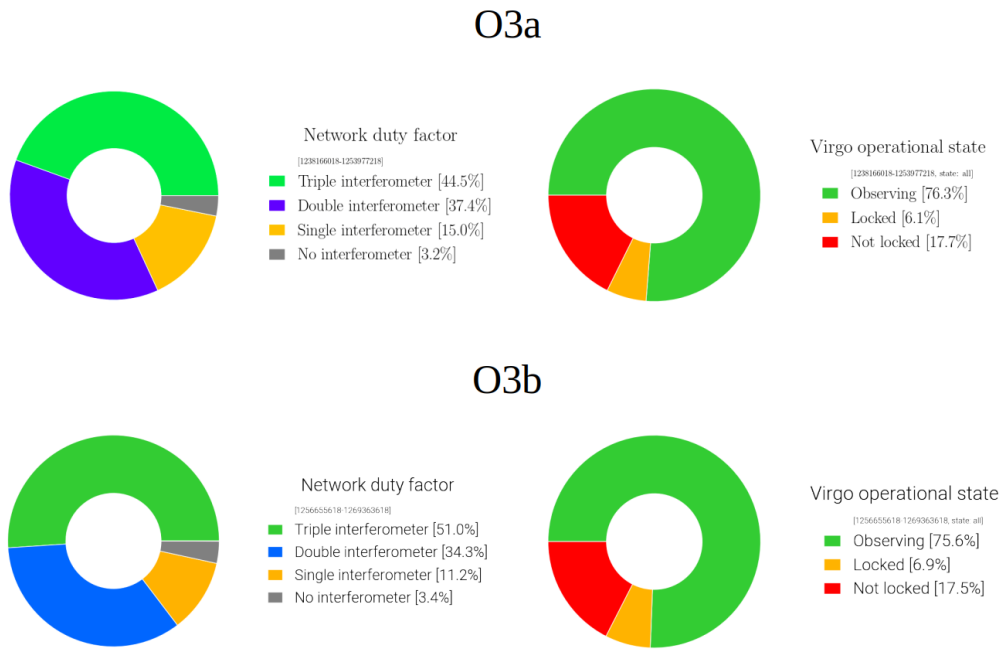

Figure 2.10: O3a and O3b LIGO-Virgo network duty cycle (*left*). For conciseness only Virgo duty cycle is specified (*right*), however both LIGO detectors duty cycle are very similar. Figure from LIGO-Virgo-KAGRA collaboration.

2.2 Data analysis

In this section I will give an overview of the various steps required to achieve a signal detection for ground interferometric gravitational wave detectors such as Virgo.

2.2.1 Calibration

The first step of the Virgo data analysis is the calibration and h(t) reconstruction. These steps are unavoidable to allow any signal detection. We first need to calibrate the sensing chain and control loop actuators (mirrors and marionette, see figure 2.5). This is done using the interferometer laser wavelength as primary etalon and a calibration transfer procedure, i.e. by measuring the longitudinal mirror motion induced by an excitation signal sent to the mirror or marionette controls.

Once this is done we can compute the h(t) signal from the dark fringe one. Indeed, on permanent basis corrections are applied to the mirrors to suppress any movements with frequency between 10Hz and 100Hz, thus any signal (including true gravitational wave signal) within this range are killed. To reconstruct h(t)

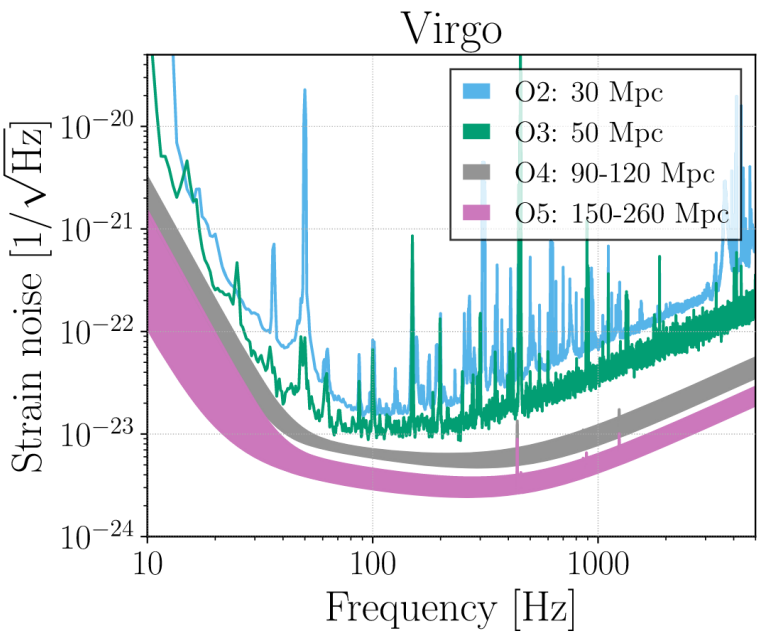

Figure 2.11: Virgo target strain sensitivities as a function of frequency measured at the beginning of the O3 run. The BNS range (in megaparsec) achieved in past observing runs and anticipated for future runs is shown. Figure from [59].

signal we remove from the dark fringe signal the contribution of the control signals by subtracting the corrections applied to the mirrors (corrected from the optical transfer function of the detector). Above 100Hz the mirrors are "free" and the dark fringe signal is used directly. Finally with the reconstructed h(t) signal one can compute the interferometer sensitivity to gravitational wave strain as function of frequency, figure 2.11 presents the measured Virgo sensitivity for the beginning of the O3 run.

Absolute timing is also a critical parameter for multi-detector analysis, in particular to determine the direction of the gravitational wave source in the sky (see section 2.2.4). The timing system is based on a master timing system controlled by GPS. Its roles are to give the rhythm of the control loops and to give the time stamps to the data acquisition system.

More details on the calibration and $h(t)$ reconstruction procedures can be found in [55, 56, 57, 58].

Signal-to-Noise Ratio (SNR)

A relevant figure of merit in comparing a signal with noise is the SNR. For a modelled signal search (see section 2.2.3), the SNR can be expressed as :

$$SNR^2 = 4\int_0^\infty \frac{|\tilde{s}(f)|^2}{P_s(f)}df \tag{2.29}$$

where $\tilde{s}(f)$ is the Fourier transform of the modelled signal and $P_s(|f|)$ is the one sided power spectral density of the noise. This expression presents the so called optimal SNR, which assumes that the template used matches the signal perfectly, i.e. that the search recover the exact SNR of the signal. For a more realistic definition of the SNR obtained with a template bank see for example [60]. For unmodelled search SNR definition see for instance section I of [61] which defines the SNR of a trigger. In this sense the noise spectral density represents the sensitivity of the detector. If the detector noise is a Gaussian noise, the SNR can be seen as the number of standard deviations in amplitude, convertible to a probability of detection. But as discussed in section 2.2.2 the detector doesn't have a purely Gaussian noise distribution, a large number of transient noises are also in the data and complicate their analysis. As a result, while the SNR is a powerful detection statistic in the presence of stationary Gaussian noise, transient signals of instrumental (i.e. non-astrophysical) origin can produce SNR values as large, or even much larger, than the values typically expected for astrophysical signals. Therefore a simple threshold in SNR is not sufficient to identify interesting triggers. A lot more of data analysis, partially presented in the following, is necessary to claim any detection.

2.2.2 Detector characterisation and data quality

Now that we saw how to reconstruct the amplitude $h(t)$ of the gravitational wave and before thinking about any signal detection we have to face the fact that the real gravitational wave data are very far from being stationary and Gaussian. As a result, a complete data quality analysis and data cleaning is essential in order to increase the significance of any signal in the data. Of course with a network of detectors, knowing that a given gravitational wave is expected to be visible in all the detectors (up to sensitivity and antenna pattern differences), any multi-detector coincidence and/or coherence techniques allow one to reduce the number of interesting triggers (see definition in section 2.2.2) coming from one detector. But in practice this is not sufficient and for ground based detector we need to suppress as much as possible, all periods of data that are known to be spoiled by disturbances to decrease the false alarm rate required for a discovery. On the other hand, we do not want, by suppressing periods of data, to reduce the observation time when the glitches are harmless for the gravitational wave search. There is a tricky trade off between observation time and excess noise reduction that needs a good understanding of the detector and the noise it can encounter, this is the purpose of the detector characterisation (detchar) work.

Omicron

`Omicron` is a software developed to perform a multi-resolution time–frequency analysis of data from ground interferometric gravitational wave detectors such as Virgo [62]. It offers a visual representation of the transient noises and gravitational-wave events using spectrograms built with whitened (frequency domain data re-weighted by the inverse noise amplitude spectral density) data streams. The `Omicron` algorithm is implementing a fast Qtransform [63] which can be parameterized with an optimized resolution to display transient noises and gravitational-wave events. Note that `Omicron` is optimized to process, in parallel, thousands of data streams. This is essential to investigate the auxiliary channels recorded by the gravitational waves detectors (see section 4.1.3) in real time.

Using the Qtransform [62], the time-frequency-quality factor space is tiled and each tile is attached with the average signal amplitude and phase at the given tile position in this space. Tiles with a signal-to-noise ratio above a given threshold are collected and clustered over time. Resulting events are called *triggers* and are given parameters, e.g. time, duration, bandwidth, frequency, quality factor, and signal-to-noise ratio, given by the tile with the highest signal-to-noise ratio in the cluster. These triggers can be written to disk to conduct offline noise characterization and gravitational-wave event validation studies. For more details on the time-frequency representation and the clustering see for instance [3, 62]. Figure 2.12 shows an example of `Omicron` spectrograms. Large fraction of the data triggers are contamination from transient noises, these short fluctuations of the amplitude in a given channel that are not described by a Gaussian process are called *glitches* (see figure 2.13 for examples).

Glitches sources

Transient noises can originate from lots of sources such as environmental perturbations, detector malfunction, technical sources, control sources... Understanding glitches relies on a complete monitoring of the instrument and its environment. To this end, alongside to the main photodiode signal, thousand of probes, called *auxiliary channels*, monitor the detector and its environment. Studying the relation between a glitch and the auxiliary channels can provide a hint about glitch origin. This investigation is very time consuming, requires a lot of patience and knowledge about the operation. These studies can take months but are essential to provide sufficiently clean data for the detection algorithms and reach the expected search sensitivity. To this aim many efforts are done permanently, during and outside the observation runs, by the detchar team to improve the quality of the data.

The presentation of transient noise sources in the detector could be the subject of very long description [64, 65, 66, 67], here I just present in figure 2.13 some

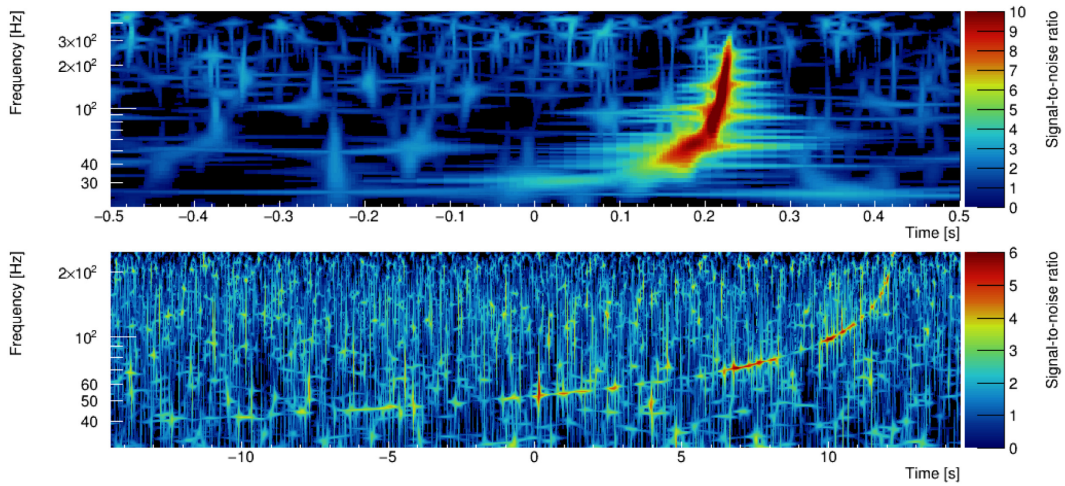

Figure 2.12: *Top:* `Omicron` spectrogram of LIGO-Hanford detector's data around the time of GW150914. The whitened data is projected in multiple time–frequency planes characterized by a constant quality factor value and the signal-to-noise ratio is measured for each tile. In this representation, all quality factor planes are stacked up and combined into one; the tile with the highest signal-to-noise ratio is displayed on top. *Bottom:* `Omicron` spectrogram of LIGO-Livingston detector's data around the time of GW170817, using data after glitch subtraction. Figure from [62].

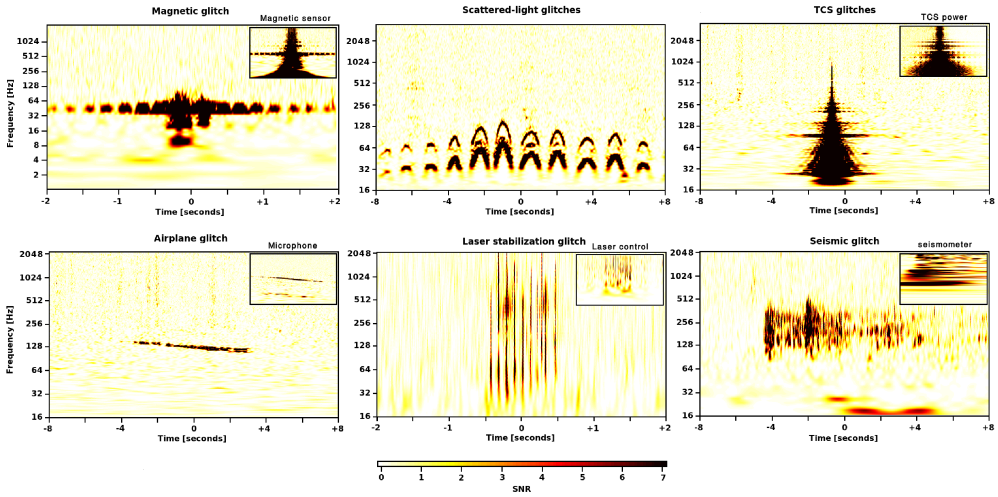

Figure 2.13: Time-frequency visualizations of some type of noise transient observed in the Virgo detector. Glitch families are identifiable by their unique time-frequency morphologies. When identified, the glitch present in the environment monitoring channel is shown in the inset plot. The first plot shows a power-line glitch also detected by the magnetometers. The second map shows a series of glitches caused by scattered light induced by seismic activity. The third glitch is caused by a thermal compensation system instability (used in Virgo to prevent mirror deformations due to high-power laser beam). The fourth plot presents an airplane event with a clear Doppler effect. The fifth event is due to a glitch in the laser stabilization loop. The last glitch with an undefined shape is due to a seismic event converted to higher frequencies. Figure from [64]

examples of noise sources identified with the help of investigation of the detector and its environment.

Data quality monitoring and Vetoes

If the strain channel $h(t)$ is too much affected by glitches, or if there is severe problems that occur while the detector is taking data the data quality can be unsuitable for the signal detection. In order to avoid any of these issues the data are flagged with status flag and data quality (DQ) flags. The status flag are dedicated to the real-time (also called online) analysis in charge to provide gravitational wave alerts. The status flag prevents the production of any triggers at times where data are the most obviously not usable for analysis (impacted with noise, interferometer lock status, data acquisition status...). A DQ flag is a list of 1s resolution time segments where the data are qualified as noisy. It can be built using the information provided by one or several of the Virgo auxiliary channels

other than the dark fringe signal channel. DQ flags can also be built after human report (electronic failure, human intrusion...). From these flags one can build *vetoes* categories, suitable for the analysis, that avoid the data quality issues. Table 2.2.2 provides a definition for each category and provides a prescription on how to use the flags in the analyses. Note that these categories can be defined slightly differently for each analysis according to specific needs. For more details on the DQ flag see [68].

Veto name	Definition and prescription
CAT1	Indicate that the data have been obviously severely impacted by noise. Offline and online analysis pipeline should run on data only after removing CAT1 time periods.
CAT2	Indicate noisy periods where the coupling between the noise source and the main photodiode signal channel is well established. Triggers should be removed if vetoed by a CAT2.
CAT3	Indicate noisy periods where the coupling between the noise source and the main photodiode signal channel is not well established. Triggers falling within CAT3 time periods should be checked carefully.
CAT4	Indicate time where simulated signals are injected in the detector (hardware injection). CAT4 time periods should be removed for any search analysis. CAT4 veto are used for specific studies [3].

Use Percentage Veto algorithm

One possibility to produce vetoes presented before and find noise origin is to study the correlation between triggers in the main photodiode signal and triggers in auxiliary channels. The general idea is to remove triggers that occur in the dark fringe signal at the same time (or nearby) as a trigger in any of the auxiliary channel. But one cannot apply this basic idea so roughly. If an auxiliary channel perfectly uncorrelated to the dark fringe signal has a very high trigger rate, it will naturally present a lot of triggers coincident with a trigger in the dark fringe channel. Hence, using them to produce vetoes may impact a genuine gravitational wave signal while not improving the rejection of noise triggers. In order to prevent this issue statistical correlation algorithm has been implemented.

The Use Percentage Veto (UPV) algorithm [69] is used to find correlations between triggers in the gravitational-wave channel and triggers in any auxiliary channels, i.e., considering auxiliary channels as insensitive to gravitational waves

[3] see 4.1.3 for an example of hardware injection usage

(see section 4.1.3), correlation between noise in the gravitational-wave channel and any auxiliary channels. In order to characterise the coupling between two channels the code finds time-coincident events and defines a use percentage value UP. For a given period T, and for a given frequency bin f_i, ρ being a SNR threshold, if there are N_{tot} triggers in the studied auxiliary channel above this threshold, and N_{coinc} of these triggers which are coincident with a trigger in the dark fringe channel the UP value is defined as:

$$UP(T, f_i, \rho) = 100 \times \frac{N_{coinc}}{N_{tot}} \tag{2.30}$$

We consider typically a non accidental coincidence if the UP value is higher than 50%. Then the channel is selected to produce veto in the corresponding trigger category. Figure 2.14 presents an example of UP computation for an auxiliary channel. Usually, two trigger sets are all the more coupled than the SNR of the auxiliary channel triggers is elevated, especially if the glitch in the dark fringe channel is a consequence of the glitch in the auxiliary channel. The period on which the UP value is estimated is a trade-off between reaching significant statistic and being sensitive to local variation of noise properties. Typically, in order to produce veto we use a week long period while to unveil noise properties we use one day of data.

2.2.3 Transient signal detection

The analysis for gravitational wave transient signal detection happens on two different timescales. First, five gravitational wave detection pipelines process the data immediately after acquisition, so called online analyses, with the goal of generating public detection alerts to the broader astronomical community within minutes. Four of these online analyses, `GstLAL` [70, 71, 72], `PyCBC` [60, 73, 74, 75, 76], `MBTAOnline` [77] and `SPIIR` [78], search for modelled compact binary sources and the last one, Coherent Wave Burst (`cWB`) [79, 80, 81, 82, 83], search for minimally-modelled transient sources. For online analysis pipeline based on modelled search a classification of the source is available from the best fitting waveform (see section 4.2 of [59]). Note that the compact binary waveform model presented in 1.3 is very basic and doesn't reflect the variety of waveforms used in the real search which accounts for a wide number and range of parameters (spin and masses of each objects...), for details on these banks see [15]. The main output of these analyses is the false alarm rate (FAR) of each ones of the candidates computed by estimating the background noise distribution (the method used depends on the search pipeline). Below a threshold of one per 10 months for compact binary search and

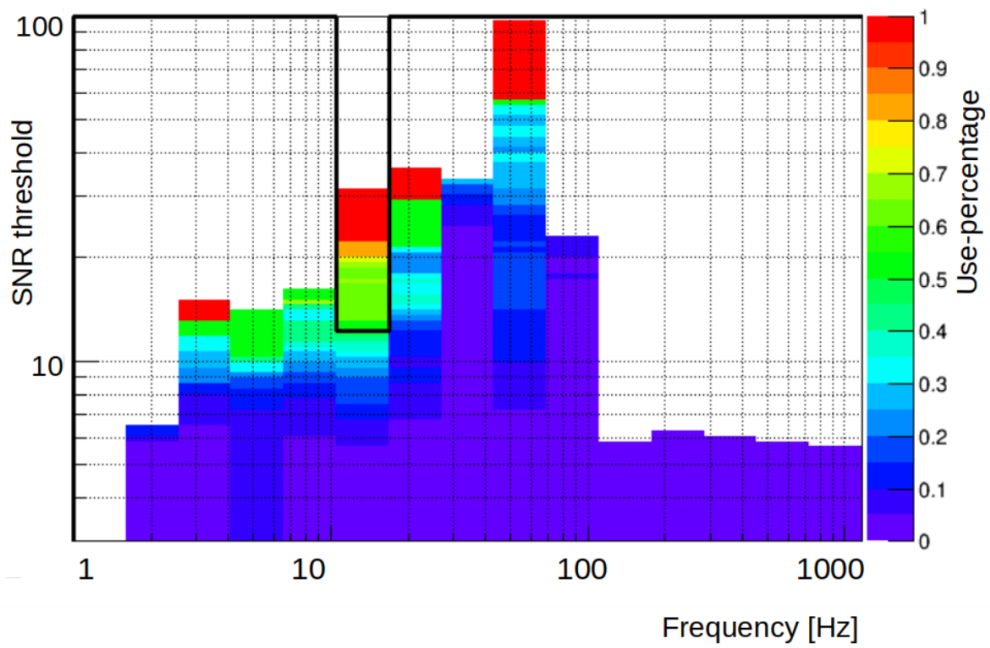

Figure 2.14: UPV tuning histogram for an auxiliary channel. The color scale represent the UP value. We observe that the use-percentage increases with the SNR, which is expected. The final veto threshold is indicated by the thick black line. When the black line is at the very top of the plot, the threshold is considered as infinite. If the statistic in a given bin is not sufficient no veto are applied, this is the case here for some bins. Figure from [4].

one per 4 years for burst search[4] the candidate is considered to be interesting and can be released with an alert. Of course any candidate is checked and can be retracted/invalided if there is any data quality issue.

Secondly, during the months following the data acquisition, the so called offline analysis is performed. The collaboration offline search has various analyses looking for basically all known or expected gravitational wave sources, burst or continuous wave, modelled (deterministic) or unmodelled[5]... Among them three, `GstLAL`, `PyCBC` and `cWB` search, similar to the online ones are performed. These offline analyses benefits from updated data calibration, data quality vetoes, the ability to estimate event significance from the full data, further algorithmic developments that take place over the course of an observing run, less computational constraints than the online search (required for fast candidate release) and different pipelines tuning. This results in a more sensitive search. The FAR threshold used to confirm a detection with the offline analyses is 2 per year. For details on these analyses see [15]. The search dedicated to gravitational waves associated to gamma ray bursts, in which I have been involved, will be discussed in 4.2.

2.2.4 Source localisation

Following the detection of a gravitational wave transients, posterior probability distributions for the source position, dedicated to the follow-up, are constructed following a Bayesian framework with the `BAYESTAR` pipeline [84]. The main resource of information allowing the gravitational wave source localisation is the consideration of time delays between sites and using triangulation. For compact binary merger the Bayesian inference algorithm constructs posterior probability distributions for the system parameters: location, mass, distance, orientation... by matching gravitational wave models to the detector strain. This allows to improve the sky localisation (*skymap*) of the source by introducing the requirement of phase, amplitude and precession effects consistency between detectors. Any sky localisation has to take into account the instrumental calibration accuracy.

Figure 2.15 shows the principle of the localisation using only time delay information between sites. For a two-site network the time delay consideration yields an annulus on the sky which can be reduced to a part of it adding the signal amplitude and phase consistency. However, even then sources will be localized to regions of hundreds to thousands of square degrees. For three detectors, the time delays usually restrict the source to two sky regions which are mirror images with respect to the plane passing through the three sites. After the signal amplitude

[4]This threshold takes into account the number of searches of each kind to get an effective rate of one per 2 months for compact binary search and one per year for burst search, for details see `https://emfollow.docs.ligo.org/userguide/analysis/index.html#alert-threshold`

[5]see for instance the collected paper list here: `https://pnp.ligo.org/ppcomm/Papers.html`

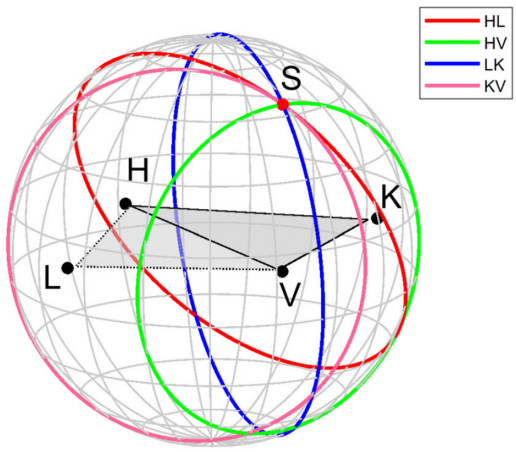

Figure 2.15: Source localization by timing triangulation for the LIGO–Virgo–KAGRA network. The locations of the four detectors are indicated by black dots, with LIGO Hanford labeled H, LIGO Livingston as L, Virgo as V and KAGRA as K. The locus of constant time delay (with associated timing uncertainty) between two detectors forms an annulus on the sky concentric about the baseline between the two sites (labeled by the two detectors). For clarity the HK and LV combinations are omitted. For four or more detectors there is a unique intersection region, S. Figure from [59].

and phase consistency only one of these regions, with a typical areas of several tens to hundreds of square degrees, is left. The previous assumption requires a detection in each detectors of the network, but with the significant difference in sensitivity between detectors the source can be worst localised (even so, the non detection in one detector can also lead to good constraint, see GW170817 detection for example; section5.3). The duty cycle of the detectors needs also to be taken into account, for a given network all detectors are not necessarily observing at a given time. For the O4 observing run with the joining of KAGRA as fourth instrument of the network one can expect events with localisation regions smaller than ten square degrees for some signals. Figure 2.16 shows an example of obtained skymaps for a two and a three detectors detection. The follow-up of such skymaps are discussed in chapter 4.

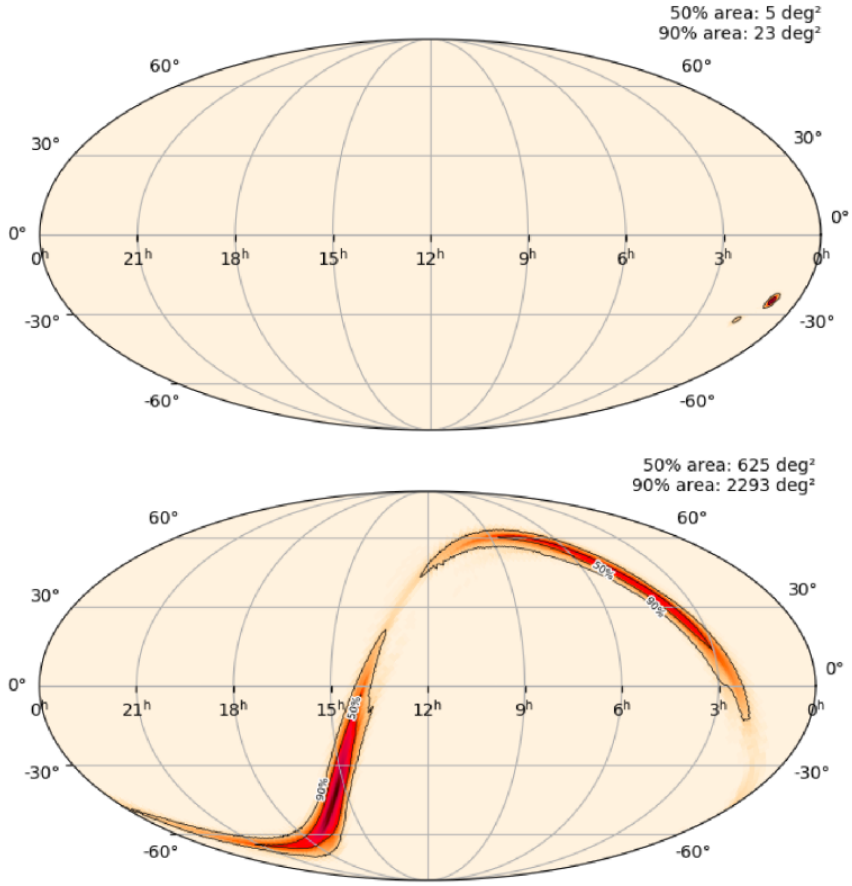

Figure 2.16: Mollweide projection of the skymap for two gravitational wave events [15], the darker the colour, the higher the probability for the source to be in this position. *Top:* GW190814, BBH merger detected by three detectors. *Bottom:* GW200128, BBH merger detected by two detectors. Figure from LIGO-Virgo-KAGRA collaboration. The probability distributions for the distance are not displayed here.

2.2.5 Parameters estimation

When one of the online analyses report an interesting compact binary merger gravitational wave candidate, Bayesian parameter estimation of compact binary signals, using the `LALInference` software library [85], is triggered. This software is able to efficiently produce the posterior probability density functions (PDFs) of the unknown parameters that describe a given model of the data and to compute the so-called evidence of the model itself. From the PDFs it generates probability credible regions for any set of parameters. Of course the sky localisation is a source parameter reconstructed by this technique. But, while the method presented in

2.2.4, dedicated to the follow-up, is taking minutes to produce the skymap, the `LALInference` software takes hours to days to produce it which makes it often too slow to help for the rapid follow-up. The computational cost of such Bayesian inference is a well known issue. It is especially true in our case knowing the large number of unknown parameters that describe our models (sky position, the masses of each objects, the spin of each objects, inclination, precession, eccentricity...), for the waveform model used see for instance table 3 of [15]. The amount of parameters and the degeneracy between some of them lead to non negligible uncertainties on the source parameters estimation (see table 6 of [15]). The widely-used software used since the first observing run O1 has been `LALInference` but the recently developed `BILBY-MCMC` [86] and `RIFT` [87, 88] algorithms propose new methods for a rapid parameter inference and will likely have an utility in the coming observing runs.

Chapter 3

Gamma-ray bursts

In this section, I will review the fundamental of the physics involved in the Gamma-ray burst (GRB) emission. I will focus on the key role they play in multi-messenger astronomy and their relation with gravitational waves. Finally, I will present GRB detectors with a particular emphasis on the Space-based multi-band astronomical Variable Objects Monitor (SVOM) mission in which I have been involved in my thesis. This chapter mainly follows the results given by [3] and [89].

3.1 History

Gamma-ray bursts (GRB) are transient bright electromagnetic emissions in gamma-rays observed on the sky. Fortuitously discovered in the early 70's by the Vela spacecrafts [90] launched by the US government in order to monitor the application of the Partial Test Ban Treaty on nuclear weapon tests signed with the Soviet Union.

After this initial discovery a large number of dedicated detectors have been designed and operated in order to understand the nature of these transient events. Most of these detectors are spacecrafts looking for direct detection of the gamma-ray emission but more recently ground based detectors observing the atmospheric cascades, either through the atmospheric Cherenkov light they comprise, or via the direct detection of the charged particles they carry have been used. The involvement of the community has allowed a more detailed study of the gamma-ray light curve and spectroscopy. The Burst And Transient Source Experiment (BATSE) detector launched by the NASA in 1991 on board of the Compton Gamma-Ray Observatoy (CGRO) spacecraft lead to the first revolution of our knowledge of GRBs. Firstly, during its nine years of operation BATSE detected 2704 GRBs and confirmed the isotropy of the angular distribution with a large sample (see Figure 3.1) [91]. Secondly, it confirmed the classification of GRBs in two different classes based on their duration [91], defined using the T_{90} which is the time over which a burst emits from 5% of its total measured above background counts to 95%, on a large and homogeneous sample: short GRBs defined by $T_{90} < 2s$ and long GRBs defined by $T_{90} > 2s$ (see Figure 3.2). The short bursts are also found to have harder spectra than long ones [92]. This BATSE detection catalog

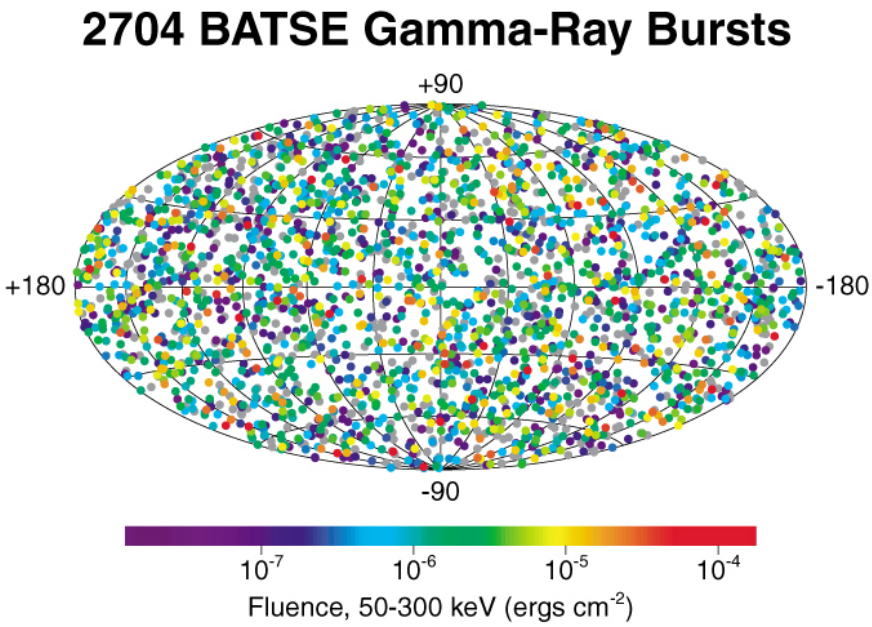

Figure 3.1: BATSE All-Sky Plot of Gamma-Ray Burst localisations. Figure from NASA[2]

put severe constraints on GRB origin models and the hypothesis of extra-galactic sources became more credible, but the gigantic amount of energy at stake remained difficult to explain. The debate on the extra-galactic origin was closed thanks to GRB970228 and its X-ray counterpart detected by the BeppoSax spacecraft [93]. The localisation of the GRB was good enough to be sent to ground-based telescopes who further discovered the first optical counterpart of a GRB [94, 95] and the brightness of the afterglow allowed the measurement of its spectrum which exhibited absorption lines at redshift $z \sim 0.835$ [96].

3.2 Emission processes

3.2.1 From jet properties to emission models

An important constraint on the emission models and the source determination is the observed variability in GRB light curve on timescales $\Delta t \lesssim 100$ ms. Indeed, the shortest time fluctuations, Δt, of an astronomical source constrain its size to be $R < c\Delta t$, because all temporal fluctuations faster than the light crossing time of the source are smeared out by propagation delays within the source. As a result

[2] `https://heasarc.gsfc.nasa.gov/docs/cgro/cgro/batse_src.html`

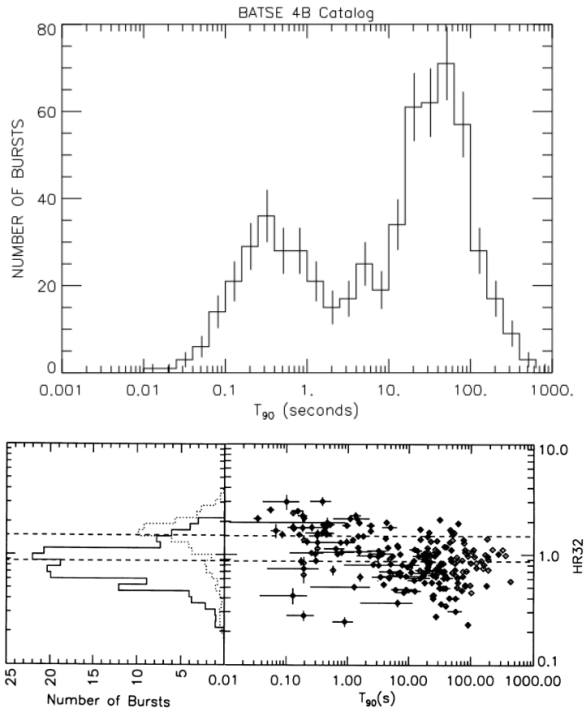

Figure 3.2: *Top:* Distribution of T_{90} from the 4B BATSE Catalog [97]. *Bottom:* Distribution of hardness as a function of T_{90}. The hardness ratio is defined as the ratio of counts in two BATSE channels : Channel 3 (100-300 keV) divided by Channel 2 (50-100 keV). Figure from [91, 92]

the observed millisecond variability of the GRB light curve restricts an emitting region with size $R < 300km$ for a non-relativistic source. This observation leaded the idea of a compact emitting region with a high temperature ejecta, the so called "fireball" composed of high energy photons and electron-positron pairs (created via pair production $\gamma\gamma \rightarrow e^+e^-$). This vision is relaxed if one considers a surface moving at relativistic speed, with a Lorentz factor $\Gamma = 1/\sqrt{1-(\frac{v}{c})^2}$. In this condition the time evolution of the surface for an observer at rest is $x(t) = vt$. Thus, for photons emitted at positions x_1 and x_2 the time difference between their arrivals for an observer along the direction of propagation is

$$\Delta t = \frac{x_2 - x_1}{v} - \frac{x_2 - x_1}{c} \sim \frac{x_2 - x_1}{2c\Gamma^2} \qquad \text{for} \qquad \Gamma \gg 1 \tag{3.1}$$

The condition on the size of the emitting region if we consider $\Gamma \sim 100$ is then relaxed to $c\Delta t\Gamma^2 \sim 3 \times 10^6 km$. This consideration of a relativistic source is in agreement with the observation of photons with an energy above $\sim 1MeV$. Indeed with such high energy photon pair production is very efficient and with the high density imposed by the fireball model such photons should not be observed in GRBs. But they have been observed in many GRBs. Imposing source of radiation with a relativistic velocity ($\Gamma > 100$, [98]) dilutes the density of photon (increasing the size of the emitting region as presented before) and lowers the energy of the photons in the source frame (thus fewer photons have sufficient energy to produce pairs).

Fireball model

The initial condition of the fireball model processes is the deposit of an amount of energy E_0 into a region of size $R_{in} \sim 10^5$m containing a mass M_0. At $R = R_{in}$, the gas particles initial thermal energy will lead to an expansion with a bulk Lorentz factor starting at $\Gamma \sim 1$. By conservation of energy, this expansion decreases the internal energy per particle and converts it into expansion-related energy (bulk kinetic energy). Since the bulk Lorentz factor per particle cannot increase beyond the initial value of random internal energy per particle it reaches its saturation at $\Gamma_{sat} \sim \eta = \frac{E_0}{M_0c^2}$ for a typical radius $R_{sat} = \eta R_{in}$ [99, 100, 101]. If we consider, at this saturation, $\Gamma_{sat} \sim 100$ this implies that the energy mass ratio $\eta \sim 100$ and $R_{sat} = 10^8$m. As η is not too large ($\eta \leq 10^5$, i.e. baryon load not too small) the optical depth, dominated by the "baryonic" electrons (associated to the protons), is large at the considered radius [99, 100, 102]. This prevents any efficient radiative energy transport and the expansion from R_{in} to R_{sat} can be considered as adiabatic with $TV^{\frac{1}{3}} = TR = cte$.

After the saturation of the initial accelerating expansion the fireball grows linearly with a constant bulk Lorentz factor $\Gamma \sim \Gamma_{sat}$. While expanding the fireball

becomes optically thin and the thermal spectrum, expected to be a black-body starts to be visible. However, in practice because of the conversion of internal energy into expansion energy this thermal emission is very weak, most of the energy being in the kinetic energy of the associated protons, rather than in photons. As a consequence electrons need to be re-accelerated in order to produce gamma-rays. This is in agreement with the observed gamma-ray spectrum which is generally a broken power law, i.e., highly non-thermal. The standard scenario proposes that this re-acceleration occurs through internal shocks in the outflow or through magnetic acceleration. The central engine energy deposition is supposed to be fluctuating, producing expanding shells with different Lorentz factors. As a result, if a given shell with Lorentz factor Γ_1 is followed by a faster shell with $\Gamma_2 > \Gamma_1$ the two shells will eventually collide and produce a shock. In these shocks the accelerated electrons produce gamma-rays mostly by synchrotron and inverse Compton scattering. GRB are due to internal medium and not to the interaction with any external medium. By opposition, when the shell ejecta start to fill the external medium (either a cold interstellar medium or a stratified wind ejected by the progenitor [103]) the interaction will produce two shocks, a forward shock propagating into the surrounding external medium and a reverse shock propagating back into the ejecta. The electrons accelerated within these shocks eventually cool through synchrotron emission producing the multi-wavelength (from TeV to radio) *afterglow* emission. The different phases of the fireball model are illustrated in Figure (3.3).

Geometry of the jet

Still remains to be explained the gigantic amount of energy emitted during these events. Indeed knowing that the sources are extra-galactic, in view of the detected energies we can estimate the total energy emitted by the source in the form of GRB, assuming an isotropic emission, at $\sim 10^{54-55}$ erg [98]. This amount of energy emitted is very hard to explain, but in practice this constrain on the energy is relaxed because of the jet geometry which is not planar but conic. The idea of a conic emission is also supported by the observation of achromatic breaks in the afterglow light curves, which can be explained by the observer seeing the edge of the relativistic jet as it slows down. As presented in figure (3.4) the surface to consider is a spherical shell with a Lorentz factor Γ limited to a cone of opening angle θ. Due to the relativistic beaming, for an observer at infinity only the interior of a conic cut with an opening angle Γ^{-1} is visible. For any observer whose line of sight forms an angle with regard to the jet axis greater than $\sim \theta + \Gamma^{-1}$ the jet is completely invisible. This geometry explains why for an observer at infinity, the end of the GRB emission appear to be spread out in time (with a rapid decay) rather than observed with an instantaneous cut-off. Because photon are emitted by

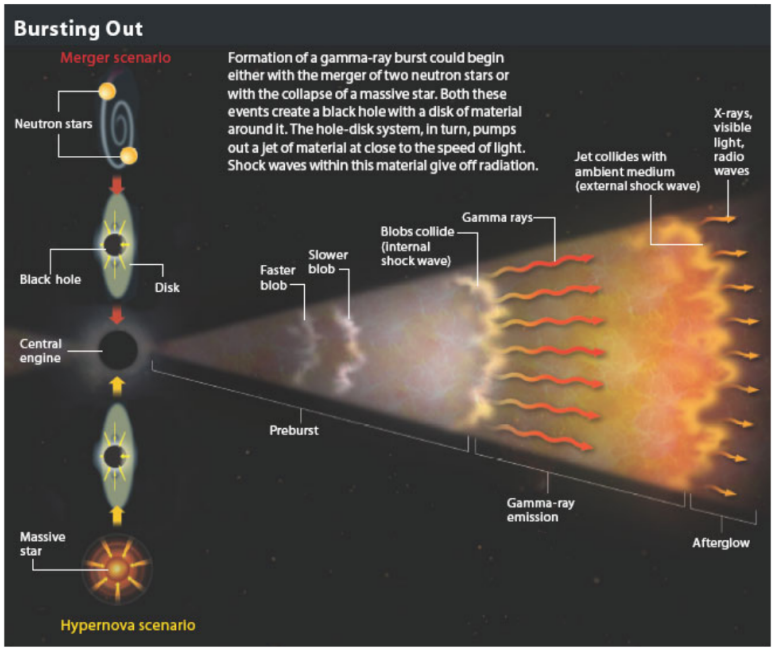

Figure 3.3: Illustration of the internal-external shock fireball model. On the left are illustrated the two most favoured progenitors leading to the creation of a black hole with an accretion disk. Figure from [104]

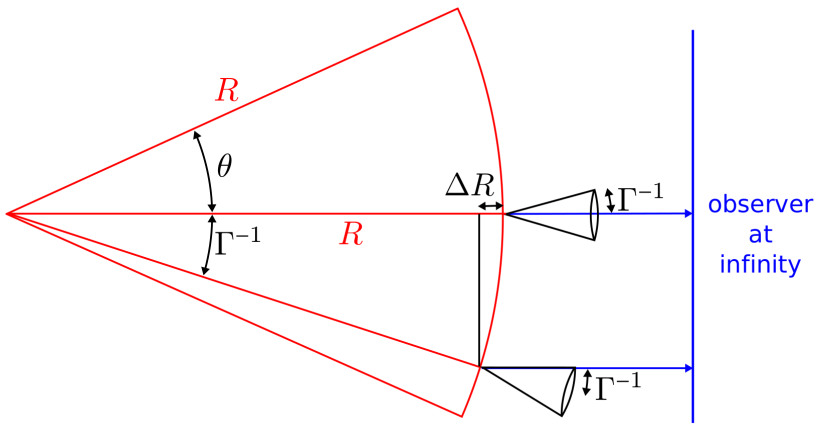

Figure 3.4: Geometry of the outflow of a single shell in a jet. The shell is limited in a jet opening angle θ. For a shell with Lorentz factor Γ only a conic cut with angle Γ^{-1} is visible to an observer at infinity due to relativistic beaming. The width of the shell due to the spherical curvature as seen by an observer at infinity is $\Delta R = R(1 - \cos\Gamma^{-1})$. Figure from [3].

different visible parts of a shell at radius R. This time difference can be expressed as

$$\Delta t_{ang} = \frac{R}{c}(1 - \cos(\Gamma^{-1})) \sim \frac{R}{2c\Gamma^2} \qquad \text{for} \qquad \Gamma \gg 1 \tag{3.2}$$

Note that we find the same expression as Δt (3.1).

3.2.2 GRB progenitors

As we saw in the previous section the GRB emission is released far from the central engine. The progenitor cannot commonly be directly observed with electromagnetic signal and its properties are inferred by indirect means. The total duration of the burst lasting up to few tens of seconds and the short time variability implies that the central engine is composed by a compact object with a prolonged activity but likely to be destroyed as there is no repetition of these events. There are thus two main astrophysical events expected to create GRBs: a compact binary coalescence involving at least one neutron star, or the collapse of a massive star. Both of them are expected to be associated with a newborn black hole massive with a massive accretion disk ($\sim 0.1 M_\odot$). In the following I will briefly review both of these models associated to the short and long GRBs.

Stellar collapse model

The model that provides the theoretical framework of the long GRBs/supernovae association is known as the collapsar model [105, 106]. According to this model, the collapsar is a very massive ($20 - 30M_{\odot}$) and fast rotating star whose iron core directly collapses to form a magnetar or a black hole at the end of its stellar evolution [107]. The residual matter of the progenitor released after the collapse is accreted by the black hole. A few tens to hundreds of seconds after the collapse, the accretion of matter at the polar regions becomes less intense and a partial evacuation of matter in the polar regions is achieved with the fast rotation of the black hole [108]. A proposed mechanism is that the energy deposed in the accretion disk is then dissipated by neutrinos annihilation which produces relativistically expanding blast wave of radiation and pairs along the rotational axis [109, 107, 110]. In a second mechanism proposed by [111], it is the rotational kinetic energy of the newly formed black hole that is directly extracted via the magnetic field lines attached to it. There is a long line of evidence connecting long GRBs (LGRBs) to collapsing massive stars (for recent reviews see [112, 113]). To avoid the problem of a significant baryonic contamination discussed in the fireball description section, the progenitor should have lost its hydrogen envelope before the collapse. One proposed mechanism is the removal of the hydrogen envelope by stellar winds [105]. Another proposed mechanism involves a binary system where the hydrogen envelope of the progenitor star is removed by the binary companion [114, 115]. Those relate to type Ib/Ic supernovae characterised by a lack of hydrogen lines in their spectra.Those relate to type Ib/Ic supernovae characterised by a lack of hydrogen lines in their spectra. For more detailed review of the stellar collapse model see for instance [108, 116, 117, 115]. The first unambiguous association of such kind is the association of long GRB980425 and the type Ic supernovae SN1998bw [118]. For a summary of the observational status of the supernova/long gamma-ray burst connection see [119].

Coalescence model

The prefered scenario for short GRBs is the coalescence of two neutron stars (BNS) or a black hole with a neutron star (NSBH). By comparison with long GRBs, short GRBs afterglows are much less luminous making the detection of an optical spectrum more difficult and rare. Furthermore, the lack of association of short GRBs with supernovae and the localisation of short GRBs afterglow in elliptical galaxies confirmed the difference in progenitors with long GRBs. This makes it more difficult to identify the progenitors, therefore the coalescence of two compact objects was firstly supported by some indirect evidence like the estimated rate of BNS merger [120, 121, 122] (similar to the rate of short GRBs [123]) and the large

offsets between short GRBs afterglow position and the host galaxy centre, larger than for long GRBs [124, 125, 126].

A more convincing evidence that the progenitor of short GRBs are compact binary merger are the associations of such GRBs with kilonovae emission. The physics of kilonovae can be resumed in a neutron rich merger ejecta expanding at constant mean velocity. This expansion can be considered at first order as spherically symmetric. The matter freshly ejected is heated by radioactivity due to r-process nuclei and free neutrons. As a result, the kilonovae can be observed as a point source with thermal emission from UV to IR with an absolute magnitude $\sim$ 15 in near infrared bands [127]. Hint of such observation has been associated with short GRBs several times (see for instance GRB130603B [128] and GRB150101B [129]), the ultimate one was obtained recently with the joint observation of the gravitational wave GW170817 with the short GRB170817A resulting in the coalescence of 2 neutron stars with a total mass system of $\sim 2.8 M_{\odot}$ [130]. Details on the follow-up of this event are discussed in section 5.3.

3.3 Gamma-ray burst detectors

Among the various missions/instruments dedicated to the detection of GRBs I will focus in this section on the Gamma-Ray Burst Monitor on the Fermi spacecraft [131] and telescopes on the Swift spacecraft [131, 132, 133, 134]. This choice is motivated by the fact that these missions are used in the various research and analyses of my thesis work presented in chapters 4 and 5. While most of the recent GRBs have been detected by these missions they are definitely not representative by themselves of the diversity of methods developed by the scientific community for the detection of GRBs. I will also present more in details the Space-based multi-band astronomical Variable Objects Monitor (SVOM) mission which will start in the middle of 2022 and will play a key role in the time-domain/multi-messenger astronomy. Personal works related to the SVOM mission are presented in chapters 4 and 5.

Neil Gehrels Swift Observatory

The Burst Alert Telescope (BAT) on board of the Swift spacecraft is sensitive to fluxes $\sim 10^{-8}$ erg cm^{-2} s^{-1} in the 15-150 keV energy range. This detector is equipped with a coded aperture telescope with a field of view of 1.4 steradian and a sky localisation accuracy of several arcminutes. This sky localisation is performed by analyzing the shadow pattern of a coded mask onto an array of CdZnTe detector elements. This localisation is often refined in case of afterglow detection by the on board X-ray Telescope (XRT), with few arcseconds localisation error, and/or

the Ultraviolet/Optical Telescope (UVOT) with sub-arcsecond localisation error. The BAT instrument alone detected, since 2004, more than 1000 GRBs [135]. The Swift mission, with its various detectors and its automatic repointing capability is designed to play an a key role in the multi-wavelength follow-up of GRBs, detects and provides accurate localisation of the afterglow allowing ground based follow-up by the community. It also plays an important role in the multi-messenger follow-up of neutrino and gravitational wave alerts [136, 137].

Fermi/GBM

The Gamma-Ray Burst Monitor (GBM) on board of the Fermi spacecraft is sensitive to fluxes ~ 0.4 photons cm^{-2} s^{-1} in the 8 keV-40 MeV energy range. GBM is composed of NaI and BGO detectors which cover a field of view of 9 steradians. The typical sky localisation error for this detector is ≥ 1 degree. In ten years, the GBM detector observed ~ 2500 GRBs [138]. While the Fermi GBM detection alerts are numerous, they are challenging for the follow-up because of the poor localisation of the source (typically ~ 17 deg for the localisation 90 % error radius [139]). On the other hand, with its extremely wide field of view (all sky but for Earth occultation) the GBM detector is particularly effective in the search for gravitationnal wave GRB counterpart.

SVOM mission

The SVOM mission is a ground and space-based multi-wavelength observatory aiming at detecting GRBs and other transient sky sources [140]. Planned to be launched in mid 2023, this mission is a collaboration between French and Chinese space agencies (CNES and CNSA). The scientific objectives of the SVOM mission are to study the entire GRB continuum, to perform a complete phenomenology of GRBs of all types over a wide detection band by observing the prompt emission and the afterglow. To probe the nature of the GRB progenitors, the physics of the GRB explosion using faint/soft nearby GRBs; and the study of high-redshift GRBs (z>5) as a probe of the early universe. As presented in figure 3.5 the SVOM satellite will be equipped with four instruments: two dedicated to the observation of the GRB prompt emission, a coded-mask gamma-ray imager (ECLAIRs) with field of view of 2 sr operating in the 4-150 keV energy range; and a gamma-ray spectrometer (GRM) with field of view of 5.6 sr operating in the 15-5000 keV energy range. Two telescopes dedicated to the observation of the GRB afterglow, a Microchannel X-ray Telescope (MXT) with a field of view of 64×64 arcmin^2 operating in the soft X-ray range (0.2-10 keV); and a 40 cm aperture Ritchey-Chrétien Visible-band Telescope (VT) with a field of view of 26×26 arcmin^2 observing in visible (400-650 nm) and in near-infrared (650-950 nm). One can

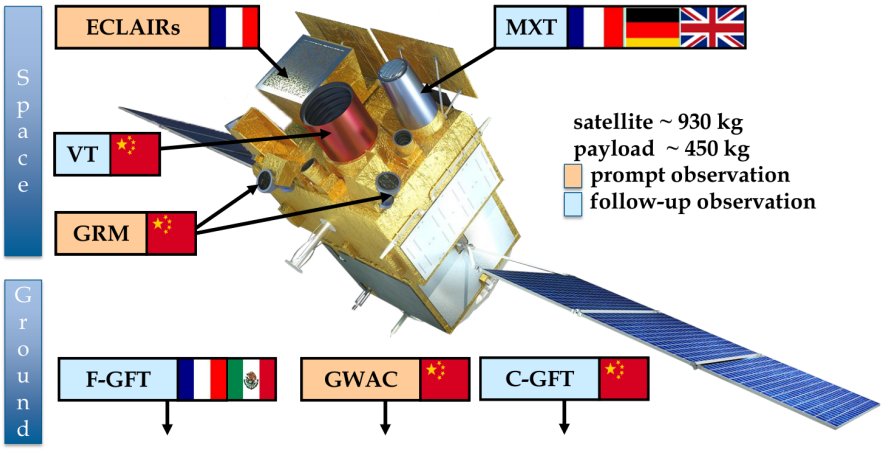

Figure 3.5: View of the SVOM space-based and ground-based instruments. Figure from [140].

notice the similarity with the Swift telescopes whose SVOM can be considered as successor.

The SVOM ground segment is composed of 5 instruments: a wide angle optical camera (GWAC), composed of 36 cameras for a total field of view of 5400 square degrees, monitoring in real-time the ECLAIRs field of view aiming at the optical prompt emission observation; the F30 and F60 telescopes, with a field of view of respectively ~ 4 deg^2 and $\sim 19 \times 19$ arcmin^2, both located alongside of the GWAC and equipped with Johson-basal filters UBVRI, aiming to confirm and study the optical transient candidates detected by the SVOM/GWAC systems in multiple wavelengths; and two 1m class robotic ground telescopes (C-GFT and F-GFT), one based on China operating only in the visible and one based in Mexico operating in visible and near-infrared, both dedicated to the follow-up of ECLAIRs GRBs with ~ 1 minute of delay.

The general strategy for the detection and the follow-up of GRBs is described in details in [140]. In a few words, the SVOM satellite will observe according to a pointing law described in [141], wich optimises the constraints from both space and ground segments waiting for a GRB. Note that the expected GRB rate is estimated to be around 60-70 per year [140]. After the detection, ECLAIRs provides a localisation of the source with an accuracy better than ~ 13 arcmin. The spacecraft then slews automatically in a few minutes to this position for the follow-up of the GRB afterglow emission with the narrow field of view telescopes (MXT and VT). In the meantime the GRB position and its main characteristics determined by ECLAIRs are also quickly sent to the ground using the SVOM VHF emitter. In case of detection, X-ray and visible counterparts are also sent to the

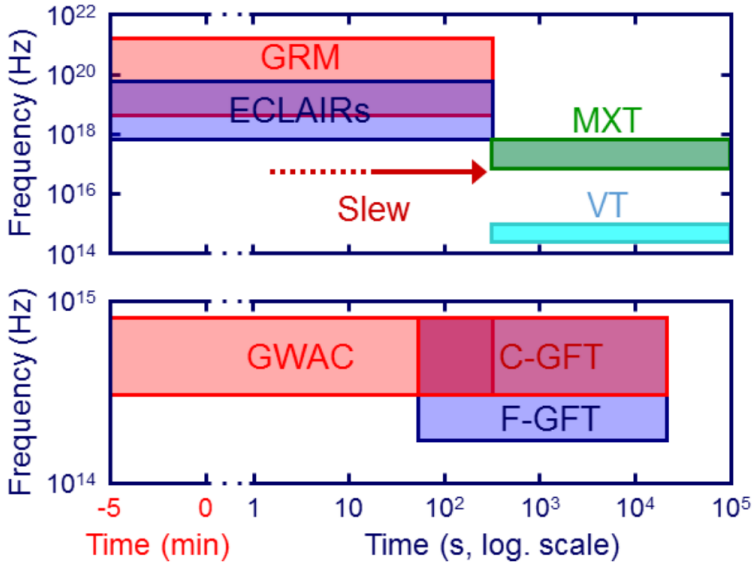

Figure 3.6: Follow-up strategy of a GRB prompt emission with SVOM space and ground instruments. Upper panel represents the instruments on-board the satellite and the bottom panel the ground facilities. When the GRB is detected at t=0, the spacecraft starts to slew to align the narrow FoV telescopes (MXT and VT) with the GRB position and a VHF alert is sent to the ground follow-up telescopes (C-GFT and F-GFT) which start to observe approximately at t+1 minute and produce first results within 5 minutes. GWAC which is monitoring in real-time the ECLAIRs and GRM field of view will collect data starting before the prompt emission trigger. Figure from [140].

ground via VHF, with a sub-arcmin localisation accuracy for MXT and sub-arcsec for VT. The SVOM ground VHF receivers network is composed of $\sim$ 50 stations distributed all around the globe under the satellite track. This network ensures that most of the alerts are received within 30 seconds at the science centers which forward the information via internet to the SVOM ground instruments and to the scientific community. The satellite stays pointed towards the source for 14 orbits ($\sim$ 1 day). Ground follow-up telescopes are expected to provide first results and sub-arcsec localisation within 5 minutes of observations. The F-GFT, thanks to its near-infrared coverage is expected to provide an information on the source distance after 5 minutes of observations. A visual representation of this follow-up strategy is proposed in figure (3.6).

From its capacity to obtain multi-wavelength follow-up observations from its space and ground instruments the SVOM mission will play a key role in the time-domain/multi-messenger astronomy. In order to contribute to this new era, in

addition to ground follow-up of multi-messenger triggers, the time allocated by the SVOM spacecraft to the observation of targets of opportunity is set to be at least 15% of the lifetime of the nominal mission. My work about the follow-up of gravitational wave events with the SVOM instruments are presented in chapter 4 and 5.

3.4 Electromagnetic counterparts of gravitational waves

Gamma-ray burst and gravitational wave time delay

Progenitors of gamma-ray bursts are also expected to be sources of gravitational waves (the case of compact binary coalescence will be illustrated with the observation of the gravitational wave GW170817 in the following). In order to process any coincidence analysis one should question the expected time delay between the arrival of the gamma-ray T_γ and gravitational wave T_{GW}. We will place ourselves from the point of view of an observer located on/near Earth and consider the gravitational wave speed to be exactly the speed of light (see [130] for constrain on the difference between the speed of gravitational waves and the speed of light).

For short GRBs resulting from a compact binary coalescence, gravitational wave are detectable with ground based detectors during the inspiral phase at most few minutes before the merger. Hence the gravitational wave detection time T_{GW} is contained in $[-$ few minutes$, 0]$ s (the signal amplitude being higher close to the merger time), where $t = 0$ is the merger time. To estimate the gamma-ray arrival time T_γ, one needs to take into account the time delay between the merger and the launch of the relativistic jet and the time delay between the start of the jet and the arrival of the gamma-rays to the observer. Being inclusive taking various jet models one can constrain T_γ in $[0, \sim 200]$ s [3]. At the end the time delay between the arrival of the gamma-ray T_γ and gravitational wave T_{GW} can be safely estimated to lie in the range $T_{GW} - T_\gamma \in [-250, 0]$ s.

For long GRBs resulting from a stellar collapse, the relativistic jet is expected to be created several seconds to several minutes (depending on the supernovae type) after the proto-neutron star [3]. The jet is expected to plows through the stellar envelope in less than few minutes. Finally jet accelerates to relativistic speeds and produce gamma-rays trough internal shocks within up to few minutes. For stellar collapse, gravitational wave mechanisms predict an emission within seconds of the creation of the proto-neutron star or the black hole and accretion disk system [3, 16, 17, 18].

At the end, taking both the coalescence and the stellar collapse model into account the relative time of arrival between gravitational wave and gamma-rays

can be estimated to lie in the range

$$T_{GW} - T_{\gamma} \in [-400, 5] \tag{3.3}$$

However for long GRBs the light curve can be composed of multiple peaks and the spacecraft may have a trigger time T_{GRB} on a small burst preceding the main emission peak. In order to conservatively take this into account one can assume that the main emission peak is anywhere in the observed light curve, that is $T_{\gamma} - T_{GRB} \in [0, T_{90}]$. Hence gravitational waves should arrive in a time window around the GRB trigger time

$$T_{GW} - T_{GRB} \in [-400, T_{90} + 5] \tag{3.4}$$

In the catalog of GRBs detected by BATSE a *precursor*, significant gamma-ray emission arriving before the main emission, has been observed in approximately 10% of the cases [142]. 20% of these precursors are separated by more than 100 s from the following emission. Various models try to explain this precursor emission (see for instance [143, 144, 145]) and coincidence time window used in the analysis has to take it into account. For instance the `X-Pipeline` analysis presented in chapter 4 uses a window of

$$T_{GW} - T_{GRB} \in [-600, \max(T_{90}, 60)] \tag{3.5}$$

which includes an additional 50% in the lower bound to account for estimation errors. A lower limit of 60 s for the upper bound is set to take into account that roughly 20% of BATSE GRBs have a duration above 60s and the duration is not reported for all the GRBs. The additional 5 seconds to the T_{90} value are neglected as $< 10\%$ errors on the T_{90} are not relevant.

3.5 GW170817 and GRB170817A as an illustration of counterpart to gravitational waves

In this section I propose to use the example of the GW170817 detection as a illustration of what can be expected as gravitational wave counterpart.

3.5.1 Overview of the detection

The 17th August 2017, the LIGO-Virgo collaboration reports the identification of a binary neutron star candidate coincident with a Fermi GBM near threshold trigger [146] named afterward GRB170817A. This GRB is 2 to 6 orders of magnitude less energetic than other short GRBs [130]. While there is a glitch in LIGO Livingston

data overlaying the signal (see figure 3.7), the signal is clearly visible in both LIGO Livingston and LIGO Hanford detectors and was reported after $\sim$ 30mn. About 1h after the trigger, the INTEGRAL team reported a short and relatively weak coincident transient [147]. This detection is the first gravitational wave detection from a BNS source and the first with an electromagnetic counterpart.

Following this alert, a worldwide follow-up started with both ground based and spacecraft instruments (see figure 3.8). The LIGO-Virgo localization region ([148, 149]) became observable to telescopes in Chile about 10hr after the merger. The One-Meter Two-Hemisphere (1M2H) collaboration, who was using a *galaxy targeting* strategy (see section 5.2.3 for development) for their observations, first announced the discovery of a transient (named SSS17a then AT2017gfo) in an image acquired with the 1m Swope telescope at Las Campanas Observatory in Chile $\sim$ 11hr after the LIGO-Virgo detection [150]. The optical transient is located approximately 2.2 kpc from the centre of its host NGC4993, an early-type galaxy at z=0.009727 ($\sim$ 39.5 Mpc). At the time most groups focused their effort to define the transient nature and to rule out that it was a chance coincidence of an unrelated transient.

This transient marked very quickly the worldwide community by its rapid and unusual luminosity decline. For the bluer optical bands the photometric measurements presented a fading of more than 1 magnitude per day. On the contrary, the near-infrared monitoring showed that the source faded more slowly in the infrared and even showed a late-time plateau in the K_s band, see [151] for a summary of the observations. Early spectroscopic observations, $\sim$ 30mn after the first transient observation, presented a blue and featureless continuum between 400 and 1000 nm [152, 153]. This first spectrum, consistent with a power law, present common characteristics with cataclysmic–variable stars and young core-collapse supernovae (see for instance [154, 155]). But the absence of absorption lines common in supernova-like transients and the exceptionally fast spectral evolution ruled out the possibility of a young supernova of any type in NGC4993, decreasing the likelihood of a chance coincidence between the transient and GW170817. Later spectroscopic observation [151] presented a rapidly fading spectral energy distribution and the emergence of a broad spectral feature similar to kilonovae models (see for instance [156]). Finally, the observation of signature of the radioactive decay of r-process nucleosynthesis elements [157] and the production of lanthanides within the ejecta gave the last word to the classification of the transient as kilonovae [157, 158, 159, 160, 161, 162, 163]. Figure 3.9 presents the combined lightcurve of kilonova from ultraviolet to near-infrared with aggregated and homogenized data alongside with fitted kilonovae models [164].

Nine days post-trigger, observers [165] reported the discovery of the X-ray counterpart with Chandra in a 50 ks exposure observation. This X-ray detection

was associated to an off-axis afterglow of the short GRB170817A. The first radio counterpart detection consistent with the transient position was obtained with the VLA on 2017 September 2 and 3 at two different frequencies ($\sim$ 3GHz and $\sim$ 6GHz) via two independent observations: the Jansky VLA mapping of Gravitational Wave bursts as Afterglows in Radio (JAGWAR ; [166]) and VLA/16A-206 [167]. Marginal evidence for radio excess emission at the localisation of transient was also confirmed in ATCA images taken on September 5 at similar radio frequencies (7.25 GHz; [168]). This radio detection was also associated to be the afterglow of GRB170817A. Both X-ray and radio counterparts (see [151] for details) combined with the multi-wavelength evolution within the first 12-24h confirmed the association with GW170817 (and GRB170817A).

Since the event, the localisation of the transient has been observed for years to characterise the evolution of the GRB afterglow and to look for the potential kilonovae afterglow (see for instance [169, 170, 171]). First clues of such detection was proposed with the emergence of a new source of X-rays, more than 3 years after the merger, consistent with synchrotron emission from a kilonova afterglow[171].

3.5.2 The scientific outcome of this event

This event of the 17th August 2017 is unprecedented for the multi-messenger astronomy. It was the first electromagnetic counterpart (at all wavelengths) detected for a gravitational wave and the first unambiguous observational evidence of a kilonova. The multi-wavelength observations improved our understanding of the physics of strong-gravity and put some constraints on astrophysical models related to matter during the merger and post-merger phase. A first constraint of the speed of gravitational waves and violation of Lorentz invariance has been determined from this event [130]. Both kilonova and afterglow observations provide information about the neutron star equation of state, energy of the ejecta, merger remnant, ambient medium and so on [127, 173, 174, 175]. It confirms the kilonova as a source of r-process and heavy elements factory. Such event also provides a new independent derivation of the Hubble Constant [176, 177, 178]. It is a convincing evidence that the progenitor of (at least some) short GRBs are BNS mergers. The GRB detection combined with the X-ray and radio afterglow observation provide information on the energetic of the explosion, the geometry of the ejecta, as well as the environment of the merger pointing out to a very unusual slightly off-axis short GRB observation [179, 180, 181].

3.5.3 Neutrino counterpart

High-energy neutrino counterpart can be expected for BNS mergers [182, 183, 184]. Particle acceleration and high-energy emission by compact objects are currently

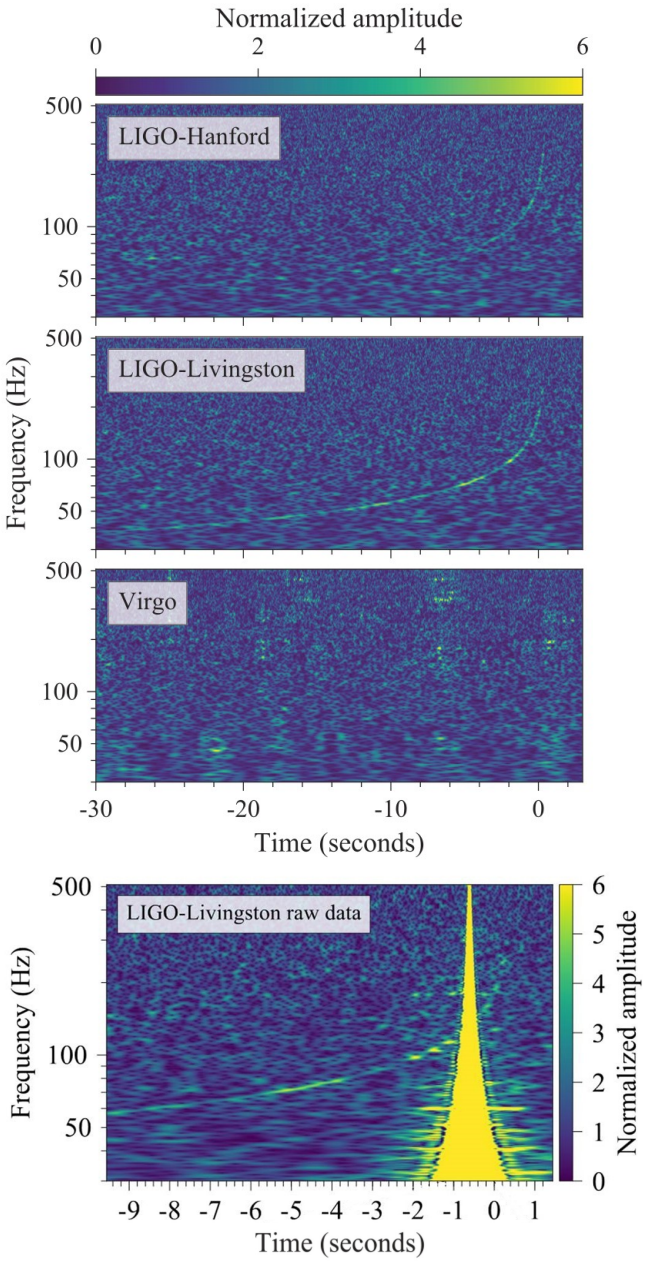

Figure 3.7: *Top:* spectrograms containing the gravitational-wave event GW170817, observed by the LIGO-Hanford (top), LIGO-Livingston (middle), and Virgo (bottom) detectors. Times are shown relative to August 17, 2017 12:41:04 UTC. *Bottom:* spectrogram of the LIGO-Livingston data before the glitch removal. Figures from [172].

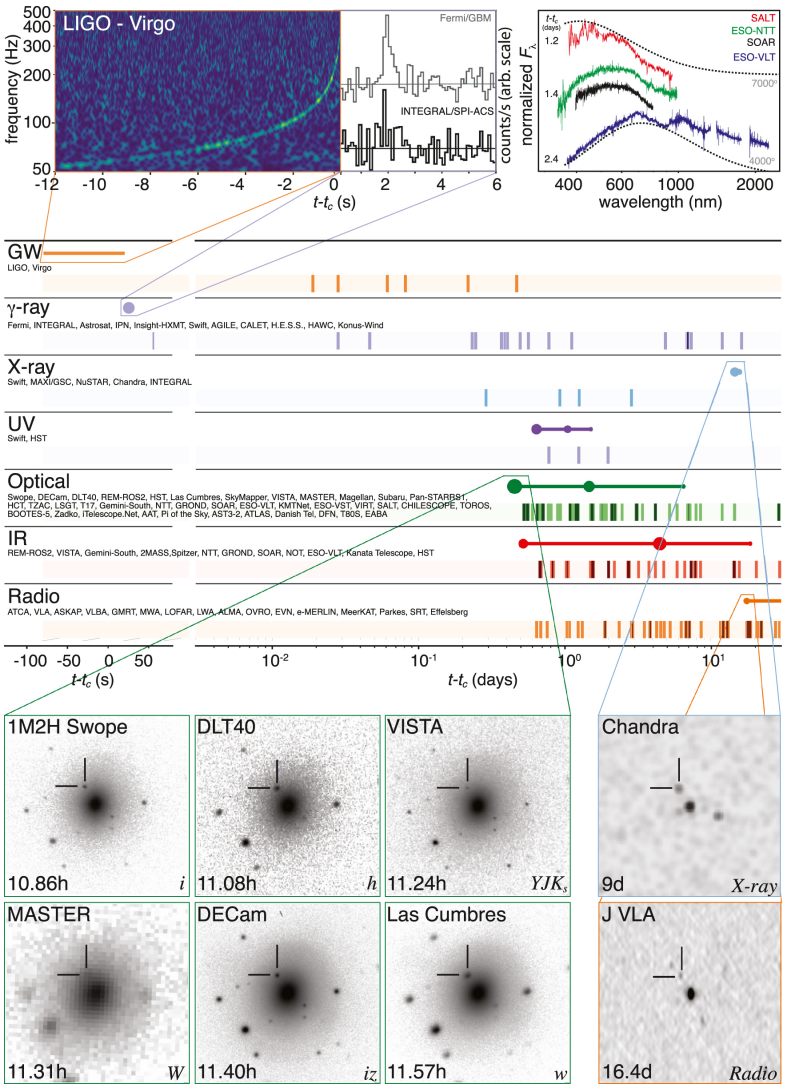

Figure 3.8: Timeline of the discovery of GW170817, GRB170817A, SSS17a/AT2017gfo, and the follow-up observations are shown by messenger and wavelength relative to the time t_c of the gravitational-wave event. Two types of information are shown for each band/messenger. First, the shaded dashes represent the times when information was reported in a Gamma-ray Coordinates Network (GCN) Circular. The names of the relevant instruments, facilities, or observing teams are collected at the beginning of the row. Second, representative observations in each band are shown as solid circles with their areas approximately scaled by brightness; the solid lines indicate when the source was detectable by at least one telescope. Figure from [151].

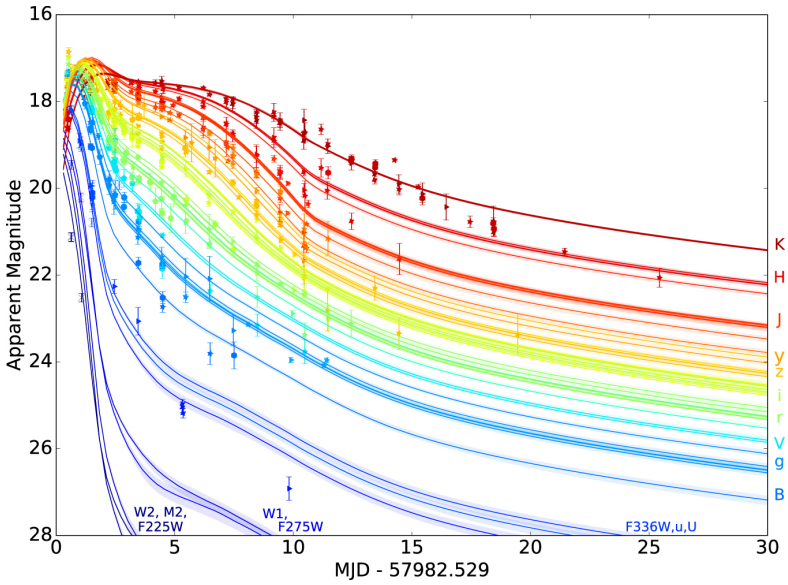

Figure 3.9: Lightcurves from the combined data set (see Table 3 of [164]), along with the spherically symmetric three-component models with the highest likelihood scores. Solid lines represent the realizations of highest likelihood for each filter, while shaded regions represent the 1σ uncertainty ranges. For some bands there are multiple lines that capture subtle differences between filters. Figure from [164].

not well understood [185, 186] and could be clarified by combined information on the neutron star masses, GRB properties and ejecta mass, as can be expected from multi-messenger detection. In particular, the observation of high-energy neutrinos would reveal the hadronic content and dissipation mechanism in relativistic outflows [187]. But while the ANTARES, IceCube, and the Pierre Auger Observatory, high-energy neutrino observatories continuously monitoring the whole sky or a large fraction of it making them well suited for studying emission from GW sources [188, 189], were observing at the time of the GW170817 event no neutrino burst signal was detected coincident with the merger [190]. While the localisation of this source was nearly ideal for Pierre Auger observatory, it was well above the horizon for IceCube and ANTARES for prompt observations, this limited the sensitivity of the two detectors. Independent search with the Super-Kamiokande detector resulted with no significant coincident neutrino signal [191].

3.5.4 GW170817 a very lucky observation

As presented in the previous section, the GW170817 event was a particularly fruitful event. One can expect more similar detections in the future but such event can be shown to be very rare. Indeed there are several properties which make this event very prone to provide multi-messenger and multi-wavelength observations which are not common for BNS merger gravitational wave detection. The first one is the distance of the event ($\sim$ 40Mpc) which is very small, the rate of BNS merger detection at this distance with O3 run sensitivity can be estimated to one every $\sim$ 12 yrs [192]. The second one is the viewing angle which has to be small enough to expect a detection of the associated short GRB or the X-ray/radio afterglow. Taking this second restriction into account the expected rate of triggers suitable to get a full GW170817-like multi-messenger data set can be estimated to one per $\sim$ 239 yrs [192]. The last important point is localisation of the event provided by the gravitational wave detection. The GW170817 event was a relatively well localised event with an error box of $\sim$ 30 deg^2 (thanks to the fact that there were three gravitational wave detectors operating at the time and the combination with the GRB error box), but larger error could lead to more difficulties to identify any counterpart candidate and thus the miss of the early counterpart emission or even the whole counterpart. The O3 observing run of LIGO-Virgo-KAGRA collaboration illustrates this difficulty, while there was BNS merger detections no unambiguous counterpart was found [15]. Nevertheless, one can expect that deep surveys will, however, be able to identify non gravitational wave triggered kilonovae with possible short GRB associations in the future [192].

3.6 Host galaxies population

In this section I will review the GRB host galaxies population properties for long and short GRBs respectively. Short GRBs host population will be studied in chapter 5 with a new sample of host galaxies constructed during this thesis. The identification of the first samples of host galaxies of GRBs was performed in the early 2000s [193, 194, 195, 196, 197, 198, 199]. However the systematic and rapid follow-up of the GRB alerts only started the mid 2000s with the Swift spacecraft (bringing its ability of arc-second level localisation from XRT) and the apparition of fully robotic optical or/and near-infrared telescopes (for instance REM [200]) or semi-robotic telescopes (for instance PAIRITEL [201], GROND [202] and RATIR [203]). Hence, most identified GRB host galaxies are from GRBs detected after this date.

3.6.1 Long GRB host galaxies

For a galaxy one can determine its star formation activity from its location on the main sequence of star-forming galaxies. In general, star-forming galaxies exhibit a linear correlation between their star formation rate (SFR) and stellar masses (see Figure 3.10), forming the so called main sequence. In this plot, one can basically understand that galaxies above the main sequence are forming much more stars than typical galaxies and galaxies below the main sequence are forming fewer stars to almost no star (see Figure 3.10 and [204]). Long GRBs have been observed to be hosted by galaxies with stellar masses ranging from $\sim 10^8 M_\odot$ for optical bright GRBs up to $\sim 10^{11} M_\odot$ for dusty GRBs [205, 206]. In average, long GRB host galaxies have lower stellar mass than normal star-forming galaxies [207, 208, 209, 205, 210] (see for instance figure 3.11). While solar and super-solar metallicities are observed for some host galaxies [211, 212, 213, 205, 210] they are generally found to be sub-solar [207, 205, 214, 210, 215]. Because of the selection effects in optical, two X-ray selected samples were built to study properties of GRB host galaxies in an unbiased way: The Optically Unbiased GRB Host survey (TOUGH, [216]) and the Swift GRB Host Galaxy Legacy Survey (SHOALS, [217]). They contain 69 and 119 GRBs respectively and SHOALS is the largest sample of GRB host galaxies up to now. Because of their extreme luminosity GRBs can be detected at very high distance (up to redshift ~ 10). As explained in section 3.2.2 long GRBs are associated with massive, short-lived stars. This implies that they offer a unique probe to study star formation up to very high redshift [205, 214, 215, 215].

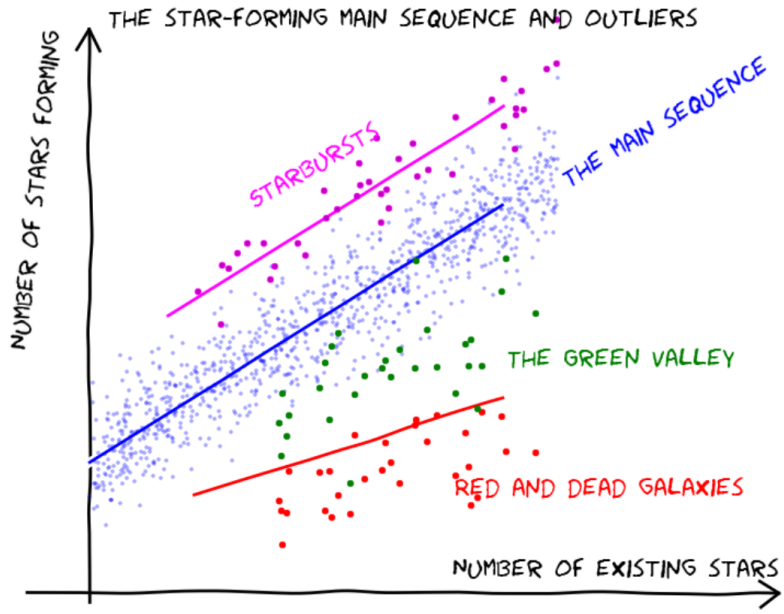

Figure 3.10: Main sequence of star-forming galaxies. Normal galaxies are forming stars at a rate proportional to the number of stars they already formed (blue points). Galaxies forming stars at a higher rate are called starbursts (purple points). Galaxies that are forming few stars are located in the region called the "green valley" (green points). Galaxies that are not forming stars anymore are called quiescent galaxies (red points). (Credit : Cosmic Assembly Near-infrared Deep Extragalactic Legacy Survey (CANDELS)).

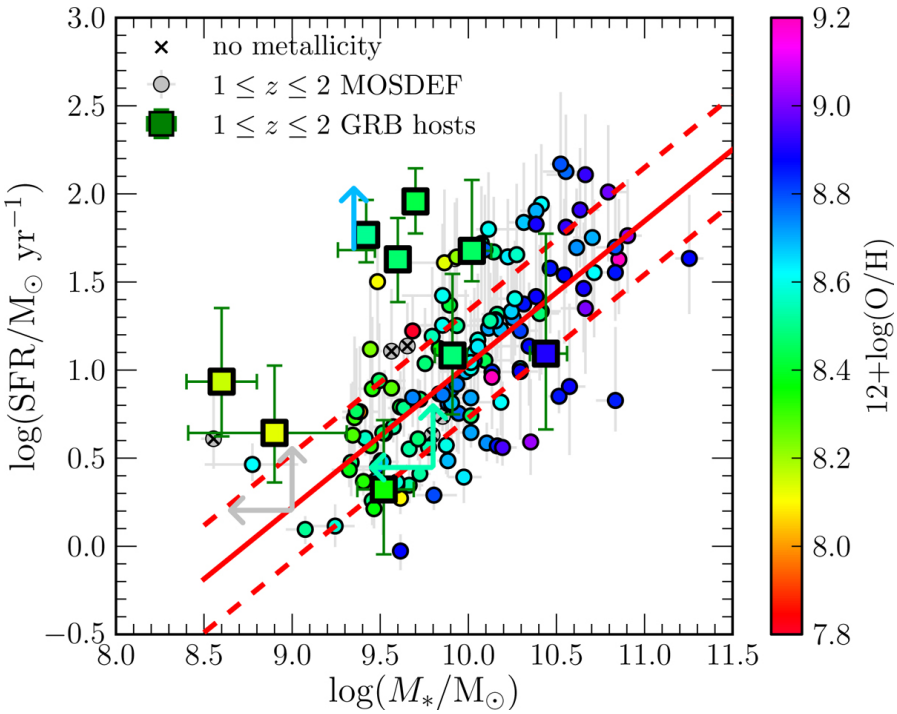

Figure 3.11: SFR versus stellar mass plot for the BAT6 sample of galaxies at 1<z<2(squares). The circles are from the MOSFIRE Deep Evolution Field (MOSDEF) sample of galaxies at 1<z<2 [218], representing the backgroud distribution of galaxies in this SFR versus stellar mass plot. The red line is the best fit to the MOSDEF [218] data and the dotted lines represent the intrinsic scatter, following the method of [219]. The points are coloured by metallicity [215]. Galaxies where no metallicity could be measured are coloured in grey with a cross. Figure from [215].

3.6.2 Short GRBs host galaxies

In this section I will review the current knowledge of the short GRBs host population properties. This section is mostly based on the [220, 221] results which are built on the most recent and most complete short GRBs host galaxies compilation. In chapter 5, I will present a new analysis of short GRBs host population properties updated in the light of a most recent sample of host galaxies.

The Redshift Distribution

Up to now, essentially all short GRB redshift (spectroscopic or photometric) have been obtained from the associated hosts [222, 223, 224, 225, 226]. Exceptions are GRB 090426 at $z = 2.609$ [227, 228] and GRB 130603B at $z = 0.356$ [229, 230] for which redshifts have been determined from afterglow absorption spectra. While [231] suggests that some hosts without a known redshift reside at $z > 1$, the measured redshifts of host galaxies span $z \sim 0.01 - 1.3$ (the smallest being NGC4993 host of GW170817 and GRB170817A see section 5.3) as shown in figure 3.12. For short GRBs the median redshift infered from [220, 221] sample is $\langle z \rangle \sim 0.5$. In the sample of short bursts [221], only 6 lack XRT positions despite rapid follow-up, and hence the ability to identify hosts. Therefore the observed redshift distribution represents relatively well the redshifts of Swift short GRBs. As shown in figure 3.12 there is no evidence in this sample for a trend between redshift and host galaxy type, both early and late type galaxies span in the same redshift range. The Swift short GRB population is substantially more local than the long one which shows a median value of $\langle z \rangle \sim 2$ (see figure 3.12) [232, 233]. This can be partly explained by the lower energy scale of short GRBs, but this may also be the reflection of a longer delay time between the star formation activity and the occurrence of the short GRBs.

Lack of Supernova Associations

Among the population of short GRB with identified host galaxy, there are several events at sufficiently low redshift to allows a clear detection of any associated supernovae [221]. Figure 3.13 presents the upper limits for associated supernovae for 7 shorts bursts, measured relative to the peak absolute magnitude of the canonical long GRB supernova SN1998bw. One can see that supernovae associated with long GRBs span a brightness range with a median and standard deviation relative to SN1998bw of $+0.18 \pm 0.45$ magnitude. Upper limits on supernovae associations for short GRBs presented range from ~ 0.5 to ~ 7.5 magnitude fainter than SN1998bw. From this sample, an association with supernovae that are drawn from the same distribution than long GRBs supernovae can be ruled out. Again this is a important indicator that short GRBs doesn't share common progenitor system

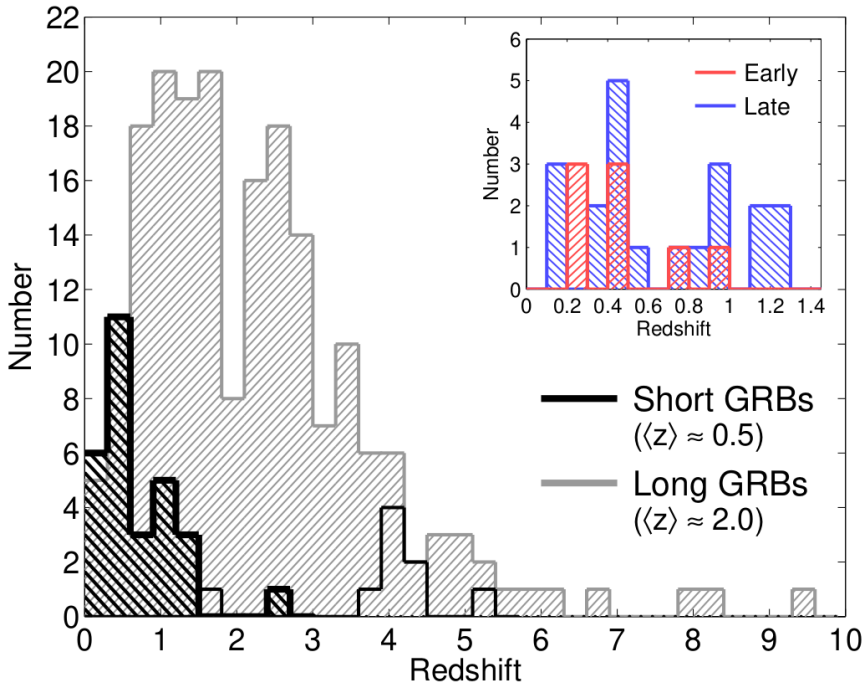

Figure 3.12: The redshift distribution of short GRBs (black) and long GRBs (gray). The open histogram marks redshift upper limits based on the lack of a Lyman-α break in afterglow and/or host galaxy optical detections. The inset shows the redshift distribution of short GRBs separated by host galaxy type, which exhibits no discernible difference between early-type (red) and late-type (blue) hosts. Figure from [214].

with long GRBs, or at least that the short GRBs with deep supernovae limits are not produced by massive star explosions. Note that 6 over 7 short bursts with limits on associated supernovae are located in star-forming galaxies [221]. This suggests that while the hosts exhibit on-going star formation activity, the short GRB progenitors themselves do not belong to a young population of massive stars.

Galaxy host type

While, as seen in previous section, long GRBs occur in star-forming galaxies (as expected for young massive star progenitors), short GRBs on the other hand tend to occur in a mixed population of early-type and star-forming galaxies [223, 222, 224, 239, 220] (see figure 3.14). This may indicate that their progenitors span a wide range of ages. [221] suggests, knowing that in the range of existing short GRB population ($0 < z < 1$) there is a roughly equal fraction of the cosmic stellar mass density in early-type (with almost no star formation activity [240]; SFR $\lesssim 0.1\ M_{\odot}\mathrm{yr}^{-1}$) and late-type galaxies [241, 242], an exclusively old progenitor population (i.e., tracking stellar mass alone) should also exhibit an equal fraction of early- and late-type hosts galaxies, which is not the case here in the light of this sample. [220, 221] propose that the dominance of late-type galaxies visible in figure 3.14 indicates that the short GRB rate does not depend on stellar mass alone, and is instead influenced by recent star forming activity. Additionally they propose that the role of the star formation in the short GRB rate is visible through the rate of luminous and ultra-luminous infrared galaxies (U/LIRG) host. Indeed two short GRBs (i.e. $\sim 5 - 10\%$ of the sample) have been associated with (U/LIRG) galaxies [243, 244]. This fraction is higher than progenitor population that tracks stellar mass alone ($\sim 1\%$, [245]) and lower than progenitor population that tracks only star formation ($\sim 25\%$, [246, 247]). This may indicate a mixed role of the stellar mass and star formation activity in the progenitor population.

Stellar Masses and Stellar Population Ages

In [221] sample the stellar masses inferred from modeling the spectral energy distributions of the host with optical and near-infrared photometric observation with single stellar population models span $M_* \sim 10^{8.5-11.8} M_{\odot}$ (see figure 3.15). The median for the full sample is $\langle M_* \rangle \sim 10^{10.0} M_{\odot}$ for short GRBs. On the other hand the stellar masses of long GRB hosts are lower, with a median value of about $10^{9.2} M_{\odot}$ [199, 250]. Looking only at the star-forming hosts of short GRBs the median is then $\langle M_* \rangle \sim 10^{9.7} M_{\odot}$. This indicates that even the star-forming hosts of short GRBs are typically more massive than the hosts of long GRBs, [221] suggest that this point to a more dominant role of stellar mass in determining the rate of short GRBs.

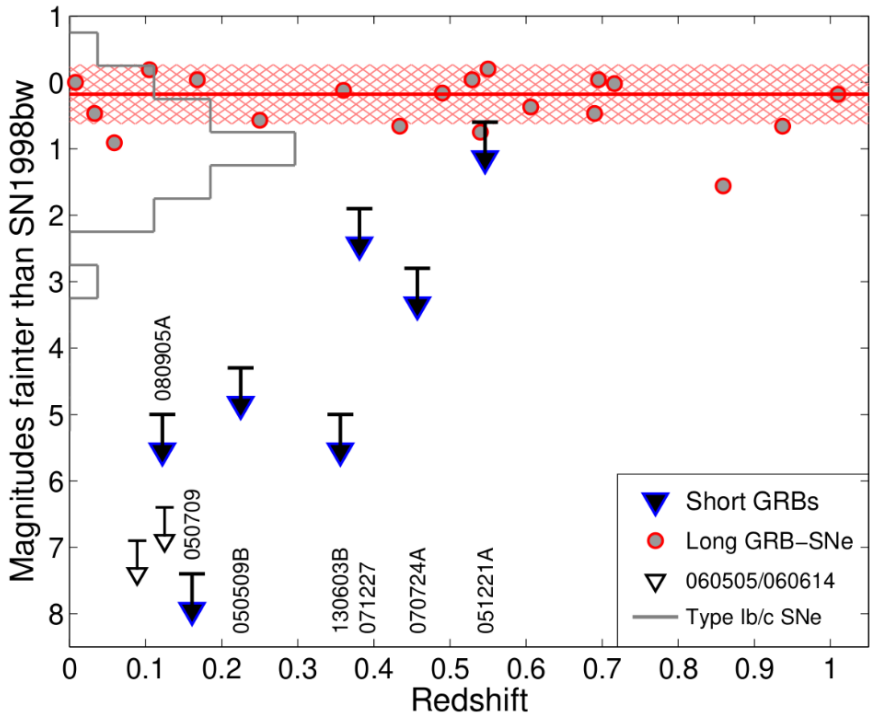

Figure 3.13: Limits on supernovae associated with short GRBs (filled triangles) relative to the peak absolute magnitude of the canonical long GRB SN1998bw. Also shown are the distribution of SN peak magnitudes for long GRBs (filled circles; hatched region marks the median and standard deviation for the population; [113]), local Type Ib/c SNe (histogram; [234]), and two unusual long GRBs that lacked associated SNe (060505 and 060614; [235], [236], [237], [238]). The latter may represent a long duration or extended emission tail of the short GRB population. With the exception of GRB 050509b, all short bursts with limits on associated SNe occurred in star-forming galaxies, indicating that despite the overall star formation activity, the short GRB progenitors were not massive stars. Figure from [221].

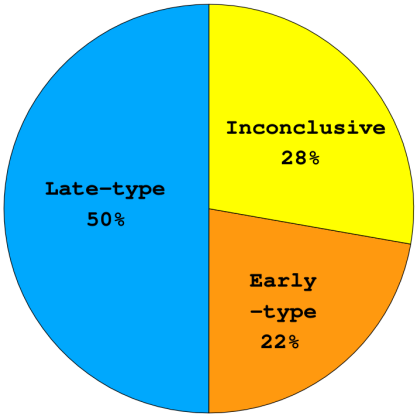

Figure 3.14: Demographics of the galaxies hosting short GRBs. In this classification all GRBs with sub-arcsecond positions or Swift/XRT positions are assigned to an host galaxy with as last resort the choice of the galaxy with the lowest probability of chance coincidence [221, 248, 249]. Figure from [221].

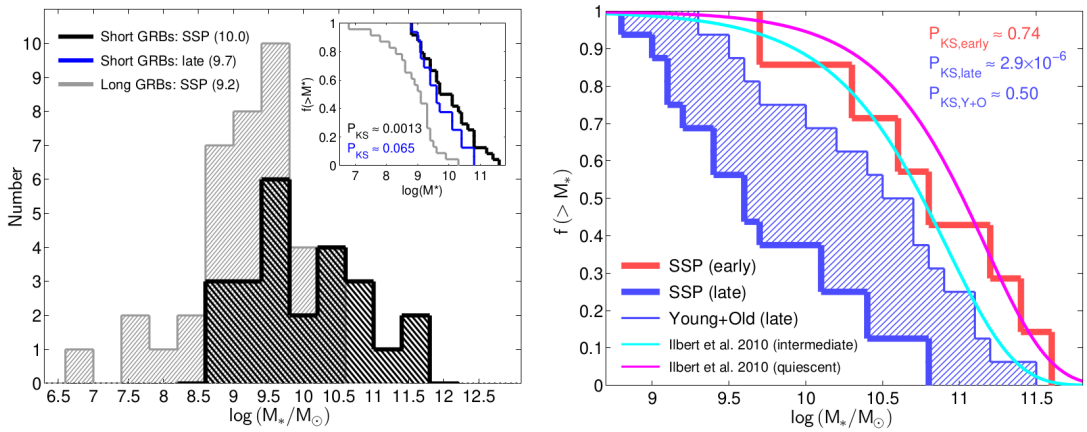

Figure 3.15: Histogram of host galaxy stellar masses for short GRBs (black) and long GRBs (gray). Median values for each population (and separately for short GRB late-type hosts) are quoted in parentheses. The inset shows the cumulative distributions along with Kolmogorov-Smirnov probabilities that the short and long GRB hosts are drawn from the same parent population. Right: Comparison of the cumulative distributions of stellar masses for late-type (blue) and early-type (red) short GRB hosts to the expected distributions for a mass-weighted selection from the field galaxy mass function (cyan and magenta lines, respectively). The resulting Kolmogorov-Smirnov probabilities indicate that the early-type hosts are consistent with pure mass selection, while the late-type hosts have lower than expected stellar masses. This indicates that star formation activity plays a role in the short GRB rate. Figure from [221].

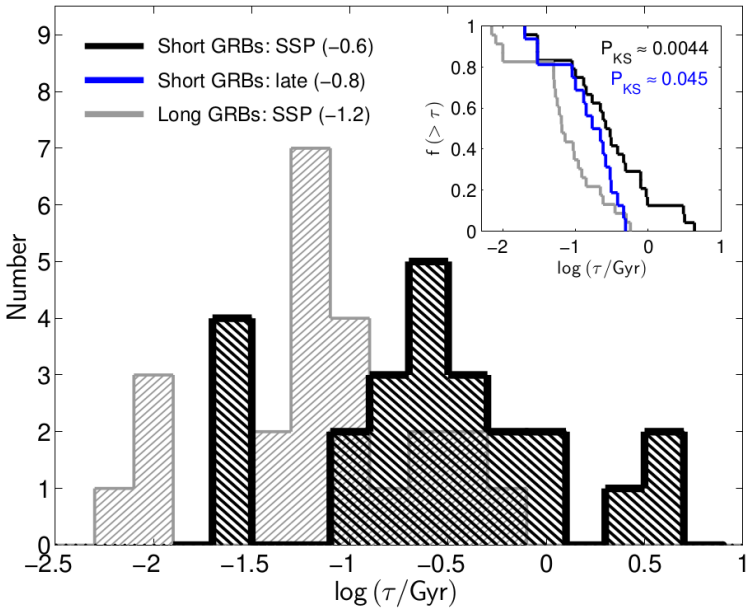

Figure 3.16: Histogram of host galaxy stellar population ages for short GRBs (black) and long GRBs (gray). Median values for each population (and separately for short GRB late-type hosts) are quoted in parentheses. The inset shows the cumulative distributions along with Kolmogorov-Smirnov probabilities that the short and long GRB hosts are drawn from the same parent population. The results indicate that short GRB hosts, even the late-type galaxies, have systematically older stellar population than long GRB hosts. Figure from [221].

Figure 3.15 also shows the comparison of the cumulative distributions of stellar masses for the early- and late-type host galaxies of short GRBs with the expected distribution for mass-selection from the field galaxy mass function [241, 242]. If the progenitor population tracks the stellar mass alone, one can expect that the observed stellar mass distribution of short GRB host will closely track the mass-weighted mass distribution of field galaxies. Figure 3.15 shows that this is indeed the case for the early-type mass function but the late-type hosts have visible lower stellar masses than expected from mass-selection alone [250]. [221] suggests that this is an indication that in late-type galaxies the short GRB rate per unit stellar mass is higher than in early-type galaxies, due to the presence of star formation activity. This may agree with the observed abundance of late-type galaxies in the short GRB host population.

As shown in figure 3.16 the distribution of stellar population ages also show a significant difference between short and long GRB hosts. With a median value of $\langle \tau_* \rangle \sim 0.25$ Gyr, the distribution for short GRB hosts spans a wide range of

stellar population ages, from a few tens of Myr to about 4 Gyr [250]. On the other hand, the long GRB hosts have a median stellar population age of $\langle \tau_* \rangle \sim 60$ Myr [250]. Since the observed sample of short GRB is limited by the Swift sensitivity, the inferred age has to be used as an upper bound.

The Offset and kick Distributions

In order to determine the offset (locations of short GRBs relative to their host centers) distribution of the short GRBs, a study based on Hubble Space Telescope (HST) observations combined with ground-based optical/radio afterglow observations was performed on a sample of 32 short GRB host galaxies [251, 220, 252, 221] (see figure 3.17). In this sample the projected offsets between 0.5 and 0.75 kpc with a median of about 5 kpc. On the other hand, longs have a median offset about 4 times smaller [253]. Core-collapse and Type Ia supernovae have a median offset about 1.5 times smaller [254]. Note that essentially only short GRBs exhibit offset $\gtrsim 20$ kpc, this subset has been specifically studied and named "host-less" since these offsets are larger than the typical visible extent of galaxies [255, 220]. These association with very large offsets are validated by optical limits of $\gtrsim 27$ magnitude and near-IR limits of $\gtrsim 26$ magnitude confirming that any undetected coincident host galaxies with similar properties than the rest of the sample will have to reside at $z > 3$ or to have an host luminosity an order of magnitude below to evade detection, both being equally unlikely [221]. Finally the observed offset distribution for short GRBs is in good agreement with the population synthesis predictions for compact object mergers, particularly the fraction of events with large offsets [256, 108, 257]. Note that the sample is mainly based on short GRBs with optical/radio afterglows which may be biased toward higher circumburst densities, and hence to smaller offsets. The broad offset distribution could also be explained by a non negligible portion of the short GRB progenitors originating from globular clusters, due to dynamically-formed compact object binaries, or to the tidal capture and collisions of compact objects [221].

From the offset distribution one can retrieve indication on systemic kicks, but this is limited by the projection effects and the uncertainty about the age of any specific short GRB progenitor relative to the host mean stellar population age. Nevertheless it is still possible to determine a characteristic kick velocities. From the [221] sample the resulting projected kick velocities is between $v_{kick} \sim 20$ and ~ 140 km s^{-1} which is consistent with the kick velocities derived for Galactic NS-NS binaries based on population synthesis models $v_{kick} \sim 5 - 500$ km s^{-1} [258, 259, 260, 261].

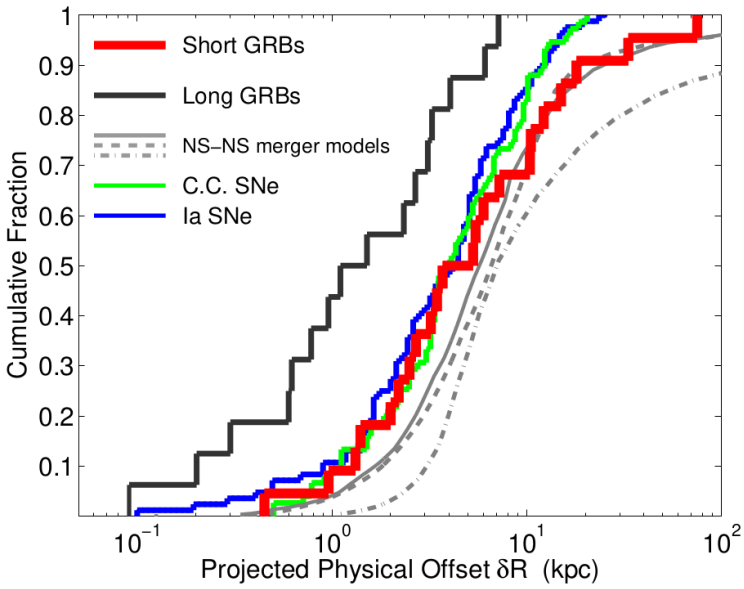

Figure 3.17: Cumulative distribution of projected physical offsets for short GRBs with sub-arcsecond positions (red; [251, 220]), compared to the distributions for long GRBs (black; [253]), core-collapse supernovae (green; [254]), Type Ia supernovae (blue; [254]), and predicted offsets for BNS from population synthesis models (grey; [256, 108, 257]). Short GRBs have substantially larger offsets than long GRBs, and match the predictions for compact object binary mergers. Figure from [220].

3.7 Modeling the spectral energy distributions of GRBs host galaxies

It is usually difficult to obtain spectroscopic observation for a sample of GRB host galaxies, hence such compilation usually relies on spectral energy distributions (SED) fitting algorithm. As the galaxy emission from gamma-ray to radio outcome of the complex physical interplay between their main baryonic components (stars of all ages and their remnants; molecular, atomic, and ionised gas; dust, and supermassive black holes) the SED of a galaxy contains the imprint of the baryonic processes that drove its formation and evolution along cosmic times. Hence modelling a SED of a galaxy is a heavily intricate problem as galaxies with significantly different properties can have very similar SED. This task is particularly difficult while studying a restricted wavelength range with only limited data. There are several approaches with different physical motivations to achieve a SED fitting. In chapiter 5 we will use, for the study of the short GRB host population, the Code Investigating GALaxy Emission (`CIGALE`) [262] open-source software written in `python` aiming to model the far-ultraviolet to radio spectrum of galaxies and their physical properties (star formation rate, stellar mass, attenuation, dust luminosity, stellar population ages...). `CIGALE` uses an energy balance principle where the energy emitted by dust in the mid- and far-infrared exactly corresponds to the energy absorbed by dust in the ultraviolet-optical range. This approach makes `CIGALE` particularly robust for the estimation of the attenuation properties of the galaxies, the estimation of the star forming rate, the estimation of stellar mass and the separation of the emission of active galactic nuclei. Therefore, `CIGALE` fits particularly well the needs for the study of the sample of GRB host galaxies. The drawback of this energy balance approach is that it specifically requires (near-) infrared data to provide reliable results and such observation are less common during GRB follow-up, hence it requires a specific data compilation with all sky (near-)infrared for instance (see chapter 5 for details).

Chapter 4

Multi-messenger astronomy with gravitational waves

In this chapter I will discuss in greater detail multi-messenger astronomy related to gravitational wave detections with LIGO-Virgo-KAGRA detectors. I will describe the different implication of my work in the searches for electromagnetic counterparts to gravitational waves within the LIGO-Virgo-KAGRA collaboration including the analysis which looks for gravitational waves associated with Swift and Fermi GBM detections.

4.1 Gravitational wave alerts

In this section I present the topic related to the gravitational wave alerts production (presented in chapter 2) which I worked on during my thesis.

4.1.1 Candidate validation and release

As presented in section 2.2.3, the online analyses process the data immediately after the acquisition, producing triggers in real time. If any of these triggers is below the FAR threshold defined to consider the event as interesting (see section 2.2.3), it is automatically released publicly with an alert distributed through the Gamma-ray Coordinates Network (GCN[1]). Within $\sim$ 10 mn after the gravitational wave trigger, the first and second preliminary notices are sent fully automatically (see for instance figure 3 of [263]). At the same time, the trigger information becomes publicly available in the Gravitational-Wave Candidate Event Database (GraceDB[2]). In addition to this fully-automated procedure, the trigger is also manually vetted by instrument scientists and analysts. This vetting, in which I participated during my thesis for Virgo, has to be fast enough to facilitate any follow-up. It requires availability at any time of the days to the dedicated team as no-one can predict when the gravitational wave will be detected. As a part of this vetting duty, human inspections are carried out for data quality, instrumental conditions, and pipeline

[1] https://gcn.gsfc.nasa.gov/
[2] https://gracedb.ligo.org/

behavior. On detchar side most of the tests are unified in the automatically produced Data Quality Report (DQR[3]). The DQR is designed to format and display via an interactive html checklist (within GraceDB) many different data quality products associated with the gravitational wave candidate. One of the roles of the detchar team is to go through the DQR tests (spectrograms, glitch categorization, stationarity check, thunderstorms and Earthquake check, lock check...), interpret in real time the results and provide the human input where it is needed to understand the data quality and instrumental conditions. In the next section I present the test I implemented during my thesis for the DQR pipeline. The collaboration is committed to provide an human vetting within $\sim$ 24h after the GW trigger (see table 2 of [264] for O2 human vetting latency, O3 latency was similar). After this human vetting the candidate will either be confirmed by an initial notice and circular (including an updated sky localization and source classification) or withdrawn by a Retraction notice and circular. Because they likely are multi-messenger sources, priority is given to the case of BNS or NSBH triggers to submit this human vetting within a few hours to enable rapid follow-up.

In parallel to this procedure, the parameter estimation algorithm `LALInference` (see section 2.2.5) is started and an update notice and circular are sent whenever the sky localization area and source parameters are obtained. Update notices and circulars can also be a result of glitch removal or other improved analysis. Figure 4.1 presents a schematic flowchart of the LIGO-Virgo-KAGRA alert system.

UPV 24h

During my thesis I worked on the improvement of the DQR by implementing a specific UPV (see section 2.2.2) test automatically triggered for each gravitational wave candidate within the DQR. This test is performed on all the auxiliary channels for a period of 24h before the gravitational wave candidate. Its goal is to unveil any change of the noise distribution within the detector near the time of the gravitational wave candidate (this is something expected for example with weather variation producing micro-seismic noise) and reject gravitational wave candidates detected during periods suspiciously affected by noise. No automatic rejection is produced with this test, it only reports the need of an human check and vetting. This test was used during the entire O3 run, i.e. for all the DQR runs triggered. No coincidence was found between auxiliary channels and the event time and so no candidate was rejected in the light of this test. Nevertheless it helped to validate the Virgo data quality around the triggers during the whole run.

[3]https://docs.ligo.org/detchar/data-quality-report/index.html

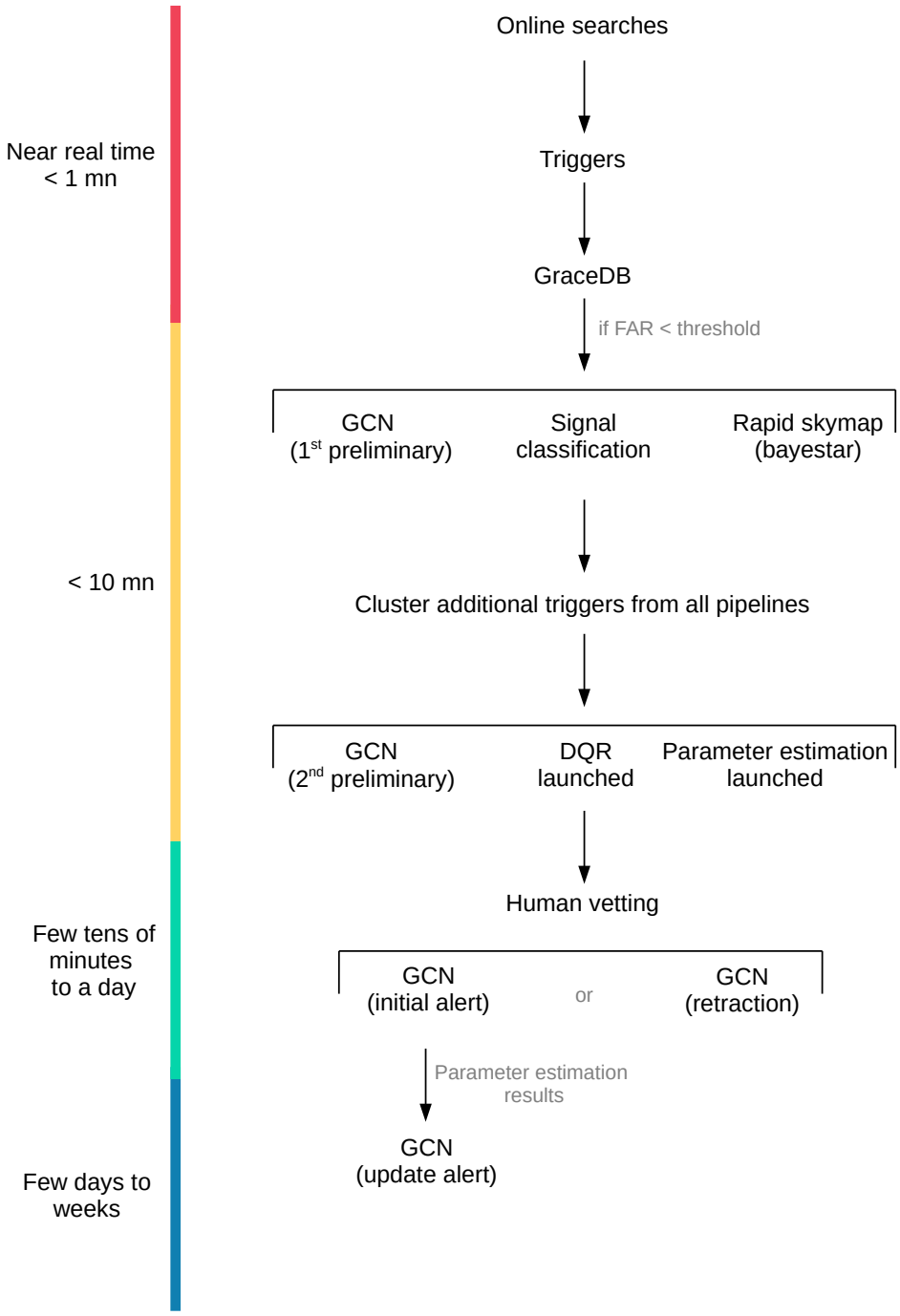

Figure 4.1: Flowchart of the LIGO-Virgo alert system.

4.1.2 RAVEN

GRB notices are provided directly from satellite observatories through the Gamma-ray Coordinates Network (GCN) within $\sim$ 1 minute for a typical GRB. On the other hand, very low latency searches for gravitational waves have a demonstrated ability to provide triggers within few tens of seconds after the coalescence time. Such technologies opened the possibility of a hierarchical, low latency coincidence search for associations between GRBs and gravitational waves candidates and this is the aim of the `RAVEN` (Rapid, on-source VOEvent Coincidence Monitor) pipeline[4]. Both GW and GRB triggers are, if everything goes well, uploaded to GraceDB, then `RAVEN` is triggered automatically to search for temporal coincidence. The coincidence window depends on the type of gravitational wave candidate found. If a sky map is also available (from e.g. the `BAYESTAR` [265, 84] or `cWB` pipelines [79, 80, 81, 82, 83]) then `RAVEN` will perform a second step searching for coincidence using sky localisations. If a pair of coincident triggers is found to be significantly associated, an alert is automatically broadcasts in near-real time over the GCN to the wider astronomical community to encourage the follow-up.

During my thesis I worked on the development of the RAVEN system producing automatically GCN notices. In particular I contributed to the setting of the wording of GCN circulars, built up with the `jinja` template engine [5], necessary to provide information in a clear and consistent manner to the community.

4.1.3 Channel safety analysis

As presented in section 2.2.2 a lot of the Virgo data quality analyses aim to ensure that gravitational wave candidates are astrophysical and not caused by terrestrial noise by searching for correlations between auxiliary channels and h(t) strain channel to produce vetoes. But this strategy is efficient only if the auxiliary channels used to produce vetoes are insensitive to gravitational waves. Indeed, since transfer functions between the h(t) strain channel and most auxiliary channels are not well understood, one needs to study the coupling of auxiliary channels to h(t) strain channel to determine which channels are *safe* to produce vetoes. The so called auxiliary channel safety analysis is performed for this purpose.

This analysis is performed using the method proposed in [266] which consists on a null test applied to a broad set of hardware injections mimicking the effect of gravitational-wave on the detector. The comparison of the significance of a trigger (pvalue defined below) in any channel obtained at the time of the hardware injections (onsource time) and at time randomly drawn outside of the hardware injections (offsource time) allow to quantify the sensitivity of this channel to the

[4] `https://git.ligo.org/lscsoft/raven`
[5] `https://jinja.palletsprojects.com/en/3.0.x/`

passing of gravitational waves (the safety of the channel). Hardware injections are used to unveil transfer functions between the h(t) strain channel and auxiliary channels. For Virgo, hardware injections consists of injecting 0.6 second long sine-Gaussian signals of various central frequencies (between 19Hz and 811Hz) and amplitudes (between SNR[6] 20 and SNR 500) acting directly on the mirrors (hence on the h(t) strain channel). Each injection are spaced 15 seconds apart to allow the power dissipation and avoid any power overlap. I will call *set* in the following all the injections of different frequencies performed at different SNR within a certain period with frequency among [19,31,47,73,129,211,409,811] and SNR among [20,50,100,500] (i.e. 32 injected signal by set). The frequencies injected are chosen to scan the entire detection band while avoiding any resonant frequency (like violin modes). For this analysis we used 3 sets of hardware injections. This analysis assumes that triggers in each channel are independent of events in other channels and that triggers in any channel are distributed according to a Poisson process with a constant rate, i.e. the time between consecutive events in a single channel is distributed according to

$$P(\Delta t|\lambda) = \lambda e^{-\lambda \Delta t} \tag{4.1}$$

where λ is the rate of triggers in the given channel. Then, by integrating, we can define the probability of observing an event as close or closer than τ to an uncorrelated time-of-interest (pvalue) by

$$P(\Delta t \leq \tau|\lambda) = 1 - e^{-2\lambda\tau} \tag{4.2}$$

where the factor of two comes from the fact that we search both backwards and forwards in time to find the nearest trigger. One can show that using the point estimate $\lambda = N/T$, where T is a time period and N is the number of triggers within this period, we get a precise estimate of λ as long as $N \gg 1$ [266]. With this expression we can simplify the pvalue expression to

$$P(\Delta t \leq \tau \ll T|\lambda) \sim 2\tau\frac{N}{T} \tag{4.3}$$

One important features of the method is that it takes into account the significance, which is, in this case, expressed in terms of SNR ρ of the triggers occurring within a channel. To do so, we define a list of SNR threshold ρ_{thr}. For each one of the SNR threshold we select the subset of triggers above this threshold and computes the statistic for this subset. Then we minimize the pvalue over the different subsets such that

$$P_{min}(\Delta t \leq \tau) = \min_{\rho_{thr}} \{P(\Delta t \leq \tau|N(\rho \geq \rho_{thr}), T)\} \tag{4.4}$$

[6]see for instance section I of [61] for the definition of the SNR of a trigger

where $N(\rho \geq \rho_{thr})$ is the number of triggers in that subset. Finally, as we are using more than one set of hardware injections the computation combines the previous expression into the final pvalue

$$P_{joint} = \prod_{i=1}^{N_{set}} P_{min}^{(i)} \tag{4.5}$$

From this expression we can compute the pvalue for each time t of interest for any of the auxiliary channels. In the following, I will call *timeseries* of the channels this quantity of pvalue(t). Finally, by comparing the pvalue at the time of the hardware injection and at time randomly drawn outside of the hardware injection one can quantify the sensitivity of any channel to the passing of gravitational waves.

Virgo O3b channel safety analysis

During my thesis I carry out at the end of the O3 run the channel safety analysis for the Virgo detector and its $\sim$ 2500 auxiliary channels. An important part of the work consisted in adapting the tools provided by [266], normally used only on LIGO data only, to Virgo data. The main change was the choice to use `Omicron` triggers instead of KleineWelle [266, 267, 268] triggers. This choice required a lot of development but doesn't fundamentally change the analysis method. The hardware injections needed for the analysis have been done the 25th March 2021 (see figure 4.2). The analysis was complicated by a lock loss of the interferometer in the middle of the injection sets (see figure 4.2). This especially complicated the choice of the offsource period used to draw the background distribution of triggers. The offsource period has to be close enough to the hardware injection, to measure the noise distribution at the time of the injection, but should not overlap with it in order not to bias the trigger distribution with the injection. The offsource period was chosen to be 10 minutes of data after the re-locking of the interferometer (see figure 4.2). Then we compute within the offsource period the timeseries for all of the auxiliary channels. Figure 4.3 shows an example of two timeseries obtained for a channel expected to be safe (a central building radio frequency monitor "ENV_CEB_RF") and one expected to be unsafe (highly correlated to h(t) signal "LSC_DARM"). We define the classification threshold by plotting the cumulative histogram of the offsource pvalue distribution drawing 1000×3 GPS times in the offsource period. The number 1000 is choose to have a sufficiently full histogram and the factor 3 is chosen to fit with the number of injection sets used and to combine the pvalue according to the expression 4.5. While 5 sets of hardware injection have been injected only 3 of these sets are used for the channel safety analysis, those with the same SNR injected. With $\sim$ 2500 channels and 8 different

frequencies injected in a set, we expect less than one wrong classification if we take a threshold according to a fraction equal to $\frac{1}{2500\times 8} = 5 \times 10^{-5}$. Then we choose to define the threshold in pvalue as the value corresponding to this fraction in the offsource distribution (see figure 4.4), which at the end is log(pvalue) ~ -8.25. Finally we compare the defined threshold with the obtained pvalue at the time of the hardware injection for each frequency-SNR pair and we set the classification as follows:

- log(pvalue) < -8.25 ⇒ Danger : channels that are too correlated with hardware injections to occur by chance

- -8.25 < log(pvalue) < -7.25 ⇒ Warning : channels that are correlated with hardware injections at a reasonably high level, but less significantly than danger

- -7.25 < log(pvalue) ⇒ Ok : channels that do not appear to be correlated with hardware injections

The classification is then combined to obtain a classification by SNR. For a given SNR the classification is "Danger" if it is "Danger" at least in one of the frequency injected at this SNR, otherwise, the classification is "Warning" if it is "Warning" at least in one of the frequency injected at this SNR, otherwise, the classification is "Ok". In the same way an overall classification is defined by combining the classification by SNR. At the end, over $\sim$ 2500 channels, we have 53 channels classified as "Danger", 16 classified as "Warning" and all the others as "Ok". The list of warning and danger channels are available in appendix 2 and 3. These results were checked to be compatible with the most obvious expectations (channels undoubtedly expected to be safe/unsafe) and the previous (O3a) channel safety analysis, done via a more "hand-made" method with visual inspection of spectrograms. At the end only channels classified as "Ok" by this analysis are considered as safe and are used to produce vetoes. For O3b, this analysis was performed only once using hardware injection performed at the very end of the run. For O4, the channel safety analysis is expected to be reproduced in a regular basis during the run. This will strengthen the statistics used in this method (background distribution, classification threshold...) and may unveil variation of the coupling between auxiliary channels and h(t) channel over time (which may evolve with the detector operation changes or environmental conditions). To this aim I carried out a work specifically dedicated to improving the automation and user-friendliness of this analysis.

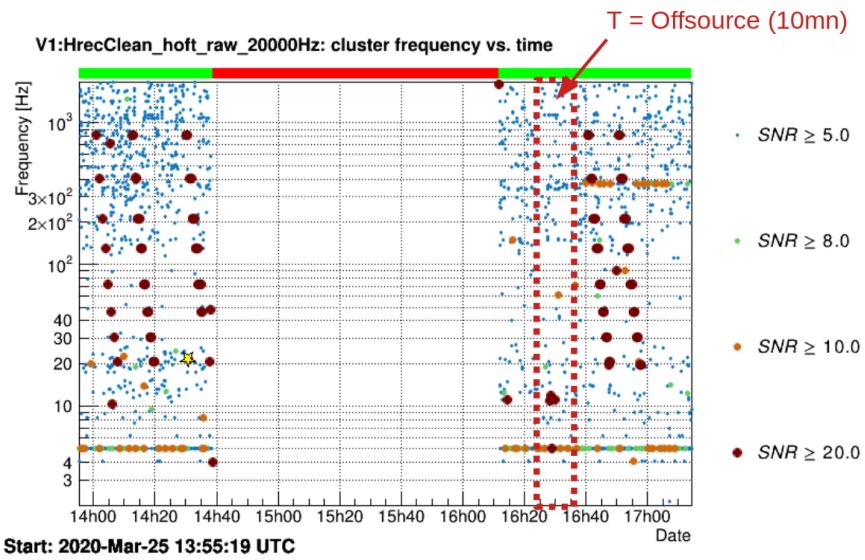

Figure 4.2: `Omicron` plot, representing triggers in a time frequency map, of the nearby time of the hardware injections performed at the end of the O3b run. The 5 sets of hardware injections are visible in this plot as vertical lines of triggers with SNR>20 (brown dots). Only 3 of these sets were used for the channel safety analysis (the one with the same SNR injected, i.e. one before the lock loss starting at 14:12 UTC and two after the re-lock of the interferometer tarting at 16:40 UTC and 16:50 UTC respectively). The interferometer lock loss mentioned in the text is indicated in red color on the top of the plot. The offsource period T chosen for the channel safety analysis is displayed with a dotted red rectangle. The star shows the trigger with the highest SNR.

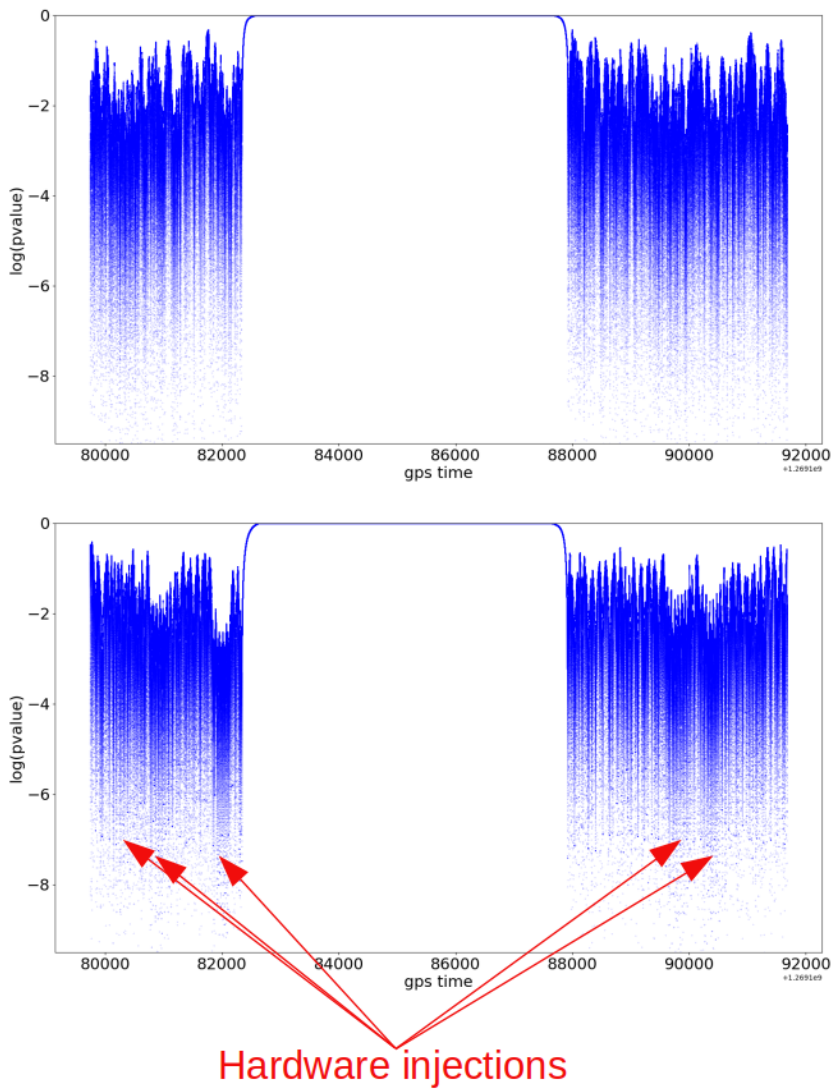

Figure 4.3: Timeseries of an environmental auxiliary channel expected to be safe, a central building radio frequency monitor "ENV_CEB_RF" (top) and an auxiliary channel expected to be unsafe, highly correlated to h(t) signal "LSC_DARM" (bottom). The effect of the 5 hardware injection sets, lowering the nearby pvalue, on the unsafe channel are pointed with red arrows. The effect of the first hardware injection set is less visible because the SNR injected is ten times smaller.

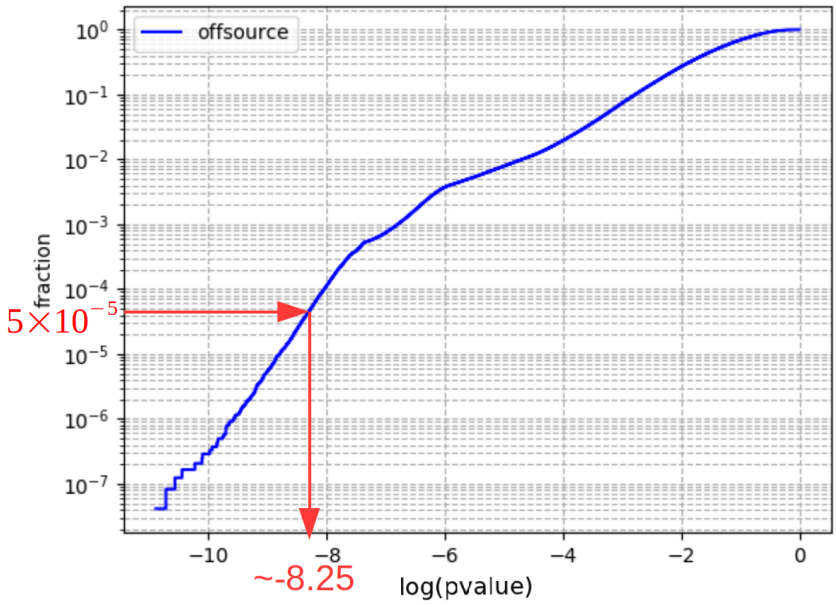

Figure 4.4: Cumulative histogram of the offsource auxiliary channels pvalue obtained by randomly drawing 1000×3 GPS times. The classification threshold is obtained according to a fraction equal to 5×10^{-5} as described in the text.

4.2 Search for gravitational waves associated with GRBs

Within the LIGO-Virgo-KAGRA collaboration I contributed in the search for gravitational wave signals associated with GRBs detected by the Fermi and Swift satellites during the first part of the third observing run O3a [269]. This search is divided in two different analyses. The first one is a modelled search dedicated to compact binary merger sources, hence it focuses on short GRB triggers coincident with the O3a run. The second one is an unmodelled search for generic gravitational wave transients used on all the GRB triggers coincident with the O3a run. In this section I will present the GRB sample used for the analysis, analysis methods and results on the O3a data.

4.2.1 GRB sample

The GRB sample used for this analysis is built on GRB events occurring between 1 April 2019 15:00 UTC to 1 October 2019 15:00 UTC. Most of these events were collected in low-latency via notices circulated by GCN and then refined using

information from the Swift/BAT catalog[7], the online Swift GRBs Archive [8] and the Fermi/GBM catalog[9]. This is done via a dedicated processing system, Vetting Automation and Literature Informed Database (VALID, [270]). It ensures that the latest GRB results are use for the gravitational wave analysis looking for updates in GRB parameters, time and localisation. It also uses an automated literature search to identify particularly noteworthy events. The modelled search is looking for BNS and NSBH merger events. To identify GRB from compact binary coalescences within the sample, we classify each one as long or short based on their T_{90}, as presented in chapter 3. This classification only provides a general trend and not a perfect discrimination. More robust classification can use spectral properties like peak energy or spectral hardness. This analysis does not employ such GRB properties since it combines observations from multiple observatories with different spectral sensitivities. In order to maximize our chances at identifying potential compact binary coalescence candidates the GRBs are classified in three classes as follow:

- *short* when $T_{90} + |\delta T_{90}| < 2$ s
- *long* when $T_{90} - |\delta T_{90}| > 4$ s
- *ambiguous* for all others

We apply our modelled search to all short and ambiguous GRBs which correspond to 20 short GRBs and 13 ambiguous GRBs for O3a. The unmodelled search is applied to all events, regardless of classification but we require a minimum amount of coincident data from at least two gravitational wave detectors around the time of a GRB to assess the significance of a gravitational wave candidate with sub-percent level accuracy (see the following method description for details). This results in 105 GRBs being analysed with this method (out of the 141 recorded) for O3a.

4.2.2 Modelled search dedicated to compact binary mergers

This analysis is carried out by a coherent (i.e. combining data from the gravitational wave network before the processing) matched filtering pipeline, `PyGRB` [271, 272] that is part of the general open-source software `PyCBC` [273] and has core elements in the `LALSuite` software library [274]. It aims to achieve high sensitivity by leveraging detailed knowledge of signal morphology. This search seek to find gravitational wave signals coincident with GRB triggers arising from the

[7] `https://swift.gsfc.nasa.gov/results/batgrbcat/`
[8] `https://swift.gsfc.nasa.gov/archive/grb_table/`
[9] `https://heasarc.gsfc.nasa.gov/W3Browse/fermi/fermigbrst.html`

merger of BNS or NSBH. This search also benefits from the sky localisation of the source from the GRB detection to improve its sensitivity. This analysis can be performed with data from one or more gravitational wave detectors. One of the most important parameters of this analysis is the search window around each GRB trigger. This *onsource window* is defined as [-5,+1] s relative to the GRB trigger time based on the expectation that a gravitational wave should preceed the prompt GRB emission by several seconds [275, 276]. Note that here we are considering the merger time as the time of gravitational wave detection because it can be recovered from the binary coalescence models used in the search, hence this window is consistent with the one described in section 3.4. The surrounding $\sim$ 90 minutes of offsource data around each GRB trigger are used to estimate the background. This is done by dividing this offsource period into 6 seconds long windows to match the width of the onsource window. Note that a minimum of $\sim$ 30 minutes is required in order to accurately estimate the noise power spectral density of the available instruments and ensure that the search can assess at sub-percent level accuracy the significance of any candidate event found in the onsource window down to sub-percent level.

This analysis performs a matched filtering, i.e. that it scans each data segment and the onsource window in the 30-1000 Hz frequency band using a predefined bank of templates. This bank is generated using both geometric and stochastic methods [277] for the BNS and NSBH signals. Phenomenological inspiral–merger–ringdown waveform models of the IMRPhenomD family [278, 279] are used to generate the template bank. Additionally limits are placed on the template bank such that NS masses are limited to [1.0, 2.8] $M_\odot$ and BH masses are within [2.8, 25] $M_\odot$ [269]. The BH mass limit and the mass cutoff between NS and BH are based upon X-ray binaries observation [280, 281] and NS equation of state respectively [282]. In this bank the BH spin is limited to 0.998 based on theoretical results [283]. The maximum dimensionless spin magnitude[10] for NS is 0.05 from the largest observed NS spin in a binary system [284], furthermore the bank only contains aligned spin BNS and NSBH. Finally, all potential binaries are checked to ensure that they are viable GRB progenitors—creation of an accretion disk able to power a GRB [285]. This bank is used to calculate a coherent SNR for each time and template, and a candidate event is recorded when the SNR crosses a predefined threshold. The coherent SNR for a given candidate is re-weighted according to how well the template matches the identified signal [271, 272]. Using the offsource window the significance of any event is then ranked against the background. The amount of offsource data is artificially increased by performing time slide as described in [272], this improves the ranking statistic. Finally, in order to determine the sensitivity of this search, signals are injected into the offsource data and an attempt to recover

[10]Defined as $\frac{c}{GM^2}S$ where S is the norm of the spin angular momentum vectors.

them is performed. The injected signals are generally the same NSBH and BNS waveforms as in the template bank but with a few differences (see [269] for details). These injections allow to compute the 90% and 50% exclusion distances (D_{90} and D_{50}), which are the distances at which 90% and 50% of the injected signals are recovered with a ranking statistic higher than the highest ranked onsource candidate.

4.2.3 Unmodelled search for generic transients

This analysis, carried out with the `matlab` -based `X-Pipeline` software package [286, 287], uses the sky localization and time window for each GRB, and looks for consistent excess power that is coherent across the network of gravitational wave detectors. As opposed to incoherent methods, which look for events with similar properties (frequency, duration...) that occur simultaneously in different detectors, coherent methods like the one used in `X-Pipeline` combine data from the gravitational wave network before the processing. The created list of triggers, is in this case, the same for the whole network. The main advantage of such coherent analysis is its efficiency in rejecting glitches [288, 289, 290]. They are usually easier to tune as detectors data are naturally weighted by their relative sensitivity, so the candidate events are not generated through the tuning of relative thresholds in each detector. The main drawback of coherent methods is the computational cost. Coherent combinations are typically a function of the sky position, with around 1000 resolvable directions on the sky for the detector network resolution [291]. This cost is compounded by the need to estimate the background, which requires repeated re-analysis of the data using time shifts. However, in our case the analysis is triggered by the GRB detection for which the source localisation is often known to high accuracy (compared to gravitational wave detector spatial resolution). This leads to relatively small amount of data to be analysed (typically hours) hence a modest computational cost. This allows triggered searches to take advantage of the benefits of coherent methods while avoiding or minimizing most of the drawbacks. As presented in section 3.4 this analysis uses a search window of $T_{GW} - T_{GRB} \in [-600, \max(T_{90}, 60)]$, expected to encapsulate the time delay between gravitational wave emission from a progenitor and any GRB prompt emission [292, 293, 106, 294, 295, 145, 296, 142, 297, 298]. While some emission models, such as radiation from core-collapse supernovae, are expected to contain frequencies up to few kHz [299], the search frequency range is restricted to the most sensitive band of the gravitational wave detectors, namely 20-500 Hz because looking beyond the burst detection is not energetically favorable (see for example Fig.4 in [300]) and will significantly increase the computational cost.

`X-Pipeline` loads the requested data, whiten the data and estimate the power spectrum [290, 267]. Then it creates a grid of sky position on the sky localisation

of the GRB. For each one of the sky positions in this grid it time-shifts the data from each detector to respect the time delay between the detector positions [286]. The data are divided into overlapping segments and Fourier-transformed, producing time–frequency maps for each detector. `X-Pipeline` then sums and squares the time-frequency maps of the individual detector data streams $\tilde{d}$ to produce time–frequency maps of the desired coherent energies. The considered coherent energies are [286]:

- $E_{tot} = \sum_k |\tilde{d}|^2$: the total energy in the data
- $E_+ = \sum_k |e^+ . \tilde{d}|^2$: the energy in the h_+ polarization
- $E_\times = \sum_k |e^\times . \tilde{d}|^2$: the energy in the $h_\times$ polarization
- $E_{SL} = \sum_k \left[|e^+ . \tilde{d}|^2 + |e^\times . \tilde{d}|^2 \right]$: the standard likelihood energy
- $E_{soft} = \sum_k \left[|e^+ . \tilde{d}|^2 + \epsilon |e^\times . \tilde{d}|^2 \right]$: the soft constraint likelihood energy
- $E_{null} = E_{tot} - E_{SL}$: the null stream energy

where $e^+ = f^+/|f^+|$ and $e^\times = f^\times/|f^\times|$ are the unit vectors of the dominant polarization frame (frame in which the network antenna patterns are real and positively defined) [301, 81], f^+ and $f^\times$ being the antenna response vector in this frame. $\epsilon = |f^\times|^2/|f^+|^2$ is a weighting factor [286]. k indexes the time-frequency pixels. For each coherent energy E presented above one can define the corresponding incoherent energy I by decomposing the coherent energy expression into its cross-correlation terms $\tilde{d_\alpha}^\dagger \tilde{d_\beta}$ and its auto-correlation terms $\tilde{d_\alpha}^\dagger \tilde{d_\alpha}$ († denote the conjugate transpose), where α and β index the number of detectors in the network. For example one can write

$$I_+ = \sum_k \sum_\alpha |e^+ \tilde{d_\alpha}|^2 \tag{4.6}$$

See [286] for details and the expression of the other incoherent energies. As pointed out in [290], if the transient signal is not correlated between detectors (as is expected for glitches), then the cross-correlation terms will be small compared to the auto-correlation terms. As a result, for a glitch we expect the energy to be dominated by the auto-correlation components, i.e. $E \sim I$. The figure 4.5 presents an example of a time–frequency map which gives easy access to the temporal evolution of the spectral properties of the signal and allows to search for clusters

of pixels with excess energy, referred to as *events*. Each cluster is also assigned an approximate statistical significance based on the χ^2 distribution [286]. This procedure is particularly appropriate for gravitational wave burst whose shape in the time–frequency plane is connected.

The obtained events, considered as candidate detections, are assigned a detection statistic based on energy, and ranked accordingly. Then, X-Pipeline vetoes events that have properties similar to the noise background. This is done through two pass/fail tests. The first one is a simple threshold on the ratio I/E. Following the discussion above, in order to reject glitches a cluster is conserved only if it passes the following test:

$$\begin{aligned} I_{null}/E_{null} &\geq r_{null} \\ |\log_{10}(I_+/E_+)| &\geq \log_{10}(r_+) \\ |\log_{10}(I_\times/E_\times)| &\geq \log_{10}(r_\times) \end{aligned} \tag{4.7}$$

where the thresholds r_{null}, r_+, and $r_\times$ may be specified by the user or chosen automatically by the pipeline. The form of equations for + and × makes these tests two-sided; i.e., they pass clusters that are sufficiently far above or below the diagonal. The second veto test is called the median-tracking veto test. In this test, the exclusion curve is nonlinear and designed to approximately follow the measured distribution of background clusters. In the scatter plots of I vs. E noise events are expected to be scattered about the diagonal with a width that is proportional to $I^{1/2}$ [286]. In this test the median value I_{med} is estimated as a function of E for background events (see [286] for details on this computation), then for each cluster to be tested `X-Pipeline` computes n_σ (how far the cluster is above or below the median) as:

$$n_\sigma = \frac{I - I_{med}(E)}{I^{1/2}} \tag{4.8}$$

Events are kept if they pass the following test:

$$\begin{aligned} n_{null} &> r_{null} \\ |n_+| &> r_+ \\ |n_\times| &> r_\times \end{aligned} \tag{4.9}$$

The figure 4.6 presents an I_{null} vs. E_{null} scatter plot where the median-tracking veto is presented. Finally, in addition to the coherent glitch vetoes, clusters may also be rejected because they overlap data quality vetoes presented in section 2.2.2.

In order to claim a gravitational wave detection, `X-Pipeline` needs to be able to establish with high confidence that a candidate event is statistically inconsistent

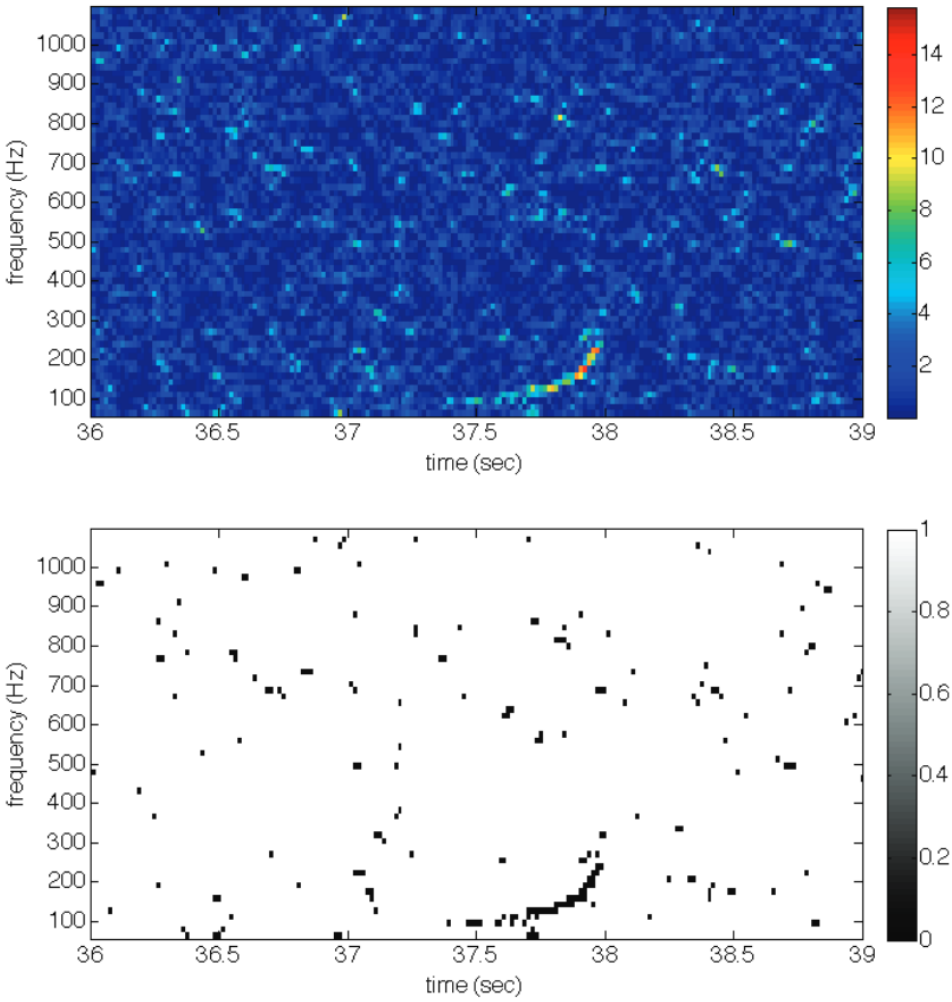

Figure 4.5: A simulated $1.4M_\odot$–$10.0M_\odot$ neutron star black hole inspiral at an effective distance of 37 Mpc, added to simulated noise from two gravitational wave detectors. (Top) Time–frequency map of the energy in the h_+ polarization. (Bottom) The highest 1% of pixels highlighted. The inspiral "chirp" is clearly visible. Figure from [286].

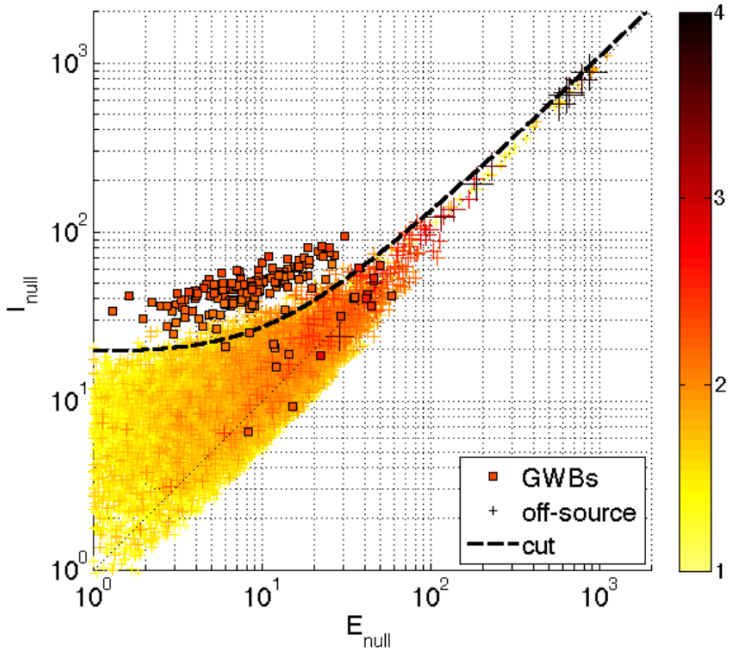

Figure 4.6: I_{null} vs. E_{null} for clusters produced by background noise (+) and by simulated gravitational wave signals (□). The color axis is the base-10 logarithm of the cluster significance. Loud glitches are vetoed by discarding all clusters that fall below the dashed line. Figure from [286].

with the noise background. To do that, the significance of the loudest surviving cluster in the onsource interval is compared to the cumulative distribution of loudest significance measured using background noise. The signal incompatibility with background alone is quantified with the probability of background noise producing a cluster in the onsource interval with the significance of the loudest surviving cluster (pvalue). If this pvalue is sufficiently small (for instance 1%) the event is considered as a possible gravitational wave detection and further investigations can be performed.

To quantify the sensitivity of this search, simulated signals are injected into the off-source data. While no template bank is directly used in this unmodelled search the simulated signals injected to recover the sensitivity of the search use the following waveform families:

- Circular Sine-Gaussian (CSG): signals that represent the gravitational wave emission from stellar collapses defined in equation 1 of [302] with varying center frequency of 70 Hz, 100 Hz, 150 Hz and 300 Hz. In all cases, an optimistic emission of energy in gravitational waves of $E_{GW} = 10^{-2} M_{\odot} c^2$ is assumed.

- Binary inspiral: signals representing emission from BNS and NSBH mergers addressed for the case of short GRB events, such as the ones used in the modelled search.

- Disk instability models (ADI): signals representing long-lasting waveforms which are due to the instabilities in the magnetically suspended torus around a rapidly spinning black hole, causing gravitational wave emission. For details on the used waveform see [302, 303, 269].

For each waveform family injected, the largest significance of any surviving cluster associated with the injections is determined. The percentage of injections that have a significance higher than the best event candidate is computed and the amplitude at which this percentage is above 90% is set as the upper limit. Calibration errors are included by jittering the amplitude and arrival time according to a Gaussian distribution representative of the calibration uncertainties. As for the modelled search these injection sets allow us to calculate 90% and 50% exclusion distances (D_{90} , D_{50}).

In the recent search the sensitivity of this unmodelled search for long-duration (≥ 10 s) was very often limited by glitches. This was especially true during the O3a run analysis where the improvement of the sensitivity of the detectors have unveiled new families of glitches. These glitches are easily vetoed by the `X-Pipeline` coherent consistency tests, however many long-duration simulated signals will randomly overlap such glitches. In these cases the simulated signal and the glitch would be

clustered together and subsequently vetoed together. To address this problem, recent development (post-publication of the O3a analysis) of the pipeline implemented an "autogating" procedure. For each detector, the total energy in the whitened data stream is computed over a 1 s window. If this total fluctuates upwards by more than 50 standard deviations above the median value then the data is zeroed out over the interval above threshold, and an inverse 1 s Tukey window is applied at each end of the zeroed interval to transition smoothly between the whitened and zeroed data. The gate is cancelled if there is a simultaneous energy excursion above 10 standard deviations in any other detector. This minimises the risk to gate a loud gravitational wave signal. Tests on several O3a GRBs showed that this procedure is very effective at reducing the impact of loud glitches in the search, without affecting the sensitivity to low-amplitude gravitational wave signals. This autogating is planned to be used for the latest (O3b) analysis, but not in a systematic manner. Standard procedures (without autogating) will be run first and a rerun will be performed with autogating only when there where a clear evidence of glitch contamination in the efficiency of the search (especially for long duration waveforms).

4.2.4 Results

During the O3a run the unmodelled search and the modelled search analysed 105 (12 of them analysed by myself) and 33 GRBs triggers respectively. The searches produced no evidence for deviations from the background distibution of pvalue. This result is consistent with the estimated gravitational wave/GRB joint detection rate with Fermi/GBM (0.07–1.80 per year) reported in [303] for the LIGO-Virgo O3a observing run. On the modelled search side the most significant event found had a pvalue of 2.7×10^{-2} (GRB190601325). For the unmodelled search, the most significant event found had a pvalue of 5.5×10^{-3} (GRB190804058).

Figure 4.7 presents the cumulative distribution of pvalue obtained with the modelled and unmodelled search in O3a. Both show that the pvalue distributions are consistent with the background. To test the probability of observing our set of pvalues under the null hypothesis, a weighted binomial test has been performed. This type of test, presented in [304], makes use of the lowest 5% of the pvalues obtained from the searches. The probability obtained for the modelled search is 0.43 for O3a [269]. For the unmodelled search the probability obtained is 0.30 [269]. Therefore, both searches gave no significant evidence for a population of unidentified subthreshold GW signals.

The figure 4.8 presents the cumulative 90% exclusion distances for the short and ambiguous GRBs followed up with the modelled search in O3a. The few first steps in the histogram with relatively low exclusion distance are due to GRBs where only Virgo data was available. The figure 4.8 also presents the cumulative

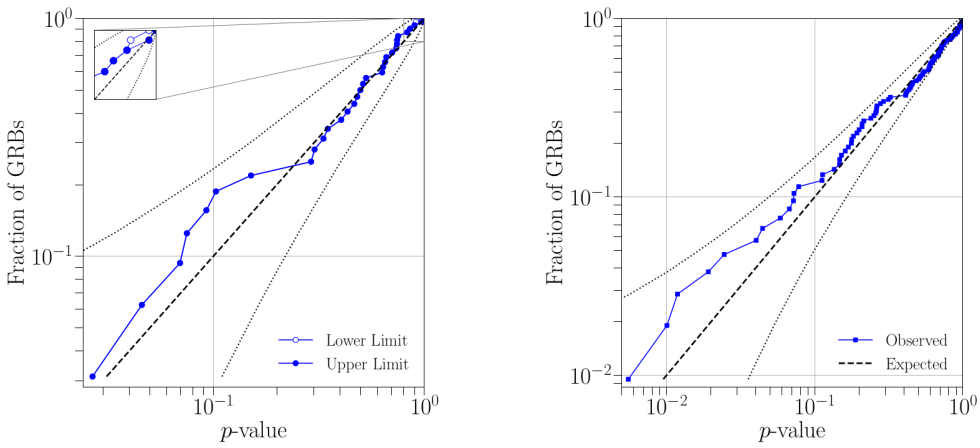

Figure 4.7: *Left :* The cumulative distribution of pvalues for the loudest on-source events for the modelled search in O3a. If a trigger is found in the onsource the upper and lower limits are identical to the reported pvalue. If no trigger is identified in the onsource window, we set an upper limit on the pvalue of 1, and a lower limit equal to the fraction of offsource trials that also did not contain a trigger. The upper limits are plotted as the curve with full circles and the lower limits are plotted as the curve with empty circles. The dashed line indicates the expected uniform distribution of pvalues under a no-signal hypothesis, with the corresponding 90% band as the dotted lines. *Right :* The cumulative distribution of pvalues for the loudest events from the unmodelled search. The dashed line represents the expected distribution under the no-signal hypothesis, with dotted lines indicating a 2σ deviation from this distribution. Figures from [269].

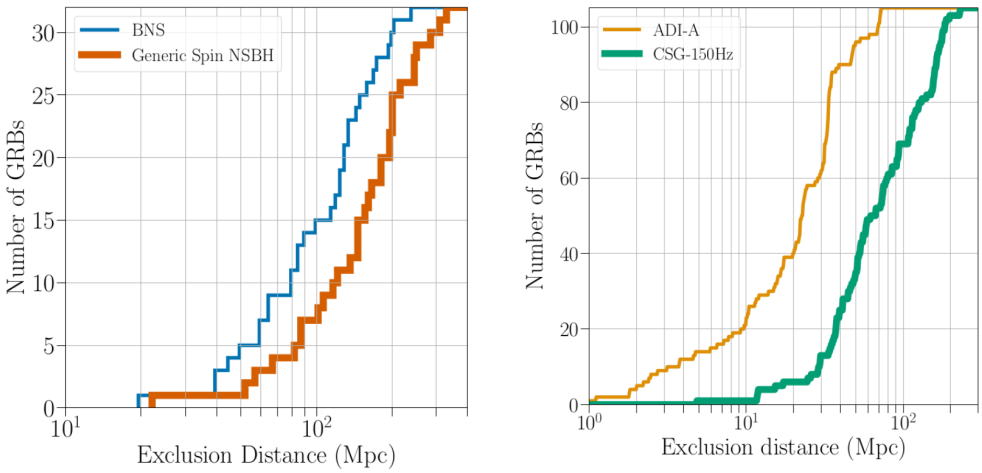

Figure 4.8: *Left :* Cumulative histograms of the 90% exclusion distances, D_{90}, for the modelled search followed up in O3a. The thin blue line shows generically spinning BNS models and the thick orange line shows generically spinning NSBH models. *Right :* Cumulative histograms of the 90% confidence exclusion distances, D_{90}, for accretion disk instability signal model A [302, 303, 269] and the circular sine-Gaussian 150 Hz model [302]. Figures from [269].

90% exclusion distances obtained for ADI model A [305, 306] and for a CSG with central frequency of 150 Hz [302] with the unmodelled search. These limits depend on gravitational wave detectors network sensitivity which change with time and sky location of the GRB events, and have been also marginalized over errors introduced by detector calibration. Table 4.1 summarises the search sensitivity by displaying the mean D_{90} exclusion distance for the set of GRBs with modelled and unmodelled search in O2 (second observing run [307]) and O3a. The exclusion distance for each individual GRB can be found in [307, 269].

Modelled search (Short GRBs)	BNS	NSBH Generic Spins	NSBH Aligned Spins
D_{90} [Mpc]			
O2	80	105	144
O3a	119	160	231

Unmodelled search (All GRBs)	CSG 70 Hz	CSG 100 Hz	CSG 150 Hz	CSG 300 Hz
D_{90} [Mpc]				
O2	112	113	81	38
O3a	146	104	73	28

Unmodelled search (All GRBs)	ADI A	ADI B	ADI C	ADI D	ADI E
D_{90} [Mpc]					
O2	32	104	40	15	36
O3a	23	123	28	11	33

Table 4.1: Median 90% exclusion distances (D_{90}) for both modelled and unmodelled transient searches during O2 and O3a. For the modelled search, the table reports the median (D_{90}) values for all three simulated signal types. For the unmodelled search, the table reports results obtained with the CSG [302] and ADI [305, 306] models.

Chapter 5

OPTIMISATION OF GRAVITATIONAL WAVE FOLLOW-UP

In this chapter I present in details the challenge of the electromagnetic follow-up of gravitational wave events. I will present the work I developed for the optimisation of the follow-up of by network of telescopes such as GRANDMA and SVOM. I will also detail the observation plan I developed specifically for the SVOM satellite. Finally, I will present the study of short GRB host galaxies and its use for the follow-up of gravitational wave events.

5.1 Key points of the gravitational wave follow-up challenge

In this section I present the electromagnetic follow-up of gravitational wave candidates and my involvement in this topic within the GRANDMA and SVOM collaborations. While, as presented in sections 1.3 and 3.4, there are a lot of different expected sources of gravitational waves for which one can look for electromagnetic counterpart, I choose to focus in this section on compact binary mergers and especially on BNS mergers as they represent the most promising sources of electromagnetic counterparts from gamma-ray to radio.

The general objective of the follow-up of gravitational wave candidates with optical or X-ray telescopes is to detect counterparts, to perform a multi-wavelength follow-up with as much as possible a highly-sampled light curve of the counterpart. One can also expect to measure the redshift and the spectral features of the counterpart. These objectives face several difficulties which are presented below.

Large uncertainties on localisation

As presented in section 2.2.4 the localisation of a source of gravitational waves vary from a few tens to more than 1000 square degrees. By comparison, the typical field of view (FoV) of an optical telescope is ~ 0.1 deg^2. For such a telescope it is impossible to observe the entire skymap for most of the alerts. Optical observers have to prioritise their observations to maximise their chance of observing a coun-

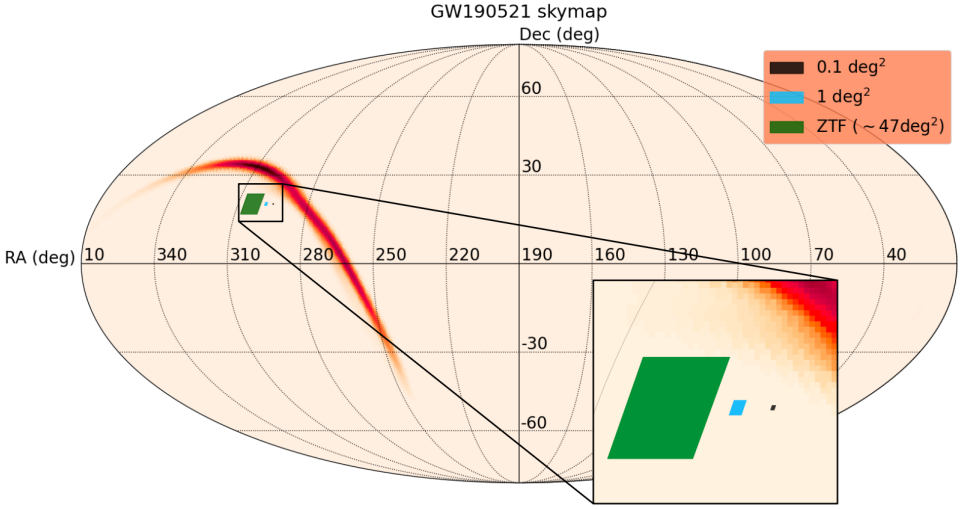

Figure 5.1: Mollweide projection of GW190521 BAYESTAR skymap. Black, blue and green squares represent telescopes with square field of view of 0.1 deg^2, 1 deg^2 and 47 deg^2 (like ZTF).

terpart (see 5.2 for development). Telescopes like the Zwicky Transient Facility (ZTF) [308] dedicated to the detection of transients try to deal with this issue with a specifically large FoV ($\sim$ 47deg^2 for ZTF) but this is often at the cost of sensitivity, the cost of the resolution and/or the cost of the device. Figure 5.1 presents an example of skymap comparisons with telescopes FoV of 0.1 deg^2, 1 deg^2 and 47 deg^2 (like ZTF). The skymap chosen for this plot is GW190521 BAYESTAR skymap as it has a 90% localisation of $\sim$ 501 deg^2 which illustrate the median 90% localisation for all BBH skymap alerts sent during 03 ($\sim$ 500 deg^2), see for instance figure 3 of [309]. Furthermore, with ground based observatories the visible sky is limited by the horizon. Hence, a large fraction of the gravitational wave candidate skymap is not observable (or partially observable) from a given site which limits again the chance to observe and detect any counterpart.

Faint and fast decaying transients

The main optical counterparts follow-up observations are looking at are the kilonova emissions. But as presented in section 3.4, the expected absolute magnitude of such object is relatively low. For GW170817, the kilonova apparent magnitude peaked at $\sim$ 17 mag in r band. Knowing this was a very close event ($\sim$ 40 Mpc) the expected apparent magnitude for a further away event is challenging for the detection. Figure 5.2 presents the r band apparent magnitude expected for a kilonova from GW170817 observations for various distances of the source. One can see that,

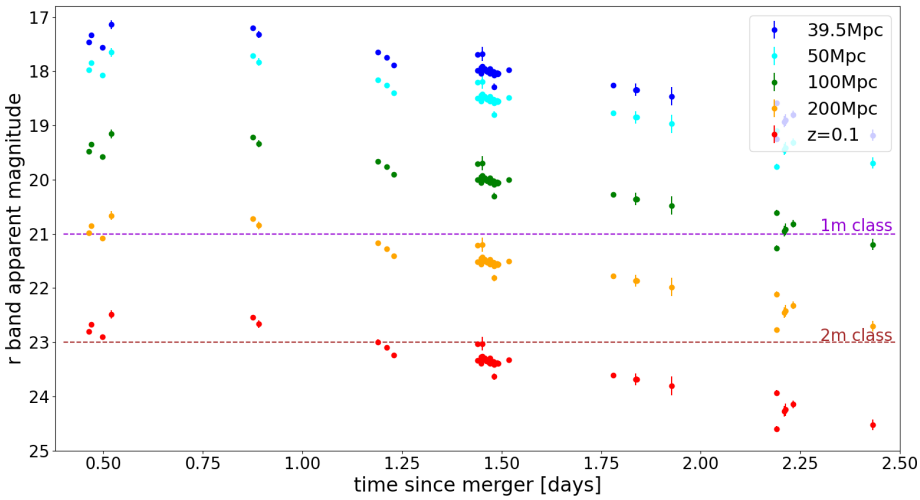

Figure 5.2: First few days of observed GW170817 kilonova r band magitude (blue dots). Same data shifted as if the source was at a luminosity distance of 50Mpc, 100Mpc, 200Mpc and redshift equal to 0.1 ($\sim$ 460Mpc) are represented by cyan, green, orange and red dots respectively. All data are taken from [164]. No K-correction are taken into account. Violet and brown dotted lines represent a rough estimation of the limiting magnitude for a 1 meter mirror class and 2 meters mirror class telescope with a standard exposure time[2].

for distances above 200 Mpc, the apparent peaking magnitude in r band is below 21 which requires specifically sensitive telescopes and/or specifically long exposure time to be achieved. Furthermore, the kilonova emission decays very rapidly and is expected to be detectable for only few days with a typical telescope. Hence this kind of follow-up requires a fast response and a fast observation of the source which is complicated by the large uncertainty on localisation presented before. As the GW170817 kilonova is the only one for which we observed a multi-wavelength lightcurve we do not know yet the diversity of kilonova emission [310, 311]. The short GRB afterglows are also relatively faint transients. As presented in figure 5.3 short GRB afterglows are for instance less bright than the mean brightness of long GRB afterglows.

[2]For example ZTF installed on the 1.2-meter diameter Samuel Oschin Telescope can reach $\sim$ 20.5 mag with a 30 s exposure time in r band.

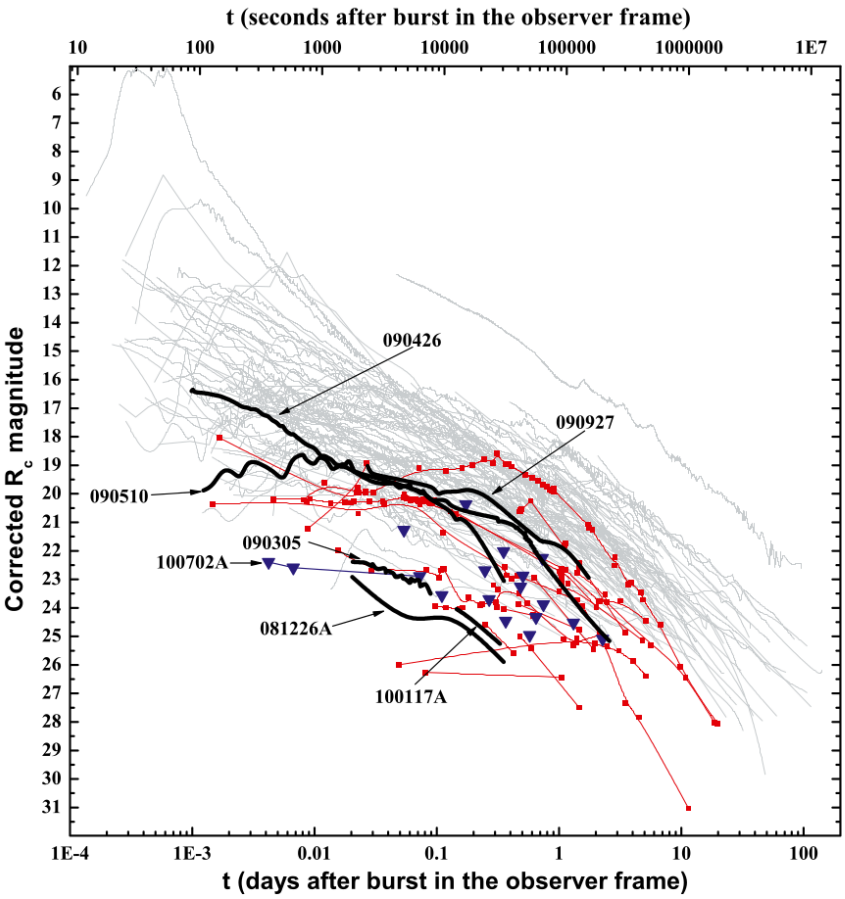

Figure 5.3: Lightcurves in R band of long and short GRB afterglows. These lightcurves have been corrected individually for galactic foreground extinction following [312], and, if possible, for host galaxy contributions. The thin gray lines are the long GRB sample of [313]. The red squares connected by splines represent the short GRB afterglow detections reported by [313]. The short GRB afterglows from [314] are given as labeled thick black lines. Upper limits presented in [314] are given as blue triangles. Figure from [314].

Identification of candidates

The large uncertainties on localisation from gravitational wave detection necessarily lead to the observation of large regions of the sky. Hence a lot of transient candidates are detected in the images, most of them being unrelated transients (supernovae, variable star...) or fake transients (cosmics, dead pixels...). As a result, powerful tools dedicated to quickly identify and classify the transients (automatised image subtraction, deep machine learning, likelihood algorithm...) are mandatory to engage further follow-up on the most promising one.

In conclusion, the gravitational wave follow-up is very demanding for observers and does not guarantee any detection despite the efforts made. We can summarise the requirements of such follow-up as follows: one needs to use the largest FoV possible, to perform the observation as fast as possible, to be deep in photometry and to be efficient in identifying the electromagnetic counterparts. One telescope alone is usually not able to fulfill all these requirements at once. For this reason several collaborations around the world have been initiated to coordinate the observations from different sites within a network of telescopes.

5.2 Optimisation of the observations

In this section I present the work I developed for the optimisation of the follow-up of gravitational waves with networks of telescopes like GRANDMA and SVOM. As the SVOM collaboration has been presented in section 3.3 I only introduce in the following the GRANDMA collaboration.

5.2.1 GRANDMA: a network to coordinate them all

The Global Rapid Advanced Network Devoted to the Multi-messenger Addicts (GRANDMA) is a network of 24 telescopes of different sizes which include photometric and spectroscopic facilities spread across the world [315] created initially for the follow-up of the O3 LIGO-Virgo run. The GRANDMA collaboration involves $\sim$ 70 scientists and $\sim$ 30 institutes. The network aims at coordinating follow-up observations of multi-messenger events like gravitational-wave candidate alerts. It possesses some telescopes with specifically large FoV and telescopes in both hemispheres with a very good longitude coverage. The list of GRANDMA telescopes can be found in table 5.1. This makes it especially efficient for large skymaps. Figure 5.4 presents a world map with the location of the GRANDMA observatories. With deep photometric telescopes equipped with various filters from near-ultraviolet to near-infrared and spectroscopic facilities, the GRANDMA net-

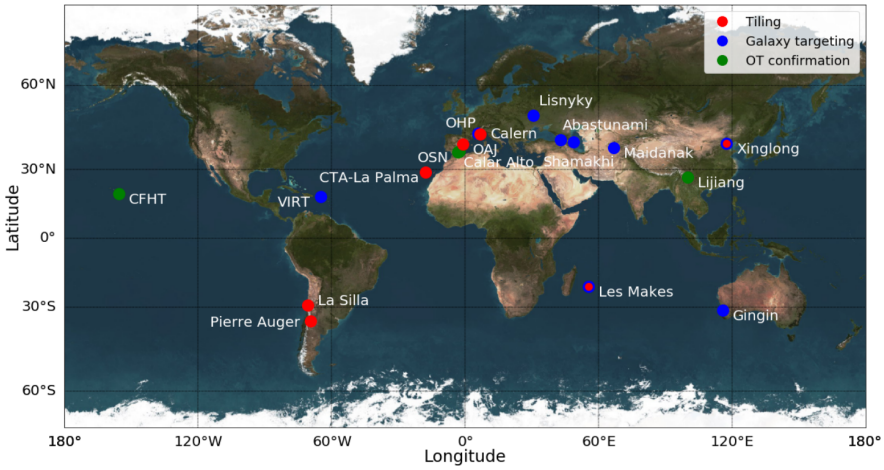

Figure 5.4: The wold-wide network of the GRANDMA collaboration. Each dot represents an observation site of the network, the color shows the observation strategy used with the telescope. Figure from [315].

work is also very efficient in the characterisation of transients and thus reduces the delay between the initial detection and the optical confirmation.

ICARE, *GMADET* and *MUPHOTEN*

In order to connect the telescopes, GRANDMA developed the *ICARE* (Interface and Communication for Addicts of the Rapid follow-up in multi-messenger Era) infrastructure providing a set of tools dedicated to the coordination of the telescopes. It is specifically built to monitor facilities for rapid follow-up of multi-messenger alerts with a central system responsible for ingesting the transient alerts coming from various platforms, such as GCN notices. The system is also able to receive the real-time status of the network observatories (weather, maintenance, technical issue...). The ICARE infrastructure distributes dedicated observation plans to all the telescopes within the network via a broker delivering standardized VO events. Alerts information and observation plans are stored into the GRANDMA database as soon as they are received/produced. These information can be visualized on a dedicated web portal. All results of the observations and counterpart candidates are also centralised in the GRANDMA database.

To analyse the images from the whole network, GRANDMA developed a common detection pipeline *Gmadet* (GRANDMA detection pipeline). This pipeline is dedicated to the image analysis (astrometric calibration, alignment, stacking, image subtraction, sources extraction, rejection of known transients) necessary

Telescope Name	Location	Aperture (m)	FOV (deg)	Filters	Typical lim mag (AB mag)	Maximum Night slot (UTC)
TAROT/TCH	La Silla Obs.	0.25	1.85×1.85	Clear, $g'r'i'$	18.0 in 60s (Clear)	00h-10h
FRAM-Auger	Pierre Auger Obs.	0.30	1.0×1.0	BVR_CI_C, Clear	17.0 in 120s (R_C)	00h-10h
CFHT/WIRCAM	CFH Obs.	3.6	0.35×0.35	JH	22.0 in 200s (J)	10h-16h
CFHT/MEGACAM	CFH Obs.	3.6	1.0×1.0	$g'r'i'z'$	23.0 in 200s (r')	10h-16h
Thai National Telescope	Thai National Obs.	2.40	0.13×0.13	Clear, $u'g'r'i'z'$	22.3 in 3s (g')	11h-23h
Zadko	Gingin Obs.	1.00	0.17×0.12	Clear, $g'r'i'I_C$	20.5 in 40s (Clear)	12h-22h
TNT	Xinglong Obs.	0.80	0.19×0.19	$BVg'r'i'$	19.0 in 300s (R_C)	12h-22h
Xinglong-2.16	Xinglong Obs.	2.16	0.15×0.15	$BVRI$	21.0 in 100s (R_C)	12h-22h
GMG-2.4	Lijiang Obs.	2.4	0.17×0.17	$BVRI$	22.0 in 100s (R_C)	12h-22h
UBAI/NT-60	Maidanak Obs.	0.60	0.18×0.18	BVR_CI_C	18.0 in 180s (R_C)	14h-00h
UBAI/ST-60	Maidanak Obs.	0.60	0.11×0.11	BVR_CI_C	18.0 in 180s (R_C)	14h-00h
TAROT/TRE	La Reunion	0.18	4.2×4.2	Clear	16.0 in 60s (Clear)	15h-01h
Les Makes/T60	La Reunion.	0.60	0.3×0.3	Clear, BVR_C	19.0 in 180s (R_C)	15h-01h
Abastumani/T70	Abastumani Obs.	0.70	0.5×0.5	BVR_CI_C	18.2 in 60s (R_C)	17h-03h
ShAO/T60	Shamakhy Obs.	0.60	0.28×0.28	BVR_CI_C	19.0 in 300s (R_C)	17h-03h
Lisnyky/AZT-8	Kyiv Obs.	0.70	0.38×0.38	$UBVR_CI_C$	20.0 in 300s(R_C)	17h-03h
TAROT/TCA	Calern Obs.	0.25	1.85×1.85	Clear, $g'r'i'$	18.0 in 60s (Clear)	20h-06h
FRAM-CTA	ORM	0.25	0.43×0.43	Clear, BVR_Cz',	16.5 in 120s (R_C)	20h-06h
IRIS	OHP	0.50	0.4×0.4	Clear, $u'g'r'i'z'$	18.5 in 60s (r')	20h-06h
T120	OHP	1.20	0.3×0.3	$BVRI$	20.0 in 60s (R)	20h-06h
OAJ/T80	Javalambre Obs.	0.80	1.4×1.4	r'	21.0 in 180s (r')	20h-06h
OSN/T150	Sierra Nevada Obs.	1.50	0.30×0.22	BVR_CI_C	21.5 in 180s (R_C)	20h-06h
CAHA/2.2m	Calar Alto Obs.	2.20	0.27	$u'g'r'i'z'$	23.7 in 100s (r')	20h-06h
VIRT	Etelman Obs.	0.50	0.27×0.27	$UBVRI, Clear$	19.0 in 120s (Clear)	22h-04h

Table 5.1: List of telescopes of the GRANDMA collaboration and their photometric performance when using their standard setup. Table from [309].

to identify interesting transient in the observations[3]. The Gmadet pipeline was specifically built in a way which is adaptable to fit the different properties of the telescopes in the network.

Any interesting transient detected by Gmadet and followed up with further imaging is then characterised with the *MUPHOTEN* (a MUlti-band PHOtometry Tool for TElescope Network) software (see Duverne et al. in preparation). This tool is a generic and fast-computation photometric pipeline, particularly effective for the calibration of transient brightness over multi-telescopes and multi-bands networks such as GRANDMA. The final goal of the pipeline is to provide a single photometric timeseries of the transient, allowing a fast classification.

The GRANDMA and SVOM observation strategies use two different approaches depending on the FoV of the telescopes. Both strategies are implemented within the `gwemopt`[4] open-software [316] designed to optimize the scheduling of the gravitational wave follow-up with ground based telescopes either *tiling* or *galaxy targeted* strategies.

[3]For details see the Gmadet documentation: `https://github.com/dcorre/gmadet`
[4]`https://github.com/mcoughlin/gwemopt`

5.2.2 Tiling strategy

The tiling strategy usually used by large FoV ($\gtrsim$ 1 deg^2) telescopes consists of the construction of an optimized tiling of the sky where the scheduling of the observation is defined using the 2D sky localisation (probability distribution) from the gravitational wave skymap. In this strategy tiles are defined to fit the telescope field of view and typically correspond to one image. They are built in such a way that the overlap between the tiles is minimized to observe the largest sky area possible. Prior of any observation, a complete tiling of the sky is computed so that all tiles are defined in advance. For a given alert one need then to schedule the observations of these tiles. The gravitational wave skymaps are provided through all-sky pixelised images in the HEALPix (Hierarchical Equal Area isoLatitude Pixelization) format [317]. In these skymaps one can fetch for each pixel the probability for the source to be in the sky direction of the pixel (2D probability). This is used to schedule the tile observations according to the 2D probability they contain, summing the probability of each pixel in the tiles. In the computation only the tiles observable from the telescope site during the observation night are kept.

I participated in recent developments to optimise the tiling strategy for networks of telescopes [318]. In these development of the strategies, the telescopes are not considered independently but the observation plans are produced in common to share the sky coverage. This "hierarchical" approach used by the GRANDMA collaboration starts by selecting the telescope using tiling strategy with the best sensitivity and computing the first night observation plan for this given telescope. The region covered by this first telescope is assigned a null probability before computing the observation plan for the second telescope, and so on. In this strategy, the overlap between the region of the sky observed by a given telescope of the network and the region of the sky observed by any other one is minimised. This optimises the total sky coverage of the network. One of the major downsides to this schema is the case where a telescope is not able to observe, for instance because of weather conditions. Indeed, in this case the region of the sky assigned to this given telescope will not be observed by any other telescopes (because of the optimisation of the sharing of the sky coverage). This may lead to a miss observation to a very high likelihood regions of the skymap. For safety reasons the idea of "golden" regions, regions of the sky that are not decremented at each step (the probability is not set to zero), has been implemented. These golden regions are usually defined as the few first tens of percents of the gravitational wave skymap. This ensures that the most interesting regions of the skymap are imaged several times by the network. Results of the O3 observations using this development are presented in section 5.4.

5.2.3 Galaxy targeting strategy

In this section, I describe the development of the galaxy targeting I worked on, presented in [319], i.e. how to take into account the galaxies properties in the galaxy ranking process. This problem has been studied by various works, see for instance [320, 321, 322]. We chose to focus on the stellar mass of the galaxies as both BNS population simulation [323, 324, 325] and short GRBs host galaxies studies [326, 327, 240] present the stellar mass as one of the most important parameter in determining the rate of BNS merger. This strategy was firstly developed for the follow-up of BNS events (knowing in particular their link with short GRBs described in chapter 3) but in practice this can be used for any binary coalescence alerts.

Standard approach

The galaxy targeting strategy is typically used for small FoV telescopes. As its name suggests, this strategy is trying to take advantage of galaxy catalogs to focus the observations on interesting galaxies within the horizon of interest for a given alert. This strategy starts from the hypothesis that the source is located within (or nearby) a galaxy, the host galaxy of the BNS system. This is expected knowing in particular the link with short GRBs described in chapter 3. For compact binary coalescence, the HEALPix skymap provided with the gravitational wave alert also provide the estimated distance of the source. For each pixels of the skymap, one can fetch the probability distribution for the source distance at the given sky position of the pixel. To infer the probability P_{pos} of a given galaxy to be the host of the merger according to its celestial position, we use the following relation:

$$P_{pos} = \frac{P_{pixel}}{Pixel\ area} N_{pixel}\, e^{-\frac{1}{2}\left(\frac{D_{galaxy}-\mu_{pixel}}{\sigma_{pixel}}\right)^2} \tag{5.1}$$

where P_{pixel} is the 2D probability included in the given HEALPix pixel, N_{pixel} is the normalisation factor for the given pixel, μ_{pixel} is the mean distance value at the given pixel, σ_{pixel} is the standard deviation at the given pixel. P_{pixel}, N_{pixel}, μ_{pixel} and σ_{pixel} for any pixel of the sky are provided by the LIGO-Virgo-KAGRA collaboration within each alert skymap. D_{galaxy} is the luminosity distance of the galaxy fetched from the catalog. In this expression, P_{pixel} is divided by the pixel area to recover the probability of a point on the sky. Hence, the P_{pos} expression can be seen as the expression of the probability of a small volume element at a given 3D point of the sky. If the distance of the galaxy D_{galaxy} is estimated with a large error, for example with photometric estimation, this can have a significant effect on equation 5.1 and the ranking it produces. It is therefore preferable to

use much as possible catalogues with a precise estimation of the distance, like with spectroscopic estimation. This suggestion is limited by the currently publicly available galaxy catalog, see section 5.3 for development. In this strategy we consider as "compatible" with the skymap, a galaxy which fulfills the two following conditions:

- its 2D position in the sky has to be in the 90% of the 2D skymap probability distribution;
- its distance has to fall within 3 times the distance error σ_{pixel}

With such conditions we ensure that telescopes do not point outside of the 90% skymap probability distribution. The conservative choice of 3σ on the distance constraint is motivated by the fact that galaxies with a low distance probability are always penalised in the ranking process. Regarding the condition on the distance, we use the pixel by pixel information and not the mean distance estimation for the LIGO-Virgo candidate. This choice is motivated by the fact that the distance estimation can be very inhomogeneous in a given skymap. Figure 5.5 shows the distribution pixel by pixel of the mean distance μ and the standard deviation σ inside the the 90% of the 2D skymap probability distribution for the S190425z candidate during the O3 run. This example of a BNS candidate shows that for a large portion of the skymap the μ and σ at a given pixel are far away from the mean distance evaluation for the whole skymap (155 $\pm$ 45 Mpc in this case). Using pixel by pixel information prevents to dismiss compatible galaxies or select incompatible ones.

One of the main advantages of the galaxy targeting is to reduce the amount of observations necessary to cover a given skymap. Figure 5.6 shows the result of the galaxy targeting for GW170817 with a standard field of view of 20 arcmin. A large part of the skymap is not worth observing because it does not contain any compatible galaxies. A total of 44 pointings are needed to observe all galaxies compatible with the 90% skymap whereas it would have required 144 tiles to cover the entire 90% skymap without checking with a galaxy catalog, which results on significant gain of observational time allocation and revisits.

Grade reformulation with stellar mass

Given the large size of error boxes from gravitational wave detections, the number of galaxies compatible with an event can be very large (>few thousands). In such cases, the classification using the 3D probability is only limited because it produces similar values for a large number of galaxies. Adding galaxy properties to the ranking is a way to reduce the sample size of interesting galaxies, accelerating the possible identification of any counterpart. In the following, I present the

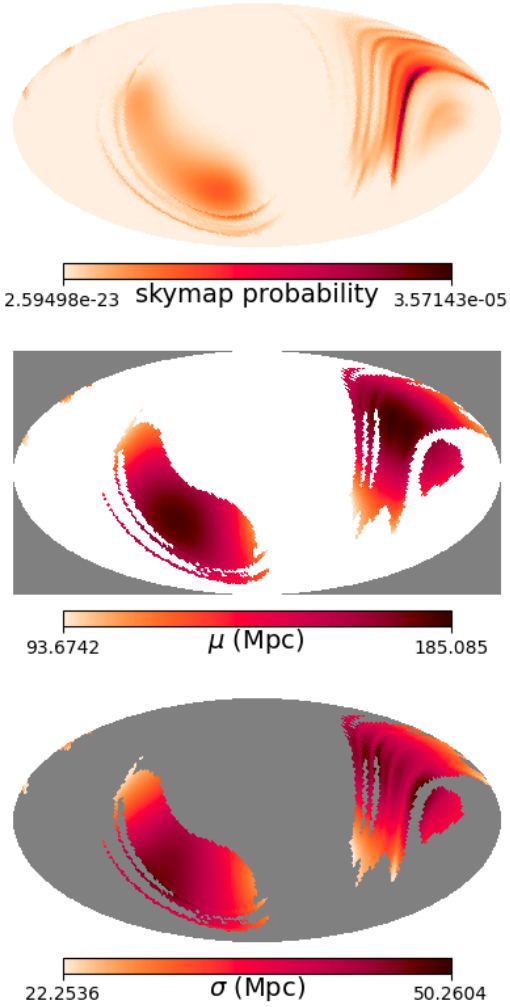

Figure 5.5: The top plot shows the probability distribution for the BNS candidate S190425z of O3. The middle and bottom plots are respectively the mean distance and the standard deviation distributions for the pixels inside the 90% of the 2D skymap probability distribution.

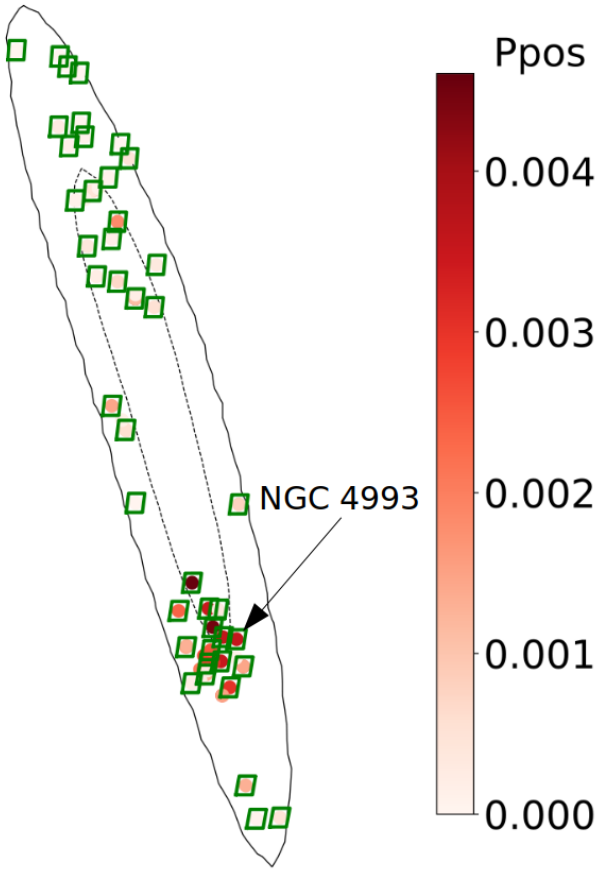

Figure 5.6: Skymap of GW170817. The dashed and the solid lines enclose the 50% and the 90% of the skymap respectively. The green squares represent the pointing of a telescope with a field of view of 20'. The red color scale shows the grade of the galaxies according to equation 5.1. The black arrow shows the position of the gravitational wave host galaxy, NGC4993.

implementation of galaxy properties in the raking that are specially dedicated for the follow-up of BNS merger events.

Among the various galaxy properties that could influence the rate of BNS mergers, such as star formation rate (SFR), stellar mass and metallicity, several works pointed out a significant dependence to the stellar mass [323, 324, 325]. Furthermore, short GRB host galaxies are known to be associated to BNS mergers since GW170817, and are found in massive galaxies. The short GRB host galaxies are more massive than the long GRB host galaxies, pointing to the importance of the stellar mass in determining the rate of short GRBs [326, 327, 240] (see section 5.6 for development). So far, the only one known (by gravitational waves) host galaxy of BNS merger is NGC4993 from GW170817 event. This galaxy presents a very high mass ($0.3 - 1.2 \times 10^{11} M_{\odot}$) and a low star formation rate [328, 329, 330, 331, 332]. The host galaxy of GRB150101B presented as a analogue of GRB170817A [333] is also a very massive galaxy. In the light of those information we chose to focus on the stellar mass for the selection of gravitational wave host galaxy candidates. In the following, quantities used to characterise interesting galaxies will be named grades, and noted G, as the following modifications can not be interpreted directly as probabilities.

We introduce a new term G_{mass} defined as:

$$G_{mass} = \frac{M_{*,galaxy}}{\sum M_{*,galaxy}} \tag{5.2}$$

where $M_{*,galaxy}$ is the stellar mass of a given galaxy and the sum is over all of galaxies compatible with a given skymap (see previous section for the definition). We first combine this term to the standard grade defined in equation 5.1 for each galaxy computing the product:

$$G_{tot} = P_{pos} \times G_{mass} \tag{5.3}$$

The equation 5.3 fits the expression used in [321] ($P_{tot} = P_{pos} + P_{lum}$, where P_{lum} is defined similarly as G_{mass} but using B band luminosity) to allows a direct comparison of the results (see Section 5.3). The drawback of this expression with a simple product is that galaxies for which no stellar mass information is available are simply not considered. In order to keep galaxies without stellar mass information, and still use their 3D localisation probability, P_{pos}, we propose to redefine the grade defined in equation 5.3 as:

$$G_{tot} = P_{pos} \left(1 + \alpha\beta G_{mass}\right) \tag{5.4}$$

where α and β are positive real parameters. With such a definition, G_{mass} is set to 0 when the stellar mass information is not available to fall back on P_{pos}. The

parameter α is defined such that the two terms in equation 5.4 contribute equally to the total grade, G_{tot}:

$$\frac{\sum P_{pos}}{N} = \frac{\sum P_{pos}\,\alpha\,G_{mass}}{N} \tag{5.5}$$

$$\Rightarrow \alpha = \frac{\sum P_{pos}}{\sum P_{pos}\,G_{mass}} \tag{5.6}$$

where N is the total number of galaxies compatible for a given skymap having a determined stellar mass. The sum is over all galaxies compatible for a given skymap having a determined stellar mass. The parameter β is used to weight the importance of G_{mass} in the total grade. This parameter is independent of the alert (skymap). Ideally, β should be fitted on a statistically significant sample of gravitational wave host galaxies. As only one event has been detected so far, we simply chose to set $\beta = 1$.

Previous works [321, 334] chose to include another factor for the grade which describes the likelihood to detect the counterpart according to the limiting magnitude of the observing telescope and the expected magnitude of the source. Such factor can be added to the expression 5.3 and 5.4 if needed. We chose not to develop such a strategy. First, the limiting magnitude of a telescope can vary a lot between two observations (seeing, horizon...). Secondly, only one detection of gravitational wave electromagnetic counterparts has been achieved at the moment. Assuming a standard lightcurve for the kilonova on only one set of data could be risky.

Although the presented reformulation of the grade is specifically targeting BNS merger events, it can also be used for any other gravitational wave events like NSBH or BBH mergers. For as long as the dependence to the stellar mass can still be supported for such event. However, because NSBH and BBH mergers involve more mass than BNS mergers, they are usually detected at larger distances. Hence, such events are more limited by the catalog completeness than BNS merger. The reformulation of the grade presented here is independent of the method used to determine the stellar mass of galaxies. In the next section I present the method we have chosen to obtain the stellar mass of galaxies in a homogeneous way for a catalog over the whole sky.

5.3 Mangrove: a catalog with stellar mass information

To allow the use of information related to galaxies, one must rely on a galaxy catalog that is sufficiently complete to be compatible with the interferometer sensitivity range. The Census of the Local Universe (CLU) catalog [335] for the north hemisphere contains the WISE1 (3.4 μm) luminosity information as well as spectroscopic measurements of local galaxies, however CLU is non publicly available. Therefore, for the purpose of this work, we relied on the publicly available GLADE galaxy catalog [336] which is all-sky and complete up to 100 Mpc, and nearly complete up to 150 Mpc. Unfortunately, the GLADE galaxy catalog provides the B, J, H and K band magnitudes for some of the galaxies but not the stellar mass. We did not choose to compile the stellar masses from various works for homogeneity reasons as it would bring systematics in the ranking process due to possibly quite different methods in the stellar mass estimation. Previous work [321] used the B band magnitude as an indicator of the stellar mass. However, the B band is sensitive to the star formation history and can be strongly affected by dust extinction [337, 338]. The near-infrared luminosity emitted by the old stellar population is fairly insensitive to dust extinction, and is thus considered as a reliable indicator of the total stellar mass of a galaxy [339, 340]. In this work, we restrict the distance to 400 Mpc as it is reasonably above the limiting sensitivity distance of LIGO-Virgo for binary neutron star mergers with O3 sensitivity [341]. Up to 400 Mpc, there are only $\sim 67\%$ of the galaxies with a K band magnitude in the version 2.3 of the GLADE catalog. As showed by [342, 343], the WISE1 (3.4 μm) luminosity is a reliable indicator of the stellar mass. Moreover the AllWISE catalog [344] has the advantage to be an all-sky catalog. Therefore we made the choice to perform a crossmatch between the GLADE and the AllWISE catalogs to derive a reliable stellar mass estimation. The resulting catalog is named *Mangrove* (Mass AssociatioN for GRavitational waves ObserVations Efficiency).

Using WISE1 luminosities, [342, 343] showed that the stellar mass of galaxies can be reliably estimated with a constant mass to light ratio: $\Upsilon_*^{3.4\mu m} \sim 0.60\ M_\odot/L_{\odot,3.4\mu m}$ where $M_\odot/L_{\odot,3.4\mu m}$ is the mass-to-light ratio in units of solar masses over the solar luminosity in the WISE 3.4 μm band ($m_{\odot,3.4}\ \mu m = 3.24\ mag; L_{\odot,3.4}\ \mu m = 1.58 \times 10^{32}\ ergs^{-1}$; [345]). This approach derives stellar masses with an error of 0.10 dex[5] [342, 343]. Although the value of $\Upsilon_*^{3.4\mu m}$ can vary from ~ 0.5 to ~ 0.65 in the litterature, this results on small changes on the derived stellar mass and will not affect the ranking of galaxies as it is a constant ratio.

We spatially crossmatched the GLADE catalog cut to 400 Mpc with the AllWISE

[5] an error of $10^{0.1}$

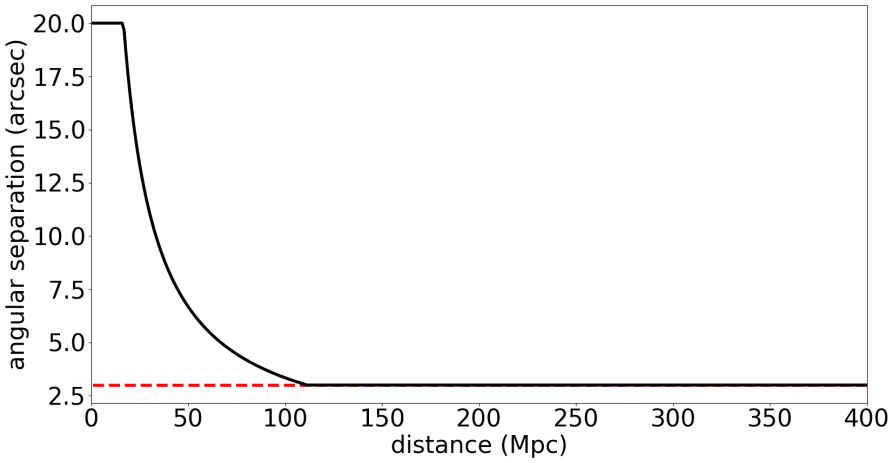

Figure 5.7: Angular separation condition used for the crossmatch as a function of the distance. The red dashed line shows the limit value of 3 arcseconds.

catalog using a radius crossmatch varying with the distance as seen in figure 5.7. The radius is defined as 5% of the angular diameter of the Milky Way (0.0324 Mpc) and we impose a minimum and maximum of 3 and 20 arcseconds respectively. This strategy was chosen to optimize the match at low distance where galaxies can have a very large angular size.

A same AllWISE object can appear more than once in the preliminary crossmatched catalog, meaning that there is more than one GLADE galaxy around the given AllWISE object. For such a case, knowing the angular resolution of the WISE telescope in the WISE1 band (6.1 arcseconds), we only kept the closest object if it is the only one in a radius of 6.1 arc seconds around the GLADE galaxy. The presence of an AGN implies a significant emission in the infrared and near-infrared [346, 347, 348], and thus bias our stellar mass estimation for such galaxies. We identify active galactic nucleus (AGN) from the resulting catalog using the mid-infrared color criterion with the WISE band $W1 - W2 \geq 0.8$ as used in [349, 350]. This corresponds to 3346 galaxies, that are still present in the catalog but without stellar mass estimation.
We use the elliptical aperture photometry flux from ALLWISE catalog whenever available for the source, otherwise the profile fitting photometry is used. This ensures that these fluxes encompass each galaxy full radial extent. At the end we obtain the stellar mass information for 743780 objects, knowing that the GLADE catalog, cut to 400 Mpc have, 800,986 galaxies, we have a $\sim 93\%$ match efficiency.

Before the conversion of WISE1 magnitudes to stellar masses using the mass-to-light ratio provided by [342], we apply a K-correction to correct for the redshifting. The K-correction is the conversion of the measured magnitude of an astronomical objects into its rest frame magnitude. Because we are using bandpassed observations, we only have information on a fraction of the total spectrum, redshifted into the frame of the observer. The K-correction converts this redshifted magnitude into the rest frame magnitude in the same band.

In order to estimate the K-correction we use 31 spectral energy distribution (SED, see 3.7 for description) templates covering all known types of galaxies, from red elliptical to blue star-forming galaxies [351]. We compute the K-correction both without dust attenuation and with $E(B-V)$=0.5 mag using the Calzetti attenuation law [352]. The K-correction is insensitive to the galaxy type and dust attenuation up to z=0.12 as seen in figure 5.8. Given the distance limitation of 400 Mpc (z$\sim$ 0.085) for our catalog, we computed the K-correction at a given distance as the mean value for the 31 galaxies SED templates with and without dust attenuation. For this range of distances, the effect is negligible, however this will become important for future catalogs that will need to be deeper to encompass the sensitivity improvement of LIGO-Virgo interferometers. I recall that all stellar masses used in this work were derived using the same method to ensure homogeneity. Regarding the reliability of our stellar mass estimates, although we aimed at an homogeneous estimation, [342] showed that for low redshift galaxies the stellar mass estimation using a constant mass-to-light ratio using the WISE1 luminosity is in good agreement with the one predicted from a more elaborate SED fitting technique.

We aimed at quantifying the completeness of the Mangrove catalog in terms of stellar mass. The stellar mass function is well described by a Schechter function [353], $\Phi(M)$, which parametrises the density of galaxies, $n_{galaxies}$, as a function of their stellar mass. In this work, we use the low-redshift galaxy stellar mass function derived from the Galaxy And Mass Assembly (GAMA) [354], using a double Schechter function in logarithmic mass space defined as:

$$\begin{aligned} n_{galaxies} &= \Phi(M)\ d\log M \\ &= ln(10)\ e^{-10^{\log M - \log M^*}} \left[\Phi_1^*.\left(10^{\log M - \log M^*}\right)^{\alpha_1+1}\right. \\ &\left. +\Phi_2^*.\left(10^{\log M - \log M^*}\right)^{\alpha_2+1}\right]\ d\log M \end{aligned} \tag{5.7}$$

where $\log M^*$= 10.78, Φ_1^* = 2.93·10^{-3} $h^3.Mpc^{-3}$, Φ_2^* = 0.63·10^{-3} $h^3.Mpc^{-3}$, α_1 = -0.62 and α_2 = -1.5 [354].
Following the approach of [355, 336] regarding the luminosity function, we divided galaxies into 12 luminosity distance shells, with a width of 33.3 Mpc. For each

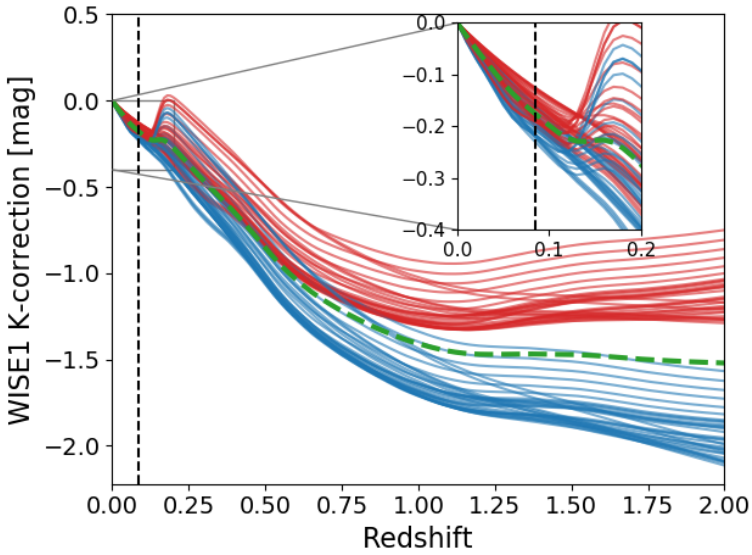

Figure 5.8: K-correction for 31 galaxies SED templates for the redshift ranging from 0 to 2 with a zoom-in from 0 to 0.2. The blue solid lines are for the SED templates without dust attenuation, red solid lines are with a dust attenuation of $E(B-V)$=0.5 mag using the Calzetti law [352]. The green dashed line is the mean value at a given distance of the K-correction for all the galaxies SED considered in this study. The black dashed line corresponds to 400 Mpc.

shell, we construct histograms of WISE1 band derive stellar mass and integrate the double Schechter function for the same stellar mass bins in figure 5.9. As the luminosity distance increases more and more, low mass galaxies are missing. Regarding the double Schechter function derived from GAMA, the new catalog is fairly complete up to 33 Mpc. In this work, we are interested in the more massive galaxies, so we computed the stellar mass, $M_{1/2}$, for which half of the logarithmic stellar mass density is contributed by galaxies below and above this value. By computing $\int_{\log M_{1/2}}^{13} \log M \Phi(M) d \log M = 0.5 * \int_{7}^{13} \log M \Phi(M) d \log M$, we find $\log M_{1/2} = 10.674$. For all the luminosity distance shells, the Mangrove catalog distribution follows the double Schechter function for $\log M > \log M_{1/2}$ as seen in figure 5.9. Our method is prioritising the more massive galaxies, consequently the completeness relative to the double Schechter function for galaxies at $\log M > \log M_{1/2}$ minimises the lack of low mass galaxies as the distance increases.

Validation using the GW170817 event

To date, the 17th August 2017 event is the only gravitational wave event with a detected electromagnetic counterpart, so our new method has to be tested on this event. The GW170817 released distance is 40 ± 8 Mpc, the 90% skymap spans around 30 deg^2 and as shown in figure 5.6, according to our criteria, there are 65 compatible galaxies. Table 4 shows the results for this event on the selection of galaxies and their ranking according to the standard approach (equation 5.1), according to the grade using B band luminosity [321], according to our method with a product (equation 5.3) and according to our method with an addition (equation 5.4). The NGC4993 host galaxy of GW170817 is ranked in the 5th position with the standard approach. The grade using B band luminosity [321] improved its rank to the 2nd position and is ranked first with our method for both (equation 5.3) and (equation 5.4) expressions. This comes from the fact that NGC4993 is more massive than the galaxies ranked at the few first positions with the standard grade (see table 4 for details). These results show that if we had used our grade to monitor this event, there would have been a gain in the speed of observation of the host galaxy. An important thing to see in those results is that the new grades are behaving as expected i.e. galaxies with high stellar masses are prioritized compared to galaxies with small stellar masses (see table 4 where the list of galaxies for the four methods are reported with their grade and stellar masses if used). We also stress that galaxies with a high 3D probability but without stellar mass information also appear in the list (see table 4). For instance, galaxy WINGSJ125701.38-172325.2 is ranked in the 9th position. Keeping such a host candidate is a real improvement of equation 5.4 compared to equation 5.3.

The GW170817 event localisation was relatively good thanks to the distance of

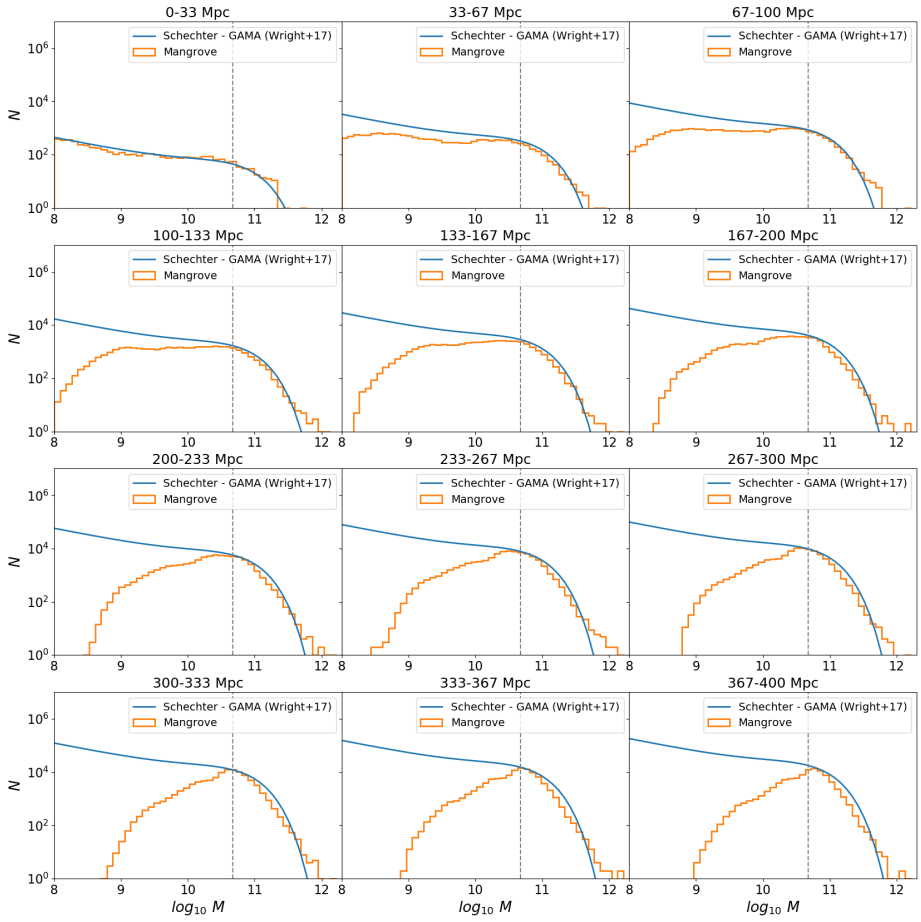

Figure 5.9: Stellar mass histograms for the Mangrove catalog at different luminosity distance shells compared to the double Schechter function derived from GAMA [354] weighted by the volume of each shell. Each panel is divided in 50 bins of $logM$. The black dashed line represents the stellar mass, $\log M_{1/2}$ for which half of the stellar mass density is contributed by galaxies at $\log M > \log M_{1/2}$.

the source and the availability of data from the three gravitational wave detectors. However, as the three inteferometers are not always in operating mode, this is very common to have a two inteferometer detection resulting in a poorer localisation [356]. In order to test our method on a larger skymap, i.e. a two inteferometer event, we choose to use the GW170817 skymap without Virgo data. The 90% skymap spans ~ 190 deg^2: this is a good example of two gravitational wave detector localisation for which we can be sure of the counterpart host. According to our criteria, there are 205 galaxies compatible with this skymap. Table 5 shows the resulting ranking for this skymap using the four presented grades. The NGC4993 galaxy hosting the event is ranked in the 27th position in the standard approach. The grade using B band luminosity [321] ranks it at the 6th position and our grade is even more successful by putting NGC4993 in the 4th position with both equations 5.3 and 5.4 expressions. Those results show that the gain of our method to follow up gravitational waves events is even bigger in the case of wide a skymaps. This example of wider skymap allows us to see that sometimes the grade using B band luminosity and our grades behave differently and even oppositely. For example the galaxy PGC043966 is ranked in the 37th position with the standard grade, while the grade using B band luminosity raise its rank to the 30th, both of our grades (equations 5.3 and 5.4) downgrade its rank to the 54th and 49th position respectively. We can also note that the grade using B band luminosity ranked the NGC4658 galaxy in first position due to his high B band luminosity but this galaxy is ranked in position 8 with our final grade definition. For these two examples, the stellar mass estimation is not as high as the B band luminosity might suggest. Using the B band luminosity in those cases would have led to observe preferentially less massive galaxies. We illustrate the difference in the behavior between our grade and the one using B band luminosity from [321] in figure 5.10, where we plot the stellar mass estimation using WISE1 band as a function of the B band luminosity for the same galaxies. We see that for a given B band luminosity there is an important scatter in stellar mass spanning a few orders of magnitudes. It means that the probability associated to a galaxy with respect to its stellar mass estimation can behave very differently for both methods. For example, for the host galaxy associated to GW170817, NGC4993, we derived a stellar mass of $\sim 2.14 \times 10^{10} M_\odot$. But galaxies with similar B band luminosity ($\sim 10^{10} L_\odot$) in the catalog span a stellar mass range from $\sim 3.8 \times 10^7 M_\odot$ to $\sim 1.0 \times 10^{12} M_\odot$ which represents almost five order of magnitudes. This highlights, assuming that our derivation of the stellar mass is reliable, that the B band luminosity is a poor indicator of the stellar mass and explains the different behaviour between our grade and grade using B band luminosity. In addition to this different behavior, we also illustrate the flexibility of the grade defined in equation 5.4 by noting that using the grade defined in equation 5.3 would have led not to use $\sim 7\%$ of the galaxies

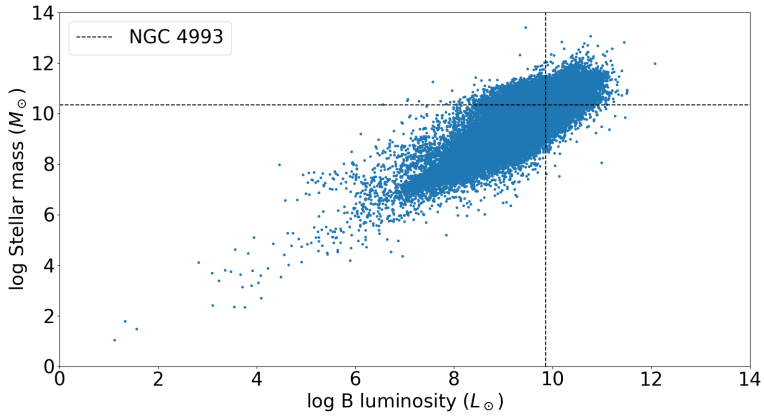

Figure 5.10: B band luminosity provided by GLADE as a function of the stellar mass determined with the constant mass to light ratio using the W1 band. The crossing of the dashed lines shows the NGC4993 (host of GW170817) position on this plot.

inside the 400 Mpc of the Mangrove catalog, and $\sim 5\%$ of the galaxies when using the B band luminosity as in [321].

5.3.1 Use of the galaxies for the tiling

As presented in previous sections, for the optimisation of wide FoV telescope ($\gtrsim 1deg^2$) follow up observations the standard approach consists in defining tiles over the sky and rank them according to a given grade [316, 357]. A first version of the grade of a tile one can build is:

$$Grade_{tile} = \sum_{pixel \in tile} P_{pixel} \tag{5.8}$$

where we sum up the 2D probability of the pixels $P_{2D,pixel}$ within the tile. When using a catalog of galaxies one can define a "galaxy weighted" grade for the tile using the grade of the galaxies:

$$Grade_{tile} = \sum_{gal \in tile} Grade_{gal} \tag{5.9}$$

where we sum up the grade of the galaxies within the tile. In this expression any galaxy grade can be used, such as the expression in equation 5.4 that will optimise the chance to find the GW electromagnetic counterpart. The biggest

issue of this approach is the catalog completeness. Usually, the approach used is to define a distance threshold above which the completeness of the catalog is high enough to use the equation 5.9. Then, Above this threshold one has to switch back to equation 5.8 in order to prevent using only galaxy information at a distance where the catalog is not complete enough. We present a reformulation of the tile grade using our developments which allows to use galaxy catalogs and a galaxy weighted grade at any distances. As presented before, we are able to define the mass completeness of the catalog, $C^{d1,d2}_{m1,m2}$, between distances d_1 and d_2 for a stellar mass range between m_1 and m_2 compared to the double Schechter function:

$$C^{d1,d2}_{m1,m2} = \frac{\int_{m1}^{m2} M_* \; catalog(M_*) \; dM_*}{\int_{m1}^{m2} M_* \; f_{Schechter}(M_*) \; dM_*} \tag{5.10}$$

With this parameter defining the completeness, we can define the grade of a given tile by:

$$G_{tile} = \sum_{pixel \in tile} \left[\sum_{gal \in pixel} C^{d1,d2}_{m1,m2} G_{tot,gal} + (1 - C^{d1,d2}_{m1,m2}) P_{pixel} \right] \tag{5.11}$$

where the first sum over all pixels inside the tile, the second sum over all compatible galaxies falling in the 2D location of the pixel. $G_{tot,gal}$ is the grade of a given galaxy defined in Section 5.2.3, P_{pixel} is the 2D probability of the pixel, d_1 and d_2 are chosen as $\mu_{pixel} \mp \sigma_{pixel}$ respectively and m_1 and m_2 are fixed to 10^7 and 10^{13} (stellar mass range validity of the Schechter function fitted by [354]). This expression removes any distance limitation for the use of galaxies weighted tiles. Note that with this expression we simply sum up the probability of the galaxies within a tile when the catalog is complete, whereas we sum up the 2D probability of all pixels within a tile when the catalog is not complete. With the expression of $C^{d1,d2}_{m1,m2}$ one can compute the completeness in terms of mass for the whole catalog (from 0 to 400Mpc) which is $\sim 50\%$. Note that the completeness in terms of mass is 100% for up to ~ 40 Mpc.

Mangrove tools available for the community

In a general way we wanted to make the tools developed for the galaxy targeting strategy widely open for the community. As said before the whole strategy is implemented within the `gwemopt` open-software [316]. Furthermore a dedicated website[6] was built to provide tools needed to achieve galaxy targeted observation with the strategy presented above. On this website one can download the full Mangrove catalog. Any user can use the web interface to download the list of

[6] `https://mangrove.lal.in2p3.fr/`

compatible galaxies, ranked by our grade, for each compact binary coalescence event below 400 Mpc. In addition the user can add its observational configurations and limitations (latitude, longitude, elevation, horizon, distance to the Moon, maximum airmass) to fetch only the galaxies observable from its observation site at the time of its choice. Finally, during O3, for each event below 400 Mpc a GCN was sent to provide to the community the list of most compatible host candidates from the Mangrove catalog, see for instance [358].

5.4 GRANDMA and SVOM observations during the O3 run

The observation strategies presented in the previous sections were used by the GRANDMA and the SVOM (ground telescopes) during the O3 LIGO-Virgo-KAGRA run. During my thesis I actively participated for both collaboration to the follow-up of the O3 run. My main contributions are the development and production of the observation plans, the participation to the follow-up advocates shifts (supervisor dedicated to monitor the follow-up of events, see [315] for details) and the production of GCNs, their wording, automation and submission.

During O3 GRANDMA followed up about 90% of the gravitational-wave candidate alerts, i.e. 49 out of 56 candidates. This shows how effective a telescope network can be in responding to alerts in comparison with a single observation site which can be much more affected by its observational constraints (weather, observability, maintenance...). GRANDMA also excelled in its ability to respond very quickly to alerts. The network performed its first observation at most 1.5 hours after the gravitational wave trigger time for more than half of the alerts, and at most 30 minutes for 15 % of the alerts during O3. The minimal delay between a gravitational wave trigger and a first observation was $\sim$ 15 min, which includes $\sim$ 5 min of delay by the LIGO-Virgo-KAGRA collaboration to send the alert and $\sim$ 5 min for the computation of the observation plan. These very high performance in the response of the alerts was in particular achieved thanks to the two robotic networks TAROT and FRAM included in GRANDMA and using wide FoV observations to search for very early optical counterpart [309]. During O3, over 9000 deg^2 was covered by the GRANDMA network with an average of $\sim$ 213 deg^2 per gravitational wave alert and more than 100 deg^2 for more than half of the alerts. An example of what GRANDMA can achieve in terms of follow-up is presented in figure 5.11 for the S200213t gravitational wave candidate. In this example the complementarity between the tiling telescope and the galaxy targeting telescope is visible. During O3, and for almost all the gravitational wave alerts, the GRANDMA observations have been reported via GCN to the community to

provide counterpart candidates or upper limits on detection. Unfortunately, the GRANDMA near real-time analysis did not find any interesting kilonova or interesting transient candidates [309]. As presented in figure 2 of [309], the median distance of O3 BNS merger candidate is $\sim$ 200 Mpc and 1.3 Gpc for BBH merger. Considering an apparent limiting magnitude of 17, this corresponds to an approximate absolute magnitude non-detection limits of -19.5 for BNSs and -23.6 for BBHs [309].

The most promising event of O3, followed by GRANDMA, to derive constraints on transients is S200213t. Numerous GRANDMA telescopes searched for a kilonova counterpart to this event. The largest sky area was observed by the telescopes using tiling strategy, i.e the OAJ telescope (about 18% of the skymap probability with a limiting magnitude of r'>20.1) and the TAROT telescopes (about 30% of the skymap probability with a limiting magnitude of 18 in CR band). Furthermore, a number of individual galaxy-targeted searches also reached limiting magnitudes around 18 (see table 5 of [309] for a list of all the observations). Even taking as assumption that TAROT (which achieved 30% coverage of the relevant sky area) or OAJ (which achieved 18% coverage of the relevant sky area) covered the relevant sky location, GRANDMA observations are not able to derive a constraint on the ejecta mass. Even very large ejecta masses of the order of $\sim 0.4 M_{\odot}$, that are typically disfavoured by numerical-relativity simulations [359], cannot be ruled out (see figure 5.12). For comparison, the ejecta mass of GW170817 is estimated to be $\sim 0.05 M_{\odot}$, i.e., about one order of magnitude smaller.

The O3 follow-up from the SVOM ground segment was performed with the F30, F60 and GWAC telescopes (see section 3.3). In total $\sim$ 17 alerts were followed up and $\sim$ 15 GCNs reporting the observation were sent. Thanks to his very large FoV (5400 square degrees), the GWAC telescopes was very efficient to observe wide skymaps with maximum of 95% of it observed for a given event (the BBH event S190412m with 156 deg^2 90% skymap). The smallest time delay achieved between the gravitational wave trigger and the first image is $\sim$ 1h. The F60 telescope, using galaxy targeting approach, achieved a maximum of $\sim$ 500 galaxies observed for a given alert (the BNS alert S190901ap). The typical limiting magnitude of these observations was 16 mag in the R band for GWAC and 17 mag in the R band for the F30 and F60.

The *kilonova-catcher* citizen science program

Alongside with the main GRANDMA network, the GRANDMA collaboration developped, since the beginning of O3, a citizen science program called *kilonova-catcher* [360]. For O3, a total of 33 kilonova-catcher users around the globe registered to the GRANDMA alert stream. During O3 I was in charge of the production

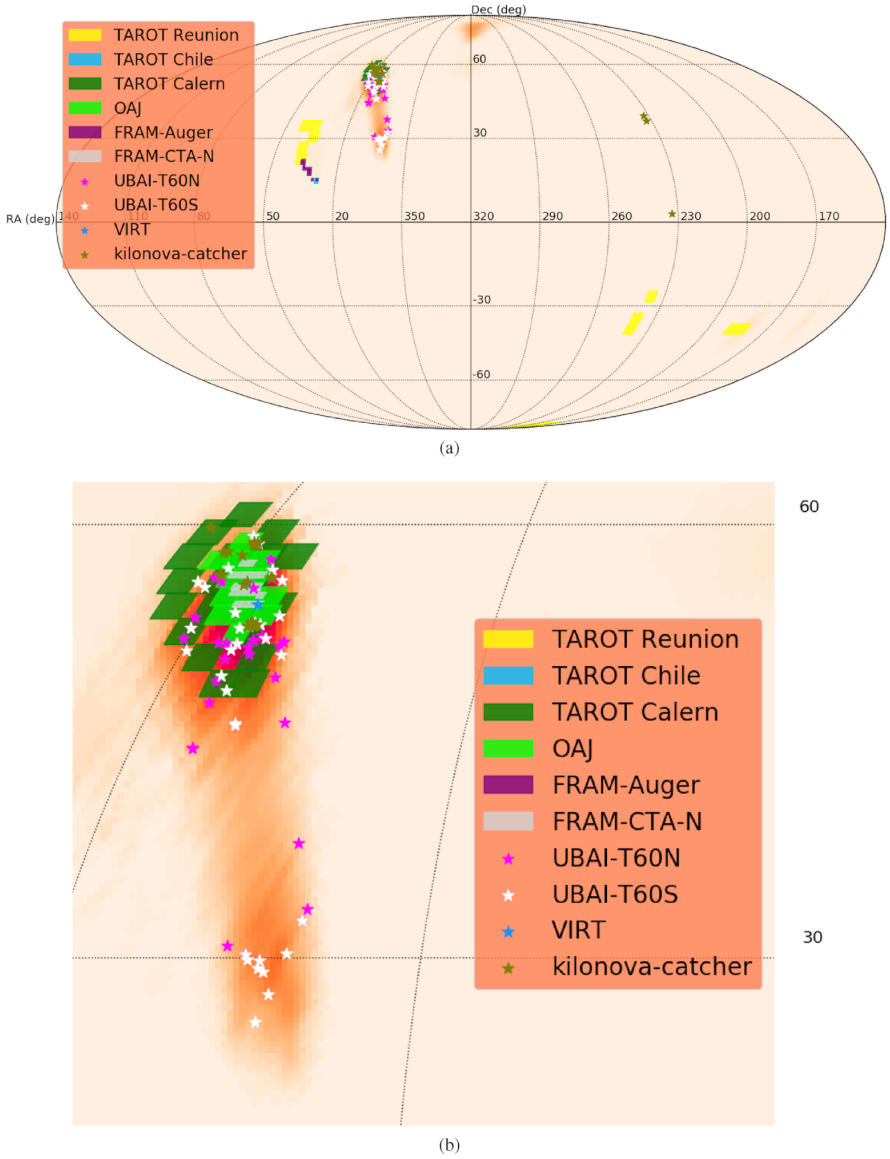

Figure 5.11: GRANDMA follow-up of the gravitational wave candidate S200213t: a BNS merger. Yellow, blue and dark green tiled areas represent tiles observed by the TAROT network. Purple and grey tiled areas represent tiles observed by the FRAM network. Light green tiled areas represent tiles observed by OAJ. In red, the `LALInference` sky localisation area of S200213t is shown. We note that TAROT Reunion tiles covered 193 deg^2 yet only 1% of the final localisation probability. Stars represent galaxy-targeting fields obtained by UBAI and VIRT (several days after the gravitational wave trigger time) and the citizen science program *kilonova-catcher* (with first images taken a few hours after the gravitational wave candidate trigger time). Figure from [309].

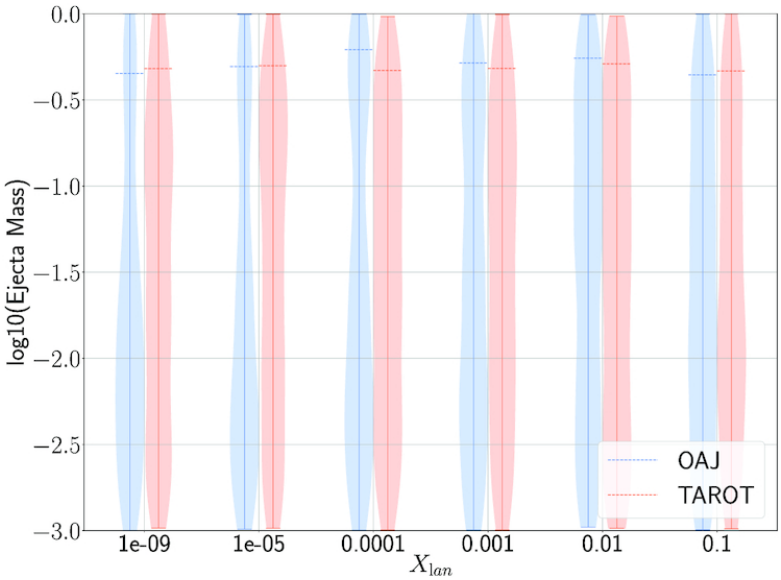

Figure 5.12: Constraints on the ejecta mass in terms of lanthanide fractions X_{lan} for the BNS candidate S200213t based on the OAJ and TAROT observations. The thickness of the vertical bands represents the probability density for this particular ejecta mass. Thick regions mark more probable regions of the parameter space, thin regions less probable ejecta masses. For lower lanthanide fractions X_{lan} observations are able to disfavour high ejecta masses, while for large lanthanide fractions no real constraints can be extracted. The 90% upper limits are marked as horizontal dashed lines, where one can see that for most scenarios upper bounds are reflecting the prior. Figure from [309].

of the observation plan for all of these users. Mainly because the kilonova-catcher members uses narrow field of view telescopes, we chose to use the tool developed within the Mangrove galaxy targeting strategy presented in section 5.2.2. For O3 the kilonova-cather program was active mostly during the follow-up of two BNS merger candidates S191213g and S200213 (with implication on the validation of some transients) for a total of ~ 60 images with limiting magnitude up to ~ 20 (mostly with clear filter). I participated to the analysis of an important portion of those images using the tools presented in 5.2.1. Although this first collaboration with amateur astronomers proved its ability to respond to alerts quickly and efficiently and their ability to provide very good quality images, no interesting transient was found in any of these images. To date there is more than 100 kilonova-catcher users registered and we expect more than 200 for O4.

5.5 SVOM satellite follow-up optimisation

During my thesis I was in charge of the simulation of the observation plan for the SVOM-MXT telescope in case of gravitational wave alert follow-up. These simulations are used, in prevision of the mission, to test the strategies proposed for the follow-up of gravitational wave alerts and quantify the capacity to detect a counterpart. This work is specifically important for a space mission such as SVOM because the follow-up properties (number of alerts followed, number of slew, exposure time, total time allocated for the follow-up...) are limited by the spacecraft platform and the program of the mission. The principal instrument used for such follow-up is MXT with its relatively wide FoV. MXT is expected to detect the X-ray afterglow up to ~ 1 day after the initial prompt emission. All the developments previously presented were used to produce these simulations, the improvements relative to these developments (already presented) will not be described in this section. Instead, in the following, I will focus on the following question: should SVOM-MXT telescope use the tiling strategy or the galaxy targeting strategy for its observations? Indeed the MXT FoV (~ 1 deg^2) is in a range where this choice is not obvious (see figure 5.1 for illustration).

In order to determine which strategy is the most efficient, I carried out the simulation of many observation plans . I selected a set of 15 gravitational wave skymaps, 8 true alert skymaps published by LIGO-Virgo-KAGRA (GW170817, GW170817 without Virgo data, S190425z, S190718y, S190814bv, S190901ap, S191213g, S200213t) and 7 mock skymaps provided by LIGO-Virgo-KAGRA (MS191219a, MS191221a, MS191221b, MS191221c, MS191222a, MS191222o, MS191222t). All of them are selected to be with a mean distance plus standard deviation below 400 Mpc to fit with the requirement to use the Mangrove catalog (see section 5.3). They are also chosen to represent the variety of sky localisations provided by the gravitational

wave detectors alone, with 2 or 3 detectors like skymaps (see section 5.1). The observation plan was produced using the `gwemopt` software, but it was meant a priori to produce plans for ground based observatories and not a satellite. During my thesis I implemented within `gwemopt` the tools necessary to produce plans for the SVOM satellite observation. This can be roughly resumed in getting rid of the ground observations limitation (horizon, azimuth...) and adding the limitation required by the SVOM observations which are mostly Sun and Moon occultations. Furthermore, to take these satellite limitations into account in a robust way, for each skymap the observation plan was produced as if the alert was triggered at 10 different GPS time randomly drawn. The results are then obtained averaging over the GPS times.

The resulting mean cumulative distribution of number of observed galaxies and observed probability (defined as in equation 5.9) are presented for each skymap in figures 23 to 52. The comparison between the two strategies is resumed in figures 5.13 and 5.14 which present the difference between the mean number of galaxies (quantity of grade) observed with galaxy targeting strategy and the mean number of galaxies (quantity of grade) observed with the tiling strategy, normalised by the maximum of observed galaxies (quantity of grade). In one hand, there is no clear evidence in figure 5.13 for an advantage of any of the strategy in terms of number of galaxies observed. On the other hand, figure 5.14 clearly shows the optimisation of the amount of grade observed with the galaxy targeting strategy. This comes from the fact that the galaxy targeting strategy is "free" in the way it set its tiles on the sky and it is more efficient in encompassing very interesting galaxies in the same tile while the tiling strategy is "stuck" by its pre-computed tiling of the sky. The result in terms of observed grade is the one that is decisive as it is set up to quantify how likely one will find a counterpart. In conclusion these simulations show that the MXT FoV is still in a range where it can benefit from the galaxy targeting approach for the follow-up of gravitational waves. Furthermore the inboard VT, observing the center of the MXT FoV, will benefit from the galaxy targeting strategy as it will basically ensure that there is at least on interesting galaxy in the VT FoV. For this simulation the exposure time of the MXT telescope is set to 10 minutes for each pointing. Further work will needs to study the speed/depth balance to optimise the chance to detect the source. Moreover, Further work will have to deal with the slew limitation of the satellite platform as optimised strategy may leads to more slew distance.

Figure 5.13: Difference between the mean number of galaxy observed with galaxy targeting strategy and the mean number of galaxy observed with the tiling strategy, normalised by the maximum of observed galaxy.

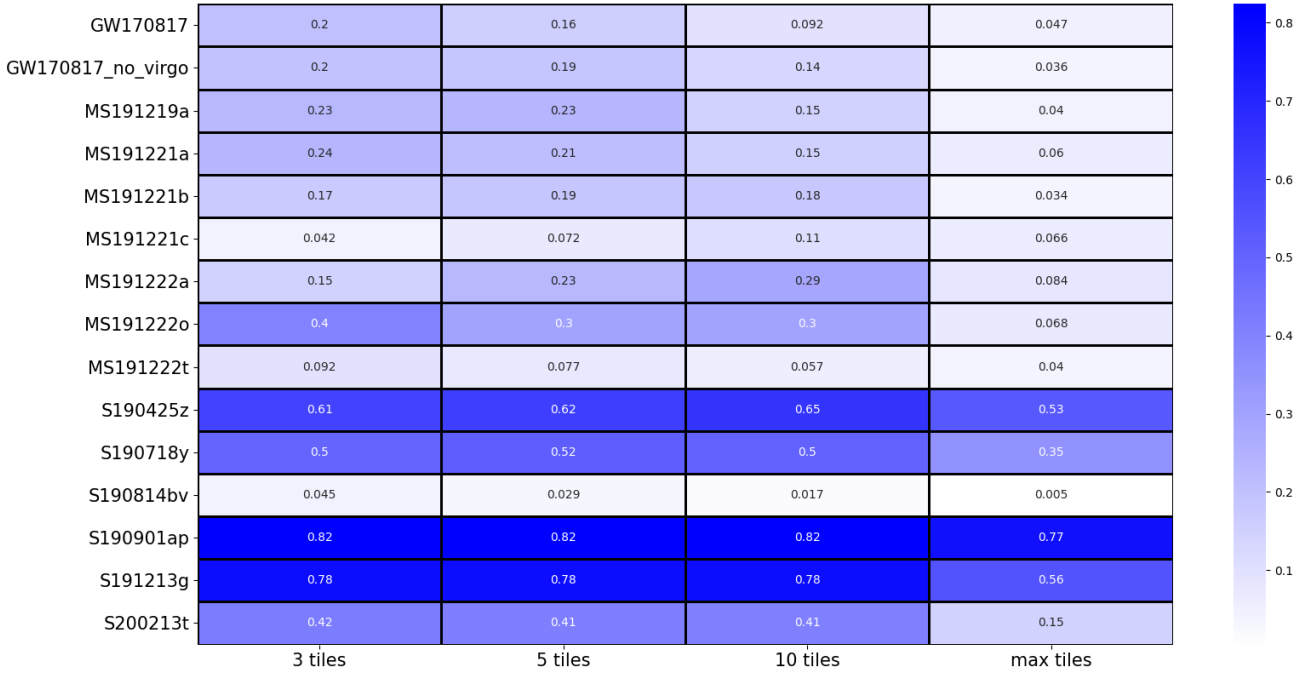

Figure 5.14: Difference between the mean quantity of grade observed with galaxy targeting strategy and the mean quantity of grade observed with the tiling strategy, normalised by the maximum of observed quantity of grade.

5.6 Study of short GRB host galaxies

In this section I present the study of short gamma ray burst host galaxy population I worked on during my thesis. This study aims to update the previous results available in the literature (see section 3.6.2), the latest compilation being almost ten years old. The selection of the sample of short gamma ray bursts, presented in the following, is based on high energy criterion and the identification of the host galaxy is based on a new association code, also presented in the following. Properties of the galaxies, such as stellar mass and SFR, will be inferred through SED fitting algorithm for the whole sample (leading to an homogeneous determination of the properties). The ultimate goal is to use these properties to optimise the gravitational wave follow-up (as presented in section 5.2.3).

The work presented in this section will lead to a more exhaustive publication (Corre, Ducoin et al. in prep.). The compilation of the GRBs, the association with host galaxy, the compilation of the host data, the SED fitting and the determination of the host properties have been already performed.

5.6.1 Short GRB sample

To select short GRBs we use the classical criteria based on the T_{90} duration as described in [361, 244]. The short GRB T_{90} distribution does not exhibit an abrupt cut at 2s, there are some short GRBs with a $T_{90} > 2$ s. In order to catch those, we start from the BAT catalog[7] selecting GRBs with $0 \leq T_{90}$ - $T_{90\ err} \leq 2$s, which corresponds to 138 GRBs. For the GRB whose classification short/long is not clear, the properties that we will infer later with the SED fitting might help to classify some GRBs. To build our short GRBs sample we also include the 13 short GRBs with extended emission as flagged in [361], as well as the 26 GRBs flagged as possible short GRBs with extended emission. We also included two short bursts detected by HETE-2 (GRBs 050709 and 060121 [222, 362, 363, 364]), one detected by INTEGRAL (GRB070707, [365, 366]), and one detected by Fermi GBM (GRB 170817A, [146]). This represents a total of 181 GRBs.

5.6.2 Association with host

The association between a given GRB and its host galaxy is a very complex issue especially when there is no optical or radio afterglow detected to provide a sub-arcsecond localisation. This association is made by estimating the chance alignment between a given GRB localisation and nearby galaxies [253, 255, 367]. Within this work the probability of chance alignment for a given GRB and a given

[7] https://swift.gsfc.nasa.gov/results/batgrbcat/

galaxy i is expressed as:

$$P_i = 1 - e^{-\pi r_i^2 \sigma(\leq m_i)} \tag{5.12}$$

where r_i is the angular distance between the GRB localisation and the galaxy center, $\sigma(\leq m_i)$ is the number of galaxies per arcsecond square having a magnitude below m_i (magnitude of the galaxy i). The galaxies are taken from survey catalogs. In this study we rely on the Pan-STARRS catalog [368], the Hubble Source Catalog (HSC) [369] and the AllWISE catalog [344]. The Pan-STARRS and HSC catalogs provide a good resolution and a relatively deep photometry, two essential properties for the chance alignment estimation, but none of them is all-sky. The Pan-STARRS catalog is limited to -30 deg in declination and the HSC one is a visit-based discontinuous catalog. The AllWISE catalog [344] on the other hand has the advantage of being all-sky but with worse resolution and depth. In the case where no association is made with a galaxy of these surveys, but an association is made in the literature we provide the chance alignment association from the literature. In order to compute the σ parameter we chose to follow the principle proposed by [367] which is based on a local estimation of the galaxy density in a given catalog, this allows to take into account clustering which is not the case if σ is estimated on a whole catalog or using deep optical galaxy surveys as in [370, 248].

For the Pan-STARRS and AllWISE catalogs, we first fetch all galaxies within a 30 arcseconds radius centered on the GRB localisation center (candidate galaxies). Then in order to estimate the galaxy density we fetch all galaxies within a 3 arcminutes radius from the GRB position center where we remove the candidate galaxies not to bias the estimation of the local galaxy density. For each candidate galaxy i and for each photometric band in the catalog we can then compute the $\sigma(\leq m_i)$ counting the number of galaxies, within the shell from 30 arcseconds to 3 arcminutes, with magnitude $\leq m_i$. In order to discard stars from catalogs, for the Pan-STARRS catalog we apply the color criteria $(imag_{PSF} - imag_{Kron}) \geqslant 0.05$ up to a magnitude of 21 as proposed by [368]. For the AllWISE catalog, we used the color criteria $W1_{mpro} - J_{2MASS} < 1.7$ (in the range of $12 < W1_{mpro} < 15$) proposed by [371] to select galaxies. For both catalogs, if the photometry is not sufficient or available for a given object to apply these color criteria, we decide to keep such objects as it will lead to a slightly over estimation of the galaxy density, i.e. penalise the alignment chance probability and hence harden any significant association.

For the HSC, we follow the same procedure but as the all-sky coverage is sparse and discontinuous we modify the way galaxies used to compute the galaxy density are retrieved. We identify in each band of the catalog in which image lies the GRB localisation and use all the galaxies within this image. Knowing the field of view of the catalog images (202×202 arcseconds square) we have a cross-matched area

which is comparable with the 3 arcminutes radius area used for Pan-STARRS and AllWISE. In order to identify galaxies in the HSC we simply used the extended flag provided.

Finally, for each galaxy we only keep as final P_i in each catalog the photometric band which provides the lowest P_i.

Chance alignment threshold

In order to identify good host galaxy candidate in the light of the chance alignment computation we need to define a threshold in P_i below which we can consider a galaxy as the GRB host galaxy candidate. We chose to first compute the P_i for a subset of GRB, a golden sample, where there is an evidence not based on chance alignment computation (afterglow spectrum/redshift, kilonova detection, afterglow britghtness...), for the host association in the literature. The golden sample is composed by GRB 050509B [372, 224, 251], GRB 050724 [373], GRB 061006 [374, 251], GRB 090510 [375, 125], GRB 100117A [239], GRB 130603B [125, 230], GRB 140903A [376] and GRB 150101B [377, 378].

On this golden sample, we find that the GRB host galaxy always has a $P_i \leq 0.02$ in at least one photometric band from catalogs while other galaxies have a $P_i > 0.02$. For cases where the host galaxy is not present in Pan-STARRS, HSC or AllWISE catalogs (too faint or contaminated by a foreground star as for GRB 140903A), all other galaxies have a $P_i > 0.02$. We conclude that a threshold of 0.02 allows to separate interesting and uninteresting host galaxy candidates.

When several photometric bands from different catalogs provide a $P_i \leq 0.02$ we visually inspect that it corresponds to the same galaxy. If more than one host galaxy candidates has a $P_i \leq 0.02$, we only assign the host galaxy candidate with the lowest P_i to the GRB if the other galaxies have a P_i ten times higher, i.e. we do not make the host galaxy association if two galaxies have comparable chance of alignment, that are < 0.02.

Reliability of the chance alignment computation

The key for associating a host galaxy to a GRB is the localisation accuracy of the GRB. If an optical or radio afterglow is detected then the localisation accuracy is at sub-arcsecond level, whereas if only the X-ray afterglow is detected the localisation accuracy is few arcseconds and if no afterglow is detected the localisation accuracy can reach few arcminutes. This affects the P_i computation through the uncertainty on the parameter r_i in equation 5.12 which corresponds to the angular distance between the GRB localisation center and the galaxy center. To study the reliability of chance alignment computation for GRB localisation accuracy higher

than sub-arcseconds, we select GRBs with a detected optical/radio afterglow, i.e. a sub-arcsecond localisation accuracy, and compute the chance alignment using the GRB position from X-ray measurement. For all GRBs the preferred host galaxy candidate remains the same and no new galaxy candidate have a $P_i \leq 0.02$. We conclude that this method of chance alignment computation is robust enough even with few arcseconds GRB localisations. This is not case for GRB localisation of few arcminutes, so we require to have at least an X-ray detection for a robust host galaxy association. After applying this criteria, 139 GRBs remain. Finally, adopting the threshold of $P_i \leq 0.02$ we find 46 galaxies that are associated to a GRB (see table 6). 6 galaxies are below the threshold but at least another galaxy is also below the threshold with a P_i less than ten times the one of the preferred galaxy. The results of the chance alignment computation for the associated host are showed in table 7. For 8 of the galaxies shown in table 7 no P_i are available, these are associations proposed by the literature (see references in the table) which we kept because the afterglow position lies within the extent of the proposed host. For these proposed hosts we do not have a P_i to confirm the association because the proposed host is to faint for the catalogs we are using (or no image is available at the proposed host position for Pan-STARRS/HSC).

5.6.3 GRB host photometry

In this study we intend to infer physical parameters of short GRB host galaxies using a SED fitting technique. In order to obtain reliable estimate of the physical parameters such as the stellar mass and the star formation rate (SFR) we require that a galaxy has photometric measurements in at least 5 photometric bands covering from the UV to NIR rest-frame, with at least one detection above 1500 nm rest-frame to help constrain the stellar mass estimation.

During my thesis I have widely participated to the compilation of the GRB host photometry. This is a very time consuming work where we looked at each GRB one by one and collected the data from the various catalogs (making use for instance use of the *Centre de Données astronomiques de Strasbourg*[8] and the *NASA Infrared Science Archive*[9]). For each catalog the photometric error and data quality flags are checked in order to select the most reliable data. When available, all catalog images are checked by eye to visually inspect the associated object (confirm the object association, prevent the use of any photometric data which contains critical contribution of more than one object...). For each GRB we also compiled the available data in the literature, papers and GCNs, and crosschecked if any source proposes the same host or any other host. Any compiled data are

[8]https://cds.u-strasbg.fr/
[9]https://irsa.ipac.caltech.edu/

converted in the standard calibration system, check for Galactic extinction and corrected in a same manner using [379]. All of this usually can take hours to days for each of the GRB with a proposed association.

Among the 46 galaxies that are associated (see table 6 for a list and their properties) the requirement of at least 5 photometric bands is fulfilled by 37 galaxies, with 3 of them whose classification short/long is not clear (see table 6 or 7). Table 10 presents the compiled GRB host photometry used for the SED fitting presented in the following section.

5.6.4 SED fitting procedure

In order to determine the galaxies properties in an homogeneous way we chose to use a SED fitting algorithm in the whole sample. The SED fitting is performed with the version v2018.0 of the `CIGALE` code (Code Investigating GALaxy Emission)[10]. CIGALE combine a UV-optical stellar SED with a dust component emitting in the IR and fully conserves the energy balance between dust absorbed emission and its re-emission in the IR. Star formation histories as well as dust attenuation characteristics, including the attenuation law, are input parameters that can be either taken free or fixed according to the available data or the specific aims. The main characteristics of the code are described in [380]. Within CIGALE a large grid of models is fitted to the data to estimate the physical properties through the analysis of the likelihood distribution. The choice of parameters used in this work is presented more in detail in appendix 5.6.6.

5.6.5 Results of the fits

Figures 54 to 90 present the best-fitted SED obtained for each one of the short GRB host. Table 9 presents the summary of the SED fitting results for our short GRB hosts sample. Figure 5.15 presents the stellar mass, SFR and specific SFR (sSFR; SFR/M_*) distributions obtained with the SED fitting. In order to compare our results with previous works we represented in the figure 5.16 the comparison of the obtained stellar mass for each GRB host in common with [326]. For the whole sample, the obtained stellar mass are compatible to those obtained in [326]. Figure 5.17 presents the comparison of the stellar mass distribution for [326] sample and our sample. Both distribution present a similar trend, the widening of the sample proposed in this work widely extend the statistic of this distribution.

In figure 5.18, we report the position of the short GRB hosts on the SFR-Stellar mass relation in comparison to the Main Sequence. Most of the short

[10]http://cigale.lam.fr

GRB hosts are below the Main Sequence, especially the more massive. In order to clarify this tendency and precisely locate the position of the short GRB hosts on the Main Sequence, we report in figure 5.19 the excess of SFR of our short GRB hosts compared to the Main Sequence as parametrised in [204], computed at the redshift of the corresponding short GRB host. In figure 5.19 the galaxy classification follows the sSFR cut suggested by [242] (figure 6). About 2/3 of the galaxies are classified as intermediate or quiescent. By opposition long GRBs host at $z < 1$ are composed of young star-forming galaxies [381]. Figure 5.20 presents the position of the short GRB hosts on the SFR-Stellar mass relation for various redshift bins and the comparison with the field galaxies (COSMOS2015, [382]). The figure 5.20 shows that the short GRB hosts appear to be more passive than the field galaxies. While some hints of an evolution with the redshift may be visible, the poor statistic at the highest redshifts does not allows to conclude.

Offset

In order to study the location of short GRBs with respect to their host galaxy we computed the distribution of projected angular offset, as we have an estimation of the redshift for the whole sample by construction (see section 5.6.1) we computed from the angular offset the projected physical offsets. As shown in figure 5.21 the range of offset is $\sim$ 1-80 kpc with a median of about 8.38 kpc. For comparison we show in figure 5.21 the short GRB sample from [125], both distribution look similar. In figure 5.21 we also show the predicted distribution from population synthesis model of BNS merger from [256], we display the distribution obtained with velocity kick within $95-270$ km/s, with galaxy circular velocity equal to 100 km/h and $M_{\odot}$ equal to 0.278×10^{11} as it fits the best our offset median and stellar mass sample (see section 5.6.5). Figure 5.21 also shows the long GRBs [253], core-collapse SNe and type Ia SNe [254] cumulative distributions. A Kolmogorov–Smirnov test between our short GRBs sample and [125] short GRB , long GRBs, core-collapse SNe and type Ia SNe samples gives a pvalue of ~ 0.52, $\sim 1.4 \times 10^{-4}$, $\sim 4.51 \times 10^{-5}$, $\sim 6.4 \times 10^{-4}$ respectively. This comforts the assumption that only the [125] short GRBs sample follow the same distribution.

5.6.6 Gravitational wave follow-up

As I presented in section 5.2.3, one can use the galaxy properties in order to optimise the galaxy targeting strategy used for the follow-up of gravitational wave events. Supported by the association of short GRBs and gravitational waves from GW170817, one could try to use the inferred properties of the short GRB hosts in order to optimise such gravitational wave event follow-up. Figure 5.22 shows the 2D Kernel density estimation on the SFR-Stellar mass relation for our short GRB

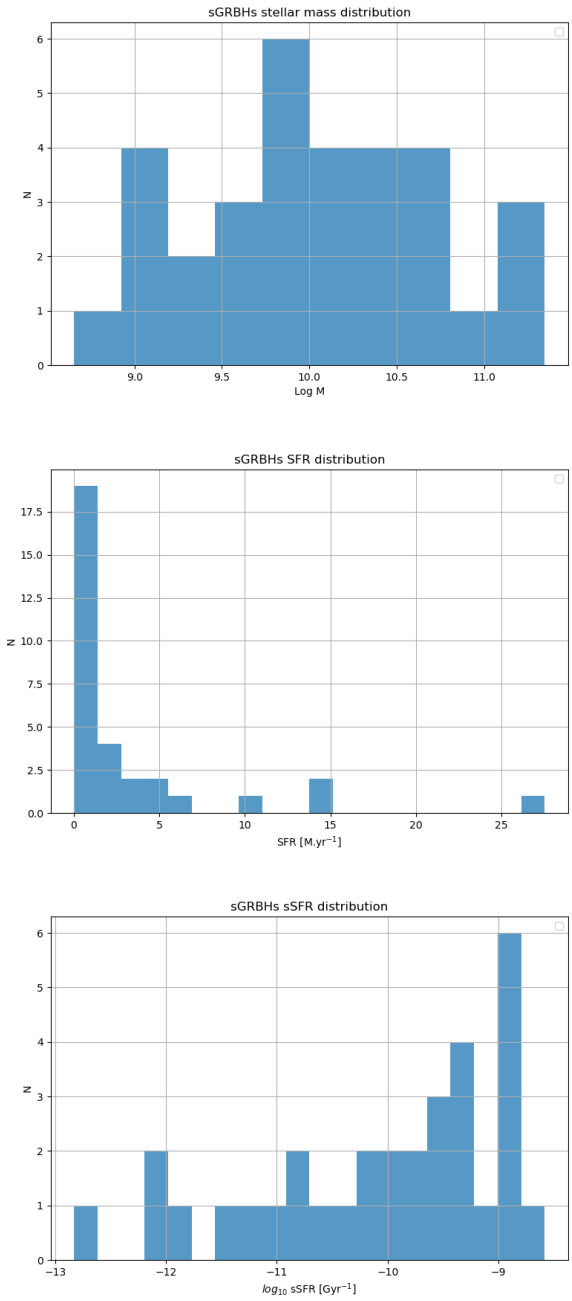

Figure 5.15: Stellar mass, star formation rate (SFR) and specific SFR (sSFR) distributions obtained with SED fitting for the GRB hosts.

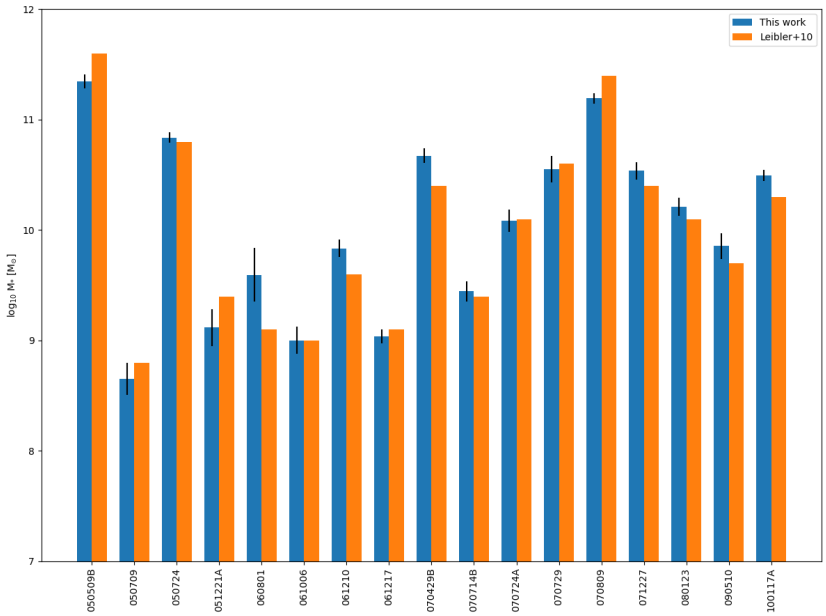

Figure 5.16: Comparison of the obtained stellar mass using SED fitting for each GRB host in common with [326].

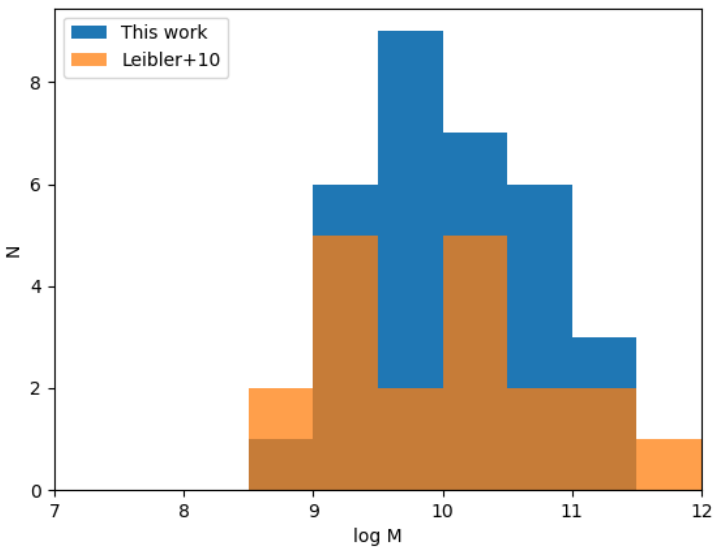

Figure 5.17: Comparison of the obtained stellar mass distribution using SED fitting with the one from [326].

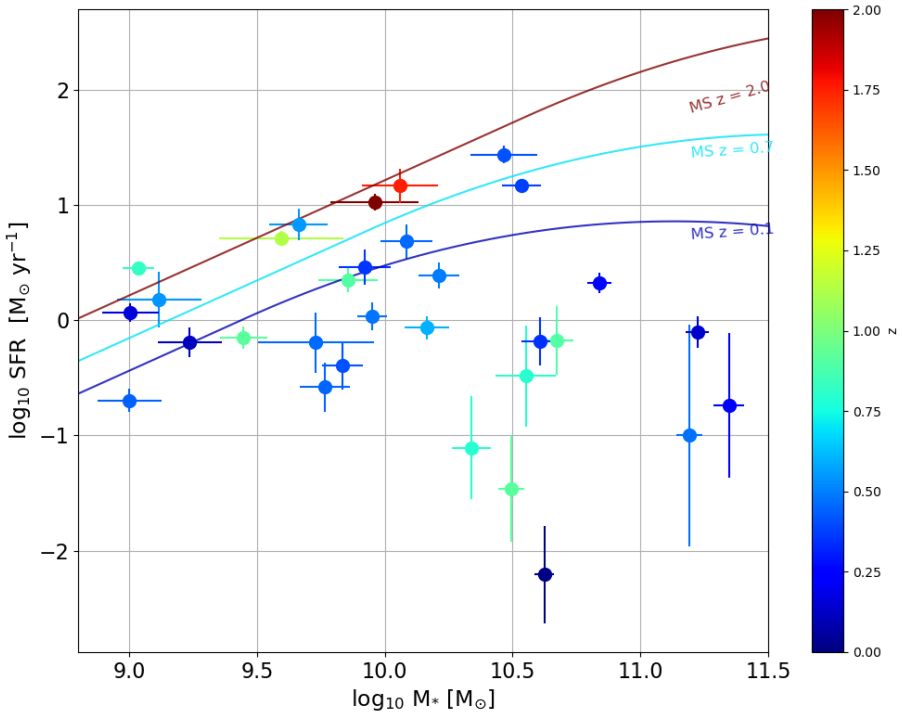

Figure 5.18: SFR-stellar mass relation. The colour map encodes the redshift. The grey lines represent the main sequence relation from [204] at different redshifts.

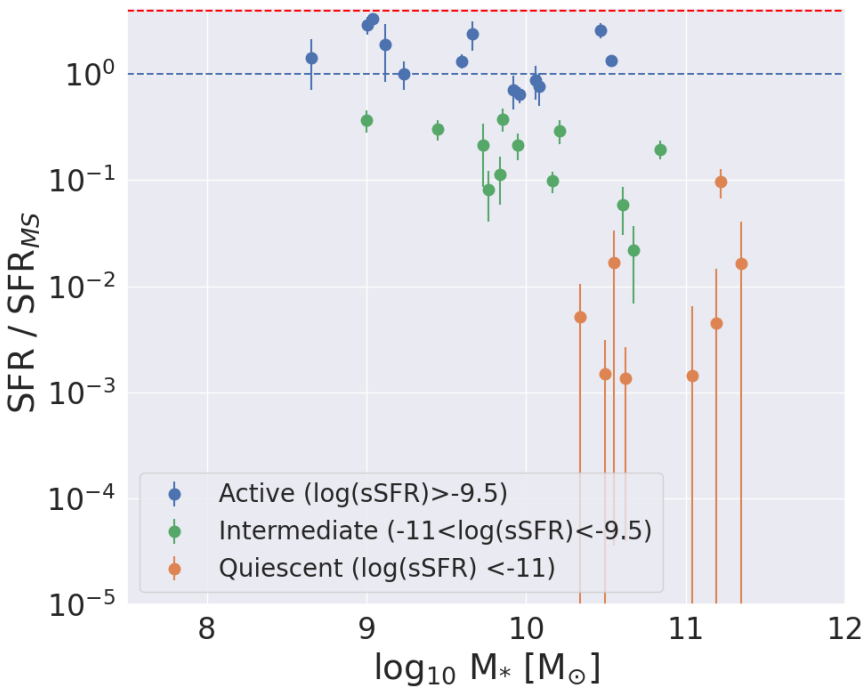

Figure 5.19: SFR excess compared to the Main Sequence (parametrised as in [204]) of galaxies for a given stellar mass. Galaxy classification follow the sSFR cut suggested by [242] (figure 6).

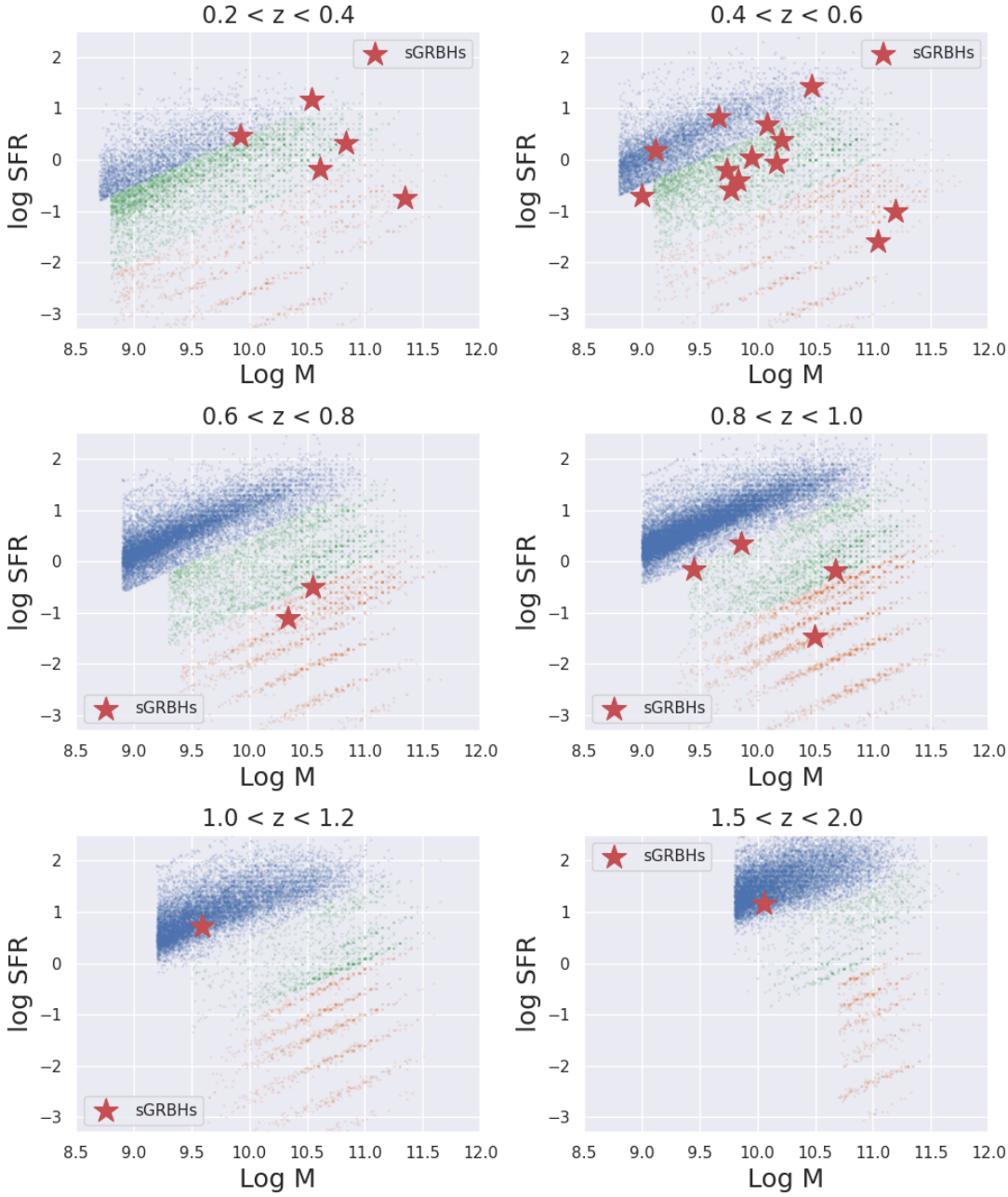

Figure 5.20: Position of the GRB hosts on the SFR-Stellar mass relation for various redshift bins. Underneath dots show the COSMOS2015 galaxies [382], colors represent the classification as in figure 5.19.

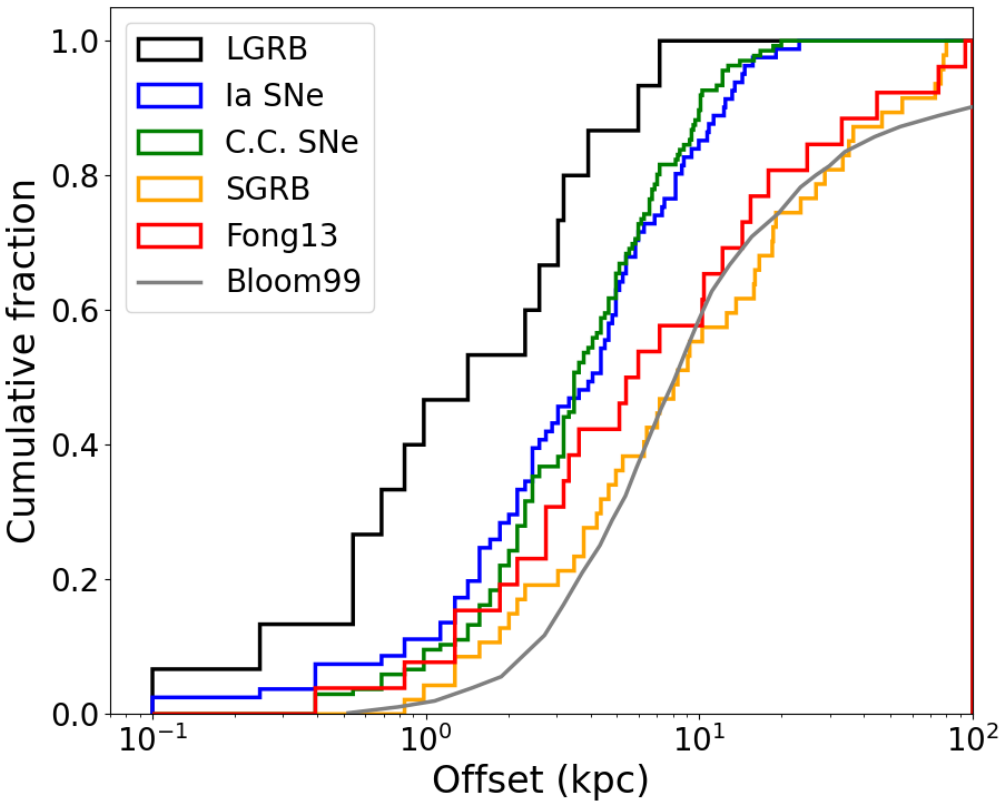

Figure 5.21: Cumulative distribution of projected physical offsets for short GRBs in our sample (orange), in [125] SGRB sample (red), long GRB (black; [253]), core-collapse SNe (green; [254]), type Ia SNe (blue; [254]), predicted offsets for NS-NS binaries from population synthesis models from [256] (grey solid line).

host sample and the COSMOS2015 field galaxies in the redshift bin $0.4<z<0.6$. This figure gives an hint on how one could use the short GRB hosts properties inferred within this work for the gravitational wave follow-up. Indeed, one can try to prioritise the observation of galaxies that fall in the regions of this plane strongly represented in the population of short GRB host galaxies and lightly present in the population of field galaxies. But this requires a catalog of galaxies that contains information on both stellar mass and SFR. Hence such strategy require a lot of developments on the currently available catalog such as Mangrove and will be done in the next years.

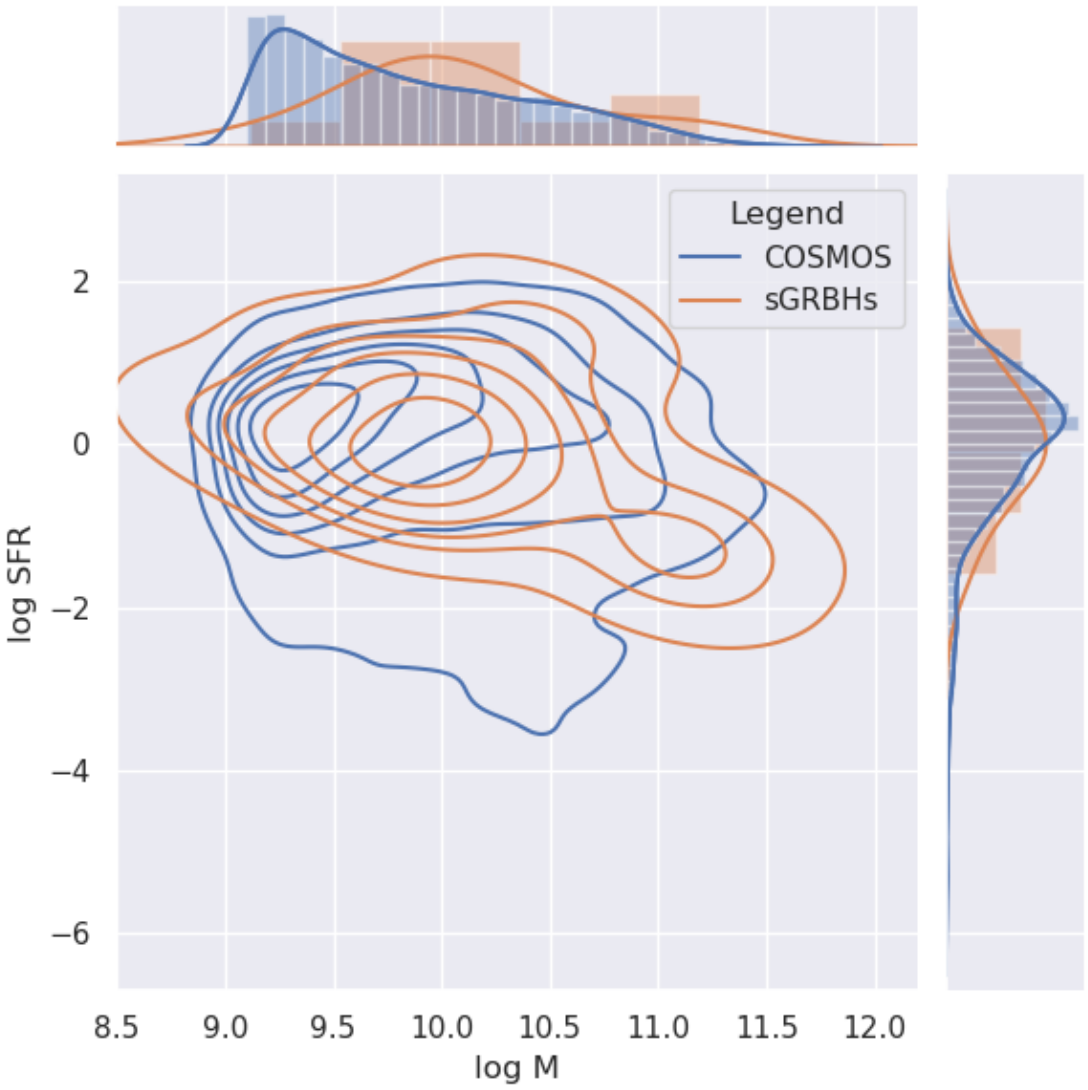

Figure 5.22: 1D and 2D kernel density estimation on the SFR-Stellar mass relation for our short GRB host sample and the COSMOS2015 field galaxies in the redshift bin 0.4<z<0.6.

Conclusion and prospects

The development of the second generation of ground-based interferometric gravitational wave detectors culminated in the first direct detection of a gravitational wave during the first observing run (O1), which started on September 2015 and ended on January 2016, GW150914. For the second observing run (O2), which took place between the 30th of November 2016 and the 25th of August 2017, various upgrades were incorporated to the detectors and Advanced Virgo joined the network of detectors. This second run leaded to several detections of gravitational waves from compact binary systems. In particular, GW170817 resulting from the coalescence of a binary neutron star system represented a real breakthrough for the multi-messenger astronomy with the first electromagnetic counterpart (at all wavelengths) detected for a gravitational wave and the first unambiguous observational evidence of a kilonova. Such multi-messenger observations are particularly fruitful as they carry a huge amount of scientific information (understanding of the physics of strong-gravity, constraints on astrophysical models related to matter during the merger and post-merger phase, first constraint of the speed of gravitational waves and violation of Lorentz invariance, new independent derivation of the Hubble Constant, information about the neutron star equation of state, energy of the ejecta, merger remnant, ambient medium and so on). However, this follow-up requires a lot of effort for the observers yet does not guarantee any detection. This is well illustrated by the third observing run (O3), which lasted 11 months from the 1st of April 2019, achieved with again upgraded gravitational wave detectors, which shared its load of gravitational wave detections from compact binary systems without any evidence for any multi-messenger counterpart, despite the worldwide effort of the follow-up community.

In this thesis I presented the development I carried out for the data analysis of the LIGO-Virgo-KAGRA gravitational wave detectors data, from the detector characterisation to the production of gravitational wave alerts. I also presented the search for gravitational waves associated to gamma-ray bursts during the first half of the O3 run which resulted in no evidence for a significant signal and provided exclusion distance for the expected sources of the gamma-ray bursts. Finally I presented in this thesis my participation in the optimisation of gravitational wave follow-up for ground based telescopes and satellite telescopes for the GRANDMA and SVOM collaborations. These optimisations included the development of the production of the observation plans for gravitational wave follow-up, including the production of a dedicated galaxy catalog, named mangrove, the usage of the galaxy properties for the follow-up, and the study of short gamma-ray burst host galaxies

as a probe of the gravitational wave host one.

The coming year and the coming fourth observing run (O4) will require again a lot of developments from the community to expect any multi-messenger detection. These developments will have to be of course on gravitational wave detector side for the implementation of the latest upgrades, the detector characterisation, the data analysis and the release of gravitational wave alerts. But these developments will also have to be on the follow-up side so difficult is it to detect any counterpart. In a more general way, the multi-messenger astronomy is a very young field of science and the community, as pioneers of this field, has to discover and face new difficulties to acquire scientific results in addition to those already obtained. But this field is promised to a bright future in view of the enthusiasm it carries, as evidenced by the many upcoming experiments and missions.

Bibliography

[1] Steven Weinberg. *Gravitation and Cosmology: Principles and Applications of the General Theory of Relativity.* 1972.

[2] David Langlois. *Relativité générale: Des fondements géométriques aux applications astrophysiques.* 2013.

[3] Michal Was. *Searching for gravitational waves associated with gamma-ray bursts in 2009-2010 LIGO-Virgo data.* PhD thesis, Paris, U. XI, 2011.

[4] Imène Belahcene. *Searching for gravitational waves produced by cosmic strings in LIGO-Virgo data.* Theses, Université Paris Saclay (COmUE), October 2019.

[5] Marie-Anne Bizouard. *Search for gravitational wave transient sources in LIGO-Virgo data.* Habilitation à diriger des recherches, Université Paris Sud, December 2017.

[6] Adam G. Riess et al. Observational Evidence from Supernovae for an Accelerating Universe and a Cosmological Constant. *Astronomical Journal*, 116(3):1009–1038, September 1998.

[7] S. Perlmutter et al. Measurements of Ω and Λ from 42 High-Redshift Supernovae. *Astrophysical Journal*, 517(2):565–586, June 1999.

[8] Scott Dodelson and Lloyd Knox. Dark Energy and the Cosmic Microwave Background Radiation. *Physical Review Letters*, 84(16):3523–3526, April 2000.

[9] G. Efstathiou et al. Evidence for a non-zero Λ and a low matter density from a combined analysis of the 2dF Galaxy Redshift Survey and cosmic microwave background anisotropies. *Monthly Notices of the RAS*, 330(2):L29–L35, February 2002.

[10] Lloyd Knox, Nelson Christensen, and Constantinos Skordis. The Age of the Universe and the Cosmological Constant Determined from Cosmic Microwave Background Anisotropy Measurements. *Astrophysical Journall*, 563(2):L95–L98, December 2001.

[11] Planck Collaboration et al. Planck 2013 results. XVI. Cosmological parameters. *Astronomy and Astrophysics*, 571:A16, November 2014.

[12] Angelique Lartaux-Vollard. *Beating the standard quantum limit for the gravitational wave detector Advanced Virgo*. Theses, Université Paris-Saclay, November 2020.

[13] J. M. Weisberg, D. J. Nice, and J. H. Taylor. Timing Measurements of the Relativistic Binary Pulsar PSR B1913+16. *Astrophysical Journal*, 722(2):1030–1034, October 2010.

[14] B. P. Abbott et al. GWTC-1: A Gravitational-Wave Transient Catalog of Compact Binary Mergers Observed by LIGO and Virgo during the First and Second Observing Runs. *Physical Review X*, 9(3):031040, July 2019.

[15] R. Abbott et al. GWTC-2: Compact Binary Coalescences Observed by LIGO and Virgo During the First Half of the Third Observing Run. *arXiv e-prints*, page arXiv:2010.14527, October 2020.

[16] Chris L. Fryer, Daniel E. Holz, and Scott A. Hughes. Gravitational Wave Emission from Core Collapse of Massive Stars. *Astrophysical Journal*, 565(1):430–446, January 2002.

[17] Viktoriya Morozova, David Radice, Adam Burrows, and David Vartanyan. The Gravitational Wave Signal from Core-collapse Supernovae. *Astrophysical Journal*, 861(1):10, July 2018.

[18] Ernazar Abdikamalov, Giulia Pagliaroli, and David Radice. Gravitational Waves from Core-Collapse Supernovae. *arXiv e-prints*, page arXiv:2010.04356, October 2020.

[19] Tito Dal Canton and Ian W. Harry. Designing a template bank to observe compact binary coalescences in Advanced LIGO's second observing run. *arXiv e-prints*, page arXiv:1705.01845, May 2017.

[20] Benjamin J. Owen. Detectability of periodic gravitational waves by initial interferometers. *Classical and Quantum Gravity*, 23(8):S1–S7, April 2006.

[21] R. N. Manchester, G. B. Hobbs, A. Teoh, and M. Hobbs. The Australia Telescope National Facility Pulsar Catalogue. *Astronomical Journal*, 129(4):1993–2006, April 2005.

[22] B. P. Abbott et al. First Search for Gravitational Waves from Known Pulsars with Advanced LIGO. *Astrophysical Journal*, 839(1):12, April 2017.

[23] The LIGO Scientific Collaboration et al. Gravitational-wave constraints on the equatorial ellipticity of millisecond pulsars. *arXiv e-prints*, page arXiv:2007.14251, July 2020.

[24] L. P. Grishchuk. Amplification of gravitational waves in an isotropic universe. *Soviet Journal of Experimental and Theoretical Physics*, 40:409, September 1975.

[25] Riccardo Apreda, Michele Maggiore, Alberto Nicolis, and Antonio Riotto. Gravitational waves from electroweak phase transitions. *Nuclear Physics B*, 631(1-2):342–368, June 2002.

[26] R. Brustein, M. Gasperini, M. Giovannini, and G. Veneziano. Relic gravitational waves from string cosmology. *Physics Letters B*, 361:45–51, February 1995.

[27] Alessandra Buonanno, Michele Maggiore, and Carlo Ungarelli. Spectrum of relic gravitational waves in string cosmology. *Physical Review D*, 55(6):3330–3336, March 1997.

[28] T. W. B. Kibble. Topology of cosmic domains and strings. *Journal of Physics A Mathematical General*, 9(8):1387–1398, August 1976.

[29] Xavier Siemens, Vuk Mandic, and Jolien Creighton. Gravitational-Wave Stochastic Background from Cosmic Strings. *Physical Review Letters*, 98(11):111101, March 2007.

[30] Thibault Damour and Alexander Vilenkin. Gravitational radiation from cosmic (super)strings: Bursts, stochastic background, and observational windows. *Physical Review D*, 71(6):063510, March 2005.

[31] Nelson Christensen. Stochastic gravitational wave backgrounds. *Reports on Progress in Physics*, 82(1):016903, January 2019.

[32] J. Aasi, B. P. Abbott, and R. Abbott. Improved upper limits on the stochastic gravitational-wave background from 2009–2010 ligo and virgo data. *Phys. Rev. Lett.*, 113:231101, December 2014.

[33] Jorge Cervantes-Cota, Salvador Galindo-Uribarri, and George Smoot. A Brief History of Gravitational Waves. *Universe*, 2(3):22, September 2016.

[34] Peter R. Saulson. Josh goldberg and the physical reality of gravitational waves. *General Relativity and Gravitation*, 43(12):3289–3299, December 2011.

[35] J. Weber. Detection and generation of gravitational waves. *Phys. Rev.*, 117:306–313, January 1960.

[36] J. Weber. Observation of the thermal fluctuations of a gravitational-wave detector. *Phys. Rev. Lett.*, 17:1228–1230, December 1966.

[37] J. Weber. Anisotropy and polarization in the gravitational-radiation experiments. *Phys. Rev. Lett.*, 25:180–184, July 1970.

[38] V. B. Braginskii, Iu. I. Vorontsov, and K. S. Thorne. Quantum Nondemolition Measurements. *Science*, 209(4456):547–557, January 1980.

[39] Peter R. Saulson. Physics of gravitational wave detection: Resonant and interferometric detectors. *eConf*, C9808031:05, 1998.

[40] Gabriele Vajente. *Analysis of sensitivity and noise sources for the Virgo gravitational wave interferometer*. Theses, Scuola Normale Superiore di Pisa, 2008.

[41] M. Rakhmanov, J. D. Romano, and J. T. Whelan. High-frequency corrections to the detector response and their effect on searches for gravitational waves. *Classical and Quantum Gravity*, 25(18):184017, September 2008.

[42] D. Baskaran and L. P. Grishchuk. Components of the gravitational force in the field of a gravitational wave. *Classical and Quantum Gravity*, 21(17):4041–4061, September 2004.

[43] C. Corda, S. A. Ali, and C. Cafaro. Interferometer Response to Scalar Gravitational Waves. *International Journal of Modern Physics D*, 19(13):2095–2109, January 2010.

[44] Peter R. Saulson. *Fundamentals of Interferometric Gravitational Wave Detectors*. 2017.

[45] F. Acernese et al. Quantum backaction on kg-scale mirrors: Observation of radiation pressure noise in the advanced virgo detector. *Phys. Rev. Lett.*, 125:131101, September 2020.

[46] F. Acernese et al. The virgo 3 km interferometer for gravitational wave detection. *Journal of Optics A: Pure and Applied Optics*, 10(6):064009, May 2008.

[47] F. Acernese et al. Advanced Virgo: a second-generation interferometric gravitational wave detector. *Classical and Quantum Gravity*, 32(2):024001, January 2015.

[48] Julia Casanueva Diaz. *Fabry-Perot Cavities in Advanced Virgo*, pages 37–83. Springer International Publishing, Cham, 2018.

[49] L. Pinard et al. Mirrors used in the ligo interferometers for first detection of gravitational waves. *Appl. Opt.*, 56(4):C11–C15, February 2017.

[50] F. Acernese et al. Measurements of superattenuator seismic isolation by virgo interferometer. *Astroparticle Physics*, 33(3):182 – 189, 2010.

[51] R. Bonnand et al. Upper-limit on the Advanced Virgo output mode cleaner cavity length noise. *Classical and Quantum Gravity*, 34(17):175002, September 2017.

[52] Abbott, B. P. et al. Observation of gravitational waves from a binary black hole merger. *Phys. Rev. Lett.*, 116:061102, February 2016.

[53] Abbott, B. P. et al. Tests of general relativity with gw150914. *Phys. Rev. Lett.*, 116:221101, May 2016.

[54] B. P. Abbott et al. Binary Black Hole Mergers in the First Advanced LIGO Observing Run. *Physical Review X*, 6(4):041015, October 2016.

[55] T. Accadia et al. Calibration and sensitivity of the virgo detector during its second science run. *Classical and Quantum Gravity*, 28(2):025005, December 2010.

[56] T. Accadia et al. Reconstruction of the gravitational wave signal h (t) during the virgo science runs and independent validation with a photon calibrator. *Classical and Quantum Gravity*, 31(16):165013, August 2014.

[57] F. Acernese et al. Calibration of advanced virgo and reconstruction of the gravitational wave signal h (t) during the observing run o2. *Classical and Quantum Gravity*, 35(20):205004, September 2018.

[58] D. Estevez et al. The Advanced Virgo Photon Calibrators. *arXiv e-prints*, page arXiv:2009.08103, September 2020.

[59] B. P. Abbott et al. Prospects for observing and localizing gravitational-wave transients with Advanced LIGO, Advanced Virgo and KAGRA. *Living Reviews in Relativity*, 21(1):3, April 2018.

[60] Bruce Allen et al. FINDCHIRP: An algorithm for detection of gravitational waves from inspiraling compact binaries. *Physical Review D*, 85(12):122006, June 2012.

[61] F. Robinet. Omicron: an algorithm to detect and characterize transient events in gravitational-wave detectors. Technical report, 2008. `https://tds.virgo-gw.eu/ql/?c=10651`.

[62] Florent Robinet et al. Omicron: A tool to characterize transient noise in gravitational-wave detectors. *SoftwareX*, 12:100620, 2020.

[63] Judith C. Brown. Calculation of a constant q spectral transform. *The Journal of the Acoustical Society of America*, 89(1):425–434, 1991.

[64] J. Aasi et al. The characterization of Virgo data and its impact on gravitational-wave searches. *Classical and Quantum Gravity*, 29(15):155002, August 2012.

[65] Michael W. Coughlin et al. Subtraction of correlated noise in global networks of gravitational-wave interferometers. *Classical and Quantum Gravity*, 33(22):224003, November 2016.

[66] Jade Powell et al. Classification methods for noise transients in advanced gravitational-wave detectors II: performance tests on advanced LIGO data. *Classical and Quantum Gravity*, 34(3):034002, January 2017.

[67] Irene Fiori et al. The Hunt for Environmental Noise in Virgo during the Third Observing Run. *Galaxies*, 8(4):82, December 2020.

[68] Florent Robinet and and. Data quality in gravitational wave bursts and inspiral searches in the second virgo science run. *Classical and Quantum Gravity*, 27(19):194012, September 2010.

[69] Tomoki Isogai. Used percentage veto for LIGO and virgo binary inspiral searches. *J. Phys. Conf. Ser.*, 243:012005, 2010.

[70] Cody Messick et al. Analysis framework for the prompt discovery of compact binary mergers in gravitational-wave data. *Physical Review D*, 95(4):042001, February 2017.

[71] Surabhi Sachdev et al. The GstLAL Search Analysis Methods for Compact Binary Mergers in Advanced LIGO's Second and Advanced Virgo's First Observing Runs. *arXiv e-prints*, page arXiv:1901.08580, January 2019.

[72] Chad Hanna et al. Fast evaluation of multidetector consistency for real-time gravitational wave searches. *Physical Review D*, 101(2):022003, January 2020.

[73] Bruce Allen. χ^2 time-frequency discriminator for gravitational wave detection. *Physical Review D*, 71(6):062001, March 2005.

[74] Tito Dal Canton et al. Implementing a search for aligned-spin neutron star-black hole systems with advanced ground based gravitational wave detectors. *Physical Review D*, 90(8):082004, October 2014.

[75] Samantha A. Usman et al. The PyCBC search for gravitational waves from compact binary coalescence. *Classical and Quantum Gravity*, 33(21):215004, November 2016.

[76] Alexander H. Nitz et al. Detecting Binary Compact-object Mergers with Gravitational Waves: Understanding and Improving the Sensitivity of the PyCBC Search. *Astrophysical Journal*, 849(2):118, November 2017.

[77] T. Adams et al. Low-latency analysis pipeline for compact binary coalescences in the advanced gravitational wave detector era. *Classical and Quantum Gravity*, 33(17):175012, September 2016.

[78] Qi Chu. *Low-latency detection and localization of gravitational waves from compact binary coalescences*. PhD thesis, The University of Western Australia, 2017.

[79] S Klimenko and G Mitselmakher. A wavelet method for detection of gravitational wave bursts. *Classical and Quantum Gravity*, 21(20):S1819–S1830, September 2004.

[80] S. Klimenko, S. Mohanty, M. Rakhmanov, and G. Mitselmakher. Constraint likelihood analysis for a network of gravitational wave detectors. *Physical Review D*, 72(12):122002, December 2005.

[81] S Klimenko, S Mohanty, M Rakhmanov, and G Mitselmakher. Constraint likelihood method: generalization for colored noise. *Journal of Physics: Conference Series*, 32:12–17, March 2006.

[82] S. Klimenko et al. Localization of gravitational wave sources with networks of advanced detectors. *Physical Review D*, 83(10):102001, May 2011.

[83] S. Klimenko et al. Method for detection and reconstruction of gravitational wave transients with networks of advanced detectors. *Physical Review D*, 93(4):042004, February 2016.

[84] Leo P. Singer and Larry R. Price. Rapid bayesian position reconstruction for gravitational-wave transients. *Phys. Rev. D*, 93:024013, January 2016.

[85] J. Veitch et al. Parameter estimation for compact binaries with ground-based gravitational-wave observations using the LALInference software library. *Physical Review D*, 91(4):042003, February 2015.

[86] G. Ashton and C. Talbot. B ILBY-MCMC: an MCMC sampler for gravitational-wave inference. *Monthly Notices of the RAS*, 507(2):2037–2051, October 2021.

[87] Jacob Lange, Richard O'Shaughnessy, and Monica Rizzo. Rapid and accurate parameter inference for coalescing, precessing compact binaries. *arXiv e-prints*, page arXiv:1805.10457, May 2018.

[88] Jacob Lange. *RIFT'ing the Waves: Developing and applying an algorithm to infer properties of gravitational wave sources*. PhD thesis, Rochester Institute of Technology, 2020.

[89] David Corre. *Exploring the dawn of the universe with the Sino-French SVOM mission*. PhD thesis, 2018. Thèse de doctorat dirigée par Basa, Stephane et Buat, Véronique Astrophysique et cosmologie Aix-Marseille 2018.

[90] Ray W. Klebesadel, Ian B. Strong, and Roy A. Olson. Observations of Gamma-Ray Bursts of Cosmic Origin. *Astrophysical Journall*, 182:L85, June 1973.

[91] Gerald J. Fishman et al. The First BATSE Gamma-Ray Burst Catalog. *Astrophysical Journals*, 92:229, May 1994.

[92] Chryssa Kouveliotou et al. Identification of Two Classes of Gamma-Ray Bursts. *Astrophysical Journall*, 413:L101, August 1993.

[93] E. Costa et al. Discovery of an X-ray afterglow associated with the γ-ray burst of 28 February 1997. *Nature*, 387(6635):783–785, June 1997.

[94] P. J. Groot et al. GRB 970228. *IAU Cirulars*, 6584:1, March 1997.

[95] J. van Paradijs et al. Transient optical emission from the error box of the γ-ray burst of 28 February 1997. *Nature*, 386(6626):686–689, April 1997.

[96] M. R. Metzger et al. Spectral constraints on the redshift of the optical counterpart to the γ-ray burst of 8 May 1997. *Nature*, 387(6636):878–880, June 1997.

[97] Charles A. Meegan et al. The 4B BATSE gamma-ray burst catalog. In Charles A. Meegan, Robert D. Preece, and Thomas M. Koshut, editors, *Gamma-Ray Bursts, 4th Hunstville Symposium*, volume 428 of *American Institute of Physics Conference Series*, pages 3–9, May 1998.

[98] T. Piran. Gamma-ray bursts and the fireball model. *Physics Reports*, 314(6):575–667, June 1999.

[99] B. Paczynski. Gamma-ray bursters at cosmological distances. *Astrophysical Journall*, 308:L43–L46, September 1986.

[100] J. Goodman. Are gamma-ray bursts optically thick? *Astrophysical Journall*, 308:L47, September 1986.

[101] Bohdan Paczynski. Cosmological gamma-ray bursts. *Acta Astronomica*, 41:257–267, January 1991.

[102] Amotz Shemi and Tsvi Piran. The Appearance of Cosmic Fireballs. *Astrophysical Journall*, 365:L55, December 1990.

[103] M. J. Rees and P. Meszaros. Relativistic fireballs - Energy conversion and time-scales. *Monthly Notices of the RAS*, 258:41, September 1992.

[104] Neil Gehrels, Luigi Piro, and Peter Leonard. The brightest explosions in the universe. *Scientific American*, 287:84–91, 01 2003.

[105] A. I. MacFadyen and S. E. Woosley. Collapsars: Gamma-Ray Bursts and Explosions in "Failed Supernovae". *Astrophysical Journal*, 524(1):262–289, October 1999.

[106] A. I. MacFadyen, S. E. Woosley, and A. Heger. Supernovae, Jets, and Collapsars. *Astrophysical Journal*, 550(1):410–425, March 2001.

[107] S. E. Woosley. Gamma-Ray Bursts from Stellar Mass Accretion Disks around Black Holes. *Astrophysical Journal*, 405:273, March 1993.

[108] Chris L. Fryer, S. E. Woosley, and Dieter H. Hartmann. Formation Rates of Black Hole Accretion Disk Gamma-Ray Bursts. *Astrophysical Journal*, 526(1):152–177, November 1999.

[109] R. D. Blandford and D. G. Payne. Hydromagnetic flows from accretion disks and the production of radio jets. *Monthly Notices of the RAS*, 199:883–903, June 1982.

[110] Romain Hascoët. *Modélisation des sursauts gamma et de leurs rémanences à l'ère des satellites Swift et Fermi.* Theses, Université Pierre et Marie Curie - Paris VI, June 2012.

[111] R. D. Blandford and R. L. Znajek. Electromagnetic extraction of energy from Kerr black holes. *Monthly Notices of the RAS*, 179:433–456, May 1977.

[112] S. E. Woosley and A. Heger. The Progenitor Stars of Gamma-Ray Bursts. *Astrophysical Journal*, 637(2):914–921, February 2006.

[113] Jens Hjorth and Joshua S. Bloom. *The Gamma-Ray Burst - Supernova Connection*, pages 169–190. 2012.

[114] Schuyler D. van Dyk, Mario Hamuy, and Alexei V. Filippenko. Supernovae and Massive Star Formation Regions. *Astronomical Journal*, 111:2017, May 1996.

[115] Chris L. Fryer, Aimee L. Hungerford, and Patrick A. Young. Light-Curve Calculations of Supernovae from Fallback Gamma-Ray Bursts. *Astrophysical Journall*, 662(2):L55–L58, June 2007.

[116] Weiqun Zhang, S. E. Woosley, and A. Heger. The Propagation and Eruption of Relativistic Jets from the Stellar Progenitors of Gamma-Ray Bursts. *Astrophysical Journal*, 608(1):365–377, June 2004.

[117] S. E. Woosley and J. S. Bloom. The Supernova Gamma-Ray Burst Connection. *Annual Review of Astron and Astrophys*, 44(1):507–556, September 2006.

[118] T. J. Galama et al. An unusual supernova in the error box of the γ-ray burst of 25 April 1998. *Nature*, 395(6703):670–672, October 1998.

[119] J. Hjorth. The supernova-gamma-ray burst-jet connection. *Philosophical Transactions of the Royal Society of London Series A*, 371(1992):20120275–20120275, April 2013.

[120] E. S. Phinney. The Rate of Neutron Star Binary Mergers in the Universe: Minimal Predictions for Gravity Wave Detectors. *Astrophysical Journall*, 380:L17, October 1991.

[121] Ramesh Narayan, Bohdan Paczynski, and Tsvi Piran. Gamma-Ray Bursts as the Death Throes of Massive Binary Stars. *Astrophysical Journall*, 395:L83, August 1992.

[122] E. P. J. van den Heuvel and D. R. Lorimer. On the galactic and cosmic merger rate of double neutron stars. *Monthly Notices of the RAS*, 283(2):L37–L40, November 1996.

[123] E. E. Fenimore et al. The intrinsic luminosity of γ-ray bursts and their host galaxies. *Nature*, 366(6450):40–42, November 1993.

[124] J. S. Bloom and J. X. Prochaska. Constraints on the Diverse Progenitors of GRBs from the Large-Scale Environments. In S. S. Holt, N. Gehrels, and J. A. Nousek, editors, *Gamma-Ray Bursts in the Swift Era*, volume 836 of *American Institute of Physics Conference Series*, pages 473–482, May 2006.

[125] W. Fong and E. Berger. The Locations of Short Gamma-Ray Bursts as Evidence for Compact Object Binary Progenitors. *Astrophysical Journal*, 776(1):18, October 2013.

[126] R. L. Tunnicliffe et al. On the nature of the 'hostless' short GRBs. *Monthly Notices of the RAS*, 437(2):1495–1510, January 2014.

[127] Brian D. Metzger. Kilonovae. *Living Reviews in Relativity*, 23(1):1, December 2019.

[128] N. R. Tanvir et al. A 'kilonova' associated with the short-duration γ-ray burst GRB 130603B. *Nature*, 500(7464):547–549, August 2013.

[129] E. Troja et al. A luminous blue kilonova and an off-axis jet from a compact binary merger at z = 0.1341. *Nature Communications*, 9:4089, October 2018.

[130] B. P. Abbott et al. Gravitational Waves and Gamma-Rays from a Binary Neutron Star Merger: GW170817 and GRB 170817A. *Astrophysical Journall*, 848(2):L13, October 2017.

[131] Charles Meegan et al. The Fermi Gamma-ray Burst Monitor. *Astrophysical Journal*, 702(1):791–804, September 2009.

[132] Scott D. Barthelmy et al. The Burst Alert Telescope (BAT) on the SWIFT Midex Mission. *Space Science Reviews*, 120(3-4):143–164, October 2005.

[133] David N. Burrows et al. The Swift X-Ray Telescope. *Space Science Reviews*, 120(3-4):165–195, October 2005.

[134] Peter W. A. Roming et al. The Swift Ultra-Violet/Optical Telescope. *Space Science Reviews*, 120(3-4):95–142, October 2005.

[135] Amy Lien et al. The Third Swift Burst Alert Telescope Gamma-Ray Burst Catalog. *Astrophysical Journal*, 829(1):7, September 2016.

[136] P. A. Evans et al. Swift follow-up of IceCube triggers, and implications for the Advanced-LIGO era. *Monthly Notices of the RAS*, 448(3):2210–2223, April 2015.

[137] N. J. Klingler et al. Swift-XRT Follow-up of Gravitational-wave Triggers in the Second Advanced LIGO/Virgo Observing Run. *Astrophysical Journals*, 245(1):15, November 2019.

[138] A. von Kienlin et al. The Fourth Fermi-GBM Gamma-Ray Burst Catalog: A Decade of Data. *Astrophysical Journal*, 893(1):46, April 2020.

[139] V. Connaughton et al. Localization of Gamma-Ray Bursts Using the Fermi Gamma-Ray Burst Monitor. *Astrophysical Journals*, 216(2):32, February 2015.

[140] J. Wei et al. The Deep and Transient Universe in the SVOM Era: New Challenges and Opportunities - Scientific prospects of the SVOM mission. *arXiv e-prints*, page arXiv:1610.06892, October 2016.

[141] B. Cordier, F. Desclaux, J. Foliard, and S. Schanne. SVOM pointing strategy: how to optimize the redshift measurements? In M. Galassi, David Palmer, and Ed Fenimore, editors, *Gamma-ray Bursts 2007*, volume 1000 of *American Institute of Physics Conference Series*, pages 585–588, May 2008.

[142] D. Burlon et al. Time resolved spectral behavior of bright BATSE precursors. *Astronomy and Astrophysics*, 505(2):569–575, October 2009.

[143] Li-Xin Li. Gamma-ray burst precursors as the remnant of the thermal radiation initially trapped in the fireball. *Monthly Notices of the RAS*, 380(2):621–636, September 2007.

[144] Davide Lazzati and Mitchell C. Begelman. Universal GRB Jets from Jet-Cocoon Interaction in Massive Stars. *Astrophysical Journal*, 629(2):903–907, August 2005.

[145] Xiang-Yu Wang and Peter Mészáros. GRB Precursors in the Fallback Collapsar Scenario. *Astrophysical Journal*, 670(2):1247–1253, December 2007.

[146] LIGO Scientific Collaboration and Virgo Collaboration. LIGO/Virgo G298048: Identification of a binary neutron star candidate coincident with Fermi GBM trigger 524666471/170817529. *GRB Coordinates Network*, 21509:1, August 2017.

[147] V. Savchenko et al. LIGO/Virgo G298048: INTEGRAL detection of a prompt gamma-ray counterpart. *GRB Coordinates Network*, 21507:1, August 2017.

[148] LIGO Scientific Collaboration and Virgo Collaboration. LIGO/Virgo G298048: Further analysis of a binary neutron star candidate with updated sky localization. *GRB Coordinates Network*, 21513:1, August 2017.

[149] LIGO Scientific Collaboration and Virgo Collaboration. LIGO/Virgo G298048: Updated sky map from gravitational-wave data. *GRB Coordinates Network*, 21527:1, August 2017.

[150] D. A. Coulter et al. LIGO/Virgo G298048: Potential optical counterpart discovered by Swope telescope. *GRB Coordinates Network*, 21529:1, August 2017.

[151] B. P. Abbott et al. Multi-messenger Observations of a Binary Neutron Star Merger. *Astrophysical Journall*, 848(2):L12, October 2017.

[152] M. R. Drout et al. LIGO/VIRGO G298048: Magellan Optical Spectrum of the Potential Optical Counterpart Associated with NGC 4993. *GRB Coordinates Network*, 21547:1, August 2017.

[153] B. J. Shappee et al. Early spectra of the gravitational wave source GW170817: Evolution of a neutron star merger. *Science*, 358(6370):1574–1578, December 2017.

[154] Weidong Li et al. Nearby supernova rates from the Lick Observatory Supernova Search - III. The rate-size relation, and the rates as a function of galaxy Hubble type and colour. *Monthly Notices of the RAS*, 412(3):1473–1507, April 2011.

[155] Weidong Li et al. Nearby supernova rates from the Lick Observatory Supernova Search - II. The observed luminosity functions and fractions of supernovae in a complete sample. *Monthly Notices of the RAS*, 412(3):1441–1472, April 2011.

[156] Brian D. Metzger. Kilonovae. *Living Reviews in Relativity*, 20(1):3, May 2017.

[157] E. Pian et al. Spectroscopic identification of r-process nucleosynthesis in a double neutron-star merger. *Nature*, 551(7678):67–70, November 2017.

[158] S. J. Smartt et al. A kilonova as the electromagnetic counterpart to a gravitational-wave source. *Nature*, 551(7678):75–79, November 2017.

[159] P. S. Cowperthwaite et al. The Electromagnetic Counterpart of the Binary Neutron Star Merger LIGO/Virgo GW170817. II. UV, Optical, and Near-infrared Light Curves and Comparison to Kilonova Models. *Astrophysical Journall*, 848(2):L17, October 2017.

[160] A. J. Levan et al. The Environment of the Binary Neutron Star Merger GW170817. *Astrophysical Journall*, 848(2):L28, October 2017.

[161] A. J. Levan et al. LIGO/Virgo G298048: Hubble Space Telescope observations. *GRB Coordinates Network*, 21781:1, August 2017.

[162] N. R. Tanvir et al. The Emergence of a Lanthanide-rich Kilonova Following the Merger of Two Neutron Stars. *Astrophysical Journall*, 848(2):L27, October 2017.

[163] E. Troja et al. The X-ray counterpart to the gravitational-wave event GW170817. *Nature*, 551(7678):71–74, November 2017.

[164] V. A. Villar et al. The Combined Ultraviolet, Optical, and Near-infrared Light Curves of the Kilonova Associated with the Binary Neutron Star Merger GW170817: Unified Data Set, Analytic Models, and Physical Implications. *Astrophysical Journall*, 851(1):L21, December 2017.

[165] E. Troja et al. LIGO/Virgo G298048: Discovery of X-ray emission from SSS17a in NGC4993. *GRB Coordinates Network*, 21765:1, August 2017.

[166] K. P. Mooley et al. LIGO/VIRGO G298048: Radio detection of SSS17a at 3GHz with the VLA/JAGWAR. *GRB Coordinates Network*, 21814:1, September 2017.

[167] A. Corsi et al. LIGO/VIRGO G298048: Radio detection of SSS17a at 6 GHz with the VLA. *GRB Coordinates Network*, 21815:1, September 2017.

[168] T. Murphy et al. LIGO/Virgo G298048: ATCA observations of of SSS17a in NGC 4993. *GRB Coordinates Network*, 21842:1, September 2017.

[169] G. P. Lamb et al. The Optical Afterglow of GW170817 at One Year Post-merger. *Astrophysical Journall*, 870(2):L15, January 2019.

[170] Arvind Balasubramanian et al. Continued radio observations of GW170817 3.5 years post-merger. *arXiv e-prints*, page arXiv:2103.04821, March 2021.

[171] A. Hajela et al. The emergence of a new source of X-rays from the binary neutron star merger GW170817. *arXiv e-prints*, page arXiv:2104.02070, April 2021.

[172] Abbott, B. P. et al. Gw170817: Observation of gravitational waves from a binary neutron star inspiral. *Phys. Rev. Lett.*, 119:161101, October 2017.

[173] B. P. Abbott et al. GW170817: Measurements of Neutron Star Radii and Equation of State. *Physical Review Letters*, 121(16):161101, October 2018.

[174] A. Hajela et al. Two Years of Nonthermal Emission from the Binary Neutron Star Merger GW170817: Rapid Fading of the Jet Afterglow and First Constraints on the Kilonova Fastest Ejecta. *Astrophysical Journall*, 886(1):L17, November 2019.

[175] Ramandeep Gill, Antonios Nathanail, and Luciano Rezzolla. When Did the Remnant of GW170817 Collapse to a Black Hole? *Astrophysical Journal*, 876(2):139, May 2019.

[176] B. P. Abbott et al. A gravitational-wave standard siren measurement of the Hubble constant. *Nature*, 551(7678):85–88, November 2017.

[177] Michael W. Coughlin et al. Standardizing kilonovae and their use as standard candles to measure the Hubble constant. *Physical Review Research*, 2(2):022006, April 2020.

[178] K. Hotokezaka et al. A Hubble constant measurement from superluminal motion of the jet in GW170817. *Nature Astronomy*, 3:940–944, July 2019.

[179] Jonathan Granot, Ramandeep Gill, Dafne Guetta, and Fabio De Colle. Off-axis emission of short GRB jets from double neutron star mergers and GRB 170817A. *Monthly Notices of the RAS*, 481(2):1597–1608, December 2018.

[180] N. Fraija et al. The Short GRB 170817A: Modeling the Off-axis Emission and Implications on the Ejecta Magnetization. *Astrophysical Journal*, 871(1):123, January 2019.

[181] Gavin P. Lamb, Andrew J. Levan, and Nial R. Tanvir. GRB 170817A as a Refreshed Shock Afterglow Viewed Off-axis. *Astrophysical Journal*, 899(2):105, August 2020.

[182] Shigeo S. Kimura et al. Transejecta high-energy neutrino emission from binary neutron star mergers. *Physical Review D*, 98(4):043020, August 2018.

[183] V. Decoene et al. High-energy neutrinos from fallback accretion of binary neutron star merger remnants. *Journal of Cosmology and Astroparticle Physics*, 2020(4):045, April 2020.

[184] Ke Fang et al. High-energy Neutrinos and Gamma Rays from Nonrelativistic Shock-powered Transients. *Astrophysical Journal*, 904(1):4, November 2020.

[185] Peter Mészáros. Gamma ray bursts. *Astroparticle Physics*, 43:134–141, March 2013.

[186] Pawan Kumar and Bing Zhang. The physics of gamma-ray bursts & relativistic jets. *Physics Reports*, 561:1–109, February 2015.

[187] Eli Waxman and John Bahcall. High Energy Neutrinos from Cosmological Gamma-Ray Burst Fireballs. *Physical Review Letters*, 78(12):2292–2295, March 1997.

[188] S. Adriá et al.n-Martíet al.nez et al. High-energy neutrino follow-up search of gravitational wave event GW150914 with ANTARES and IceCube. *Physical Review D*, 93(12):122010, June 2016.

[189] A. Albert et al. Search for high-energy neutrinos from gravitational wave event GW151226 and candidate LVT151012 with ANTARES and IceCube. *Physical Review D*, 96(2):022005, July 2017.

[190] A. Albert et al. Search for High-energy Neutrinos from Binary Neutron Star Merger GW170817 with ANTARES, IceCube, and the Pierre Auger Observatory. *Astrophysical Journall*, 850(2):L35, December 2017.

[191] K. Abe et al. Search for Neutrinos in Super-Kamiokande Associated with the GW170817 Neutron-star Merger. *Astrophysical Journall*, 857(1):L4, April 2018.

[192] Robert Mochkovitch, Frédéric Daigne, Raphaël Duque, and Hannachi Zitouni. Prospects for kilonova signals in the gravitational-wave era. *arXiv e-prints*, page arXiv:2103.00943, March 2021.

[193] Andrew S. Fruchter et al. Hubble Space Telescope and Palomar Imaging of GRB 990123: Implications for the Nature of Gamma-Ray Bursts and Their Hosts. *Astrophysical Journall*, 519(1):L13–L16, July 1999.

[194] E. Le Floc'h et al. Are the hosts of gamma-ray bursts sub-luminous and blue galaxies? *Astronomy and Astrophysics*, 400:499–510, March 2003.

[195] E. Berger et al. A Submillimeter and Radio Survey of Gamma-Ray Burst Host Galaxies: A Glimpse into the Future of Star Formation Studies. *Astrophysical Journal*, 588(1):99–112, May 2003.

[196] L. Christensen, J. Hjorth, and J. Gorosabel. UV star-formation rates of GRB host galaxies. *Astronomy and Astrophysics*, 425:913–926, October 2004.

[197] N. R. Tanvir et al. The submillimetre properties of gamma-ray burst host galaxies. *Monthly Notices of the RAS*, 352(3):1073–1080, August 2004.

[198] A. S. Fruchter et al. Long γ-ray bursts and core-collapse supernovae have different environments. *Nature*, 441(7092):463–468, May 2006.

[199] S. Savaglio, K. Glazebrook, and D. Le Borgne. The Galaxy Population Hosting Gamma-Ray Bursts. *Astrophysical Journal*, 691(1):182–211, January 2009.

[200] Filippo M. Zerbi et al. The REM telescope: a robotic multiwavelength facility. In Alan F. M. Moorwood and Masanori Iye, editors, *Ground-based Instrumentation for Astronomy*, volume 5492 of *Society of Photo-Optical Instrumentation Engineers (SPIE) Conference Series*, pages 1590–1601, September 2004.

[201] N. Butler et al. Rapidly Detecting Extincted Bursts with KAIT and PAIRITEL. In S. S. Holt, N. Gehrels, and J. A. Nousek, editors, *Gamma-Ray Bursts in the Swift Era*, volume 836 of *American Institute of Physics Conference Series*, pages 277–280, May 2006.

[202] J. Greiner et al. GROND—a 7-Channel Imager. *Publications of the ASP*, 120(866):405, April 2008.

[203] Nat Butler et al. First Light with RATIR: An Automated 6-band Optical/NIR Imaging Camera. In Ian S. McLean, Suzanne K. Ramsay, and Hideki Takami, editors, *Ground-based and Airborne Instrumentation for Astronomy IV*, volume 8446 of *Society of Photo-Optical Instrumentation Engineers (SPIE) Conference Series*, page 844610, September 2012.

[204] C. Schreiber et al. The Herschel view of the dominant mode of galaxy growth from z = 4 to the present day. *Astronomy and Astrophysics*, 575:A74, March 2015.

[205] T. Krü et al.hler et al. GRB hosts through cosmic time. VLT/X-Shooter emission-line spectroscopy of 96 γ-ray-burst-selected galaxies at $0.1 < z < 3.6$. *Astronomy and Astrophysics*, 581:A125, September 2015.

[206] D. A. Perley et al. The Swift GRB Host Galaxy Legacy Survey. II. Rest-frame Near-IR Luminosity Distribution and Evidence for a Near-solar Metallicity Threshold. *Astrophysical Journal*, 817(1):8, January 2016.

[207] J. F. Graham and A. S. Fruchter. The Metal Aversion of Long-duration Gamma-Ray Bursts. *Astrophysical Journal*, 774(2):119, September 2013.

[208] D. A. Perley et al. A Population of Massive, Luminous Galaxies Hosting Heavily Dust-obscured Gamma-Ray Bursts: Implications for the Use of GRBs as Tracers of Cosmic Star Formation. *Astrophysical Journal*, 778(2):128, December 2013.

[209] S. Boissier et al. A method for quantifying the gamma-ray burst bias. Application in the redshift range of 0-1.1. *Astronomy and Astrophysics*, 557:A34, September 2013.

[210] S. D. Vergani et al. The chemical enrichment of long gamma-ray bursts nurseries up to z = 2. *Astronomy and Astrophysics*, 599:A120, March 2017.

[211] T. Krü et al.hler et al. The metal-enriched host of an energetic γ-ray burst at z $\approx$ 1.6. *Astronomy and Astrophysics*, 546:A8, October 2012.

[212] S. Savaglio et al. Supersolar metal abundances in two galaxies at z $\sim$ 3.57 revealed by the GRB 090323 afterglow spectrum. *Monthly Notices of the RAS*, 420(1):627–636, February 2012.

[213] J. Elliott et al. The low-extinction afterglow in the solar-metallicity host galaxy of γ-ray burst 110918A. *Astronomy and Astrophysics*, 556:A23, August 2013.

[214] J. Japelj et al. Are long gamma-ray bursts biased tracers of star formation? Clues from the host galaxies of the Swift/BAT6 complete sample of bright LGRBs. II. Star formation rates and metallicities at z $<$ 1. *Astronomy and Astrophysics*, 590:A129, May 2016.

[215] J. T. Palmerio et al. Are long gamma-ray bursts biased tracers of star formation? Clues from the host galaxies of the Swift/BAT6 complete sample of bright LGRBs. III. Stellar masses, star formation rates, and metallicities at z $>$ 1. *Astronomy and Astrophysics*, 623:A26, March 2019.

[216] Jens Hjorth et al. The Optically Unbiased Gamma-Ray Burst Host (TOUGH) Survey. I. Survey Design and Catalogs. *Astrophysical Journal*, 756(2):187, September 2012.

[217] D. A. Perley et al. The Swift Gamma-Ray Burst Host Galaxy Legacy Survey. I. Sample Selection and Redshift Distribution. *Astrophysical Journal*, 817(1):7, January 2016.

[218] Mariska Kriek et al. The MOSFIRE Deep Evolution Field (MOSDEF) Survey: Rest-frame Optical Spectroscopy for ~1500 H-selected Galaxies at 1.37 $<$ z $<$ 3.8. *Astrophysical Journals*, 218(2):15, June 2015.

[219] Irene Shivaei et al. The MOSDEF Survey: Dissecting the Star Formation Rate versus Stellar Mass Relation Using Hα and Hβ Emission Lines at z $\sim$ 2. *Astrophysical Journal*, 815(2):98, December 2015.

[220] W. Fong et al. Demographics of the Galaxies Hosting Short-duration Gamma-Ray Bursts. *Astrophysical Journal*, 769(1):56, May 2013.

[221] Edo Berger. Short-Duration Gamma-Ray Bursts. *Annual Review of Astron and Astrophys*, 52:43–105, August 2014.

[222] D. B. Fox et al. The afterglow of GRB 050709 and the nature of the short-hard γ-ray bursts. *Nature*, 437(7060):845–850, October 2005.

[223] E. Berger et al. The afterglow and elliptical host galaxy of the short γ-ray burst GRB 050724. *Nature*, 438(7070):988–990, December 2005.

[224] J. S. Bloom et al. Closing in on a Short-Hard Burst Progenitor: Constraints from Early-Time Optical Imaging and Spectroscopy of a Possible Host Galaxy of GRB 050509b. *Astrophysical Journal*, 638(1):354–368, February 2006.

[225] E. Berger. The Host Galaxies of Short-Duration Gamma-Ray Bursts: Luminosities, Metallicities, and Star-Formation Rates. *Astrophysical Journal*, 690(1):231–237, January 2009.

[226] Edo Berger. The environments of short-duration gamma-ray bursts and implications for their progenitors. *New Astronomy Review*, 55(1-2):1–22, January 2011.

[227] L. A. Antonelli et al. GRB 090426: the farthest short gamma-ray burst? *Astronomy and Astrophysics*, 507(3):L45–L48, December 2009.

[228] Emily M. Levesque et al. GRB090426: the environment of a rest-frame 0.35-s gamma-ray burst at a redshift of 2.609. *Monthly Notices of the RAS*, 401(2):963–972, January 2010.

[229] A. Cucchiara et al. Gemini Spectroscopy of the Short-hard Gamma-Ray Burst GRB 130603B Afterglow and Host Galaxy. *Astrophysical Journal*, 777(2):94, November 2013.

[230] A. de Ugarte Postigo et al. Spectroscopy of the short-hard GRB 130603B. The host galaxy and environment of a compact object merger. *Astronomy and Astrophysics*, 563:A62, March 2014.

[231] E. Berger et al. A New Population of High-Redshift Short-Duration Gamma-Ray Bursts. *Astrophysical Journal*, 664(2):1000–1010, August 2007.

[232] E. Berger et al. Afterglows, Redshifts, and Properties of Swift Gamma-Ray Bursts. *Astrophysical Journal*, 634(1):501–508, November 2005.

[233] P. Jakobsson et al. A mean redshift of 2.8 for Swift gamma-ray bursts. *Astronomy and Astrophysics*, 447(3):897–903, March 2006.

[234] Maria R. Drout et al. The First Systematic Study of Type Ibc Supernova Multi-band Light Curves. *Astrophysical Journal*, 741(2):97, November 2011.

[235] M. Della Valle et al. An enigmatic long-lasting γ-ray burst not accompanied by a bright supernova. *Nature*, 444(7122):1050–1052, December 2006.

[236] Johan P. U. Fynbo et al. No supernovae associated with two long-duration γ-ray bursts. *Nature*, 444(7122):1047–1049, December 2006.

[237] A. Gal-Yam et al. A novel explosive process is required for the γ-ray burst GRB 060614. *Nature*, 444(7122):1053–1055, December 2006.

[238] N. Gehrels et al. A new γ-ray burst classification scheme from GRB060614. *Nature*, 444(7122):1044–1046, December 2006.

[239] W. Fong et al. The Optical Afterglow and z = 0.92 Early-type Host Galaxy of the Short GRB 100117A. *Astrophysical Journal*, 730(1):26, March 2011.

[240] Edo Berger. Short-Duration Gamma-Ray Bursts. *Annual Review of Astron and Astrophys*, 52:43–105, August 2014.

[241] Eric F. Bell, Daniel H. McIntosh, Neal Katz, and Martin D. Weinberg. The Optical and Near-Infrared Properties of Galaxies. I. Luminosity and Stellar Mass Functions. *Astrophysical Journals*, 149(2):289–312, December 2003.

[242] O. Ilbert et al. Galaxy Stellar Mass Assembly Between $0.2 < z < 2$ from the S-COSMOS Survey. *Astrophysical Journal*, 709(2):644–663, February 2010.

[243] D. A. Perley et al. The Luminous Infrared Host Galaxy of Short-duration GRB 100206A. *Astrophysical Journal*, 758(2):122, October 2012.

[244] E. Berger et al. The Afterglow and ULIRG Host Galaxy of the Dark Short GRB 120804A. *Astrophysical Journal*, 765(2):121, March 2013.

[245] K. I. Caputi et al. Further constraints on the evolution of K_s-selected galaxies in the GOODS/CDFS field. *Monthly Notices of the RAS*, 366(2):609–623, February 2006.

[246] Emeric Le Floc'h et al. Infrared Luminosity Functions from the Chandra Deep Field-South: The Spitzer View on the History of Dusty Star Formation at $0 <\sim z <\sim 1$. *Astrophysical Journal*, 632(1):169–190, October 2005.

[247] K. I. Caputi et al. The Infrared Luminosity Function of Galaxies at Redshifts z = 1 and z ~2 in the GOODS Fields. *Astrophysical Journal*, 660(1):97–116, May 2007.

[248] E. Berger. A SHORT GAMMA-RAY BURST "NO-HOST" PROBLEM? INVESTIGATING LARGE PROGENITOR OFFSETS FOR SHORT GRBs WITH OPTICAL AFTERGLOWS. *The Astrophysical Journal*, 722(2):1946–1961, October 2010.

[249] W. Fong and E. Berger. The Locations of Short Gamma-Ray Bursts as Evidence for Compact Object Binary Progenitors. *Astrophysical Journal*, 776(1):18, October 2013.

[250] C. N. Leibler and E. Berger. The Stellar Ages and Masses of Short Gamma-ray Burst Host Galaxies: Investigating the Progenitor Delay Time Distribution and the Role of Mass and Star Formation in the Short Gamma-ray Burst Rate. *Astrophysical Journal*, 725(1):1202–1214, December 2010.

[251] W. Fong, E. Berger, and D. B. Fox. Hubble Space Telescope Observations of Short Gamma-Ray Burst Host Galaxies: Morphologies, Offsets, and Local Environments. *Astrophysical Journal*, 708(1):9–25, January 2010.

[252] Ross P. Church, Andrew J. Levan, Melvyn B. Davies, and Nial Tanvir. Implications for the origin of short gamma-ray bursts from their observed positions around their host galaxies. *Monthly Notices of the RAS*, 413(3):2004–2014, May 2011.

[253] J. S. Bloom, S. R. Kulkarni, and S. G. Djorgovski. The Observed Offset Distribution of Gamma-Ray Bursts from Their Host Galaxies: A Robust Clue to the Nature of the Progenitors. *Astronomical Journal*, 123(3):1111–1148, March 2002.

[254] José L. Prieto, Krzysztof Z. Stanek, and John F. Beacom. Characterizing Supernova Progenitors via the Metallicities of their Host Galaxies, from Poor Dwarfs to Rich Spirals. *Astrophysical Journal*, 673(2):999–1008, February 2008.

[255] E. Berger. A Short Gamma-ray Burst "No-host" Problem? Investigating Large Progenitor Offsets for Short GRBs with Optical Afterglows. *Astrophysical Journal*, 722(2):1946–1961, October 2010.

[256] Joshua S. Bloom, Steinn Sigurdsson, and Onno R. Pols. The spatial distribution of coalescing neutron star binaries: implications for gamma-ray bursts. *Monthly Notices of the RAS*, 305(4):763–769, May 1999.

[257] Krzysztof Belczynski et al. A Study of Compact Object Mergers as Short Gamma-Ray Burst Progenitors. *Astrophysical Journal*, 648(2):1110–1116, September 2006.

[258] Chris Fryer and Vassiliki Kalogera. Double Neutron Star Systems and Natal Neutron Star Kicks. *Astrophysical Journal*, 489(1):244–253, November 1997.

[259] Chris Fryer, Adam Burrows, and Willy Benz. Population Syntheses for Neutron Star Systems with Intrinsic Kicks. *Astrophysical Journal*, 496(1):333–351, March 1998.

[260] Chen Wang, Dong Lai, and J. L. Han. Neutron Star Kicks in Isolated and Binary Pulsars: Observational Constraints and Implications for Kick Mechanisms. *Astrophysical Journal*, 639(2):1007–1017, March 2006.

[261] Tsing-Wai Wong, Bart Willems, and Vassiliki Kalogera. Constraints on Natal Kicks in Galactic Double Neutron Star Systems. *Astrophysical Journal*, 721(2):1689–1701, October 2010.

[262] M. Boquien et al. CIGALE: a python Code Investigating GALaxy Emission. *Astronomy and Astrophysics*, 622:A103, February 2019.

[263] Ryan Magee et al. First Demonstration of Early Warning Gravitational-wave Alerts. *Astrophysical Journall*, 910(2):L21, April 2021.

[264] B. P. Abbott et al. Low-latency gravitational-wave alerts for multimessenger astronomy during the second advanced LIGO and virgo observing run. 875(2):161, apr 2019.

[265] Neil J Cornish and Tyson B Littenberg. Bayeswave: Bayesian inference for gravitational wave bursts and instrument glitches. *Classical and Quantum Gravity*, 32(13):135012, June 2015.

[266] Reed Essick, Geoffrey Mo, and Erik Katsavounidis. A coincidence null test for poisson-distributed events. *Phys. Rev. D*, 103:042003, February 2021.

[267] S Chatterji, L Blackburn, G Martin, and E Katsavounidis. Multiresolution techniques for the detection of gravitational-wave bursts. *Classical and Quantum Gravity*, 21(20):S1809–S1818, September 2004.

[268] Lindy Blackburn. Kleine-welle algorithm. `https://dcc.ligo.org/public/0027/T060221/000/T060221-00.pdf`, 2007.

[269] The LIGO Scientific Collaboration et al. Search for Gravitational Waves Associated with Gamma-Ray Bursts Detected by Fermi and Swift During the LIGO-Virgo Run O3a. *arXiv e-prints*, page arXiv:2010.14550, October 2020.

[270] R. Coyne. *LIGO GRB searches in the aLIGO Era: An Optimized Burst Database and a New Method for Detecting Intermediate-Duration GWs*. PhD thesis, The George Washington University, 2015.

[271] I. W. Harry and S. Fairhurst. Targeted coherent search for gravitational waves from compact binary coalescences. *Phys. Rev. D*, 83:084002, April 2011.

[272] Williamson, A. R. et al. Improved methods for detecting gravitational waves associated with short gamma-ray bursts. *Phys. Rev. D*, 90:122004, December 2014.

[273] Alex Nitz et al. gwastro/pycbc: Pycbc, July 2020.

[274] LIGO Scientific Collaboration. LIGO Algorithm Library, 2018.

[275] William H Lee and Enrico Ramirez-Ruiz. The progenitors of short gamma-ray bursts. *New Journal of Physics*, 9(1):17–17, January 2007.

[276] Gilbert Vedrenne and Jean-Luc Atteia. *Gamma-ray bursts: The brightest explosions in the universe*. Springer Science & Business Media, 2009.

[277] Collin Capano, Ian Harry, Stephen Privitera, and Alessandra Buonanno. Implementing a search for gravitational waves from binary black holes with nonprecessing spin. *Phys. Rev. D*, 93:124007, June 2016.

[278] Husa, Sascha et al. Frequency-domain gravitational waves from nonprecessing black-hole binaries. i. new numerical waveforms and anatomy of the signal. *Phys. Rev. D*, 93:044006, February 2016.

[279] Khan, Sebastian et al. Frequency-domain gravitational waves from nonprecessing black-hole binaries. ii. a phenomenological model for the advanced detector era. *Phys. Rev. D*, 93:044007, February 2016.

[280] Feryal Özel, Dimitrios Psaltis, Ramesh Narayan, and Jeffrey E. McClintock. The Black Hole Mass Distribution in the Galaxy. *Astrophysical Journal*, 725(2):1918–1927, December 2010.

[281] Laura Kreidberg, Charles D. Bailyn, Will M. Farr, and Vicky Kalogera. Mass Measurements of Black Holes in X-Ray Transients: Is There a Mass Gap? *Astrophysical Journal*, 757(1):36, September 2012.

[282] Vassiliki Kalogera and Gordon Baym. The maximum mass of a neutron star. *The Astrophysical Journal*, 470(1):L61–L64, October 1996.

[283] Kip S. Thorne. Disk-Accretion onto a Black Hole. II. Evolution of the Hole. *Astrophysical Journal*, 191:507–520, July 1974.

[284] M. Burgay et al. An increased estimate of the merger rate of double neutron stars from observations of a highly relativistic system. *Nature*, 426(6966):531–533, December 2003.

[285] Francesco Pannarale and Frank Ohme. Prospects for Joint Gravitational-wave and Electromagnetic Observations of Neutron-star-Black-hole Coalescing Binaries. *Astrophysical Journall*, 791(1):L7, August 2014.

[286] Patrick J. Sutton et al. X-Pipeline: an analysis package for autonomous gravitational-wave burst searches. *New Journal of Physics*, 12(5):053034, May 2010.

[287] Michał Wąs, Patrick J. Sutton, Gareth Jones, and Isabel Leonor. Performance of an externally triggered gravitational-wave burst search. *Phys. Rev. D*, 86:022003, July 2012.

[288] L Cadonati. Coherent waveform consistency test for LIGO burst candidates. *Classical and Quantum Gravity*, 21(20):S1695–S1703, September 2004.

[289] Linqing Wen and Bernard F Schutz. Coherent network detection of gravitational waves: the redundancy veto. *Classical and Quantum Gravity*, 22(18):S1321–S1335, September 2005.

[290] Chatterji, Shourov et al. Coherent network analysis technique for discriminating gravitational-wave bursts from instrumental noise. *Phys. Rev. D*, 74:082005, October 2006.

[291] Stephen Fairhurst. Triangulation of gravitational wave sources with a network of detectors. *New Journal of Physics*, 11(12):123006, December 2009.

[292] Thomas M. Koshut et al. Gamma-Ray Burst Precursor Activity as Observed with BATSE. *Astrophysical Journal*, 452:145, October 1995.

[293] M. A. Aloy et al. Relativistic Jets from Collapsars. *Astrophysical Journall*, 531(2):L119–L122, March 2000.

[294] Weiqun Zhang, S. E. Woosley, and A. I. MacFadyen. Relativistic Jets in Collapsars. *Astrophysical Journal*, 586(1):356–371, March 2003.

[295] Davide Lazzati. Precursor activity in bright, long BATSE gamma-ray bursts. *Monthly Notices of the RAS*, 357(2):722–731, February 2005.

[296] D. Burlon et al. Precursors in Swift Gamma Ray Bursts with Redshift. *Astrophysical Journall*, 685(1):L19, September 2008.

[297] Davide Lazzati, Brian J. Morsony, and Mitchell C. Begelman. Very High Efficiency Photospheric Emission in Long-Duration γ-Ray Bursts. *Astrophysical Journall*, 700(1):L47–L50, July 2009.

[298] Gilbert Vedrenne and Jean-Luc Atteia. *Gamma-Ray Bursts*. 2009.

[299] David Radice et al. Characterizing the Gravitational Wave Signal from Core-collapse Supernovae. *Astrophysical Journall*, 876(1):L9, May 2019.

[300] B. P. Abbott et al. All-sky search for short gravitational-wave bursts in the second Advanced LIGO and Advanced Virgo run. *Physical Review D*, 100(2):024017, July 2019.

[301] S. Klimenko, S. Mohanty, M. Rakhmanov, and G. Mitselmakher. Constraint likelihood analysis for a network of gravitational wave detectors. *Phys. Rev. D*, 72:122002, December 2005.

[302] B. P. Abbott et al. Search for gravitational waves associated with gamma-ray bursts during the first advanced LIGO observing run and implications for the origin of GRB 150906b. *The Astrophysical Journal*, 841(2):89, May 2017.

[303] B. P. Abbott et al. Search for gravitational-wave signals associated with gamma-ray bursts during the second observing run of advanced LIGO and advanced virgo. *The Astrophysical Journal*, 886(1):75, November 2019.

[304] J. Abadie et al. SEARCH FOR GRAVITATIONAL WAVES ASSOCIATED WITH GAMMA-RAY BURSTS DURING LIGO SCIENCE RUN 6 AND VIRGO SCIENCE RUNS 2 AND 3. *The Astrophysical Journal*, 760(1):12, October 2012.

[305] Maurice H. P. M. van Putten. Proposed source of gravitational radiation from a torus around a black hole. *Phys. Rev. Lett.*, 87:091101, August 2001.

[306] van Putten, Maurice H. P. M. et al. On the origin of short GRBs with extended emission and long GRBs without associated SN. *Monthly Notices of the Royal Astronomical Society: Letters*, 444(1):L58–L62, 08 2014.

[307] B. P. Abbott et al. Search for Gravitational-wave Signals Associated with Gamma-Ray Bursts during the Second Observing Run of Advanced LIGO and Advanced Virgo. *Astrophysical Journal*, 886(1):75, November 2019.

[308] Richard Dekany et al. The Zwicky Transient Facility: Observing System. *Publications of the ASP*, 132(1009):038001, March 2020.

[309] S. Antier et al. GRANDMA observations of advanced LIGO's and advanced Virgo's third observational campaign. *Monthly Notices of the RAS*, 497(4):5518–5539, October 2020.

[310] B. P. Gompertz et al. The Diversity of Kilonova Emission in Short Gamma-Ray Bursts. *Astrophysical Journal*, 860(1):62, June 2018.

[311] Kyohei Kawaguchi, Masaru Shibata, and Masaomi Tanaka. Diversity of Kilonova Light Curves. *Astrophysical Journal*, 889(2):171, February 2020.

[312] David J. Schlegel, Douglas P. Finkbeiner, and Marc Davis. Maps of Dust Infrared Emission for Use in Estimation of Reddening and Cosmic Microwave Background Radiation Foregrounds. *Astrophysical Journal*, 500(2):525–553, June 1998.

[313] D. A. Kann et al. The Afterglows of Swift-era Gamma-Ray Bursts. II. Type I GRB versus Type II GRB Optical Afterglows. *Astrophysical Journal*, 734(2):96, June 2011.

[314] A. Nicuesa Guelbenzu et al. Multi-color observations of short GRB afterglows: 20 events observed between 2007 and 2010. *Astronomy and Astrophysics*, 548:A101, December 2012.

[315] S. Agayeva et al. Grandma: a network to coordinate them all. *arXiv e-prints*, page arXiv:2008.03962, August 2020.

[316] Michael W. Coughlin et al. Optimizing searches for electromagnetic counterparts of gravitational wave triggers. *Monthly Notices of the RAS*, 478(1):692–702, July 2018.

[317] K. M. Gó et al.rski et al. HEALPix: A Framework for High-Resolution Discretization and Fast Analysis of Data Distributed on the Sphere. *Astrophysical Journal*, 622(2):759–771, April 2005.

[318] Michael W. Coughlin et al. Optimizing multitelescope observations of gravitational-wave counterparts. *Monthly Notices of the RAS*, 489(4):5775–5783, November 2019.

[319] J. G. Ducoin, D. Corre, N. Leroy, and E. Le Floch. Optimizing gravitational waves follow-up using galaxies stellar mass. *Monthly Notices of the RAS*, 492(4):4768–4779, March 2020.

[320] P. A. Evans et al. Swift follow-up of gravitational wave triggers: results from the first aLIGO run and optimization for the future. *Monthly Notices of the RAS*, 462(2):1591–1602, October 2016.

[321] Iair Arcavi et al. Optical Follow-up of Gravitational-wave Events with Las Cumbres Observatory. *Astrophysical Journall*, 848(2):L33, October 2017.

[322] L. Salmon, L. Hanlon, R. M. Jeffrey, and A. Martin-Carrillo. Web application for galaxy-targeted follow-up of electromagnetic counterparts to gravitational wave sources. *Astronomy and Astrophysics*, 634:A32, February 2020.

[323] M. Celeste Artale et al. Host galaxies of merging compact objects: mass, star formation rate, metallicity, and colours. *Monthly Notices of the RAS*, 487(2):1675–1688, August 2019.

[324] Mattia Toffano et al. The host galaxies of double compact objects across cosmic time. *Monthly Notices of the RAS*, page 2085, September 2019.

[325] Michela Mapelli et al. The host galaxies of double compact objects merging in the local Universe. *Monthly Notices of the RAS*, 481(4):5324–5330, December 2018.

[326] C. N. Leibler and E. Berger. The Stellar Ages and Masses of Short Gamma-ray Burst Host Galaxies: Investigating the Progenitor Delay Time Distribution and the Role of Mass and Star Formation in the Short Gamma-ray Burst Rate. *Astrophysical Journal*, 725(1):1202–1214, December 2010.

[327] W. Fong et al. Demographics of the Galaxies Hosting Short-duration Gamma-Ray Bursts. *Astrophysical Journal*, 769(1):56, May 2013.

[328] Myungshin Im et al. Distance and Properties of NGC 4993 as the Host Galaxy of the Gravitational-wave Source GW170817. *Astrophysical Journall*, 849(1):L16, November 2017.

[329] P. K. Blanchard et al. The Electromagnetic Counterpart of the Binary Neutron Star Merger LIGO/Virgo GW170817. VII. Properties of the Host Galaxy and Constraints on the Merger Timescale. *Astrophysical Journall*, 848(2):L22, October 2017.

[330] Jens Hjorth et al. The Distance to NGC 4993: The Host Galaxy of the Gravitational-wave Event GW170817. *Astrophysical Journall*, 848(2):L31, October 2017.

[331] A. J. Levan et al. The Environment of the Binary Neutron Star Merger GW170817. *Astrophysical Journall*, 848(2):L28, October 2017.

[332] Y. C. Pan et al. The Old Host-galaxy Environment of SSS17a, the First Electromagnetic Counterpart to a Gravitational-wave Source. *Astrophysical Journall*, 848(2):L30, October 2017.

[333] E. Troja et al. A luminous blue kilonova and an off-axis jet from a compact binary merger at z = 0.1341. *Nature Communications*, 9:4089, October 2018.

[334] Om Sharan Salafia et al. Where and When: Optimal Scheduling of the Electromagnetic Follow-up of Gravitational-wave Events Based on Counterpart Light-curve Models. *Astrophysical Journal*, 846(1):62, September 2017.

[335] David O. Cook et al. Census of the Local Universe (CLU) Narrowband Survey. I. Galaxy Catalogs from Preliminary Fields. *Astrophysical Journal*, 880(1):7, July 2019.

[336] G. Dalya et al. GLADE: A galaxy catalogue for multimessenger searches in the advanced gravitational-wave detector era. *Monthly Notices of the RAS*, 479(2):2374–2381, September 2018.

[337] Jason A. Cardelli, Geoffrey C. Clayton, and John S. Mathis. The Relationship between Infrared, Optical, and Ultraviolet Extinction. *Astrophysical Journal*, 345:245, October 1989.

[338] E. L. Fitzpatrick and D. Massa. An Analysis of the Shapes of Interstellar Extinction Curves. V. The IR-through-UV Curve Morphology. *Astrophysical Journal*, 663(1):320–341, July 2007.

[339] G. Bruzual and S. Charlot. Stellar population synthesis at the resolution of 2003. *Monthly Notices of the RAS*, 344(4):1000–1028, October 2003.

[340] Claudia Maraston. Evolutionary population synthesis: models, analysis of the ingredients and application to high-z galaxies. *Monthly Notices of the RAS*, 362(3):799–825, September 2005.

[341] Hsin-Yu Chen et al. Distance measures in gravitational-wave astrophysics and cosmology. *arXiv e-prints*, page arXiv:1709.08079, September 2017.

[342] T. Kettlety et al. Galaxy and mass assembly (GAMA): the consistency of GAMA and WISE derived mass-to-light ratios. *Monthly Notices of the RAS*, 473(1):776–783, January 2018.

[343] Mark A. Norris et al. Being WISE. I. Validating Stellar Population Models and M $_{sstarf}$/L Ratios at 3.4 and 4.6 μm. *Astrophysical Journal*, 797(1):55, December 2014.

[344] R. M. Cutri and et al. VizieR Online Data Catalog: AllWISE Data Release (Cutri+ 2013). *VizieR Online Data Catalog*, page II/328, January 2014.

[345] T. H. Jarrett et al. Extending the Nearby Galaxy Heritage with WISE: First Results from the WISE Enhanced Resolution Galaxy Atlas. *Astronomical Journal*, 145(1):6, January 2013.

[346] A. Ruiz et al. Analysis of Spitzer-IRS spectra of hyperluminous infrared galaxies. *Astronomy and Astrophysics*, 549:A125, January 2013.

[347] L. Burtscher et al. Obscuration in active galactic nuclei: near-infrared luminosity relations and dust colors. *Astronomy and Astrophysics*, 578:A47, June 2015.

[348] David B. Sanders. Infrared Emission from AGN. In Y. Terzian, E. Khachikian, and D. Weedman, editors, *Activity in Galaxies and Related Phenomena*, volume 194 of *IAU Symposium*, page 25, January 1999.

[349] Daniel Stern et al. Mid-infrared Selection of Active Galactic Nuclei with the Wide-Field Infrared Survey Explorer. I. Characterizing WISE-selected Active Galactic Nuclei in COSMOS. *Astrophysical Journal*, 753(1):30, July 2012.

[350] R. J. Assef et al. The WISE AGN Catalog. *Astrophysical Journals*, 234(2):23, February 2018.

[351] O. Ilbert et al. Cosmos Photometric Redshifts with 30-Bands for 2-deg^2. *Astrophysical Journal*, 690:1236–1249, January 2009.

[352] D. Calzetti et al. The Dust Content and Opacity of Actively Star-forming Galaxies. *Astrophysical Journal*, 533:682–695, April 2000.

[353] P. Schechter. An analytic expression for the luminosity function for galaxies. *Astrophysical Journal*, 203:297–306, January 1976.

[354] A. H. Wright et al. Galaxy And Mass Assembly (GAMA): the galaxy stellar mass function to z = 0.1 from the r-band selected equatorial regions. *Monthly Notices of the RAS*, 470(1):283–302, September 2017.

[355] Neil Gehrels et al. Galaxy Strategy for LIGO-Virgo Gravitational Wave Counterpart Searches. *Astrophysical Journal*, 820(2):136, April 2016.

[356] B. P. Abbott et al. Prospects for observing and localizing gravitational-wave transients with Advanced LIGO, Advanced Virgo and KAGRA. *Living Reviews in Relativity*, 21(1):3, April 2018.

[357] Shaon Ghosh et al. Tiling strategies for optical follow-up of gravitational-wave triggers by telescopes with a wide field of view. *Astronomy and Astrophysics*, 592:A82, August 2016.

[358] J. G. Ducoin and MANGROVE Team. LIGO/Virgo S200213t: MANGROVE catalog galaxy ranking. *GRB Coordinates Network*, 27059:1, February 2020.

[359] Tim Dietrich and Maximiliano Ujevic. Modeling dynamical ejecta from binary neutron star mergers and implications for electromagnetic counterparts. *Classical and Quantum Gravity*, 34(10):105014, April 2017.

[360] S. Antier et al. The first six months of the Advanced LIGO's and Advanced Virgo's third observing run with GRANDMA. *Monthly Notices of the RAS*, 492(3):3904–3927, March 2020.

[361] Amy Lien et al. The Third Swift Burst Alert Telescope Gamma-Ray Burst Catalog. *Astrophysical Journal*, 829(1):7, September 2016.

[362] Jens Hjorth et al. The optical afterglow of the short γ-ray burst GRB 050709. *Nature*, 437(7060):859–861, October 2005.

[363] A. de Ugarte Postigo et al. GRB 060121: Implications of a Short-/Intermediate-Duration γ-Ray Burst at High Redshift. *Astrophysical Journall*, 648(2):L83–L87, September 2006.

[364] A. J. Levan et al. The Faint Afterglow and Host Galaxy of the Short-Hard GRB 060121. *Astrophysical Journall*, 648(1):L9–L12, September 2006.

[365] S. McGlynn et al. GRB 070707: the first short gamma-ray burst observed by INTEGRAL. *Astronomy and Astrophysics*, 486(2):405–410, August 2008.

[366] S. Piranomonte et al. The short GRB 070707 afterglow and its very faint host galaxy. *Astronomy and Astrophysics*, 491(1):183–188, November 2008.

[367] Ashley A. Chrimes et al. Investigating a population of infrared-bright gamma-ray burst host galaxies. *Monthly Notices of the RAS*, 478(1):2–27, July 2018.

[368] K. C. Chambers et al. The Pan-STARRS1 Surveys. *arXiv e-prints*, page arXiv:1612.05560, December 2016.

[369] Bradley C. Whitmore et al. Version 1 of the Hubble Source Catalog. *Astronomical Journal*, 151(6):134, June 2016.

[370] J. S. Bloom, S. R. Kulkarni, and S. G. Djorgovski. The observed offset distribution of gamma-ray bursts from their host galaxies: A robust clue to the nature of the progenitors. *The Astronomical Journal*, 123(3):1111–1148, March 2002.

[371] András Kovács and István Szapudi. Star-galaxy separation strategies for WISE-2MASS all-sky infrared galaxy catalogues. *Monthly Notices of the RAS*, 448(2):1305–1313, April 2015.

[372] N. Gehrels et al. A short γ-ray burst apparently associated with an elliptical galaxy at redshift z = 0.225. *Nature*, 437(7060):851–854, October 2005.

[373] J. Gorosabel et al. The short-duration GRB 050724 host galaxy in the context of the long-duration GRB hosts. *Astronomy and Astrophysics*, 450(1):87–92, April 2006.

[374] P. D'Avanzo et al. The optical afterglows and host galaxies of three short/hard gamma-ray bursts. *Astronomy and Astrophysics*, 498(3):711–721, May 2009.

[375] S. McBreen et al. Optical and near-infrared follow-up observations of four Fermi/LAT GRBs: redshifts, afterglows, energetics, and host galaxies. *Astronomy and Astrophysics*, 516:A71, June 2010.

[376] E. Troja et al. An Achromatic Break in the Afterglow of the Short GRB 140903A: Evidence for a Narrow Jet. *Astrophysical Journal*, 827(2):102, August 2016.

[377] W. Fong et al. The Afterglow and Early-type Host Galaxy of the Short GRB 150101B at z = 0.1343. *Astrophysical Journal*, 833(2):151, December 2016.

[378] Chen Xie et al. On the Host Galaxy of GRB 150101B and the Associated Active Galactic Nucleus. *Astrophysical Journall*, 824(2):L17, June 2016.

[379] Edward F. Schlafly and Douglas P. Finkbeiner. Measuring Reddening with Sloan Digital Sky Survey Stellar Spectra and Recalibrating SFD. *Astrophysical Journal*, 737(2):103, August 2011.

[380] M. Boquien et al. CIGALE: a python Code Investigating GALaxy Emission. *Astronomy and Astrophysics*, 622:A103, February 2019.

[381] S. D. Vergani et al. Are long gamma-ray bursts biased tracers of star formation? Clues from the host galaxies of the Swift/BAT6 complete sample of LGRBs . I. Stellar mass at z < 1. *Astronomy and Astrophysics*, 581:A102, September 2015.

[382] C. Laigle et al. The COSMOS2015 Catalog: Exploring the $1 < z < 6$ Universe with Half a Million Galaxies. *Astrophysical Journals*, 224(2):24, June 2016.

[383] J. X. Prochaska, J. S. Bloom, H. W. Chen, and K. Hurley. GRB 050509b: physical properties of the candidate host galaxy. *GRB Coordinates Network*, 3399:1, January 2005.

[384] S. Covino et al. Optical emission from GRB 050709: a short/hard GRB in a star-forming galaxy. *Astronomy and Astrophysics*, 447(2):L5–L8, February 2006.

[385] J. X. Prochaska et al. GRB 050724: secure host redshift from Keck. *GRB Coordinates Network*, 3700:1, January 2005.

[386] P. D'Avanzo et al. GRB050724: VLT observations of the variable source. *GRB Coordinates Network*, 3690:1, January 2005.

[387] E. Berger and A. M. Soderberg. GRB 051221: redshift from Gemini. *GRB Coordinates Network*, 4384:1, January 2005.

[388] A. M. Soderberg et al. The Afterglow, Energetics, and Host Galaxy of the Short-Hard Gamma-Ray Burst 051221a. *Astrophysical Journal*, 650(1):261–271, October 2006.

[389] E. Berger et al. A New Population of High-Redshift Short-Duration Gamma-Ray Bursts. *Astrophysical Journal*, 664(2):1000–1010, August 2007.

[390] P. A. Price, E. Berger, and D. B. Fox. GRB 060614: redshift. *GRB Coordinates Network*, 5275:1, January 2006.

[391] S. T. Holland. GRB 060614: Swift/UVOT observations. *GRB Coordinates Network*, 5255:1, January 2006.

[392] A. Cucchiara, D. B. Fox, E. Berger, and P. A. Price. GRB00801: host galaxy redshift. *GRB Coordinates Network*, 5470:1, January 2006.

[393] D. Malesani et al. GRB 061006: VLT observation. *GRB Coordinates Network*, 5705:1, January 2006.

[394] P. D'Avanzo, S. Piranomonte, G. Chincarini, and L. Stella. GRB 061201: VLT optical observations. *GRB Coordinates Network*, 5884:1, January 2006.

[395] P. A. Evans, K. L. Page, and J. A. Kennea. GRB 061217 - Swift/XRT position correction. *GRB Coordinates Network*, 5947:1, January 2006.

[396] D. A. Perley et al. GRB 070429B: probable host galaxy and redshift. *GRB Coordinates Network*, 7140:1, January 2007.

[397] J. F. Graham et al. GRB 070714B: host galaxy spectroscopic redshift. *GRB Coordinates Network*, 6836:1, January 2007.

[398] D. A. Perley, J. S. Bloom, C. Thoene, and N. R. Butler. GRB 070714B: Keck observations. *GRB Coordinates Network*, 6652:1, January 2007.

[399] A. Cucchiara et al. GRB070724: host galaxy redshift. *GRB Coordinates Network*, 6665:1, January 2007.

[400] E. Berger, S. B. Cenko, D. B. Fox, and A. Cucchiara. Discovery of the Very Red Near-Infrared and Optical Afterglow of the Short-Duration GRB 070724A. *Astrophysical Journal*, 704(1):877–882, October 2009.

[401] E. Berger. A Short Gamma-ray Burst "No-host" Problem? Investigating Large Progenitor Offsets for Short GRBs with Optical Afterglows. *Astrophysical Journal*, 722(2):1946–1961, October 2010.

[402] D. A. Perley et al. GRB 070809: Keck imaging. *GRB Coordinates Network*, 6739:1, January 2007.

[403] P. D'Avanzo et al. The optical afterglows and host galaxies of three short/hard gamma-ray bursts. *Astronomy and Astrophysics*, 498(3):711–721, May 2009.

[404] P. D'Avanzo et al. GRB 071227: optical afterglow. *GRB Coordinates Network*, 7157:1, January 2008.

[405] A. Rowlinson et al. Discovery of the afterglow and host galaxy of the low-redshift short GRB 080905A. *Monthly Notices of the RAS*, 408(1):383–391, October 2010.

[406] Emily M. Levesque et al. GRB090426: the environment of a rest-frame 0.35-s gamma-ray burst at a redshift of 2.609. *Monthly Notices of the RAS*, 401(2):963–972, January 2010.

[407] S. R. Oates and J. R. Cummings. GRB090426 Swift/UVOT observations. *GRB Coordinates Network*, 9265:1, January 2009.

[408] A. Rau, S. McBreen, and T. Kruehler. GRB090510: VLT/FORS2 spectroscopic redshift. *GRB Coordinates Network*, 9353:1, January 2009.

[409] S. McBreen et al. Optical and near-infrared follow-up observations of four Fermi/LAT GRBs: redshifts, afterglows, energetics, and host galaxies. *Astronomy and Astrophysics*, 516:A71, June 2010.

[410] W. Fong et al. The Optical Afterglow and z = 0.92 Early-type Host Galaxy of the Short GRB 100117A. *Astrophysical Journal*, 730(1):26, March 2011.

[411] D. A. Perley et al. The Luminous Infrared Host Galaxy of Short-duration GRB 100206A. *Astrophysical Journal*, 758(2):122, October 2012.

[412] W. Fong et al. Demographics of the Galaxies Hosting Short-duration Gamma-Ray Bursts. *Astrophysical Journal*, 769(1):56, May 2013.

[413] J. Selsing et al. The X-shooter GRB afterglow legacy sample (XS-GRB). *Astronomy and Astrophysics*, 623:A92, March 2019.

[414] S. R. Oates et al. GRB 100816A: Swift detection of a possibly short burst with optical afterglow. *GRB Coordinates Network*, 11102:1, January 2010.

[415] R. Chornock and E. Berger. GRB 101219A: gemini-north host redshift. *GRB Coordinates Network*, 11518:1, January 2011.

[416] D. Malesani. GRB 110106A: TNG redshift of the closeby galaxy. *GRB Coordinates Network*, 11530:1, January 2011.

[417] J. Selsing et al. The host galaxy of the short GRB 111117A at z = 2.211. Impact on the short GRB redshift distribution and progenitor channels. *Astronomy and Astrophysics*, 616:A48, August 2018.

[418] T. Sakamoto et al. Identifying the Location in the Host Galaxy of the Short GRB 111117A with the Chandra Subarcsecond Position. *Astrophysical Journal*, 766(1):41, March 2013.

[419] E. Berger et al. The Afterglow and ULIRG Host Galaxy of the Dark Short GRB 120804A. *Astrophysical Journal*, 765(2):121, March 2013.

[420] A. de Ugarte Postigo et al. Spectroscopy of the short-hard GRB 130603B. The host galaxy and environment of a compact object merger. *Astronomy and Astrophysics*, 563:A62, March 2014.

[421] R. Chornock and W. Fong. GRB 150120A: Gemini-N imaging and host redshift. *GRB Coordinates Network*, 17358:1, January 2015.

[422] E. Troja et al. An Achromatic Break in the Afterglow of the Short GRB 140903A: Evidence for a Narrow Jet. *Astrophysical Journal*, 827(2):102, August 2016.

[423] R. Chornock, W. Fong, and D. B. Fox. GRB 141212A: Gemini-N spectroscopy and photometry. *GRB Coordinates Network*, 17177:1, January 2014.

[424] W. Fong et al. The Afterglow and Early-type Host Galaxy of the Short GRB 150101B at z = 0.1343. *Astrophysical Journal*, 833(2):151, December 2016.

[425] D. A. Perley and N. J. McConnell. GRB 150424A: Keck detection of optical afterglow. *GRB Coordinates Network*, 17745:1, January 2015.

[426] T. Kruehler et al. GRB 160228A: GROND afterglow confirmation and X-shooter host candidate redshift. *GRB Coordinates Network*, 19186:1, January 2016.

[427] C. Delvaux, T. Schweyer, D. A. Kann, and J. Greiner. GRB 160228A: GROND Afterglow Candidate. *GRB Coordinates Network*, 19114:1, January 2016.

[428] A. Cucchiara and A. J. Levan. GRB160624A:possible GRB host redshift. *GRB Coordinates Network*, 19565:1, January 2016.

[429] G. P. Lamb et al. Short GRB 160821B: A Reverse Shock, a Refreshed Shock, and a Well-sampled Kilonova. *Astrophysical Journal*, 883(1):48, September 2019.

[430] D. Xu et al. GRB 160821B: NOT optical afterglow candidate. *GRB Coordinates Network*, 19834:1, January 2016.

[431] W. Fong and R. Chornock. GRB 161104A: Magellan imaging and spectroscopy. *GRB Coordinates Network*, 20168:1, January 2016.

[432] Z. Cano et al. GRB 161129A: GTC redshift of the likely host galaxy. *GRB Coordinates Network*, 20245:1, January 2016.

[433] N. P. M. Kuin and D. Kocevski. GRB 161129A: Swift/UVOT Detection. *GRB Coordinates Network*, 20217:1, January 2016.

[434] G. Paturel, P. Dubois, C. Petit, and F. Woelfel. Comparison LEDA/SIMBAD octobre 2002. Catalogue to be published in 2003. *LEDA*, page 0, January 2002.

[435] E. Berger et al. LIGO/Virgo G298048: Potential optical counterpart discovered by Swope telescope. *GRB Coordinates Network*, 21529:1, August 2017.

[436] K. Paterson et al. Discovery of the Optical Afterglow and Host Galaxy of Short GRB 181123B at z = 1.754: Implications for Delay Time Distributions. *Astrophysical Journall*, 898(2):L32, August 2020.

[437] W. Fong et al. The Broadband Counterpart of the Short GRB 200522A at z = 0.5536: A Luminous Kilonova or a Collimated Outflow with a Reverse Shock? *Astrophysical Journal*, 906(2):127, January 2021.

[438] J. S. Bloom et al. GRB 051210: Magellan imaging. *GRB Coordinates Network*, 4330:1, January 2005.

[439] A. J. Castro-Tirado et al. GRB 060801: optical observations at hanle and calar alto. *GRB Coordinates Network*, 5384:1, January 2006.

[440] E. Berger. GRB 061217: extended object in the revised XRT error circle. *GRB Coordinates Network*, 5949:1, January 2006.

[441] L. A. Antonelli et al. GRB070429B: VLT observations. *GRB Coordinates Network*, 6372:1, January 2007.

[442] E. Berger and D. L. Kaplan. GRB 070729: magellan NIR observations. *GRB Coordinates Network*, 6680:1, January 2007.

[443] A. J. Levan and N. R. Tanvir. GRB 100625A: Gemini candidate afterglow. *GRB Coordinates Network*, 10887:1, January 2010.

[444] D. A. Perley et al. GRB 101219A: gemini-south observations. *GRB Coordinates Network*, 11464:1, January 2010.

[445] D. Malesani et al. GRB 141212A: extended object within the XRT error circle. *GRB Coordinates Network*, 17170:1, January 2014.

[446] A. E. Nugent et al. The Distant, Galaxy Cluster Environment of the Short GRB 161104A at z $\sim$ 0.8 and a Comparison to the Short GRB Host Population. *Astrophysical Journal*, 904(1):52, November 2020.

[447] S.-K. Lee et al. The Estimation of Star Formation Rates and Stellar Population Ages of High-redshift Galaxies from Broadband Photometry. *Astrophysical Journal*, 725:1644–1651, December 2010.

[448] C. Maraston et al. Star formation rates and masses of z ˜ 2 galaxies from multicolour photometry. *Monthly Notices of the RAS*, 407:830–845, September 2010.

[449] J. Pforr, C. Maraston, and C. Tonini. Recovering galaxy stellar population properties from broad-band spectral energy distribution fitting. *Monthly Notices of the RAS*, 422:3285–3326, June 2012.

[450] M. Boquien, V. Buat, and V. Perret. Impact of star formation history on the measurement of star formation rates. *Astronomy and Astrophysics*, 571:A72, November 2014.

[451] G. Chabrier. Galactic Stellar and Substellar Initial Mass Function. *Publications of the ASP*, 115:763–795, July 2003.

[452] G. Bruzual and S. Charlot. Stellar population synthesis at the resolution of 2003. *Monthly Notices of the RAS*, 344:1000–1028, October 2003.

[453] R. Maiolino et al. AMAZE. I. The evolution of the mass-metallicity relation at z > 3. *Astronomy and Astrophysics*, 488:463–479, September 2008.

[454] Martin Asplund, Nicolas Grevesse, A. Jacques Sauval, and Pat Scott. The Chemical Composition of the Sun. *Annual Review of Astronomy and Astrophysics*, 47:481–522, September 2009.

[455] J. A. Cardelli, G. C. Clayton, and J. S. Mathis. The relationship between infrared, optical, and ultraviolet extinction. *Astrophysical Journal*, 345:245–256, October 1989.

[456] D. Calzetti. The effects of dust on the spectral energy distribution of star-forming galaxies. *New Astronomy Review*, 45:601–607, October 2001.

[457] D. Kashino et al. The FMOS-COSMOS Survey of Star-forming Galaxies at z ˜ 1.6. I. Hα-based Star Formation Rates and Dust Extinction. *Astrophysical Journall*, 777:L8, November 2013.

[458] A. Puglisi et al. Dust attenuation in z ˜ 1 galaxies from Herschel and 3D-HST Hα measurements. *Astronomy and Astrophysics*, 586:A83, February 2016.

[459] D. Corre et al. Investigation of dust attenuation and star formation activity in galaxies hosting GRBs. *Astronomy and Astrophysics*, 617:A141, October 2018.

[460] D. A. Dale et al. A Two-parameter Model for the Infrared/Submillimeter/Radio Spectral Energy Distributions of Galaxies and Active Galactic Nuclei. *Astrophysical Journal*, 784:83, March 2014.

[461] D. A. Dale and G. Helou. The Infrared Spectral Energy Distribution of Normal Star-forming Galaxies: Calibration at Far-Infrared and Submillimeter Wavelengths. *Astrophysical Journal*, 576:159–168, September 2002.

[462] J. A. Baldwin, M. M. Phillips, and R. Terlevich. Classification parameters for the emission-line spectra of extragalactic objects. *Publications of the ASP*, 93:5–19, February 1981.

[463] L. J. Kewley et al. Theoretical Modeling of Starburst Galaxies. *Astrophysical Journal*, 556:121–140, July 2001.

[464] T. Krü et al.hler et al. GRB hosts through cosmic time. VLT/X-Shooter emission-line spectroscopy of 96 γ-ray-burst-selected galaxies at 0.1 z 3.6. *Astronomy and Astrophysics*, 581:A125, September 2015.

[465] J. J. Condon. Radio emission from normal galaxies. *Annual Review of Astron and Astrophys*, 30:575–611, 1992.

[466] M. S. Yun, N. A. Reddy, and J. J. Condon. Radio Properties of Infrared-selected Galaxies in the IRAS 2 Jy Sample. *Astrophysical Journal*, 554:803–822, June 2001.

[467] E. F. Bell. Estimating Star Formation Rates from Infrared and Radio Luminosities: The Origin of the Radio-Infrared Correlation. *Astrophysical Journal*, 586:794–813, April 2003.

[468] J. Delhaize et al. The VLA-COSMOS 3 GHz Large Project: The infrared-radio correlation of star-forming galaxies and AGN to z 6. *Astronomy and Astrophysics*, 602:A4, June 2017.

[469] T. J. Galvin et al. The spectral energy distribution of powerful starburst galaxies - I. Modelling the radio continuum. *Monthly Notices of the RAS*, 474:779–799, February 2018.

[470] M. F. Skrutskie et al. The Two Micron All Sky Survey (2MASS). *Astronomical Journal*, 131(2):1163–1183, February 2006.

[471] J. Gorosabel et al. The short-duration GRB 050724 host galaxy in the context of the long-duration GRB hosts. *Astronomy and Astrophysics*, 450(1):87–92, April 2006.

[472] E. Berger et al. The afterglow and elliptical host galaxy of the short γ-ray burst GRB 050724. *Nature*, 438(7070):988–990, December 2005.

[473] V. Mangano et al. Swift observations of GRB 060614: an anomalous burst with a well behaved afterglow. *Astronomy and Astrophysics*, 470(1):105–118, July 2007.

[474] M. Della Valle et al. An enigmatic long-lasting γ-ray burst not accompanied by a bright supernova. *Nature*, 444(7122):1050–1052, December 2006.

[475] Jens Hjorth et al. The Optically Unbiased Gamma-Ray Burst Host (TOUGH) Survey. I. Survey Design and Catalogs. *Astrophysical Journal*, 756(2):187, September 2012.

[476] Luciana Bianchi, Bernie Shiao, and David Thilker. Revised Catalog of GALEX Ultraviolet Sources. I. The All-Sky Survey: GUVcat_AIS. *Astrophysical Journals*, 230(2):24, June 2017.

[477] R. G. McMahon et al. First Scientific Results from the VISTA Hemisphere Survey (VHS). *The Messenger*, 154:35–37, December 2013.

[478] J. F. Graham et al. GRB 070714B—Discovery of the Highest Spectroscopically Confirmed Short Burst Redshift. *Astrophysical Journal*, 698(2):1620–1629, June 2009.

[479] A. Nicuesa Guelbenzu et al. Another Short-burst Host Galaxy with an Optically Obscured High Star Formation Rate: The Case of GRB 071227. *Astrophysical Journal*, 789(1):45, July 2014.

[480] S. Klose et al. Deep ATCA and VLA Radio Observations of Short-GRB Host Galaxies. Constraints on Star Formation Rates, Afterglow Flux, and Kilonova Radio Flares. *Astrophysical Journal*, 887(2):206, December 2019.

[481] S. B. Pandey et al. A multiwavelength analysis of a collection of short-duration GRBs observed between 2012 and 2015. *Monthly Notices of the RAS*, 485(4):5294–5318, June 2019.

[482] M. J. Page et al. The XMM-Newton serendipitous ultraviolet source survey catalogue. *Monthly Notices of the RAS*, 426(2):903–926, October 2012.

[483] W. Fong. GRB 150101B / Swift J123205.1-105602: 9.8 GHz VLA observations. *GRB Coordinates Network*, 17288:1, January 2015.

[484] A. J. van der Horst et al. GRB 150101B/Swift J123205.1-105602: WSRT radio observation. *GRB Coordinates Network*, 17286:1, January 2015.

[485] Eran O. Ofek and Dale A. Frail. The Structure Function of Variable 1.4 GHz Radio Sources Based on NVSS and FIRST Observations. *Astrophysical Journal*, 737(1):45, August 2011.

[486] B. O'Connor et al. A tale of two mergers: constraints on kilonova detection in two short GRBs at z $\sim$ 0.5. *Monthly Notices of the RAS*, 502(1):1279–1298, March 2021.

[487] P. K. Blanchard et al. The Electromagnetic Counterpart of the Binary Neutron Star Merger LIGO/Virgo GW170817. VII. Properties of the Host Galaxy and Constraints on the Merger Timescale. *Astrophysical Journall*, 848(2):L22, October 2017.

Appendix

V1:DAQ_LNFS_56MHz_raw_dFreq_10000
V1:DAQ_EOM_56MHz_raw_dFreq_10000
V1:SDB2_B1p_PD2_56MHz_mag_10000
V1:SDB2_POWERSUPPLY_DBOX_RIGHT_UP_p12V_20000
V1:SDB2_B1s2_PD1_56MHz_mag_10000
V1:Sc_WI_MIR_VOUT_DR_10000
V1:Sc_WI_MIR_Z_CORR_10000
V1:Sc_WI_MIR_VOUT_DL_10000
V1:SDB2_B1_PD2_8MHz_mag_10000
V1:Sc_WI_MIR_VOUT_UR_10000
V1:SDB2_B1p_QD2_H_2000
V1:DAQ_LNFS_8MHz_raw_dFreq_10000
V1:DAQ_EOM_22MHz_raw_dFreq_10000
V1:SDB2_B1p_QD2_H_norm_2000
V1:Sc_WI_MIR_VOUT_UL_10000
V1:ASC_B1p_QD2_H_2000

Table 2: List of the Virgo auxiliary channels classified as "warning" by the channel safety analysis (see section 4.1.3).

V1:SDB2_B1_PD2_DC_20000
V1:Sc_NE_MIR_VOUT_UR_10000
V1:Sc_NE_MIR_Z_CORR_LN_10000
V1:Sc_NE_MIR_VOUT_UL_10000
V1:HrecPD1_hoft_20000Hz_20000
V1:Sc_WI_FF50HZ_P_ERR_10000
V1:Sc_WE_MIR_Z_CORR_LN_10000
V1:SDB1_B1x_DC_DARM_i_1000
V1:SDB2_B1_PD1_Audio_20000
V1:Sc_NI_MAR_Z_CORR_10000
V1:LSC_DARM_INPUT_10000
V1:Sc_WI_FF50HZ_G_ERR_10000
V1:Sc_NE_MIR_LSC_CORR_10000
V1:SDB1_B1_DC_norm_B1s2_10000
V1:Sc_WE_MIR_VOUT_DR_10000
V1:LSC_B1_DC_IN2_10000
V1:SDB2_B1_PD1_Audio_100k_100000
V1:Sc_WE_MIR_VOUT_UL_10000
V1:LSC_DARM_CORR_raw_10000
V1:SDB2_B1_PD1_Blended_20000
V1:LSC_B1_DC_INPUT_10000
V1:SDB1_B1x_DC_DARM_q_1000
V1:Sc_NE_MAR_Y_CORR_10000
V1:LSC_NI_CORR_10000
V1:LSC_DARM_10000
V1:SDB2_B1_PD2_Audio_100kHz_100000
V1:LSC_WE_CORR_10000
V1:Sc_WI_MAR_Z_CORR_10000
V1:Sc_WE_MIR_Z_CORR_10000
V1:SDB2_B1_PD1_DC_20000
V1:Sc_NE_MIR_VOUT_DR_10000
V1:LSC_NE_CORR_10000
V1:Sc_BS_CMRF_10000
V1:LSC_B1_DC_IN1_10000
V1:SDB1_B1s2_DC_norm_B1s1_10000
V1:LSC_DARM_CORR_10000
V1:LSC_WI_CORR_10000
V1:SDB2_B1_DC_10000
V1:Sc_WE_MIR_VOUT_UR_10000
V1:SDB2_B1_DC_NULL_10000

V1:SDB2_B1_PD2_Blended_20000
V1:SDB1_B1s2_DC_norm_B1p_10000
V1:SDB2_B1p_PD1_56MHz_mag_10000
V1:Sc_NE_MIR_VOUT_DL_10000
V1:SDB2_B1_PD2_Audio_20000
V1:Sc_NI_MAR_Y_CORR_10000
V1:Sc_WI_FF50HZ_PHASE_10000
V1:HrecPD2_hoft_20000Hz_20000
V1:Sc_WI_MAR_Y_CORR_10000
V1:Sc_WE_MIR_VOUT_DL_10000
V1:LSC_DARM_ERR_10000
V1:Sc_WE_MIR_LSC_CORR_10000
V1:Sc_NE_MIR_Z_CORR_10000

Table 3: List of the Virgo auxiliary channels classified as "danger" by the channel safety analysis (see section 4.1.3).

Table 4: Ranking of the galaxies compatible with the GW170817 skymap according to grades defined in equations (5.1), (5.3) and (5.4), and the grade of [321].

Galaxy name	(5.1)		[321]		(5.3)		(5.4)		BLum ($L_\odot$)	Stellar mass ($M_\odot$)
	Rank	P_{loc}	Rank	G_{tot}	Rank	G_{tot}	Rank	G_{tot}		
ESO575-053	1	0.06	8	0.043	6	0.038	6	0.05	8.32e+35	9.675
PGC803966	2	0.059	35	0.003	35	0.001	8	0.033	5.96e+34	7.835
WINGSJ125701.38-172325.2	3	0.059	59	< 0.001	–	–	9	0.033	1.52e+33	–
ESO508-014	4	0.047	20	0.013	20	0.003	11	0.027	3.20e+35	8.605
NGC4993	**5**	**0.046**	**2**	**0.111**	**1**	**0.22**	**1**	**0.123**	**2.79e+36**	**10.551**
PGC797164	6	0.046	18	0.014	17	0.005	10	0.028	3.60e+35	8.864
ESO508-004	7	0.045	14	0.016	26	0.002	12	0.026	4.17e+35	8.416
IC4197	8	0.04	1	0.137	2	0.195	2	0.109	3.96e+36	10.563
ESO508-019	9	0.04	5	0.064	16	0.005	13	0.024	1.87e+36	9.004
2MASS 13104593-2351566	10	0.038	13	0.027	–	–	14	0.021	8.14e+35	–
796755	11	0.037	44	0.001	38	< 0.001	15	0.02	3.43e+34	7.9711
NGC4968	12	0.036	4	0.072	–	–	16	0.02	2.29e+36	–
6dFJ1309178-242256	13	0.034	33	0.003	36	0.001	17	0.019	1.05e+35	8.075
ESO508-010	14	0.033	11	0.04	7	0.036	7	0.035	1.39e+36	9.914
PGC169663	15	0.031	42	0.001	30	0.001	18	0.018	4.26e+34	8.171
IC4180	16	0.027	6	0.063	5	0.105	4	0.062	2.73e+36	10.466
PGC043966	17	0.024	15	0.016	29	0.001	20	0.014	7.77e+35	8.574
PGC799951	18	0.021	36	0.003	37	< 0.001	22	0.012	1.66e+35	8.247
WINGSJ125701.40-172325.3	19	0.021	–	–	–	–	23	0.011	–	–
ESO508-015	20	0.02	19	0.013	42	< 0.001	24	0.011	8.01e+35	7.885
ESO508-024	21	0.019	10	0.04	–	–	26	0.011	2.45e+36	–
ESO575-029	22	0.019	9	0.042	15	0.008	19	0.014	2.59e+36	9.49
PGC169670	23	0.017	40	0.002	31	0.001	28	0.01	1.05e+35	8.428
PGC772879	24	0.017	46	0.001	46	< 0.001	29	0.01	5.72e+34	7.862
NGC4970	25	0.017	3	0.081	3	0.139	3	0.071	5.54e+36	10.791
WINGSJ125701.40-172325.3	26	0.015	–	–	–	–	31	0.008	–	–
NGC4830	27	0.011	7	0.048	4	0.11	5	0.055	5.16e+36	10.882
PGC043664	28	0.01	16	0.015	14	0.01	27	0.01	1.71e+36	9.874
ESO575-061	29	0.01	37	0.002	43	< 0.001	34	0.006	2.74e+35	8.156
PGC044023	30	0.009	43	0.001	32	0.001	36	0.005	1.41e+35	8.693
PGC044312	31	0.008	39	0.002	23	0.002	37	0.005	2.86e+35	9.321
PGC044500	32	0.007	25	0.007	33	0.001	38	0.004	1.08e+36	8.787
PGC044021	33	0.006	26	0.006	28	0.001	39	0.004	1.16e+36	9.188
ESO508-033	34	0.006	24	0.007	12	0.012	30	0.009	1.29e+36	10.152
WINGSJ125217.42-153054.2	35	0.006	–	–	40	< 0.001	40	0.003	–	8.431
ABELL_1644:[D80]141	36	0.005	–	–	–	–	42	0.003	–	–
ESO508-011	37	0.005	32	0.003	47	< 0.001	45	0.003	8.54e+35	8.302
PGC044478	38	0.004	29	0.004	45	< 0.001	46	0.002	1.08e+36	8.479
IC3799	39	0.004	12	0.028	11	0.012	33	0.008	8.50e+36	10.37
PGC183552	40	0.004	38	0.002	24	0.002	43	0.003	7.35e+35	9.568
ESO508-003	41	0.003	23	0.007	22	0.002	44	0.003	2.94e+36	9.754
NGC4763	42	0.003	17	0.015	9	0.02	25	0.011	6.15e+36	10.729
PGC044234	43	0.003	27	0.005	25	0.002	47	0.002	2.12e+36	9.679
ESO508-007	44	0.003	49	0.001	53	< 0.001	50	0.001	2.82e+35	7.609
PGC043908	45	0.003	30	0.004	18	0.003	41	0.003	1.68e+36	10.0
ESO575-035	46	0.002	34	0.003	39	< 0.001	51	0.001	1.66e+36	9.018
PGC043424	47	0.002	22	0.008	8	0.027	21	0.013	5.32e+36	11.051
IC3831	48	0.002	28	0.004	13	0.011	35	0.006	3.07e+36	10.698
PGC043505	49	0.002	55	< 0.001	44	< 0.001	53	0.001	1.66e+35	8.964
NGC4756	50	0.001	21	0.009	10	0.016	32	0.008	6.89e+36	10.904
PGC043344	51	0.001	47	0.001	–	–	54	0.001	5.20e+35	–
WINGSJ125252.62-152426.5	52	0.001	–	–	–	–	55	0.001	–	–
ESO508-020	53	0.001	48	0.001	–	–	58	0.001	5.69e+35	–

Continued on next page

Galaxy name	(5.1)		[321]		(5.3)		(5.4)		BLum ($L_\odot$)	Stellar mass ($M_\odot$)
	Rank	P_{loc}	Rank	G_{tot}	Rank	G_{tot}	Rank	G_{tot}		
PGC910856	54	0.001	57	< 0.001	49	< 0.001	56	0.001	1.06e+35	8.75
PGC908166	55	0.001	56	< 0.001	48	< 0.001	57	0.001	1.71e+35	8.763
PGC043823	56	0.001	45	0.001	27	0.001	52	0.001	1.03e+36	9.937
PGC046026	57	0.001	41	0.001	21	0.002	49	0.002	1.72e+36	10.22
NGC4724	58	0.001	31	0.004	19	0.003	48	0.002	4.58e+36	10.365
PGC170205	59	0.001	50	0.001	–	–	60	< 0.001	1.01e+36	–
PGC043913	60	0.001	51	< 0.001	34	0.001	59	0.001	9.78e+35	9.87
PGC937614	61	< 0.001	53	< 0.001	41	< 0.001	61	< 0.001	1.36e+36	9.79
PGC943386	62	< 0.001	58	< 0.001	51	< 0.001	62	< 0.001	4.77e+35	8.724
ESO575-041	63	< 0.001	54	< 0.001	50	< 0.001	63	< 0.001	1.20e+36	8.879
2MASS 12492243-1321162	64	< 0.001	52	< 0.001	–	–	64	< 0.001	2.01e+36	–
PGC942354	65	< 0.001	60	< 0.001	52	< 0.001	65	< 0.001	3.23e+35	8.723

Table 5: Ranking of the galaxies compatible with the GW170817 without Virgo data skymap according to grades defined in equations (5.1), (5.3) and (5.4), and the grade of [321].

Galaxy name	(5.1)		[321]		(5.3)		(5.4)		BLum ($L_\odot$)	Stellar mass ($M_\odot$)
	Rank	P_{loc}	Rank	G_{tot}	Rank	G_{tot}	Rank	G_{tot}		
ESO027-022	1	0.043	26	0.012	55	0.001	11	0.023	2.38e+35	7.958
ESO027-003	2	0.029	7	0.034	42	0.001	15	0.016	9.85e+35	8.461
NGC4348	3	0.028	2	0.058	1	0.145	1	0.083	1.73e+36	10.47
PGC1108616	4	0.027	88	0.001	80	< 0.001	16	0.014	1.81e+34	7.497
PGC3294456	5	0.027	101	< 0.001	92	< 0.001	17	0.014	1.14e+34	7.339
PGC3293647	6	0.025	112	< 0.001	64	< 0.001	19	0.013	7.33e+33	7.795
NGC4680	7	0.024	5	0.047	3	0.076	2	0.048	1.64e+36	10.252
1143004	8	0.024	100	< 0.001	–	–	20	0.013	1.41e+34	–
229961	9	0.021	47	0.004	46	0.001	21	0.012	1.54e+35	8.5336
NGC4663	10	0.019	14	0.025	10	0.046	6	0.032	1.13e+36	10.15
2MASS 22302645-7941381	11	0.018	32	0.009	63	< 0.001	24	0.01	4.27e+35	8.07
AGC229174	12	0.017	–	–	–	–	27	0.009	–	–
GAMAJ121158.30+012934.6	13	0.016	–	–	102	< 0.001	29	0.008	–	7.416
NGC4658	14	0.015	1	0.102	8	0.047	8	0.03	5.59e+36	10.242
PGC069012	15	0.015	21	0.015	35	0.002	26	0.009	8.28e+35	8.885
ESO575-053	16	0.015	22	0.015	17	0.012	18	0.014	8.32e+35	9.675
UGC07184	17	0.015	24	0.014	47	0.001	30	0.008	8.07e+35	8.523
PGC803966	18	0.014	71	0.001	79	< 0.001	32	0.008	5.96e+34	7.835
PGC1183373	19	0.014	115	< 0.001	125	< 0.001	35	0.007	1.01e+34	6.987
WINGSJ125701.38-172325.2	20	0.014	155	< 0.001	–	–	36	0.007	1.52e+33	–
PGC797164	21	0.013	40	0.006	41	0.002	33	0.008	3.60e+35	8.864
SDSSJ121210.92+025255.6	22	0.013	108	< 0.001	93	< 0.001	38	0.007	1.64e+34	7.653
PGC1229057	23	0.013	83	0.001	70	< 0.001	39	0.007	4.22e+34	7.981
GAMAJ122005.10+001556.4	24	0.012	–	–	86	< 0.001	40	0.007	–	7.715
PGC1066570	25	0.012	117	< 0.001	96	< 0.001	41	0.006	1.02e+34	7.65
ESO508-019	26	0.012	12	0.026	34	0.002	37	0.007	1.87e+36	9.004
NGC4993	**27**	**0.012**	**6**	**0.038**	**4**	**0.071**	**4**	**0.04**	**2.79e+36**	**10.551**
6dFJ1309178-242256	28	0.012	61	0.001	66	< 0.001	44	0.006	1.05e+35	8.075
ESO508-004	29	0.012	39	0.006	59	0.001	43	0.006	4.17e+35	8.416
ESO508-014	30	0.011	45	0.004	49	0.001	42	0.006	3.20e+35	8.605
PGC1060528	31	0.011	89	0.001	73	< 0.001	46	0.006	4.31e+34	8.025
PGC1193160	32	0.011	116	< 0.001	103	< 0.001	48	0.006	1.25e+34	7.563
IC4197	33	0.011	4	0.051	5	0.069	5	0.038	3.96e+36	10.563
796755	34	0.011	97	< 0.001	78	< 0.001	49	0.006	3.43e+34	7.9616
PGC3294393	35	0.011	119	< 0.001	82	< 0.001	51	0.006	1.16e+34	7.885
NGC4968	36	0.011	11	0.029	–	–	52	0.006	2.29e+36	–
PGC043966	37	0.01	30	0.01	54	0.001	47	0.006	7.77e+35	8.574
ESO027-001	38	0.01	3	0.056	2	0.084	3	0.045	4.61e+36	10.671
2MASS 00244271-7345157	39	0.01	27	0.011	38	0.002	45	0.006	9.43e+35	9.019
AGC229200	40	0.01	–	–	–	–	54	0.005	–	–
ESO027-008	41	0.01	8	0.033	6	0.054	7	0.031	2.85e+36	10.51
3091844	42	0.01	103	< 0.001	89	< 0.001	55	0.005	2.95e+34	7.7983
2MASS 13104593-2351566	43	0.009	31	0.009	–	–	56	0.005	8.14e+35	–
PGC3294258	44	0.009	129	< 0.001	123	< 0.001	57	0.005	8.62e+33	7.201
SDSSJ120404.33+044847.2	45	0.009	102	< 0.001	90	< 0.001	61	0.005	3.39e+34	7.834
PGC169663	46	0.009	98	< 0.001	69	< 0.001	60	0.005	4.26e+34	8.171
PGC1166504	47	0.009	113	< 0.001	99	< 0.001	62	0.005	2.05e+34	7.713
PGC772879	48	0.009	87	0.001	88	< 0.001	63	0.005	5.72e+34	7.862
UGC07185	49	0.009	79	0.001	114	< 0.001	64	0.005	7.50e+34	7.457
ESO508-010	50	0.008	25	0.014	18	0.012	23	0.01	1.39e+36	9.914
ESO508-015	51	0.008	35	0.007	91	< 0.001	67	0.004	8.01e+35	7.885
IC4180	52	0.008	15	0.024	12	0.038	12	0.022	2.73e+36	10.466

Continued on next page

Galaxy name	(5.1)		[321]		(5.3)		(5.4)		BLum ($L_\odot$)	Stellar mass ($M_\odot$)
	Rank	P_{loc}	Rank	G_{tot}	Rank	G_{tot}	Rank	G_{tot}		
NGC4123	53	0.008	16	0.02	19	0.01	28	0.009	2.18e+36	9.889
PGC3294218	54	0.007	136	< 0.001	116	< 0.001	70	0.004	9.35e+33	7.516
NGC4179	55	0.007	23	0.015	13	0.028	14	0.017	1.86e+36	10.377
PGC044021	56	0.006	33	0.009	40	0.002	66	0.004	1.16e+36	9.188
ESO027-021	57	0.006	28	0.01	20	0.01	31	0.008	1.41e+36	9.947
SDSSJ120736.32+024143.3	58	0.006	–	–	61	< 0.001	72	0.003	–	8.612
PGC1233241	59	0.006	154	< 0.001	130	< 0.001	74	0.003	3.92e+33	7.074
PGC799951	60	0.006	69	0.001	76	< 0.001	73	0.003	1.66e+35	8.247
PGC039902	61	0.005	52	0.003	81	< 0.001	75	0.003	4.15e+35	8.183
PGC037954	62	0.005	84	0.001	97	< 0.001	76	0.003	9.74e+34	7.971
ESO508-024	63	0.005	20	0.015	–	–	77	0.003	2.45e+36	–
PGC043664	64	0.005	29	0.01	25	0.007	50	0.006	1.71e+36	9.874
ESO575-029	65	0.005	19	0.015	32	0.003	68	0.004	2.59e+36	9.49
NGC5967	66	0.005	13	0.026	9	0.047	10	0.024	4.44e+36	10.739
J210518.19-824531.7	67	0.005	–	–	144	< 0.001	79	0.003	–	6.727
NGC4970	68	0.005	9	0.032	7	0.052	9	0.027	5.54e+36	10.791
UGC07332	69	0.005	68	0.001	134	< 0.001	80	0.003	2.12e+35	7.079
PGC2801913	70	0.005	–	–	27	0.005	59	0.005	–	9.819
NGC4116	71	0.005	38	0.006	33	0.002	71	0.003	1.14e+36	9.452
PGC169670	72	0.004	91	0.001	72	< 0.001	81	0.002	1.05e+35	8.428
SDSSJ121518.94+025538.2	73	0.004	145	< 0.001	129	< 0.001	82	0.002	7.72e+33	7.246
UGC07178	74	0.004	72	0.001	132	< 0.001	83	0.002	1.95e+35	7.171
WINGSJ125701.40-172325.3	75	0.004	–	–	–	–	85	0.002	–	–
NGC5967A	76	0.004	36	0.007	–	–	86	0.002	1.44e+36	–
UGC07396	77	0.004	42	0.005	67	< 0.001	84	0.002	1.11e+36	8.532
2MASS 15465869-7547149	78	0.004	49	0.003	–	–	87	0.002	6.51e+35	–
3293713	79	0.003	152	< 0.001	126	< 0.001	90	0.002	7.70e+33	7.506
ESO508-033	80	0.003	44	0.005	23	0.008	53	0.005	1.29e+36	10.152
IC3799	81	0.003	10	0.031	16	0.013	34	0.008	8.50e+36	10.37
3294175	82	0.003	164	< 0.001	153	< 0.001	93	0.002	2.11e+33	6.679
NGC4830	83	0.003	17	0.018	11	0.04	13	0.02	5.16e+36	10.882
GAMAJ121759.98+002558.1	84	0.003	–	–	154	< 0.001	94	0.002	–	6.522
WINGSJ125701.40-172325.3	85	0.003	–	–	–	–	95	0.002	–	–
PGC135791	86	0.003	123	< 0.001	142	< 0.001	98	0.001	3.90e+34	7.022
WINGSJ125217.42-153054.2	87	0.003	–	–	84	< 0.001	96	0.002	–	8.431
PGC043344	88	0.003	57	0.002	–	–	99	0.001	5.20e+35	–
PGC3271002	89	0.003	167	< 0.001	150	< 0.001	100	0.001	1.77e+33	6.814
ESO042-007	90	0.003	34	0.008	–	–	101	0.001	2.64e+36	–
SDSSJ114850.14+102655.9	91	0.003	–	–	101	< 0.001	103	0.001	–	8.229
NGC3976	92	0.002	18	0.018	15	0.018	25	0.01	5.96e+36	10.613
PGC037301	93	0.002	106	< 0.001	83	< 0.001	104	0.001	9.44e+34	8.488
ESO575-061	94	0.002	77	0.001	107	< 0.001	105	0.001	2.74e+35	8.156
PGC044023	95	0.002	99	< 0.001	71	< 0.001	102	0.001	1.41e+35	8.693
PGC3122921	96	0.002	165	< 0.001	152	< 0.001	107	0.001	2.58e+33	6.807
ESO508-035	97	0.002	105	< 0.001	117	< 0.001	108	0.001	1.01e+35	7.917
GAMAJ121732.70+002646.3	98	0.002	–	–	109	< 0.001	109	0.001	–	8.13
ESO068-002	99	0.002	67	0.001	105	< 0.001	110	0.001	4.94e+35	8.221
PGC044312	100	0.002	80	0.001	51	0.001	97	0.001	2.86e+35	9.321
PGC1070576	101	0.002	94	< 0.001	108	< 0.001	112	0.001	2.11e+35	8.248
6dFJ1258120-210246	102	0.002	95	< 0.001	95	< 0.001	114	0.001	2.18e+35	8.462
PGC044500	103	0.002	53	0.002	74	< 0.001	113	0.001	1.08e+36	8.787
SDSSJ115551.83+064354.9	104	0.002	135	< 0.001	122	< 0.001	118	0.001	3.90e+34	7.949
ESO508-007	105	0.002	92	0.001	131	< 0.001	120	0.001	2.82e+35	7.609
AGC215716	106	0.002	137	< 0.001	128	< 0.001	121	0.001	3.72e+34	7.743
PGC039799	107	0.002	118	< 0.001	151	< 0.001	123	0.001	7.89e+34	7.024
ABELL_1644:[D80]141	108	0.002	–	–	–	–	124	0.001	–	–

Continued on next page

Galaxy name	(5.1)		[321]		(5.3)		(5.4)		BLum ($L_\odot$)	Stellar mass ($M_\odot$)
	Rank	P_{loc}	Rank	G_{tot}	Rank	G_{tot}	Rank	G_{tot}		
PGC037490	109	0.002	104	< 0.001	100	< 0.001	122	0.001	1.79e+35	8.473
HIPASSJ1255-15	110	0.001	–	–	–	–	127	0.001	–	–
ESO508-011	111	0.001	63	0.001	110	< 0.001	126	0.001	8.54e+35	8.302
PGC044478	112	0.001	59	0.002	106	< 0.001	129	0.001	1.08e+36	8.479
PGC183552	113	0.001	73	0.001	52	0.001	117	0.001	7.35e+35	9.568
PGC170205	114	0.001	65	0.001	–	–	132	0.001	1.01e+36	–
IC3831	115	0.001	46	0.004	21	0.009	58	0.005	3.07e+36	10.698
PGC043424	116	0.001	37	0.007	14	0.02	22	0.01	5.32e+36	11.051
PGC1031551	117	0.001	163	< 0.001	159	< 0.001	134	< 0.001	7.36e+33	6.862
PGC3294523	118	0.001	172	< 0.001	164	< 0.001	136	< 0.001	1.86e+33	6.498
ESO508-003	119	0.001	51	0.003	50	0.001	125	0.001	2.94e+36	9.754
PGC720745	120	0.001	153	< 0.001	140	< 0.001	138	< 0.001	3.11e+34	7.62
IC0874	121	0.001	75	0.001	43	0.001	111	0.001	8.89e+35	10.016
PGC758254	122	0.001	156	< 0.001	146	< 0.001	139	< 0.001	2.69e+34	7.49
NGC4763	123	0.001	41	0.006	24	0.007	69	0.004	6.15e+36	10.729
PGC043908	124	0.001	60	0.001	45	0.001	116	0.001	1.68e+36	10.0
PGC3293619	125	0.001	180	< 0.001	162	< 0.001	141	< 0.001	6.67e+32	6.631
PGC046026	126	0.001	64	0.001	36	0.002	106	0.001	1.72e+36	10.22
NGC4724	127	0.001	48	0.004	31	0.003	92	0.002	4.58e+36	10.365
PGC685308	128	0.001	130	< 0.001	104	< 0.001	142	< 0.001	1.21e+35	8.765
PGC044234	129	0.001	58	0.002	57	0.001	131	0.001	2.12e+36	9.679
PGC091191	130	0.001	168	< 0.001	163	< 0.001	145	< 0.001	5.86e+33	6.666
NGC4756	131	0.001	43	0.005	22	0.008	65	0.004	6.89e+36	10.904
WINGSJ125252.62-152426.5	132	0.001	–	–	–	–	148	< 0.001	–	–
PGC3291384	133	0.001	179	< 0.001	170	< 0.001	149	< 0.001	8.83e+32	6.295
135794	134	0.001	174	< 0.001	166	< 0.001	150	< 0.001	2.31e+33	6.473
2MASXJ13242754-3025548	135	0.001	128	< 0.001	–	–	151	< 0.001	1.50e+35	–
PGC043505	136	0.001	125	< 0.001	98	< 0.001	147	< 0.001	1.66e+35	8.964
ESO575-035	137	0.001	70	0.001	94	< 0.001	146	< 0.001	1.66e+36	9.018
PGC043823	138	0.001	81	0.001	48	0.001	130	0.001	1.03e+36	9.937
NGC4504	139	0.001	86	0.001	68	< 0.001	140	< 0.001	9.58e+35	9.402
PGC3294233	140	0.001	178	< 0.001	–	–	152	< 0.001	9.60e+32	–
2MASXJ12490814-1124354	141	0.001	131	< 0.001	–	–	154	< 0.001	1.50e+35	–
PGC104686	142	0.001	148	< 0.001	–	–	155	< 0.001	5.98e+34	–
NGC5114	143	0.001	50	0.003	26	0.005	78	0.003	4.65e+36	10.774
ESO508-036	144	< 0.001	146	< 0.001	138	< 0.001	156	< 0.001	6.54e+34	7.924
PGC910856	145	< 0.001	139	< 0.001	111	< 0.001	153	< 0.001	1.06e+35	8.75
PGC041725	146	< 0.001	133	< 0.001	157	< 0.001	158	< 0.001	1.60e+35	7.166
NGC4487	147	< 0.001	85	0.001	65	< 0.001	144	< 0.001	1.14e+36	9.493
PGC908166	148	< 0.001	134	< 0.001	113	< 0.001	159	< 0.001	1.71e+35	8.763
PGC043913	149	< 0.001	96	< 0.001	58	0.001	135	< 0.001	9.78e+35	9.87
PGC3097711	150	< 0.001	181	< 0.001	173	< 0.001	161	< 0.001	1.14e+33	6.106
PGC141593	151	< 0.001	126	< 0.001	112	< 0.001	160	< 0.001	2.23e+35	8.8
PGC3097710	152	< 0.001	182	< 0.001	–	–	164	< 0.001	1.14e+33	–
PGC705472	153	< 0.001	144	< 0.001	156	< 0.001	163	< 0.001	9.78e+34	7.363
PGC937614	154	< 0.001	90	0.001	62	< 0.001	143	< 0.001	1.36e+36	9.79
ESO508-020	155	< 0.001	110	< 0.001	–	–	165	< 0.001	5.69e+35	–
NGC5061	156	< 0.001	54	0.002	29	0.004	89	0.002	4.95e+36	10.805
PGC135798	157	< 0.001	171	< 0.001	167	< 0.001	168	< 0.001	4.70e+33	6.665
PGC042120	158	< 0.001	173	< 0.001	169	< 0.001	169	< 0.001	3.98e+33	6.529
ESO444-026	159	< 0.001	56	0.002	–	–	170	< 0.001	4.64e+36	–
J132249.66-300651.8	160	< 0.001	–	–	119	< 0.001	166	< 0.001	–	8.706
PGC943386	161	< 0.001	114	< 0.001	118	< 0.001	167	< 0.001	4.77e+35	8.724
PGC3097712	162	< 0.001	177	< 0.001	174	< 0.001	172	< 0.001	1.80e+33	6.13
PGC3294387	163	< 0.001	184	< 0.001	172	< 0.001	171	< 0.001	4.59e+32	6.383
PGC3268622	164	< 0.001	183	< 0.001	160	< 0.001	173	< 0.001	5.02e+32	7.236

Continued on next page

Galaxy name	(5.1)		[321]		(5.3)		(5.4)		BLum ($L_\odot$)	Stellar mass ($M_\odot$)
	Rank	P_{loc}	Rank	G_{tot}	Rank	G_{tot}	Rank	G_{tot}		
PGC3097709	165	< 0.001	176	< 0.001	171	< 0.001	174	< 0.001	2.38e+33	6.406
PGC046803	166	< 0.001	93	< 0.001	53	0.001	133	< 0.001	1.43e+36	10.154
PGC104868	167	< 0.001	158	< 0.001	148	< 0.001	175	< 0.001	4.53e+34	7.848
ESO444-021	168	< 0.001	66	0.001	87	< 0.001	162	< 0.001	4.08e+36	9.381
WINGSJ132507.84-315046.2	169	< 0.001	–	–	–	–	177	< 0.001	–	–
NGC5078	170	< 0.001	55	0.002	28	0.004	88	0.002	6.52e+36	10.978
ESO444-011	171	< 0.001	111	< 0.001	120	< 0.001	176	< 0.001	7.74e+35	8.824
ESO508-039	172	< 0.001	151	< 0.001	158	< 0.001	179	< 0.001	1.09e+35	7.434
NGC4748	173	< 0.001	82	0.001	37	0.002	115	0.001	2.32e+36	10.672
J132044.59-302043.7	174	< 0.001	–	–	–	–	181	< 0.001	–	–
ESO444-012	175	< 0.001	78	0.001	56	0.001	137	< 0.001	3.17e+36	10.26
PGC141595	176	< 0.001	141	< 0.001	121	< 0.001	180	< 0.001	2.06e+35	8.881
PGC850539	177	< 0.001	122	< 0.001	127	< 0.001	183	< 0.001	5.31e+35	8.668
PGC740755	178	< 0.001	132	< 0.001	–	–	184	< 0.001	3.76e+35	–
ESO444-002	179	< 0.001	157	< 0.001	161	< 0.001	186	< 0.001	1.03e+35	7.375
PGC763675	180	< 0.001	159	< 0.001	155	< 0.001	187	< 0.001	6.22e+34	7.643
NGC5124	181	< 0.001	62	0.001	30	0.003	91	0.002	6.38e+36	11.025
ESO444-033	182	< 0.001	140	< 0.001	147	< 0.001	188	< 0.001	2.69e+35	8.095
WINGSJ132507.84-315046.2	183	< 0.001	–	–	–	–	189	< 0.001	–	–
WINGSJ132507.85-315046.2	184	< 0.001	175	< 0.001	–	–	190	< 0.001	6.71e+33	–
PGC141602	185	< 0.001	138	< 0.001	143	< 0.001	191	< 0.001	3.89e+35	8.239
NGC5048	186	< 0.001	74	0.001	44	0.001	128	0.001	5.21e+36	10.713
PGC732248	187	< 0.001	143	< 0.001	139	< 0.001	192	< 0.001	2.49e+35	8.403
SDSSJ120133.99+042759.3	188	< 0.001	160	< 0.001	137	< 0.001	194	< 0.001	7.38e+34	8.456
NGC5051	189	< 0.001	76	0.001	39	0.002	119	0.001	4.78e+36	10.85
PGC046903	190	< 0.001	150	< 0.001	–	–	195	< 0.001	1.95e+35	–
IC0879	191	< 0.001	147	< 0.001	115	< 0.001	193	< 0.001	2.54e+35	9.272
PGC141596	192	< 0.001	121	< 0.001	85	< 0.001	182	< 0.001	9.42e+35	9.764
PGC722221	193	< 0.001	170	< 0.001	168	< 0.001	198	< 0.001	2.70e+34	7.113
PGC117211	194	< 0.001	162	< 0.001	136	< 0.001	197	< 0.001	8.52e+34	8.687
ESO444-015	195	< 0.001	107	< 0.001	75	< 0.001	178	< 0.001	2.42e+36	10.053
HIPASSJ1457-67	196	< 0.001	–	–	133	< 0.001	196	< 0.001	–	8.823
PGC042964	197	< 0.001	166	< 0.001	165	< 0.001	199	< 0.001	6.01e+34	7.317
ESO575-041	198	< 0.001	127	< 0.001	135	< 0.001	200	< 0.001	1.20e+36	8.879
PGC939548	199	< 0.001	149	< 0.001	141	< 0.001	201	< 0.001	4.06e+35	8.62
PGC1295846	200	< 0.001	161	< 0.001	145	< 0.001	203	< 0.001	1.76e+35	8.642
PGC2793691	201	< 0.001	142	< 0.001	–	–	204	< 0.001	7.10e+35	–
ESO443-086	202	< 0.001	124	< 0.001	124	< 0.001	202	< 0.001	1.88e+36	9.436
PGC043964	203	< 0.001	120	< 0.001	77	< 0.001	185	< 0.001	2.56e+36	10.361
NGC5126	204	< 0.001	109	< 0.001	60	< 0.001	157	< 0.001	4.67e+36	10.816
PGC104887	205	< 0.001	169	< 0.001	149	< 0.001	205	< 0.001	8.69e+34	8.616

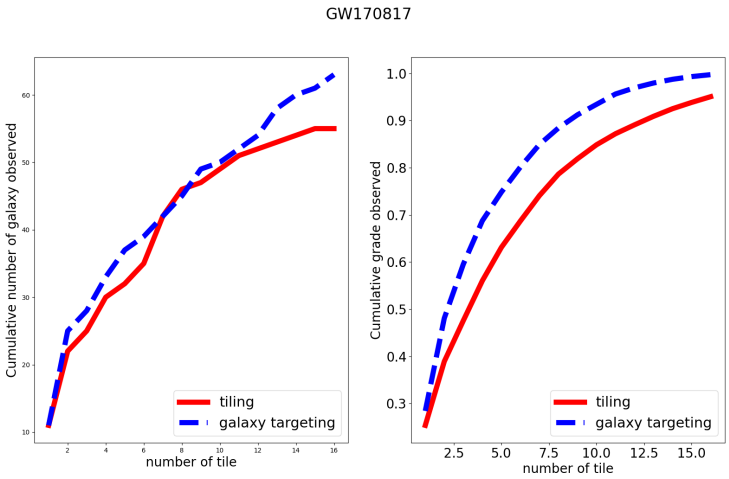

Figure 23: figure 23 to 52, mean cumulative number of galaxies observed and grade observed of the SVOM-MXT simulation for each skymap (see section 5.5).

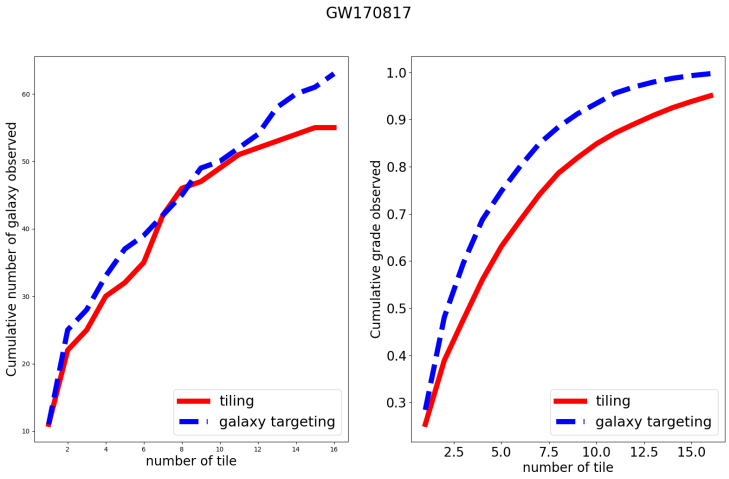

Figure 24:

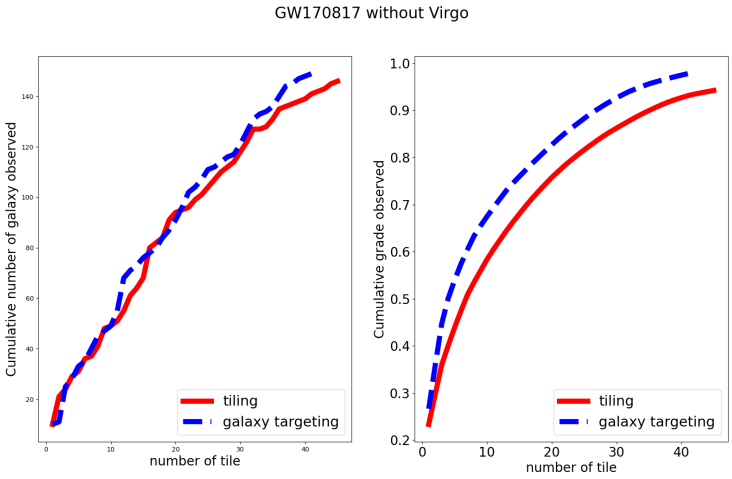

Figure 25:

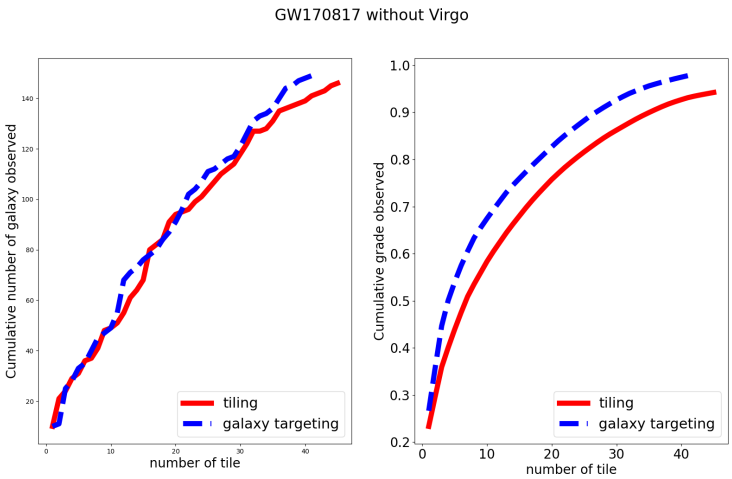

Figure 26:

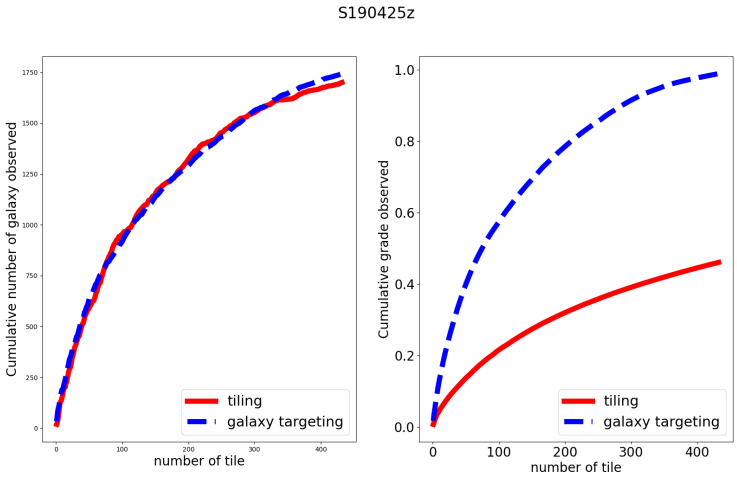

Figure 27:

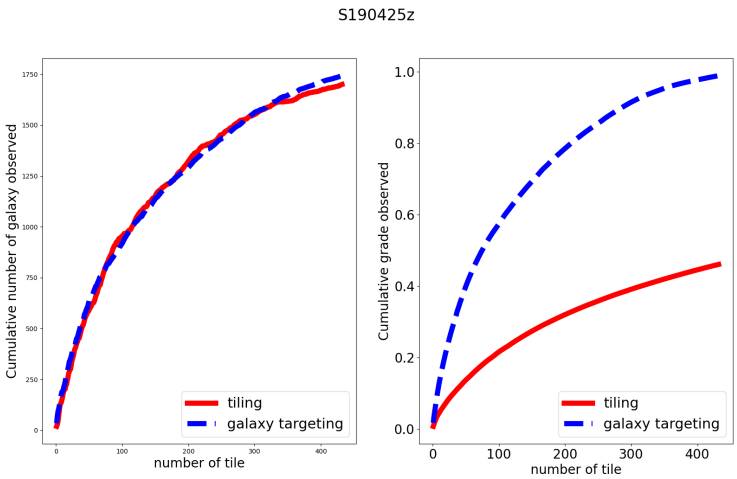

Figure 28:

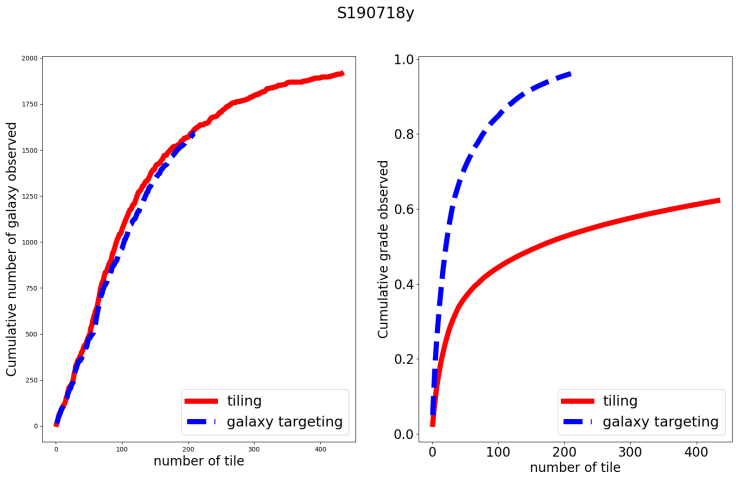

Figure 29:

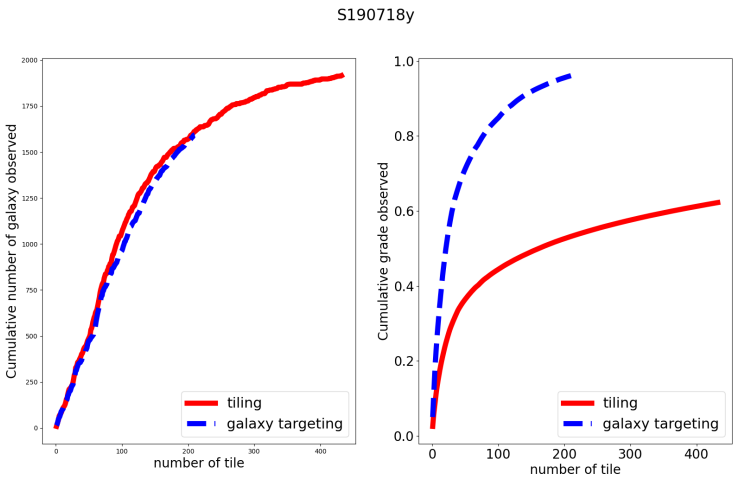

Figure 30:

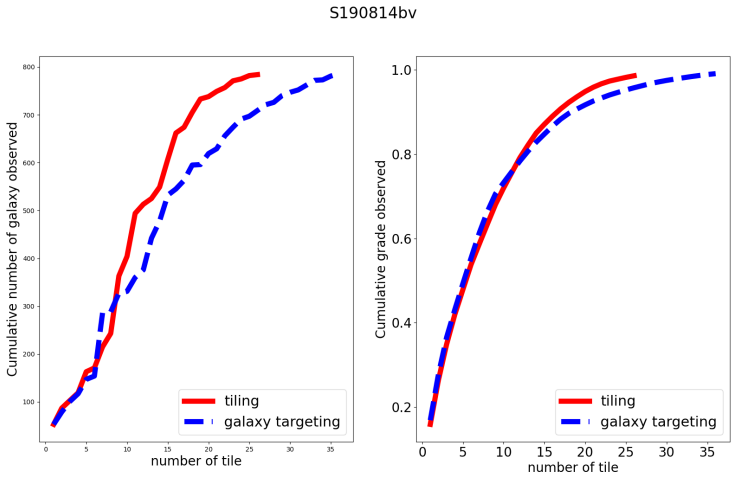

Figure 31:

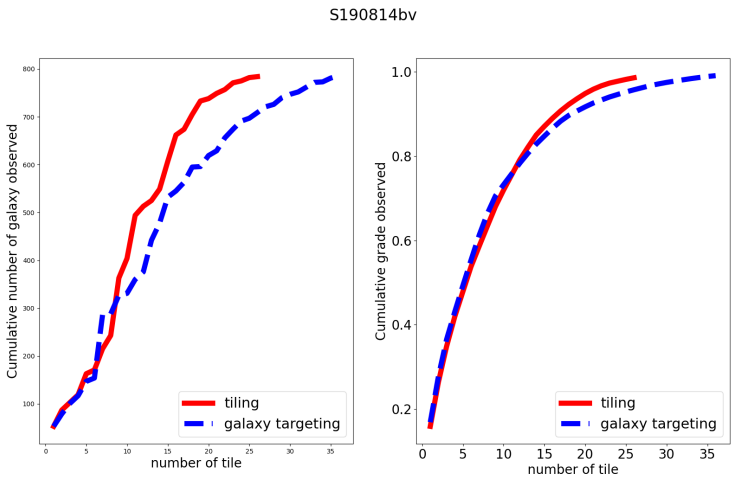

Figure 32:

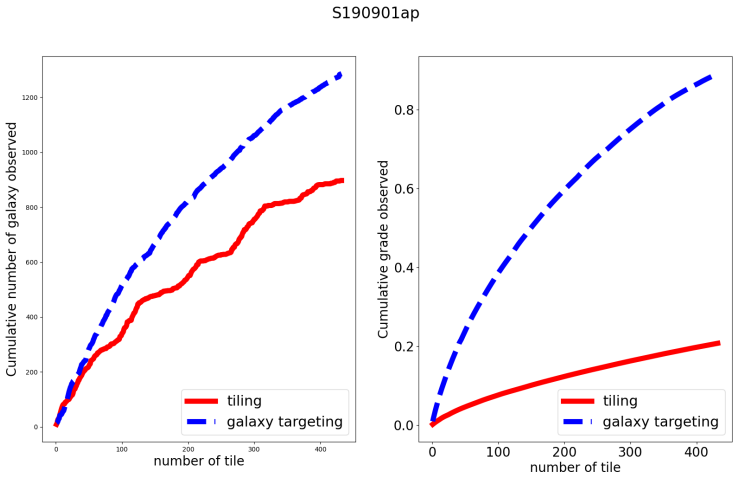

Figure 33:

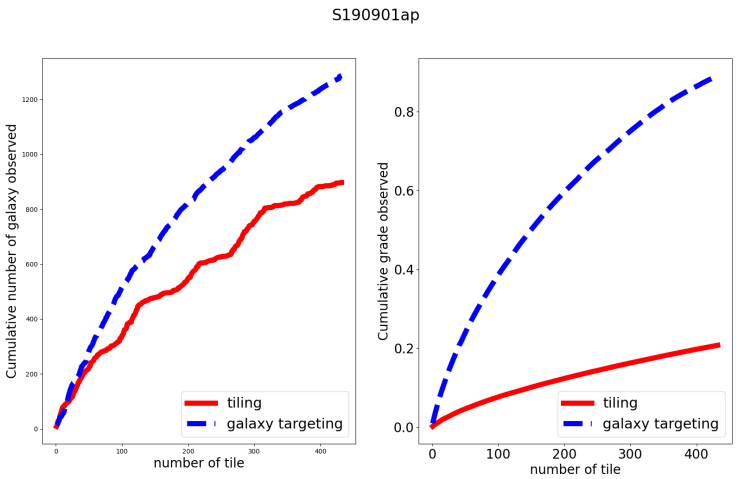

Figure 34:

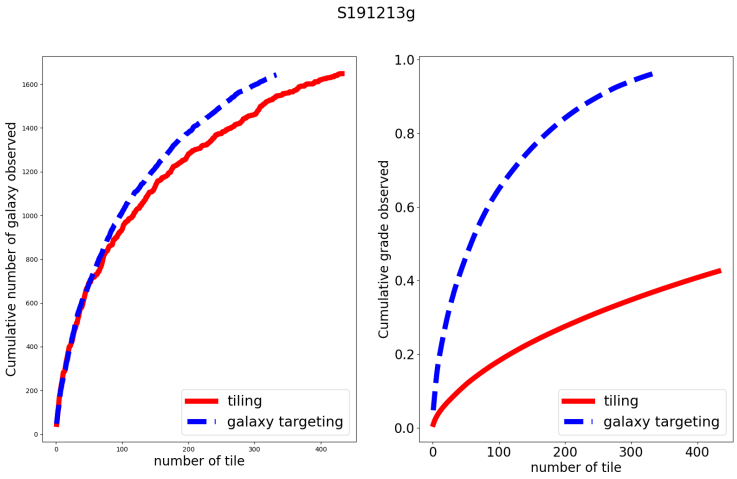

Figure 35:

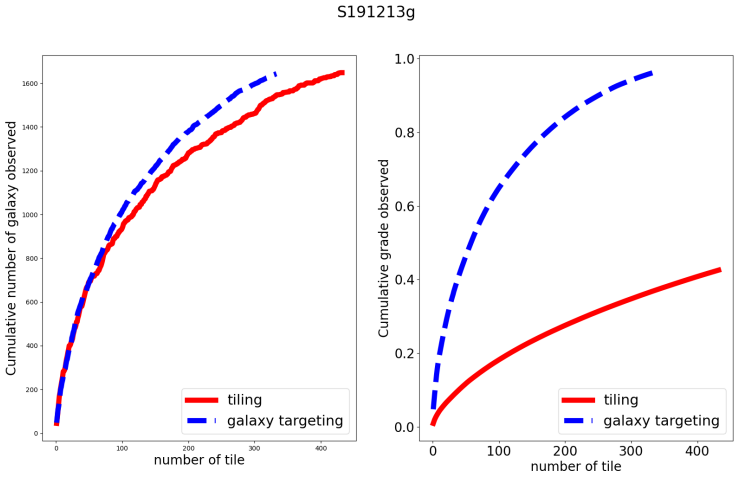

Figure 36:

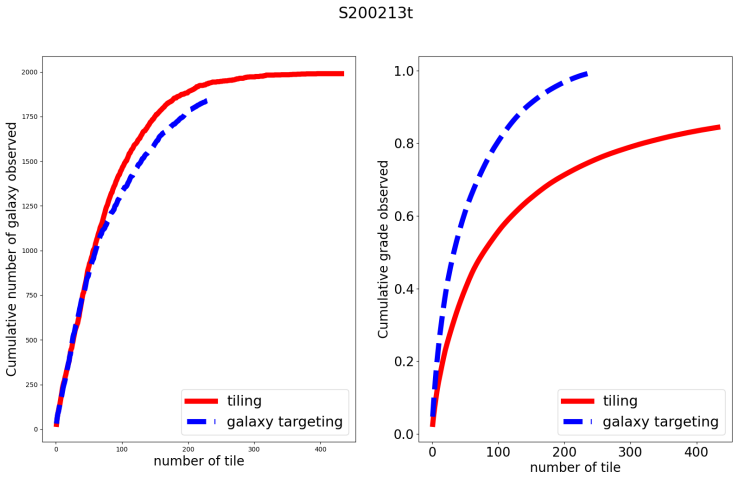

Figure 37:

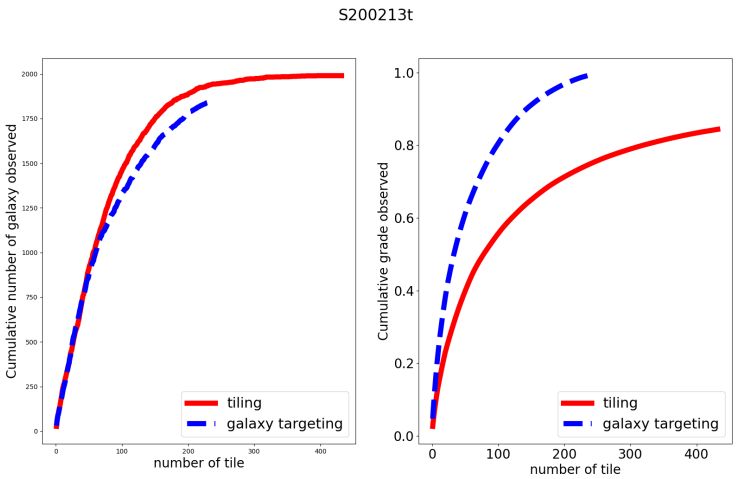

Figure 38:

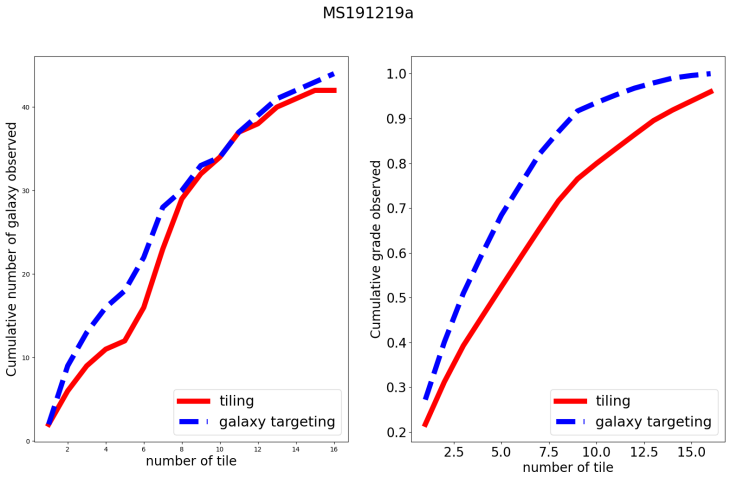

Figure 39:

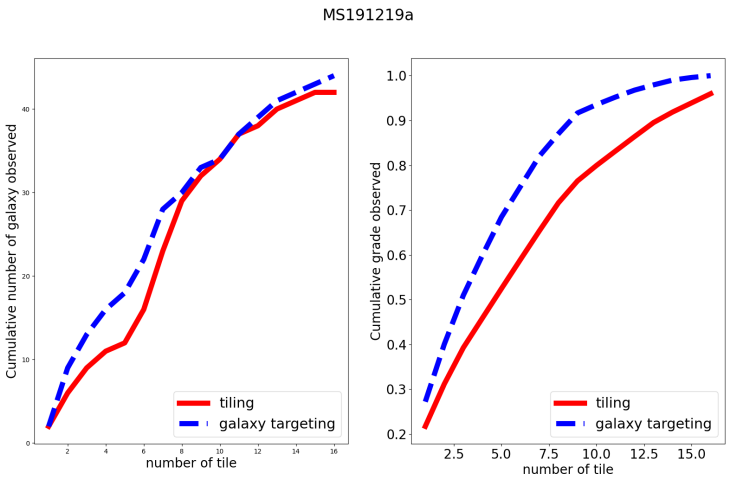

Figure 40:

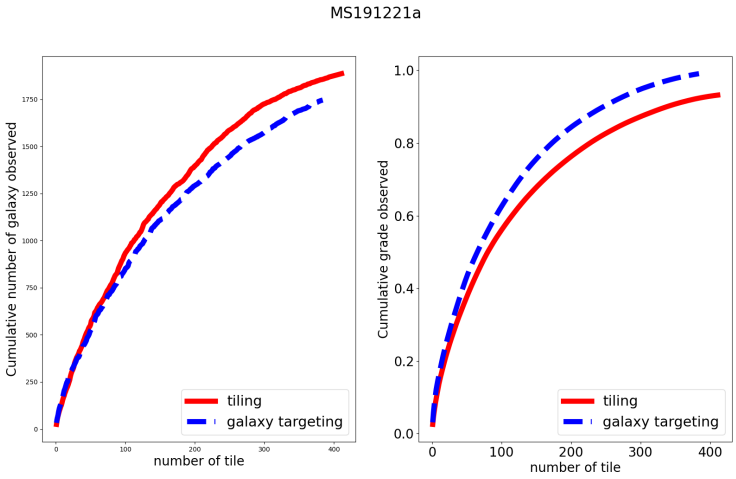

Figure 41:

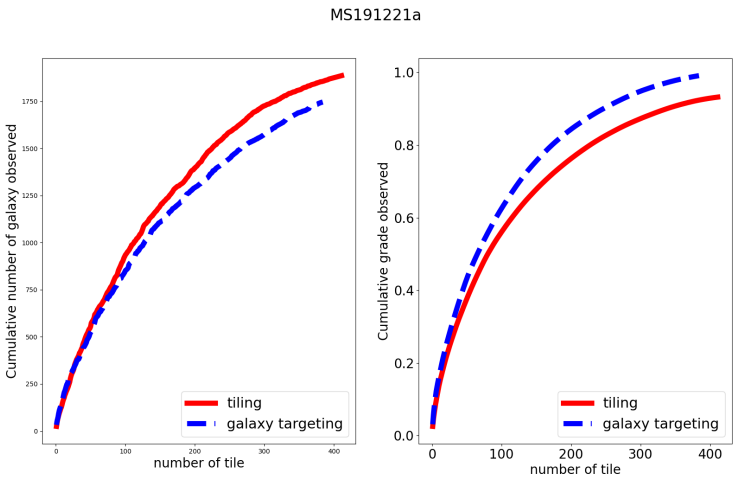

Figure 42:

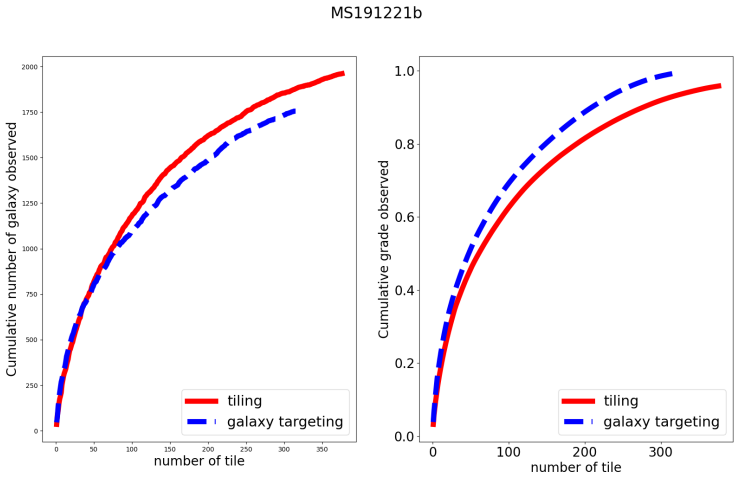

Figure 43:

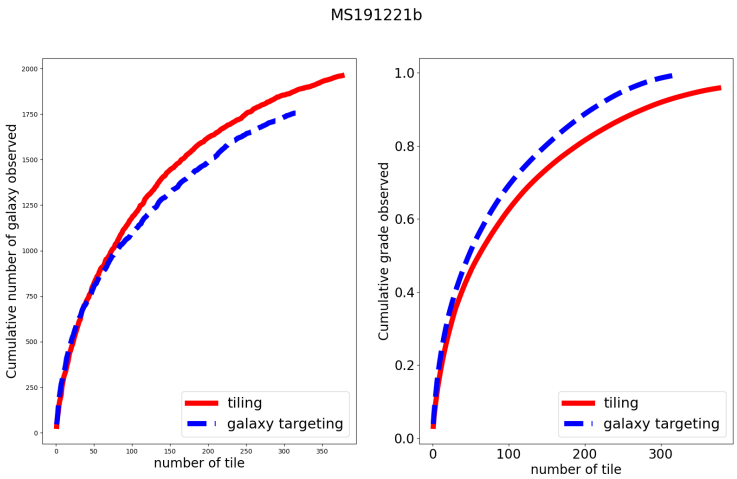

Figure 44:

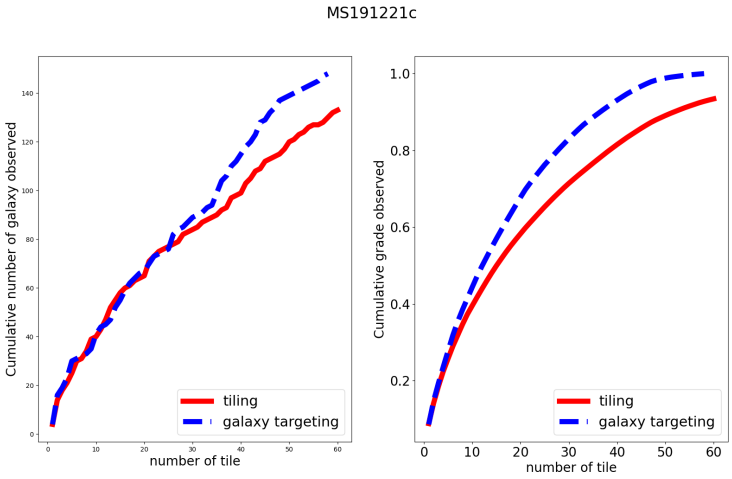

Figure 45:

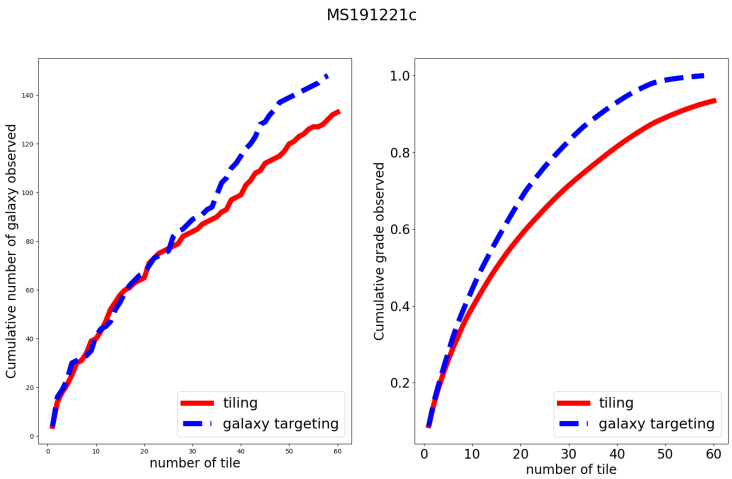

Figure 46:

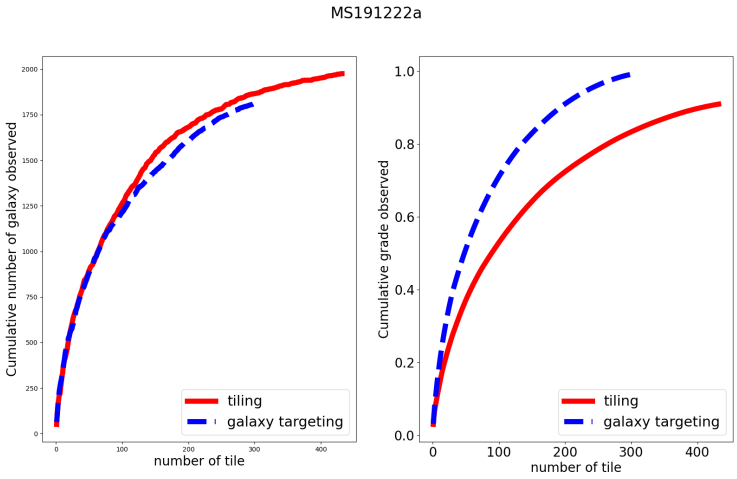

Figure 47:

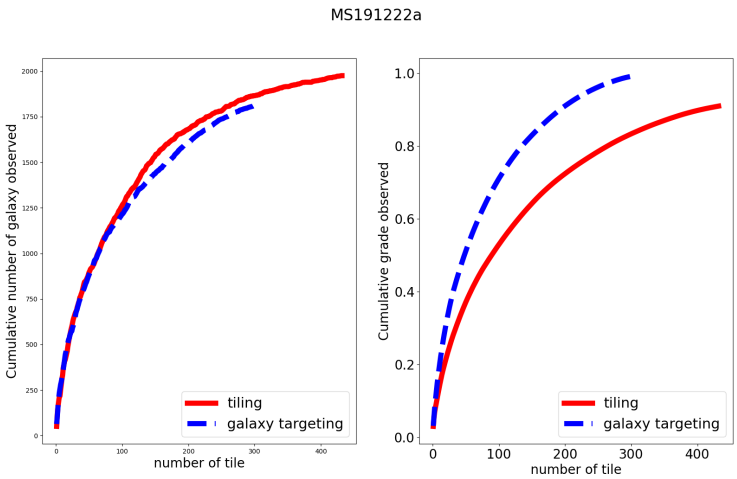

Figure 48:

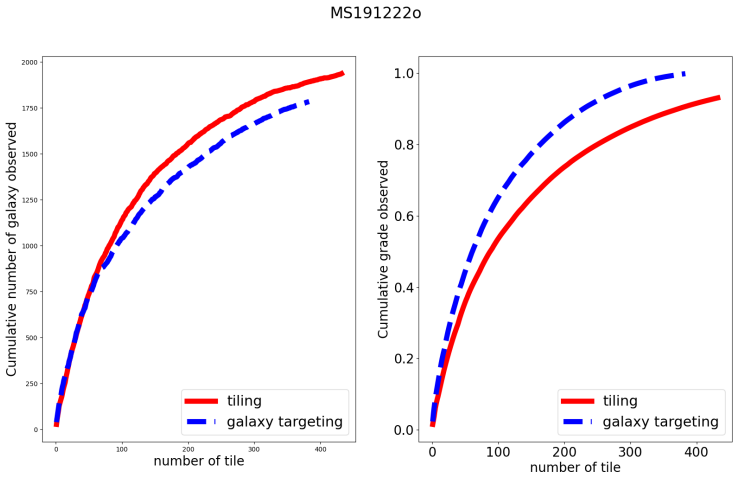

Figure 49:

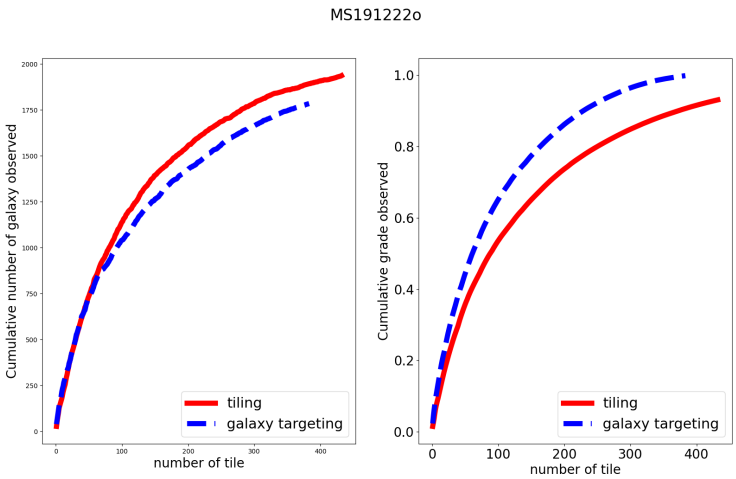

Figure 50:

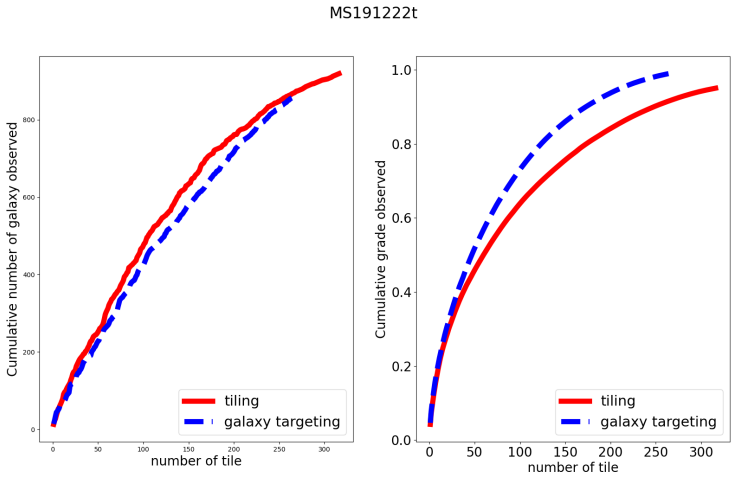

Figure 51:

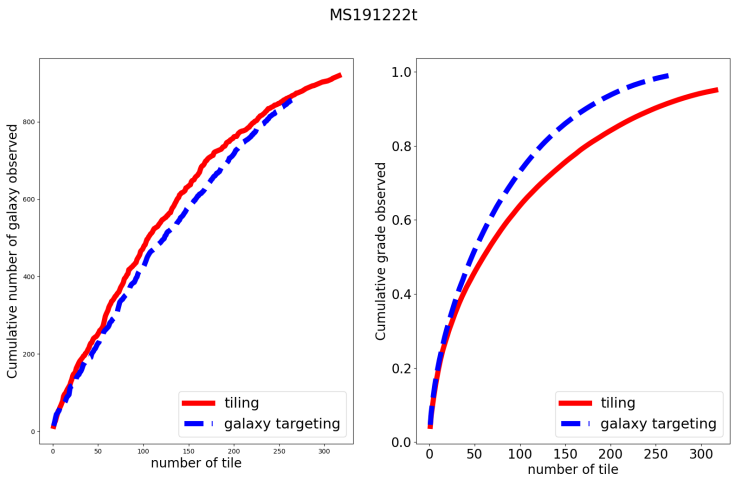

Figure 52:

Table 6: GRB sample having an associated galaxy. Columns list (1) the GRB identification, (2) redshift (**bolded if measured from the afterglow spectrum**), (3) reference for the redshift, (4) the T90 taken from the 3rd BAT catalog [361], (5) whether there is an extended emission, (6) whether an optical afterglow is detected, (7) right ascension, (8) declination , (9) radius uncertainty on the position, (10) reference for the position. The position corresponds to the optical detection if available otherwise the X detection position. The GRBs whose classification short/long is not clear are put at the end of the table.

GRB	z	refs	T_{90} (s)	EE	OA	RA (J2000)	Dec (J2000)	Pos_err (")	refs
050509B	0.2249	1	0.02 ± 0.01	no	N	12h36m13.77s	+28d59m03.30s	4.30	2
050709	0.1606	3	0.07^{a}	no	Y	23h01m26.96s	-38d58m39.30s	0.25	3
050724	0.258	4	98.68 ± 8.56	yes	Y	16h24m44.40s	-27d32m27.90s	0.50	5
051210	1.3^{p}	6	1.30 ± 0.30	no	N	22h00m41.19s	-57d36m49.40s	1.80	2
051221A	0.5465	7	1.39 ± 0.20	no	Y	21h54m48.63s	+16d53m27.40s	0.18	8
051227	-		115.40 ± 14.94	yes	Y	08h20m58.11s	+31d55m32.00s	0.08	9
060801	1.131	12	0.50 ± 0.06	no	N	14h12m01.25s	+16d58m55.00s	1.40	2
061006	0.4377	9	129.79 ± 30.68	yes	Y	07h24m07.66s	-79d11m55.10s	0.50	13
061201	0.111	9	0.78 ± 0.10	no	Y	22h08m32.09s	-74d34m47.08s	0.20	14
061210	0.4095	9	85.23 ± 13.09	yes	N	09h38m05.18s	+15d37m17.70s	4.30	2
061217	0.827	9	0.22 ± 0.04	no	N	10h41m39.10s	-21d07m26.90s	6.00	15
070429B	0.902	16	0.49 ± 0.04	no	N	21h52m03.87s	-38d49m42.30s	2.80	2
070714B	0.92	17	65.64 ± 9.51	yes	Y	03h51m22.23s	+28d17m50.80s	0.40	18
070724A	0.457	19	0.43 ± 0.09	no	Y	01h51m14.07s	-18d35m39.33s	0.18	20
070729	0.8^{p}	6	0.99 ± 0.17	no	N	03h45m15.98s	-39d19m20.90s	3.00	2
070809	0.473	21	1.28 ± 0.37	no	Y	13h35m04.55s	-22d08m30.80s	0.40	22
071227	0.381	23	142.48 ± 48.37	yes	Y	03h52m31.26s	-55d59m03.50s	0.30	24

GRB	z	refs	T_{90} (s)	EE	OA	RA (J2000)	Dec (J2000)	Pos_err (")	refs
080123	0.495	6	114.91 ± 55.27	possible	N	22h35m46.33s	-64d54m02.80s	1.80	2
080905A	0.1218	25	1.02 ± 0.08	no	Y	19h10m41.71s	-18d52m47.62s	0.76	25
090510	0.903	28	5.66 ± 1.88	possible	Y	22h14m12.54s	-26d34m59.10s	0.50	29
100117A	0.915	30	0.29 ± 0.03	no	Y	00h45m04.66s	-01d35m41.89s	0.26	30
100206A	0.4068	31	0.12 ± 0.02	no	N	03h08m39.03s	+13d09m25.20s	3.90	2
100625A	0.452	32	0.33 ± 0.04	no	N	01h03m10.95s	-39d05m18.50s	1.90	2
101219A	0.718	35	0.83 ± 0.18	no	N	04h58m20.46s	-02d32m23.10s	1.50	2
101224A	-		0.24 ± 0.04	no	N	19h03m41.72s	+45d42m49.50s	3.80	2
111117A	2.211	37	0.46 ± 0.05	no	N	00h50m46.26s	+23d00m39.98s	0.35	38
120804A	1.3 ^{p}	39	0.81 ± 0.08	no	Y	15h35m47.48s	-28d46m56.17s	0.15	39
121226A	-		1.01 ± 0.20	no	N	11h14m34.14s	-30d24m22.50s	1.60	2
130603B	**0.3565**	40	0.18 ± 0.02	no	Y	11h28m48.15s	+17d04m18.00s	0.50	41
140903A	0.351	42	0.30 ± 0.03	no	N	15h52m03.27s	+27d36m10.83s	0.40	42
141212A	0.596	43	0.29 ± 0.10	no	N	02h36m29.97s	+18d08m49.90s	3.00	2
150101B	**0.1343**	44	0.01 ± 0.01	no	Y	12h32m05.09s	-10d56m03.00s	0.24	44
150120A	0.46	41	1.20 ± 0.15	no	N	00h41m16.53s	+33d59m41.90s	1.80	2
150424A	-		81.06 ± 17.48	yes	Y	10h09m13.38s	-26d37m51.50s	0.50	45
160624A	0.483	48	0.19 ± 0.14	no	N	22h00m46.21s	+29d38m37.80s	1.80	2

GRB	z	refs	T_{90} (s)	EE	OA	RA (J2000)	Dec (J2000)	Pos_err (")	refs
160821B	0.1616	49	0.48 ± 0.07	no	Y	18h39m54.56s	+62d23m30.50s	0.20	50
161104A	0.793	51	0.10 ± 0.02	no	N	05h11m34.45s	-51d27m36.40s	3.60	2
170817A	0.009787	54		no	Y	13h09m48.09s	-23d22m53.35s	0.50	55
181123B	1.754	56	0.26 ± 0.05	no	Y	12h17m27.94s	+14d35m52.66s	0.10	56
200522A	0.5536	57	0.61 ± 0.08	no	Y	00h22m43.73s	-00d16m57.43s	0.00	57
060614	0.125	10	109.10 ± 3.37	possible	Y	21h23m32.08s	-53d01m36.20s	0.56	11
090426	**2.609**	26	1.24 ± 0.25	no	Y	12h36m18.07s	+32d59m09.60s	0.50	27
100816A	**0.8049**	33	2.88 ± 0.63	possible	Y	23h26m57.56s	+26d34m42.90s	0.50	34
110106A	0.093	36	3.00 ± 1.41	no	N	05h17m13.48s	+64d10m25.20s	1.70	2
160228A	1.64	46	98.91 ± 23.89	possible	Y	07h09m15.82s	+26d55m53.80s	0.20	47
161129A	0.645	52	35.54 ± 2.10	possible	Y	21h04m54.60s	+32d08m05.52s	0.60	53

Notes.
[a] T_{90} estimation from [362].
[p] indicates a photometric redshift estimation.

References. (1) [383]; (2) `https://www.swift.ac.uk/xrt_live_cat`; (3) [384]; (4) [385]; (5) [386]; (6) [326]; (7) [387]; (8) [388]; (9) [389]; (10) [390]; (11) [391]; (12) [392]; (13) [393]; (14) [394]; (15) [395]; (16) [396]; (17) [397]; (18) [398]; (19) [399]; (20) [400]; (21) [401]; (22) [402]; (23) [403]; (24) [404]; (25) [405]; (26) [406]; (27) [407]; (28) [408]; (29) [409]; (30) [410]; (31) [411]; (32) [412]; (33) [413]; (34) [414]; (35) [415]; (36) [416]; (37) [417]; (38) [418]; (39) [419]; (40) [420]; (41) [421]; (42) [422]; (43) [423]; (44) [424]; (45) [425]; (46) [426]; (47) [427]; (48) [428]; (49) [429]; (50) [430]; (51) [431]; (52) [432]; (53) [433]; (54) [434]; (55) [435]; (56) [436]; (57) [437];

Table 7: GRBH sample. Columns list (1) the GRB identification, (2) redshift (**bolded if measured from the afterglow spectrum**), (3) right ascension, (4) declination , (5) RA and Dec uncertainty, (6) reference used for the position, (7) angular separation from the GRB position, (8) projected distance from the GRB position, (9) probability of alignment by chance. (10) galaxy type (early- or late-type). The GRBs whose classification short/long is not clear are put at the end of the table.

GRB	z	RA (J2000)	Dec (J2000)	Pos_err (")	refs	Angular separation (")	Projected distance (kpc)	P_i^a	type
050509B	0.2249	12h36m12.88s	+28d58m58.77s	0.01, 0.01	1	12.53	46.69	4.8×10^{-3}	E
050709	0.1606	23h01m26.86s	-38d58m39.68s	0.02, 0.02	2	1.23	3.50	4.2×10^{-4}	L
050724	0.258	16h24m44.38s	-27d32m26.80s	0.02, 0.01	1	1.13	4.67	3.9×10^{-3}	E
051210	1.3 ^{p}	22h00m40.93s	-57d36m47.10s	0.50, 0.50	3	3.11	26.73		U
051221A	0.5465	21h54m48.65s	+16d53m27.02s	0.05, 0.05	2	0.48	3.13	6.2×10^{-4}	L
051227	-1	08h20m58.11s	+31d55m31.98s	0.10, 0.10	2	0.02	-inf	1.4×10^{-4}	U
060801	1.131	14h12m01.30s	+16d58m54.00s	1.00, 1.00	4	1.23	10.39	4.5×10^{-4}	L
061006	0.4377	07h24m07.75s	-79d11m55.30s	0.16, 0.16	5	0.32	1.88	1.1×10^{-3}	L
061201	0.111	22h08m29.18s	-74d34m35.92s	0.20, 0.20	2	16.10	33.61	8.2×10^{-3}	L
061210	0.4095	09h38m05.36s	+15d37m18.80s	0.25, 0.25	5	2.82	15.86	9.2×10^{-3}	L
061217	0.827	10h41m39.15s	-21d07m27.30s	0.50, 0.50	6	0.81	6.29	1.1×10^{-2}	L
070429B	0.902	21h52m03.70s	-38d49m42.90s	0.20, 0.20	7	2.08	16.63	1.5×10^{-3}	L
070714B	0.92	03h51m22.25s	+28d17m50.78s	0.10, 0.10	2	0.26	2.14	1.3×10^{-2}	L
070724A	0.457	01h51m14.05s	-18d35m38.50s	0.02, 0.03	1	0.88	5.25	1.9×10^{-4}	L
070729	0.8 ^{p}	03h45m15.52s	-39d19m28.70s	0.50, 0.50	8	9.45	73.00		E
070809	0.473	13h35m04.16s	-22d08m32.87s	0.02, 0.02	1	5.80	35.40	9.4×10^{-3}	E
071227	0.381	03h52m31.00s	-55d59m00.77s	0.10, 0.10	2	3.49	18.78	4.5×10^{-4}	L

GRB	z	RA (J2000)	Dec (J2000)	Pos_err (")	refs	Angular separation (")	Projected distance (kpc)	P_i^a	type
080123	0.495	22h35m46.96s	-64d53m54.91s	0.37, 0.38	9	8.85	55.35		L
090510	0.903	22h14m12.56s	-26d34m58.70s	0.50, 0.50	10	0.48	3.86	3.3×10^{-3}	L
100117A	0.915	00h45m04.65s	-01d35m41.95s	0.00, 0.00	1	0.16	1.30	4.0×10^{-5}	E
100206A	0.4068	03h08m39.15s	+13d09m29.02s	0.09, 0.06	1	4.20	23.51	1.7×10^{-3}	L
100625A	0.452	01h03m10.94s	-39d05m18.70s	0.50, 0.50	11	0.23	1.38		E
101219A	0.718	04h58m20.48s	-02d32m22.17s	0.50, 0.50	12	0.98	7.26	1.8×10^{-2}	L
111117A	2.211	00h50m46.26s	+23d00m40.97s	0.13, 0.13	13	0.99	8.38		L
120804A	1.3 ^{p}	15h35m47.48s	-28d46m56.44s	0.15, 0.15	14	0.27	2.32		L
130603B	**0.3565**	11h28m48.23s	+17d04m18.50s	0.03, 0.02	1	1.25	6.45	7.8×10^{-3}	L
140903A	0.351	15h52m03.28s	+27d36m10.68s	0.10, 0.10	15	0.20	1.02	3.3×10^{-3}	U
141212A	0.596	02h36m29.95s	+18d08m47.20s	0.50, 0.50	16	2.71	18.63	1.2×10^{-2}	U
150101B	**0.1343**	12h32m04.97s	-10d56m00.71s	0.01, 0.00	1	2.89	7.11	2.6×10^{-4}	E
150120A	0.46	00h41m16.56s	+33d59m42.53s	0.08, 0.38	1	0.73	4.40	8.4×10^{-4}	U
160624A	0.483	22h00m46.13s	+29d38m38.89s	0.08, 0.08	1	1.51	9.31	1.8×10^{-3}	L

GRB	z	RA (J2000)	Dec (J2000)	Pos_err (")	refs	Angular separation (")	Projected distance (kpc)	P_i^a	type
160821B	0.1616	18h39m53.98s	+62d23m34.35s	0.02, 0.04	1	5.57	16.00	8.6×10^{-3}	U
161104A	0.793	05h11m34.47s	-51d27m36.29s	0.50, 0.50	17	0.22	1.67	8.7×10^{-3}	E
170817A	0.009787	13h09m47.69s	-23d23m02.31s	0.01, 0.01	1	10.52	2.18		E
181123B	1.754	12h17m27.91s	+14d35m52.27s	0.07, 0.07	18	0.58	5.07		L
200522A	0.5536	00h22m43.72s	-00d16m57.46s	0.05, 0.05	19	0.15	1.01	5.7×10^{-5}	U
060614	0.125	21h23m32.10s	-53d01m36.57s	0.01, 0.01	2	0.41	0.95	3.6×10^{-4}	U
100816A	**0.8049**	23h26m57.54s	+26d34m41.15s	0.12, 0.12	1	1.77	13.70	6.1×10^{-3}	U
110106A	0.093	05h17m12.82s	+64d10m22.44s	0.01, 0.01	1	5.12	9.14	3.3×10^{-3}	U

Notes.
[a] empty pval indicates association from the litterature
[p] indicates a photometric redshift estimation.

References. (1) `https://catalogs.mast.stsci.edu/panstarrs`; (2) `https://catalogs.mast.stsci.edu/hsc`; (3) [438]; (4) [439]; (5) [389]; (6) [440]; (7) [441]; (8) [442]; (9) AllWISE Source Catalog; (10) [409]; (11) [443]; (12) [444]; (13) [418]; (14) [419]; (15) [422]; (16) [445]; (17) [446]; (18) [436]; (19) [437];

SED fitting procedure: choice of parameters for CIGALE

I refer to [380] for a detailed description of the new version of the code and to the online information to use the code. Here I only describe the assumptions and choices specific to the current study. The main parameters and range of input values are reported in Table 8. The output values of the parameters are estimated by building the probability distribution function (PDF) and by taking its mean and standard deviation. To assess the quality of the fit we compare the results to the SFR derived from the dust corrected H_α luminosity and the amount of dust attenuation derived from the Balmer decrement.

We have adopted a delayed star formation rate (SFR $\propto \mathrm{t}/\tau_0^2 \cdot \mathrm{e}^{-\mathrm{t}/\tau_0}$), on top of which a young burst of constant star formation with a free age and amplitude is added. This scenario aims at reproducing both the general star formation history of distant galaxies (i.e. [447, 448, 449]) and a possible recent burst of star formation. The SFH including young and old stellar populations is defined as:

$$SFR(t) \propto \begin{cases} \dfrac{t}{\tau_0^2} \cdot e^{-t/\tau_0} & \text{if } t < t_0 - t_1 \\ \dfrac{t}{\tau_0^2} \cdot e^{-t/\tau_0} + k \cdot e^{-(t-t_0+t_1)/\tau_1} & \text{if } t \geq t_0 - t_1 \end{cases} \tag{13}$$

with t_0 the age of the main stellar population and t_1 the beginning of the recent episode of star formation, τ_0 and τ_1 the peak of stellar formation for the main population and the burst respectively. The amplitude of the burst episode, k, is linked to the fraction of mass, f_{burst}, created during the burst as:

$$k = \frac{f_{burst}}{1 - f_{burst}} \cdot \frac{\sum_{t=0}^{t_0} \dfrac{t}{\tau_0^2} \cdot e^{-t/\tau_0}}{\sum_{t=t_0-t_1}^{t_0} e^{-(t-t_0+t_1)/\tau_1}} \tag{14}$$

The age of the main stellar population is free to vary from 1 Gyr up to 8 Gyrs. The peak of the star formation is free to vary from 1 to 10 Gyrs which allows to model various shape from nearly constant SFH (high τ) to a rising or declining exponential SFH (see Figure 53). Balmer lines and UV continuum are probing the recent star formation, with a typical age lower than 100 Myrs [450], so the age of the burst (i.e. the young stellar population) is allowed to vary from 1 Myr to 100 Myr. The fraction of stellar mass in the recent burst is allowed to vary from 0 to 50% of the main stellar population with a smaller sampling between 0 and 10%. The initial mass function of [451] is adopted with the stellar synthesis models of [452]. The metallicity is defined with the mass fraction and the available values are Z=0.0001, 0.0004, 0.004, 0.008, 0.02 (solar value) and 0.05. In CIGALE, the same metallicity is assumed for the stellar sources and the gas. Its value is not

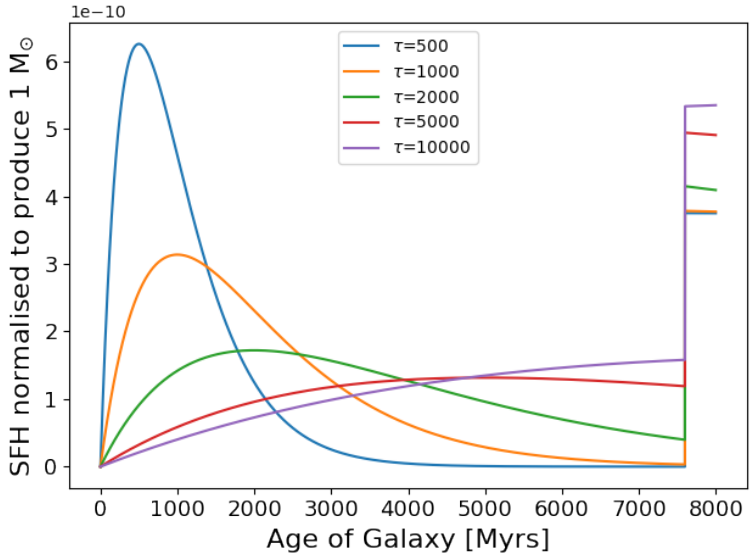

Figure 53: Delayed star forming history (SFH) + recent burst of star formation, normalised to produce 1 solar mass.

well constrained by SED fitting, and so we decided to fix it to the closest value to the measurements (see Table 6)[11]. These measurements span the range $8.34 < 12+\log(\mathrm{O/H}) < 9.12$ and we choose the metal mass fraction to be either 0.008, 0.02 or 0.05.

The dust attenuation is modelled differently for the nebular emission and the stellar continuum. For the stellar continuum, we used the possibility of varying the steepness of the original starburst law [352] and adding a bump centered at 2175 Å. The nebular emission (and therefore the Balmer lines) is attenuated assuming a simple screen model, adopting a Milky Way extinction curve using the formalism of [455] with R_V=3.1 and a color excess $E(B-V)_{lines}$. The nebular and stellar emission attenuation models are linked through the ratio $E(B-V)_{stars}/E(B-V)_{lines}$ with $E(B-V)_{stars}$ the color excess applied to the stellar continuum.

The input parameters to model the dust attenuation are the color excess of the nebular emission $E(B-V)_{lines}$, the ratio $E(B-V)_{stars}/E(B-V)_{lines}$, and the slope, δ, of the attenuation curve applied to the stellar continuum. The values adopted for the input parameters are summarized in Table 2. $E(B-V)_{lines}$ is varying from 0.01 to 2.0 mag. The ratio was found to be 0.44 for local starburst ([456]) but recent works found more similar values between the ionised gas and the stellar continuum for high-z galaxies [457, 458]. Consequently, we let this ratio

[11]The measurements were made using the method in [453] which expressed the metallicity using the oxygen abundance, 12+log(O/H), with the solar value being 12+log(O/H)=8.69 [454].

vary between 0.2 and 1. The slope, δ, is free to vary between -1 and 0.5. As seen in [459] it is extremely challenging to detect a UV bump with wide broadband photometry only, so for this analysis, no bump was added with the exception of GRBH 070802 [459]. In the following the attenuation of the continuum obtained from the SED fitting will be denoted A_V^{stars}.
The stellar emission absorbed by dust is re-emitted in the IR, using IR templates from [460] which are parametrised with a single parameter α_{IR} corresponding to the exponent of the distribution of heating intensity over dust mass. A single template ($\alpha_{IR} = 2$) is used except for galaxies detected in the MIR or FIR for which different α_{IR} between 1 and 3 are tested to cover the range of values found from quiescent to active star-forming galaxies ([461]). Using [NII]/H_α and [OIII]/H_β ratios to separate star-forming galaxies and AGNs in the Baldwin-Phillips-Terlevich (BPT) classification diagram [462, 463], [464] did not find any GRBH in the AGNs region. Consequently, IR templates are used without any AGN contribution.
In the radio domain, where some of the GRBHs have been detected, the emission is due to both thermal processes and non–thermal processes. The former ones are related to the ionisation of the gas by massive stars and the latter ones to the acceleration of charged particle through a magnetic field, i.e. a synchrotron emission. The thermal emission in the radio domain is already modelled by the nebular continuum emission. The synchrotron emission is modelled using the correlation between the radio flux at 1.4GHz and the total IR luminosity, q_{TIR}, and a power-law spectral slope α normalised at 1.4GHz. q_{TIR} is defined as:

$$q_{TIR} \equiv log_{10}\left(\frac{L_{TIR}}{3.75 \cdot 10^{12} Hz}\right) - log_{10}\left(\frac{L_{1.4GHz}}{W.Hz^{-1}}\right) \tag{15}$$

with L_{TIR} the total IR (8-1000 μm) luminosity and $L_{1.4GHz}$ the luminosity at 1.4 GHz. Knowing the total IR luminosity, q_{TIR} is used to compute the flux at 1.4GHz which gives the normalisation of the power-slope law for the non-thermal flux as:

$$F_{non-thermal} \propto \left(\frac{\nu_{1.4GHz}}{\nu}\right)^{\alpha} \cdot \frac{L_{TIR}}{10^{q_{TIR}}} \tag{16}$$

This simple recipe is assuming that the spectrum is dominated by non-thermal emission at 1.4GHz [465, 466, 467]. When no or few other data are available in the FIR domain, it can also help to constrain the IR emission. At most, GRBHs in our sample are detected in one band in the radio domain, so we fixed α to 0.7 and q_{TIR} to 2.5 which are typical values for star-forming galaxies [468]. When there is one detection in the FIR and radio, q_{TIR} is allowed to vary between 1.5 and 3 to [468]. Starbursting galaxies are expecting to be IR-excess sources, meaning high q_{TIR} ~3 [469].

Table 8: Input parameters for SED fitting with CIGALE

Parameter	Symbol	Range
Delayed star formation history + recent burst		
Age of the main stellar population	t_0	1 to 13 with steps of 1 Gyrs
e-folding time of the main stellar population model	τ	0.5, 1, 2, 3, 4 5, 6, 7, 8 ,9, 10, 20 Gyrs
Metallicity [1]	Z	0.004, 0.008, 0.02, 0.05
Dust attenuation		
Color excess for nebular emission [2]	$\mathrm{E(B-V)_{lines}}$	0.0, 0.005, 0.01, 0.05, 0.1, 0.15, 0.2, 0.25, 0.3,0.35,0.4,0.45,0.5,0.6,0.7,0.8,0.9,1.0
Ratio of color excess	$\frac{E(B-V)_{stars}}{E(B-V)_{lines}}$	0.44
Attenuation curve slope for stellar continuum	δ	-0.4
Dust emission in the IR		
powerlaw slope $\mathrm{dU/dM}_d \propto \mathrm{U}^{\alpha}$ [3]	α_{IR}	1.0, 1.5, 2.0, 2.5, 3.0
Non-thermal radio emission		
TIR/radio luminosities ratio	q_{TIR}	1.5, 2.0, 2.5, 3.0

[1] Z=0.02 being the solar metallicity)

[2] $\mathrm{E(B-V)_{lines}}$ is the color excess between the B and V bands applied on the nebular emission lines.

[3] M_d corresponds to the dust mass heated by the the radiation field intensity U. α_{IR} is fixed to 2 when no IR detection is available.

Table 9: Summary of SED fitting results. Columns list (1) the galaxy identification, (2) redshift, (3) stellar mass in log scale, (4) SFR in log scale, (5) amount of dust attenuation in the V band, (6) metallicity, (7) age weighted by stellar mass. The GRBs whose classification short/long is not clear are put at the end of the table.

GRBH	z	$\log_{10}(M_\star)$ $[M_\odot]$	$\log_{10}$(SFR) $[M_\odot\ \mathrm{yr}^{-1}]$	A_V mag	Z	t_{mass} Gyrs
050509B	0.2249	$11.35^{+0.06}_{-0.07}$	$<$ -0.35	0.04 ± 0.04	0.008 ± 0.002	7.044 ± 1.454
050709	0.1606	$8.65^{+0.13}_{-0.18}$	$-0.60^{+0.18}_{-0.30}$	0.26 ± 0.22	0.007 ± 0.005	2.048 ± 1.211
050724	0.258	$10.84^{+0.04}_{-0.05}$	$0.33^{+0.08}_{-0.10}$	0.05 ± 0.05	0.050 ± 0.001	3.899 ± 0.458
051221A	0.5465	$9.12^{+0.14}_{-0.21}$	$0.18^{+0.19}_{-0.35}$	0.28 ± 0.25	0.007 ± 0.004	1.138 ± 0.813
051227	1.12 ± 0.28	$9.19^{+0.53}_{-nan}$	$-0.14^{+0.23}_{-0.52}$	0.13 ± 0.10	0.022 ± 0.018	1.078 ± 0.578
060801	1.131	$9.59^{+0.19}_{-0.35}$	$0.71^{+0.06}_{-0.07}$	0.05 ± 0.05	0.035 ± 0.018	0.724 ± 0.443
061006	0.4377	$9.00^{+0.11}_{-0.15}$	$-0.70^{+0.09}_{-0.11}$	0.08 ± 0.06	0.008 ± 0.006	2.969 ± 1.028
061201	0.111	$9.24^{+0.11}_{-0.15}$	$-0.19^{+0.11}_{-0.16}$	0.39 ± 0.18	0.022 ± 0.014	2.596 ± 1.201
061210	0.4095	$9.84^{+0.07}_{-0.09}$	$-0.39^{+0.17}_{-0.28}$	0.05 ± 0.05	0.041 ± 0.016	2.614 ± 0.872
061217	0.827	$9.04^{+0.06}_{-0.07}$	$0.45^{+0.04}_{-0.04}$	0.04 ± 0.05	0.007 ± 0.003	0.342 ± 0.069
070429B	0.902	$10.67^{+0.06}_{-0.07}$	$-0.18^{+0.23}_{-0.50}$	0.05 ± 0.05	0.010 ± 0.006	3.198 ± 0.434
070714B	0.92	$9.45^{+0.08}_{-0.10}$	$-0.15^{+0.09}_{-0.11}$	0.08 ± 0.06	0.017 ± 0.013	1.760 ± 0.585

Continue on next page

GRBH	z	$\log_{10}(M_\star)$ $[M_\odot]$	$\log_{10}$(SFR) $[M_\odot\ \mathrm{yr}^{-1}]$	A_V mag	Z	t_{mass} Gyrs
070724A	0.457	$10.08^{+0.09}_{-0.12}$	$0.69^{+0.13}_{-0.18}$	0.17 ± 0.14	0.025 ± 0.014	2.380 ± 0.886
070729	0.66 ± 0.08	$10.55^{+0.10}_{-0.14}$	$-0.49^{+0.30}_{-2.67}$	0.04 ± 0.05	0.042 ± 0.014	4.523 ± 1.179
070809	0.473	$11.19^{+0.05}_{-0.05}$	< -0.49	0.06 ± 0.05	0.011 ± 0.005	5.803 ± 1.099
071227	0.381	$10.54^{+0.07}_{-0.08}$	$1.17^{+0.05}_{-0.06}$	1.66 ± 0.08	0.049 ± 0.005	2.182 ± 0.622
080123	0.495	$10.21^{+0.07}_{-0.09}$	$0.39^{+0.10}_{-0.13}$	0.08 ± 0.05	0.017 ± 0.010	2.528 ± 0.824
090510	0.903	$9.86^{+0.10}_{-0.13}$	$0.35^{+0.10}_{-0.12}$	0.08 ± 0.06	0.011 ± 0.012	1.723 ± 0.536
100117A	0.915	$10.49^{+0.05}_{-0.05}$	< -1.15	0.06 ± 0.05	0.007 ± 0.003	4.460 ± 0.538
100206A	0.4068	$10.47^{+0.12}_{-0.16}$	$1.44^{+0.07}_{-0.08}$	1.77 ± 0.14	0.043 ± 0.013	1.058 ± 0.548
100625A	0.452	$9.77^{+0.09}_{-0.11}$	$-0.58^{+0.17}_{-0.30}$	0.05 ± 0.05	0.037 ± 0.017	3.249 ± 1.115
101219A	0.718	$9.47^{+0.23}_{-0.52}$	$1.06^{+0.22}_{-0.46}$	1.38 ± 0.36	0.017 ± 0.006	1.662 ± 1.132
111117A	2.211	$9.96^{+0.15}_{-0.22}$	$1.03^{+0.07}_{-0.08}$	0.09 ± 0.06	0.016 ± 0.016	0.753 ± 0.271
130603B	0.3565	$9.92^{+0.09}_{-0.12}$	$0.46^{+0.13}_{-0.19}$	0.52 ± 0.17	0.026 ± 0.014	2.491 ± 0.928
140903A	0.351	$10.61^{+0.07}_{-0.08}$	$-0.18^{+0.17}_{-0.28}$	0.06 ± 0.05	0.049 ± 0.005	4.447 ± 0.894
141212A	0.596	$10.17^{+0.08}_{-0.10}$	$-0.06^{+0.09}_{-0.12}$	0.05 ± 0.05	0.046 ± 0.011	2.943 ± 0.597
150101B	0.1343	$11.22^{+0.04}_{-0.05}$	$-0.10^{+0.12}_{-0.16}$	0.26 ± 0.09	0.019 ± 0.003	6.041 ± 0.739
150120A	0.46	$9.73^{+0.18}_{-0.32}$	$-0.19^{+0.20}_{-0.40}$	0.06 ± 0.05	0.014 ± 0.014	2.848 ± 1.063
160624A	0.483	$9.95^{+0.05}_{-0.06}$	$0.03^{+0.11}_{-0.14}$	0.07 ± 0.05	0.041 ± 0.014	2.590 ± 0.579
160821B	0.1616	$9.00^{+0.10}_{-0.13}$	$0.07^{+0.07}_{-0.09}$	0.02 ± 0.03	0.005 ± 0.002	0.851 ± 0.413

Continue on next page

GRBH	z	$\log_{10}(M_\star)$ $[M_\odot]$	$\log_{10}$(SFR) $[M_\odot\ \mathrm{yr}^{-1}]$	A_V mag	Z	t_{mass} Gyrs
161104A	0.793	$10.34^{+0.07}_{-0.09}$	$<$ -0.80	0.05 ± 0.05	0.009 ± 0.009	3.946 ± 0.773
170817A	0.009787	$10.62^{+0.04}_{-0.04}$	$-2.21^{+0.29}_{-1.53}$	0.06 ± 0.00	0.020 ± 0.000	9.482 ± 1.193
181123B	1.754	$10.06^{+0.13}_{-0.18}$	$1.17^{+0.13}_{-0.19}$	0.37 ± 0.16	0.018 ± 0.017	0.738 ± 0.318
200522A	0.5536	$9.66^{+0.10}_{-0.13}$	$0.83^{+0.12}_{-0.16}$	0.41 ± 0.16	0.008 ± 0.001	0.713 ± 0.511
060614	0.125	$8.15^{+0.10}_{-0.12}$	$-1.96^{+0.15}_{-0.23}$	0.06 ± 0.05	0.005 ± 0.002	3.899 ± 1.720
100816A	0.8049	$10.57^{+0.08}_{-0.10}$	$0.74^{+0.06}_{-0.07}$	0.07 ± 0.05	0.045 ± 0.011	2.143 ± 0.522
110106A	0.093	$10.15^{+0.07}_{-0.08}$	$<$ -1.31	0.05 ± 0.05	0.010 ± 0.005	7.630 ± 2.069

Table 10: GRB host photometry. Magnitudes are given in the standard calibration system for each filter. Both magnitudes and fluxes are corrected for Galactic extinction using [379]

Host	Band	Magnitude	Flux (μJy)	Instrument	Reference
050509B	u	20.17 ± 0.11	31.06 ± 3.03	SDSS	SDSS DR12
	g	18.60 ± 0.01	131.53 ± 1.45	Pan-STARRS	PS1 DR2
	r	17.28 ± 0.01	444.30 ± 2.05	Pan-STARRS	PS1 DR2
	i	16.76 ± 0.01	715.30 ± 3.29	Pan-STARRS	PS1 DR2
	z	16.54 ± 0.01	881.19 ± 4.87	Pan-STARRS	PS1 DR2
	y	16.49 ± 0.01	916.74 ± 7.60	Pan-STARRS	PS1 DR2
	J	16.28 ± 0.09	1112.24 ± 94.25	2MASS	[470]
	H	16.09 ± 0.13	1325.77 ± 156.30	2MASS	[470]
	K	16.20 ± 0.12	1198.42 ± 131.35	2MASS	[470]
	3.4 μm	16.70 ± 0.03	756.59 ± 18.81	WISE1	ALLWISE
	4.6 μm	17.07 ± 0.04	540.03 ± 17.41	WISE2	ALLWISE
	12 μm	> 17.71	< 299.69	WISE3	ALLWISE
	22 μm	> 15.64	< 2016.67	WISE4	ALLWISE
050709	B	22.06 ± 0.10	5.45 ± 0.50	Danish	[362]

Host	Band	Magnitude	Flux (μJy)	Instrument	Reference
	V	21.32 ± 0.07	10.76 ± 0.69	VLT/FORS1	[384]
	R	21.24 ± 0.07	11.56 ± 0.75	VLT/FORS1	[384]
	I	21.06 ± 0.08	13.72 ± 1.01	VLT/FORS1	[384]
	J	20.75 ± 0.08	18.16 ± 1.34	Magellan	[326]
	K	21.04 ± 0.16	13.92 ± 2.05	Magellan	[326]
050724	U	> 20.66	< 19.76	NOT-ALFOSC	[471]
	B	20.25 ± 0.12	28.86 ± 3.19	NOT/ALFOSC	[471]
	g	19.74 ± 0.10	46.21 ± 4.04	Pan-STARRS	PS1 DR2
	V	19.11 ± 0.05	82.17 ± 3.78	NOT/ALFOSC	[471]
	r	18.92 ± 0.03	97.77 ± 2.52	Pan-STARRS	PS1 DR2
	R	18.60 ± 0.03	131.59 ± 3.64	NOT/ALFOSC	[471]
	i	18.41 ± 0.02	156.55 ± 2.45	Pan-STARRS	PS1 DR2
	I	18.12 ± 0.20	204.69 ± 37.71	GMOS	[472]
	z	18.14 ± 0.03	200.71 ± 4.81	Pan-STARRS	PS1 DR2
	y	17.96 ± 0.04	237.00 ± 9.17	Pan-STARRS	PS1 DR2
	Js	17.43 ± 0.04	388.42 ± 14.31	TNG/NICS	[471]
	H	16.97 ± 0.05	589.23 ± 27.14	TNG/NICS	[471]
	Ks	16.69 ± 0.04	766.93 ± 28.25	TNG/NICS	[471]

Host	Band	Magnitude	Flux (μJy)	Instrument	Reference
	3.4 μm	17.73 ± 0.16	293.17 ± 43.20	WISE1	ALLWISE
051210	g	24.23 ± 0.34	0.74 ± 0.23	GMOS	[326]
	r	24.00 ± 0.15	0.91 ± 0.13	GMOS	[326]
	i	24.87 ± 0.22	0.41 ± 0.08	GMOS	[326]
	z	24.03 ± 0.21	0.88 ± 0.17	GMOS	[326]
	K	> 20.90	< 15.83	Magellan/Baade - PANIC	[326]
051221A	g	23.52 ± 0.07	1.42 ± 0.09	Gemini/GMOS	[326]
	F555W	23.05 ± 0.12	2.18 ± 0.24	HST/WFPC2	HSC
	F814W	22.36 ± 0.03	4.13 ± 0.13	HST/WFPC2	HSC
	J	21.96 ± 0.20	5.95 ± 1.10	Magellan/Baade - PANIC	[326]
	K	22.27 ± 0.15	4.47 ± 0.62	Magellan/Baade - PANIC	[326]
051227	B	25.79 ± 0.15	0.18 ± 0.02	VLT/FORS1	[403]
	V	25.62 ± 0.11	0.21 ± 0.02	VLT/FORS1	[403]
	r	25.80 ± 0.15	0.17 ± 0.02	GMOS	[389]
	R	25.59 ± 0.09	0.21 ± 0.02	VLT/FORS1	[403]
	I	25.48 ± 0.40	0.23 ± 0.09	VLT/FORS1	[403]
	F814W	25.14 ± 0.10	0.32 ± 0.03	HST/ACS	HSC
	J	> 23.97	< 0.94	VLT/FORS2	[403]

Host	Band	Magnitude	Flux (μJy)	Instrument	Reference
060614	u	24.70 ± 0.23	0.48 ± 0.10	UVOT	[473]
	F435W	23.53 ± 0.02	1.40 ± 0.03	HST/ACS	HSC
	V	22.76 ± 0.07	2.86 ± 0.18	VLT/FORS1	[474]
	F606W	22.76 ± 0.02	2.87 ± 0.05	HST/WFPC2	HSC
	F606W	22.86 ± 0.02	2.61 ± 0.05	HST/ACS	HSC
	R	22.64 ± 0.04	3.21 ± 0.12	VLT/FORS1	[474]
	F814W	22.46 ± 0.02	3.76 ± 0.07	HST/WFPC2	HSC
	F160W	22.13 ± 0.02	5.11 ± 0.09	HST/WFC3-IR	HSC
	Ks	22.24 ± 0.20	4.62 ± 0.85	VLT/ISAAC	[475]
	IRAC1	22.90 ± 0.13	2.51 ± 0.30	Spitzer	[381]
060801	g	23.38 ± 0.09	1.61 ± 0.13	GMOS	[326]
	r	23.16 ± 0.11	1.98 ± 0.20	GMOS	[326]
	i	23.02 ± 0.19	2.25 ± 0.39	GMOS	[326]
	z	22.85 ± 0.10	2.62 ± 0.24	GMOS	[326]
	J	> 21.50	< 9.09	Magellan/PANIC	[326]
	K	> 19.90	< 39.77	Magellan/PANIC	[326]
061006	B	24.63 ± 0.12	0.51 ± 0.06	VLT/FORS2	[403]
	V	23.72 ± 0.07	1.18 ± 0.08	VLT/FORS1	[403]

Host	Band	Magnitude	Flux (μJy)	Instrument	Reference
	r	23.43 ± 0.09	1.53 ± 0.13	GMOS	[326]
	R	23.50 ± 0.12	1.44 ± 0.16	VLT/FORS1	[403]
	I	23.01 ± 0.12	2.27 ± 0.25	VLT/FORS1	[403]
	F814W	22.97 ± 0.07	2.35 ± 0.14	HST/ACS	HSC
	z	22.89 ± 0.25	2.53 ± 0.58	GMOS	[326]
	J	22.68 ± 0.20	3.09 ± 0.57	VLT/ISAAC	[403]
	K	22.50 ± 0.25	3.63 ± 0.84	Magellan/Baade - PANIC	[326]
061201	NUV	21.24 ± 0.34	11.59 ± 3.67	GALEX	[476]
	F450W	20.17 ± 0.01	30.93 ± 0.28	HST/WFPC2	HSC
	F606W	19.65 ± 0.01	49.93 ± 0.46	HST/ACS	HSC
	F814W	19.23 ± 0.01	73.76 ± 0.68	HST/ACS	HSC
	Y	19.40 ± 0.23	63.13 ± 13.09	VISTA	[477]
	J	19.03 ± 0.25	89.00 ± 20.21	VISTA	[477]
	F160W	18.63 ± 0.01	128.24 ± 1.18	WFC3/IR	[249]
	Ks	18.82 ± 0.26	107.38 ± 25.23	VISTA	[477]
	3.4 μm	19.15 ± 0.06	79.67 ± 4.33	WISE1	ALLWISE
	4.6 μm	19.83 ± 0.18	42.34 ± 7.02	WISE2	ALLWISE
	12 μm	> 17.50	< 363.64	WISE3	ALLWISE

Host	Band	Magnitude	Flux (μJy)	Instrument	Reference
	22 μm	> 15.51	< 2279.48	WISE4	ALLWISE
061210	g	23.29 ± 0.21	1.76 ± 0.33	PAN-STARRS	PS1 DR2
	r	21.68 ± 0.09	7.70 ± 0.67	Pan-STARRS	PS1 DR2
	i	21.50 ± 0.10	9.12 ± 0.82	Pan-STARRS	PS1 DR2
	z	20.93 ± 0.12	15.41 ± 1.76	Pan-STARRS	PS1 DR2
	J	21.30 ± 0.15	11.00 ± 1.52	Magellan/PANIC	[326]
	K	20.32 ± 0.10	26.99 ± 2.49	Magellan/PANIC	[326]
	3.4 μm	19.83 ± 0.14	42.57 ± 5.33	WISE1	ALLWISE
	4.6 μm	20.05 ± 0.33	34.68 ± 10.60	WISE2	ALLWISE
	12 μm	> 17.39	< 401.67	WISE3	ALLWISE
	22 μm	> 15.21	< 2982.87	WISE4	ALLWISE
061217	g	23.33 ± 0.10	1.70 ± 0.16	GMOS	[326]
	r	22.94 ± 0.10	2.42 ± 0.22	GMOS	[326]
	i	22.44 ± 0.06	3.84 ± 0.21	GMOS	[326]
	z	22.40 ± 0.08	3.97 ± 0.29	GMOS	[326]
	J	23.18 ± 0.35	1.94 ± 0.63	Magellan/PANIC	[326]
	Ks	23.06 ± 0.23	2.16 ± 0.46	Magellan/Baade - PANIC	[326]
070429B	g	24.31 ± 0.20	0.68 ± 0.13	GMOS	[326]

Host	Band	Magnitude	Flux (μJy)	Instrument	Reference
	F475W	24.31 ± 0.20	0.69 ± 0.13	WFC3/UVIS	[249]
	r	23.22 ± 0.04	1.87 ± 0.07	GMOS	[326]
	i	21.85 ± 0.09	6.60 ± 0.55	GMOS	[326]
	z	21.73 ± 0.12	7.40 ± 0.82	GMOS	[326]
	J	20.61 ± 0.31	20.63 ± 5.85	VISTA	[477]
	F160W	20.59 ± 0.03	21.09 ± 0.58	WFC3/IR	[249]
	3.4 μm	20.06 ± 0.15	34.34 ± 4.62	WISE1	ALLWISE
	4.6 μm	> 19.99	< 36.58	WISE2	ALLWISE
	12 μm	> 17.68	< 308.08	WISE3	ALLWISE
	22 μm	> 15.61	< 2069.35	WISE4	ALLWISE
070714B	g	25.36 ± 0.35	0.26 ± 0.08	GMOS	[478]
	F475W	24.89 ± 0.06	0.40 ± 0.02	WFC3/UVIS	[249]
	r	24.61 ± 0.22	0.52 ± 0.11	GMOS	[478]
	i	23.73 ± 0.13	1.17 ± 0.14	GMOS	[478]
	z	23.84 ± 0.13	1.06 ± 0.13	GMOS	[478]
	J	23.06 ± 0.12	2.16 ± 0.24	Gemini-S/NIRI	[478]
	F160W	22.99 ± 0.02	2.31 ± 0.04	WFC3/IR	[249]
	K	22.97 ± 0.13	2.35 ± 0.28	Gemini-S/NIRI	[478]

Host	Band	Magnitude	Flux (μJy)	Instrument	Reference
070724A	NUV	21.60 ± 0.25	8.30 ± 1.91	GALEX	[367]
	g	21.52 ± 0.06	8.97 ± 0.50	GMOS	[326]
	r	20.75 ± 0.03	18.26 ± 0.50	GMOS	[326]
	i	20.44 ± 0.03	24.30 ± 0.67	GMOS	[326]
	y	20.30 ± 0.13	27.65 ± 3.31	Pan-STARRS	[367]
	z	20.26 ± 0.04	28.49 ± 1.05	GMOS	[326]
	J	20.01 ± 0.10	35.89 ± 3.31	Magellan/PANIC	[326]
	H	19.78 ± 0.10	44.40 ± 4.09	Magellan/PANIC	[326]
	K	19.71 ± 0.10	47.39 ± 4.36	Magellan/PANIC	[326]
	3.4 μm	19.92 ± 0.16	38.98 ± 5.60	WISE1	ALLWISE
	4.6 μm	20.40 ± 0.43	25.10 ± 9.89	WISE2	ALLWISE
070729	g	24.39 ± 0.38	0.64 ± 0.22	GMOS	[326]
	r	23.32 ± 0.03	1.71 ± 0.05	GMOS	[326]
	i	21.81 ± 0.06	6.87 ± 0.38	GMOS	[326]
	z	21.82 ± 0.17	6.76 ± 1.06	GMOS	[326]
	J	20.85 ± 0.10	16.54 ± 1.52	Magellan/Baade - PANIC	[326]
	K	20.10 ± 0.10	33.08 ± 3.05	Magellan/Baade - PANIC	[326]
070809	g	21.85 ± 0.05	6.60 ± 0.30	GMOS	[326]

Host	Band	Magnitude	Flux (μJy)	Instrument	Reference
	r	19.93 ± 0.02	38.60 ± 0.71	GMOS	[326]
	i	19.31 ± 0.05	68.53 ± 3.16	GMOS	[326]
	Y	18.48 ± 0.07	147.29 ± 9.88	VISTA	[477]
	J	18.40 ± 0.09	158.56 ± 13.39	VISTA	[477]
	F160W	18.22 ± 0.01	187.08 ± 1.72	HST/WFC3	[249]
	Ks	18.10 ± 0.12	209.19 ± 23.00	VISTA	[477]
	K	17.97 ± 0.04	236.43 ± 8.71	Magellan/Baade - PANIC	[326]
071227	F438W	22.35 ± 0.05	4.17 ± 0.19	WFC3/UVIS	[249]
	g	22.83 ± 0.13	2.69 ± 0.32	GMOS	[326]
	r	20.61 ± 0.05	20.78 ± 0.96	GMOS	[326]
	i	20.48 ± 0.04	23.43 ± 0.86	GMOS	[326]
	z	19.77 ± 0.03	44.74 ± 1.24	GMOS	[326]
	J	19.16 ± 0.06	78.53 ± 4.34	Magellan/Baade - PANIC	[326]
	F160W	18.73 ± 0.01	116.96 ± 1.08	WFC3/IR	[249]
	K	18.15 ± 0.06	199.39 ± 11.02	Magellan/Baade - PANIC	[326]
	3.4 μm	18.27 ± 0.03	178.98 ± 5.28	WISE1	ALLWISE
	4.6 μm	18.47 ± 0.05	149.16 ± 6.73	WISE2	ALLWISE
	12 μm	17.13 ± 0.16	510.82 ± 73.40	WISE3	ALLWISE

Host	Band	Magnitude	Flux (μJy)	Instrument	Reference
	22 μm	16.20 ± 0.48	1202.91 ± 530.70	WISE4	ALLWISE
	5.5GHz	–	43.00 ± 11.00	ATCA	[479]
080123	g	22.07 ± 0.06	5.37 ± 0.30	GMOS	[326]
	r	20.90 ± 0.05	15.82 ± 0.73	GMOS	[326]
	i	20.50 ± 0.07	22.89 ± 1.48	GMOS	[326]
	z	20.13 ± 0.20	32.32 ± 5.95	GMOS	[326]
	J	20.30 ± 0.05	27.42 ± 1.26	Magellan/PANIC	[326]
	K	19.58 ± 0.06	53.38 ± 2.95	Magellan/PANIC	[326]
	3.4 μm	20.17 ± 0.14	31.14 ± 3.99	WISE1	ALLWISE
	4.6 μm	19.89 ± 0.20	40.21 ± 7.48	WISE2	ALLWISE
	12 μm	> 17.58	< 338.43	WISE3	ALLWISE
	22 μm	> 15.57	< 2148.99	WISE4	ALLWISE
090510	g	23.86 ± 0.20	1.04 ± 0.19	GROND	[409]
	r	23.38 ± 0.12	1.61 ± 0.18	GROND	[409]
	i	22.38 ± 0.10	4.06 ± 0.37	GROND	[409]
	z	22.38 ± 0.09	4.07 ± 0.34	GROND	[409]
	J	22.22 ± 0.17	4.68 ± 0.73	GROND	[409]
	H	21.70 ± 0.13	7.57 ± 0.91	GROND	[409]

Host	Band	Magnitude	Flux (μJy)	Instrument	Reference
	Ks	> 21.39	< 10.08	GROND	[409]
100117A	g	26.18 ± 0.30	0.12 ± 0.03	GMOS	[410]
	r	24.34 ± 0.10	0.67 ± 0.06	Magellan/IMACS	[410]
	i	22.86 ± 0.10	2.60 ± 0.24	Magellan/IMACS	[410]
	z	22.34 ± 0.10	4.22 ± 0.39	Magellan/IMACS	[410]
	J	21.87 ± 0.25	6.46 ± 1.49	Gemini-N/NIRI	[410]
	F160W	21.37 ± 0.04	10.28 ± 0.38	WFC3/IR	[249]
	H	21.26 ± 0.21	11.35 ± 2.19	Gemini-N/NIRI	[410]
	K	21.24 ± 0.20	11.57 ± 2.13	Gemini-N/NIRI	[410]
100206A	g	22.54 ± 0.17	3.48 ± 0.55	Keck/LRIS	[411]
	R	20.73 ± 0.09	18.47 ± 1.53	Keck/LRIS	[411]
	i	20.26 ± 0.08	28.65 ± 2.11	Gemini-N/GMOS-N	[411]
	z	19.74 ± 0.05	46.27 ± 2.13	Gemini-N/GMOS-N	[411]
	J	19.13 ± 0.12	80.72 ± 8.92	PAIRITEL	[411]
	H	18.46 ± 0.09	150.65 ± 12.49	PAIRITEL	[411]
	Ks	18.05 ± 0.11	217.96 ± 22.08	PAIRITEL	[411]
	3.4 μm	18.33 ± 0.05	169.30 ± 7.48	WISE1	ALLWISE
	4.6 μm	18.42 ± 0.09	155.56 ± 13.32	WISE2	ALLWISE

Host	Band	Magnitude	Flux (μJy)	Instrument	Reference
	12 μm	16.55 ± 0.18	867.50 ± 145.42	WISE3	ALLWISE
	22 μm	> 15.17	< 3109.10	WISE4	ALLWISE
	5.5GHz	–	65.00 ± 11.00	VLA	[480]
100625A	g	23.87 ± 0.19	1.03 ± 0.18	Magellan/Baade - IMACS	[412]
	r	22.63 ± 0.09	3.22 ± 0.27	Gemini-S/GMOS	[412]
	i	22.14 ± 0.04	5.06 ± 0.19	Gemini-S/GMOS	[412]
	z	22.07 ± 0.10	5.40 ± 0.50	Gemini-S/GMOS	[412]
	J	21.40 ± 0.06	10.00 ± 0.55	Magellan/PANIC	[412]
	Ks	20.76 ± 0.10	18.03 ± 1.66	Magellan/Baade - FourStar	[412]
100816A	g	22.65 ± 0.10	3.15 ± 0.29	GROND	[480]
	r	22.08 ± 0.10	5.34 ± 0.49	GROND	[480]
	i	21.19 ± 0.10	12.09 ± 1.11	GROND	[480]
	z	21.35 ± 0.15	10.51 ± 1.45	GROND	[480]
	J	20.37 ± 0.11	25.78 ± 2.61	GROND	[480]
	H	20.25 ± 0.17	28.78 ± 4.51	GROND	[480]
	K	> 19.97	< 37.18	GROND	[480]
	3.4 μm	19.75 ± 0.12	45.80 ± 5.10	WISE1	ALLWISE
	4.6 μm	20.17 ± 0.36	30.94 ± 10.17	WISE2	ALLWISE

Host	Band	Magnitude	Flux (μJy)	Instrument	Reference
	12 μm	> 17.29	< 438.80	WISE3	ALLWISE
	22 μm	> 15.39	< 2531.83	WISE4	ALLWISE
101219A	g	24.57 ± 0.08	0.54 ± 0.04	Magellan/Clay - LDSS3	[412]
	r	23.95 ± 0.05	0.96 ± 0.04	GMOS-S	[412]
	i	23.19 ± 0.08	1.92 ± 0.14	GMOS-S	[412]
	z	23.22 ± 0.16	1.87 ± 0.28	Magellan/Clay - LDSS3	[412]
	J	22.11 ± 0.19	5.20 ± 0.91	Magellan/Baade - FourStar	[412]
	Ks	21.55 ± 0.21	8.71 ± 1.68	Magellan/Baade - FourStar	[412]
110106A	g	19.00 ± 0.02	90.99 ± 1.89	Pan-STARRS	PS1 DR2
	r	18.26 ± 0.01	179.50 ± 2.48	Pan-STARRS	PS1 DR2
	i	17.73 ± 0.01	292.63 ± 2.70	Pan-STARRS	PS1 DR2
	z	17.53 ± 0.01	353.17 ± 4.55	Pan-STARRS	PS1 DR2
	y	17.53 ± 0.03	352.14 ± 8.43	Pan-STARRS	PS1 DR2
	3.4 μm	17.85 ± 0.04	264.02 ± 9.00	WISE1	ALLWISE
	4.6 μm	18.43 ± 0.08	154.83 ± 11.12	WISE2	ALLWISE
	12 μm	> 17.73	< 292.60	WISE3	ALLWISE
	22 μm	> 15.46	< 2375.94	WISE4	ALLWISE
111117A	g	23.98 ± 0.09	0.93 ± 0.08	VLT/FORS2	[417]

Host	Band	Magnitude	Flux (μJy)	Instrument	Reference
	r	23.86 ± 0.08	1.03 ± 0.08	GTC/OSIRIS	[417]
	R	23.89 ± 0.06	1.01 ± 0.06	VLT/FORS2	[417]
	i	23.84 ± 0.23	1.06 ± 0.22	GTC/OSIRIS	[417]
	I	24.17 ± 0.15	0.78 ± 0.11	VLT/FORS2	[417]
	z	23.72 ± 0.21	1.18 ± 0.23	VLT/FORS2	[417]
	J	23.11 ± 0.18	2.07 ± 0.34	VLT/HAWK-I	[417]
	H	22.93 ± 0.29	2.45 ± 0.66	VLT/HAWK-I	[417]
	Ks	23.06 ± 0.32	2.17 ± 0.64	VLT/HAWK-I	[417]
120804A	r	25.90 ± 0.20	0.16 ± 0.03	GEMINI/GMOS-N	[419]
	i	24.80 ± 0.15	0.44 ± 0.06	GEMINI/GMOS-N	[419]
	Y	23.70 ± 0.30	1.20 ± 0.33	VLT/HAWK-I	[419]
	J	23.00 ± 0.20	2.29 ± 0.42	Magellan/Baade - FourStar	[419]
	Ks	22.00 ± 0.10	5.75 ± 0.53	VLT/HAWK-I	[419]
	6.7 GHz	–	25.00 ± 4.00	VLA	[419]
	4.9 GHz	–	43.00 ± 4.00	VLA	[419]
130603B	uvw2	> 22.94	< 2.42	UVOT	[420]
	uvm2	22.48 ± 0.32	3.70 ± 1.09	UVOT	[420]
	uvw1	22.92 ± 0.28	2.46 ± 0.64	UVOT	[420]

Host	Band	Magnitude	Flux (μJy)	Instrument	Reference
	u	22.33 ± 0.37	4.26 ± 1.43	SDSS	SDSS DR12
	g	21.98 ± 0.09	5.88 ± 0.46	Pan-STARRS	PS1 DR2
	F606W	21.08 ± 0.04	13.43 ± 0.49	HST/ACS	[249]
	r	20.97 ± 0.06	14.80 ± 0.83	Pan-STARRS	PS1 DR2
	i	20.84 ± 0.06	16.75 ± 0.86	Pan-STARRS	PS1 DR2
	z	20.35 ± 0.04	26.42 ± 0.95	Pan-STARRS	PS1 DR2
	y	20.25 ± 0.11	28.84 ± 2.89	Pan-STARRS	PS1 DR2
	J	20.10 ± 0.07	32.99 ± 2.13	none	[420]
	F160W	19.83 ± 0.02	42.46 ± 0.78	WFC3/IR	[249]
	H	19.81 ± 0.06	43.26 ± 2.39	none	[420]
	K	19.58 ± 0.07	53.30 ± 3.44	none	[420]
	3.4 μm	19.73 ± 0.12	46.72 ± 4.95	WISE1	ALLWISE
	4.6 μm	20.27 ± 0.37	28.33 ± 9.71	WISE2	ALLWISE
	12 μm	> 17.77	< 283.31	WISE3	ALLWISE
	22 μm	> 15.51	< 2264.83	WISE4	ALLWISE
140903A	g	21.86 ± 0.16	6.52 ± 0.96	LMI	[422]
	r	20.51 ± 0.09	22.74 ± 1.88	LMI	[422]
	i	20.07 ± 0.05	34.11 ± 1.57	LMI	[422]

Host	Band	Magnitude	Flux (μJy)	Instrument	Reference
	z	19.63 ± 0.08	51.27 ± 3.78	LMI	[422]
	J	18.90 ± 0.05	100.32 ± 4.62	CAHA/Omega2000	[422]
	H	18.56 ± 0.07	137.31 ± 8.85	CAHA/Omega2000	[422]
	Ks	18.24 ± 0.05	183.62 ± 8.46	CAHA/Omega2000	[422]
141212A	NUV	> 21.01	< 14.36	GALEX	[367]
	g	23.52 ± 0.08	1.41 ± 0.10	GTC/OSIRIS	[481]
	r	22.58 ± 0.06	3.38 ± 0.19	GTC/OSIRIS	[481]
	i	22.15 ± 0.05	5.00 ± 0.23	GTC/OSIRIS	[481]
	z	21.56 ± 0.05	8.61 ± 0.40	Pan-STARRS	[367]
	y	> 20.74	< 18.44	Pan-STARRS	[367]
	J	> 17.31	< 432.58	2MASS	[367]
	H	> 17.39	< 402.77	2MASS	[367]
	K	> 17.53	< 353.69	2MASS	[367]
	3.4 μm	20.43 ± 0.20	24.48 ± 4.42	WISE1	ALLWISE
	4.6 μm	20.70 ± 0.54	19.01 ± 9.44	WISE2	ALLWISE
	12 μm	> 18.02	< 225.25	WISE3	ALLWISE
	22 μm	> 15.83	< 1689.80	WISE4	ALLWISE
150101B	FUV	21.14 ± 0.44	12.76 ± 5.13	GALEX	[476]

Host	Band	Magnitude	Flux (μJy)	Instrument	Reference
	uvm2	21.12 ± 0.18	12.91 ± 2.12	XMM-OM	[482]
	NUV	21.16 ± 0.26	12.52 ± 3.03	GALEX	[476]
	uvw1	20.54 ± 0.08	21.99 ± 1.60	XMM-OM	[482]
	U	19.75 ± 0.04	45.83 ± 1.86	XMM-OM	[482]
	g	17.40 ± 0.03	397.20 ± 10.98	Pan-STARRS	PS1 DR2
	V	16.87 ± 0.01	651.24 ± 8.52	XMM-OM	[482]
	r	16.51 ± 0.03	902.26 ± 24.93	Pan-STARRS	PS1 DR2
	i	16.14 ± 0.03	1265.70 ± 34.97	Pan-STARRS	PS1 DR2
	z	15.86 ± 0.03	1638.03 ± 45.26	Pan-STARRS	PS1 DR2
	y	15.70 ± 0.03	1912.66 ± 52.85	Pan-STARRS	PS1 DR2
	J	15.40 ± 0.12	2501.90 ± 281.13	2MASS	[470]
	H	14.90 ± 0.11	3980.32 ± 395.93	2MASS	[470]
	K	15.06 ± 0.16	3451.54 ± 505.46	2MASS	[470]
	3.4 μm	15.83 ± 0.01	1685.90 ± 21.74	WISE1	ALLWISE
	4.6 μm	16.28 ± 0.04	1119.06 ± 43.29	WISE2	ALLWISE
	12 μm	> 17.25	< 456.11	WISE3	ALLWISE
	22 μm	> 14.45	< 6001.16	WISE4	ALLWISE
	9.8 GHz	–	3150.00 ± 315.00	VLA	[483]

Host	Band	Magnitude	Flux (μJy)	Instrument	Reference
	4.9 GHz	–	7210.00 ± 721.00	WSRT	[484]
	1.4 GHz	–	10200.00 ± 1000.00	VLA	[485]
150120A	g	23.20 ± 0.34	1.91 ± 0.60	Pan-STARRS	PS1 DR2
	r	22.21 ± 0.10	4.74 ± 0.42	Pan-STARRS	PS1 DR2
	i	21.69 ± 0.06	7.63 ± 0.40	Pan-STARRS	PS1 DR2
	z	21.54 ± 0.10	8.79 ± 0.79	Pan-STARRS	PS1 DR2
	y	21.47 ± 0.20	9.34 ± 1.71	Pan-STARRS	PS1 DR2
	J	> 17.09	< 528.17	2MASS	[367]
	H	> 16.15	< 1261.79	2MASS	[367]
	K	> 15.94	< 1525.80	2MASS	[367]
160624A	g	23.08 ± 0.09	2.13 ± 0.18	LDT/LMI	[486]
	F606W	21.98 ± 0.01	5.84 ± 0.08	HST/ACS-WFC	[486]
	r	22.00 ± 0.08	5.75 ± 0.42	LDT/LMI	[486]
	r	22.03 ± 0.02	5.62 ± 0.10	Gemini-N/GMOS	[486]
	i	21.54 ± 0.08	8.75 ± 0.64	LDT/LMI	[486]
	z	21.39 ± 0.08	10.06 ± 0.74	LDT/LMI	[486]
	Y	21.35 ± 0.15	10.46 ± 1.45	Gemini-N/NIRI	[486]
	F125W	20.79 ± 0.01	17.49 ± 0.16	HST/WFC3	[486]

Host	Band	Magnitude	Flux (μJy)	Instrument	Reference
	F160W	20.53 ± 0.01	22.26 ± 0.21	HST/WFC3	[486]
	Ks	20.30 ± 0.08	27.57 ± 2.03	Gemini-N/NIRI	[486]
160821B	g	19.82 ± 0.02	42.77 ± 0.98	Pan-STARRS	PS1 DR2
	r	19.54 ± 0.02	55.37 ± 1.02	Pan-STARRS	PS1 DR2
	i	19.29 ± 0.02	69.93 ± 1.03	Pan-STARRS	PS1 DR2
	z	19.44 ± 0.04	60.61 ± 2.12	Pan-STARRS	PS1 DR2
	y	19.36 ± 0.09	65.76 ± 5.39	Pan-STARRS	PS1 DR2
	3.4 μm	20.49 ± 0.10	23.11 ± 2.15	WISE1	ALLWISE
	4.6 μm	21.00 ± 0.31	14.41 ± 4.13	WISE2	ALLWISE
	12 μm	> 18.68	< 122.54	WISE3	ALLWISE
	22 μm	> 16.21	< 1190.79	WISE4	ALLWISE
161104A	g	25.44 ± 0.25	0.24 ± 0.06	Magellan/IMACS	[446]
	r	23.81 ± 0.10	1.09 ± 0.10	Magellan/IMACS	[446]
	i	22.72 ± 0.06	2.97 ± 0.16	Magellan/IMACS	[446]
	z	22.14 ± 0.07	5.06 ± 0.33	Magellan/IMACS	[446]
	J	21.56 ± 0.04	8.63 ± 0.32	Magellan/Fourstar	[446]
170817A	NUV	17.91 ± 0.09	249.68 ± 19.75	GALEX	[476]
	g	12.92 ± 0.01	24660.05 ± 227.13	Pan-STARRS	PS1 DR2

Host	Band	Magnitude	Flux (μJy)	Instrument	Reference
	r	12.35 ± 0.01	41542.78 ± 382.62	Pan-STARRS	PS1 DR2
	i	11.94 ± 0.01	60737.54 ± 559.41	Pan-STARRS	PS1 DR2
	z	11.72 ± 0.01	74782.50 ± 688.77	Pan-STARRS	PS1 DR2
	y	11.55 ± 0.01	87123.59 ± 802.44	Pan-STARRS	PS1 DR2
	Y	11.41 ± 0.01	99357.62 ± 915.12	VISTA	[477]
	J	10.99 ± 0.02	146514.82 ± 2159.12	2MASS	[470]
	H	10.83 ± 0.02	169194.06 ± 3272.50	2MASS	[470]
	K	11.03 ± 0.02	140928.13 ± 3115.19	2MASS	[470]
	3.4 μm	11.92 ± 0.01	61876.90 ± 569.91	WISE1	ALLWISE
	4.6 μm	12.60 ± 0.01	33257.23 ± 306.31	WISE2	ALLWISE
	12 μm	13.72 ± 0.04	11854.09 ± 425.80	WISE3	ALLWISE
	22 μm	13.87 ± 0.18	10304.69 ± 1727.36	WISE4	ALLWISE
	97.5GHz	–	210.00 ± 20.00	ALMA	[487]
	15GHz	–	295.00 ± 18.00	VLA	[487]
	10GHz	–	288.00 ± 20.00	VLA	[487]
	15GHz	–	250.00 ± 50.00	VLA	[487]
	6GHz	–	330.00 ± 20.00	VLA	[487]
181123B	g	24.08 ± 0.23	0.85 ± 0.18	Gemini-S/GMOS	[436]

Host	Band	Magnitude	Flux (μJy)	Instrument	Reference
	r	23.84 ± 0.19	1.06 ± 0.18	Gemini-S/GMOS	[436]
	i	23.79 ± 0.19	1.11 ± 0.19	Gemini-N/GMOS	[436]
	z	23.84 ± 0.22	1.06 ± 0.21	Gemini-S/GMOS	[436]
	Y	22.78 ± 0.24	2.81 ± 0.62	MMT/MMIRS	[436]
	J	22.85 ± 0.23	2.63 ± 0.56	KeckI/MOSFIRE	[436]
	H	22.61 ± 0.19	3.28 ± 0.57	MMT/MMIRS	[436]
	Ks	22.33 ± 0.23	4.25 ± 0.90	MMT/MMIRS	[436]
200522A	u	22.33 ± 0.05	4.23 ± 0.19	LDT/LMI	[486]
	g	21.99 ± 0.03	5.80 ± 0.16	LDT/LMI	[486]
	g	22.18 ± 0.02	4.88 ± 0.09	Keck/LRIS	[437]
	r	21.24 ± 0.04	11.57 ± 0.43	Gemini-N/GMOS	[486]
	R	21.14 ± 0.02	12.71 ± 0.23	Keck/LRIS	[437]
	i	20.97 ± 0.04	14.92 ± 0.55	LDT/LMI	[486]
	I	20.93 ± 0.01	15.42 ± 0.14	Keck/DEIMOS	[437]
	Z	20.84 ± 0.01	16.75 ± 0.15	Keck/DEIMOS	[437]
	z	20.90 ± 0.03	15.84 ± 0.44	LDT/LMI	[486]
	Y	20.73 ± 0.10	18.48 ± 1.70	Gemini-N/NIRI	[486]
	F125W	20.84 ± 0.01	16.75 ± 0.15	HST/WFC3	[437]

Host	Band	Magnitude	Flux (μJy)	Instrument	Reference
	F160W	20.67 ± 0.01	19.59 ± 0.18	HST/WFC3	[437]
	Ks	20.87 ± 0.17	16.27 ± 2.55	Gemini-N/NIRI	[486]
	IRAC1	21.01 ± 0.10	14.32 ± 1.32	Spitzer	[437]
	IRAC2	21.30 ± 0.10	10.97 ± 1.01	Spitzer	[437]

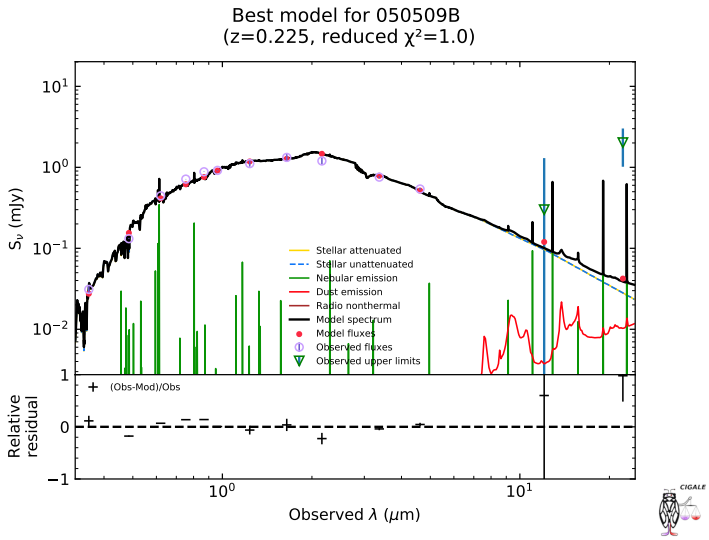

Figure 54: Best-fitted SED for GRBH 050509B. Blue squares are the observed fluxes with their uncertainties, red points are the computed fluxes for a given filter. The black line represents the best fitted spectrum composed of attenuated stellar emission, dust emission, non-thermal radio emission and nebular lines. The dashed blue line represents the unattenuated stellar emission and the blue shaded area indicates the amount dust attenuation. The lower panel shows the relative residual.

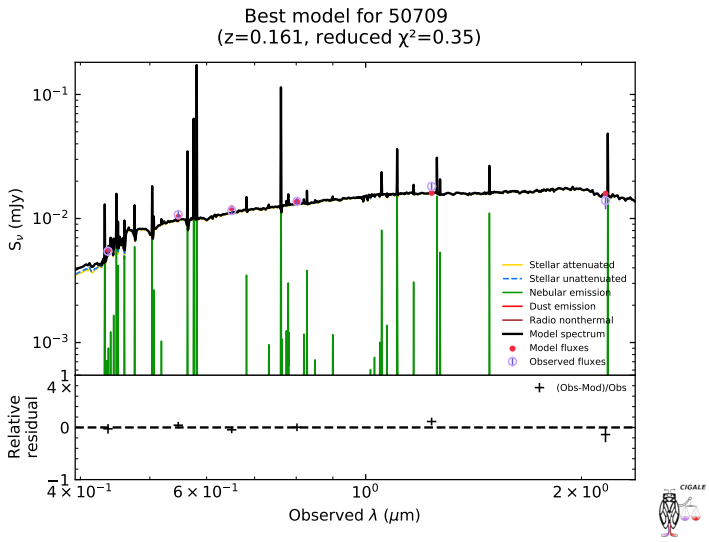

Figure 55: Best-fitted SED for GRBH 050709. Colour and symbols convention as in Figure 54.

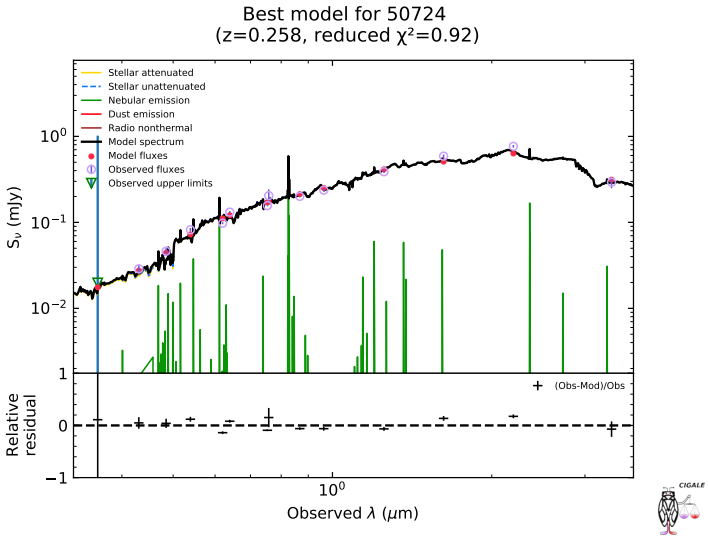

Figure 56: Best-fitted SED for GRBH 050724. Colour and symbols convention as in Figure 54.

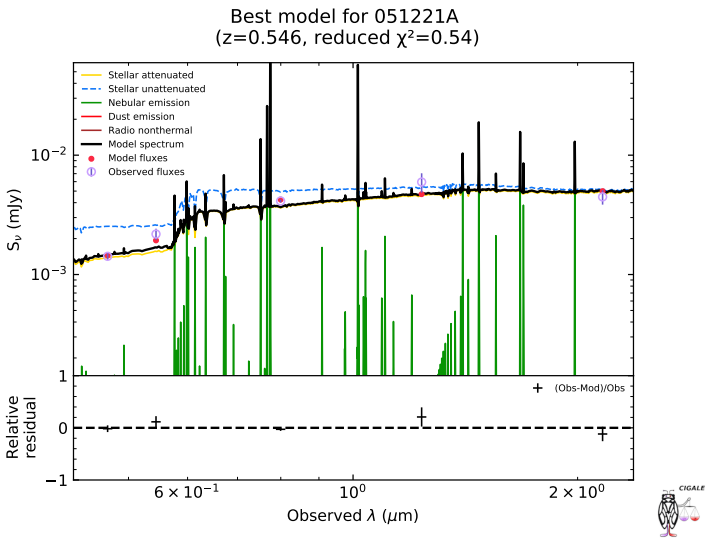

Figure 57: Best-fitted SED for GRBH 051221A. Colour and symbols convention as in Figure 54.

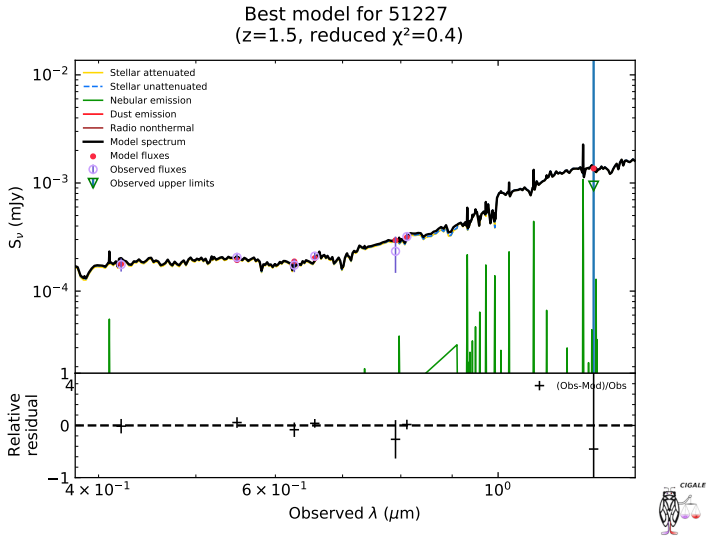

Figure 58: Best-fitted SED for GRBH 051227. Colour and symbols convention as in Figure 54.

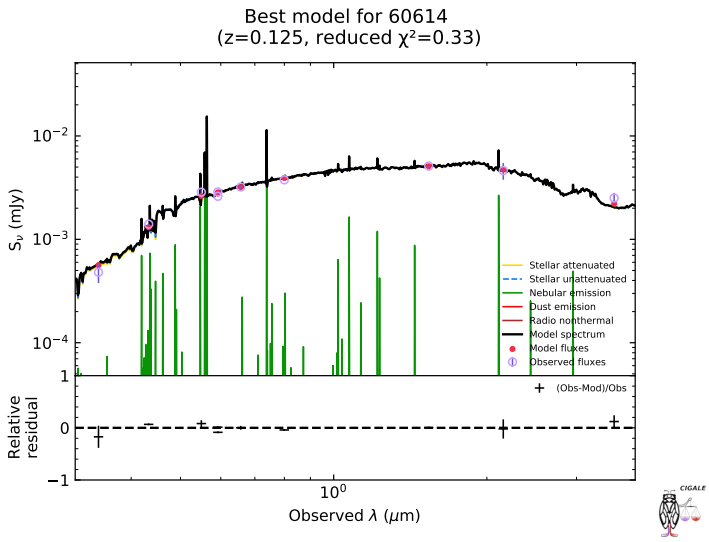

Figure 59: Best-fitted SED for GRBH 060614. Colour and symbols convention as in Figure 54.

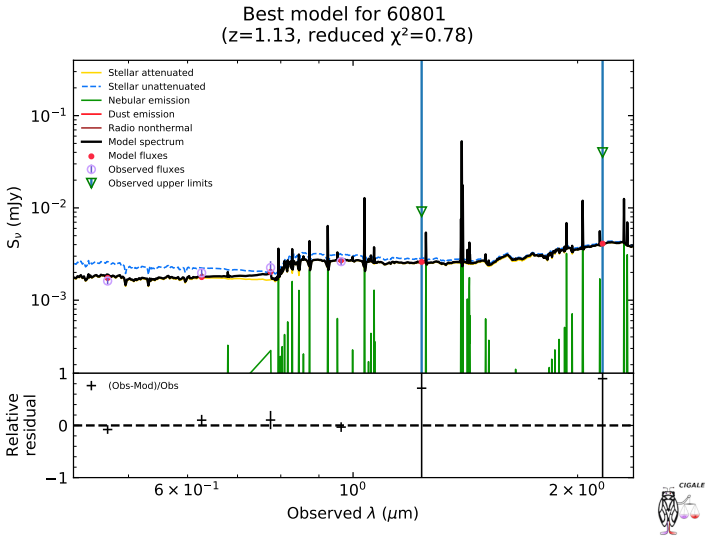

Figure 60: Best-fitted SED for GRBH 060801. Colour and symbols convention as in Figure 54.

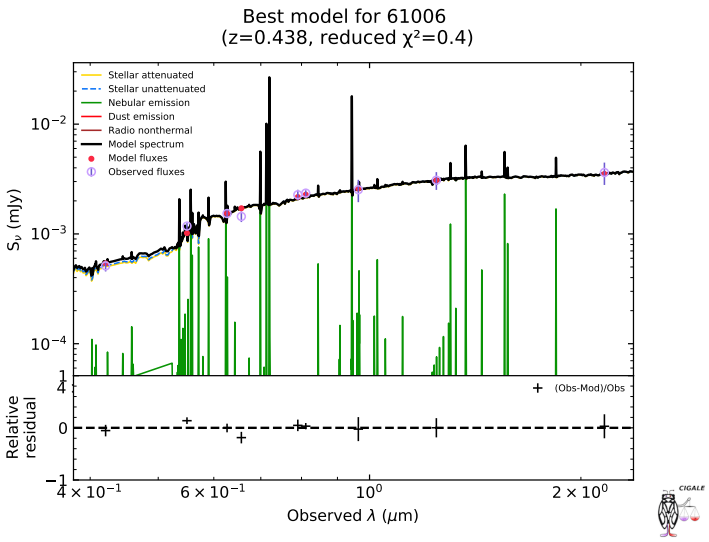

Figure 61: Best-fitted SED for GRBH 061006. Colour and symbols convention as in Figure 54.

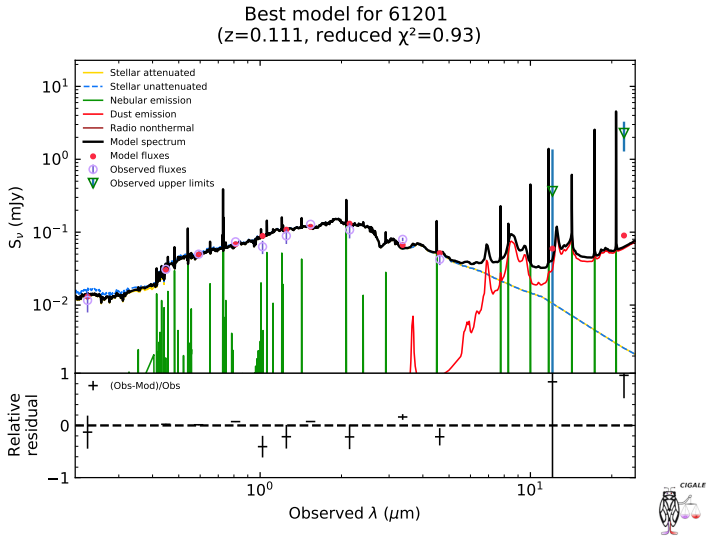

Figure 62: Best-fitted SED for GRBH 061201. Colour and symbols convention as in Figure 54.

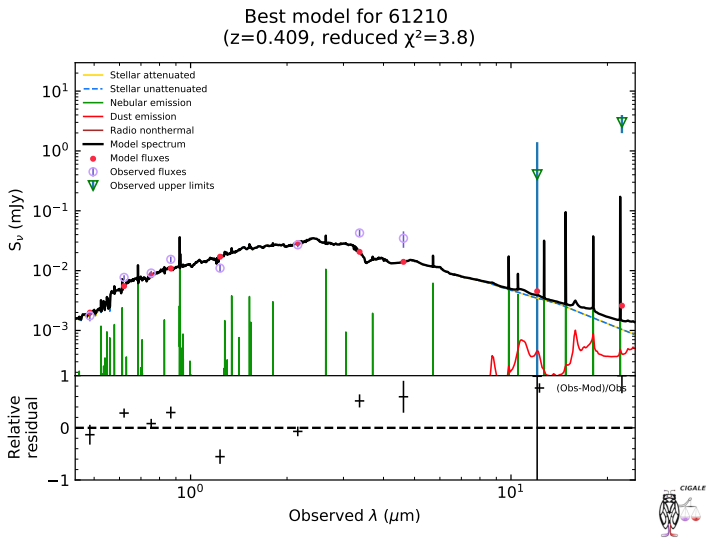

Figure 63: Best-fitted SED for GRBH 061210. Colour and symbols convention as in Figure 54.

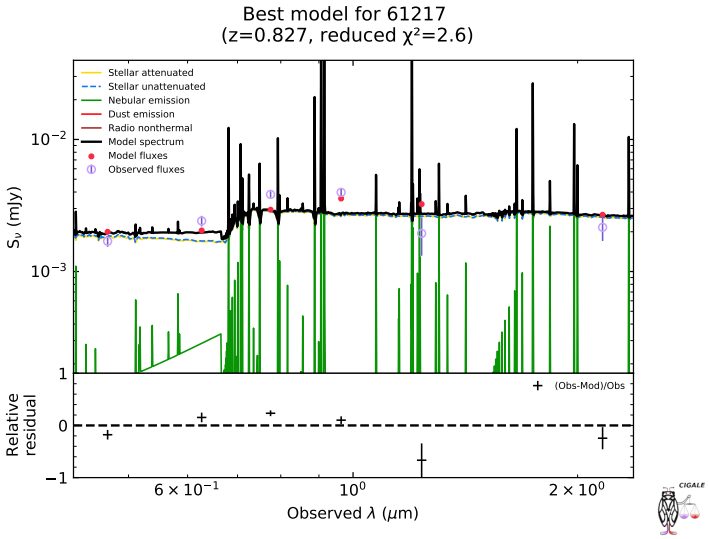

Figure 64: Best-fitted SED for GRBH 061217. Colour and symbols convention as in Figure 54.

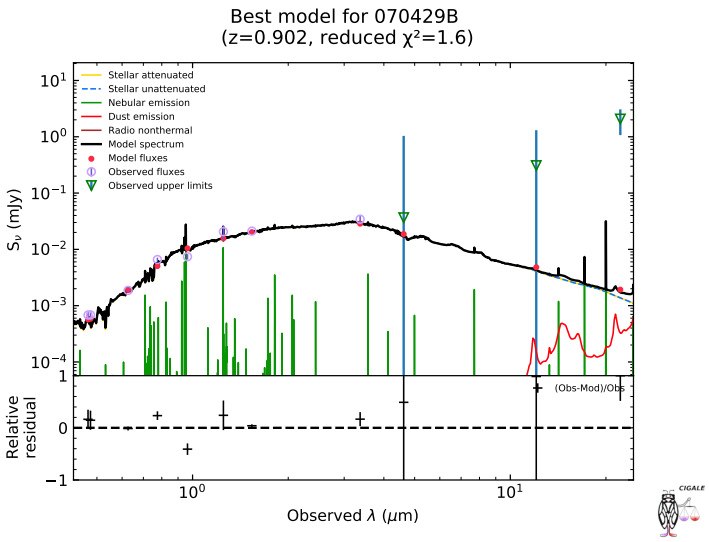

Figure 65: Best-fitted SED for GRBH 070429B. Colour and symbols convention as in Figure 54.

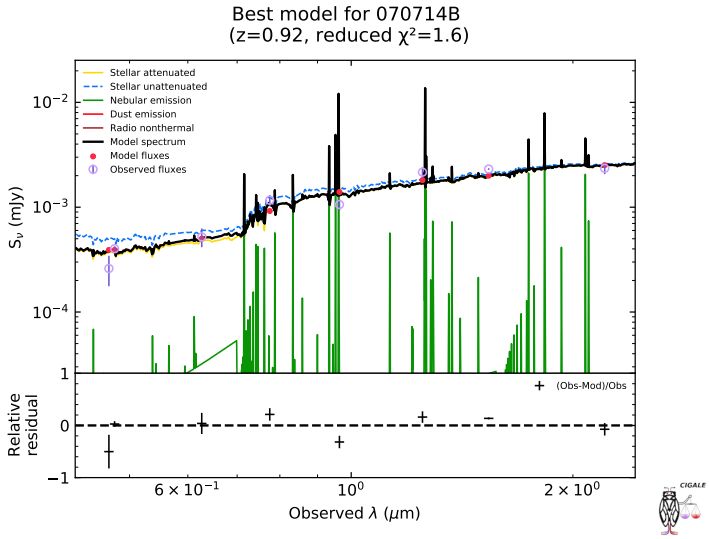

Figure 66: Best-fitted SED for GRBH 070714B. Colour and symbols convention as in Figure 54.

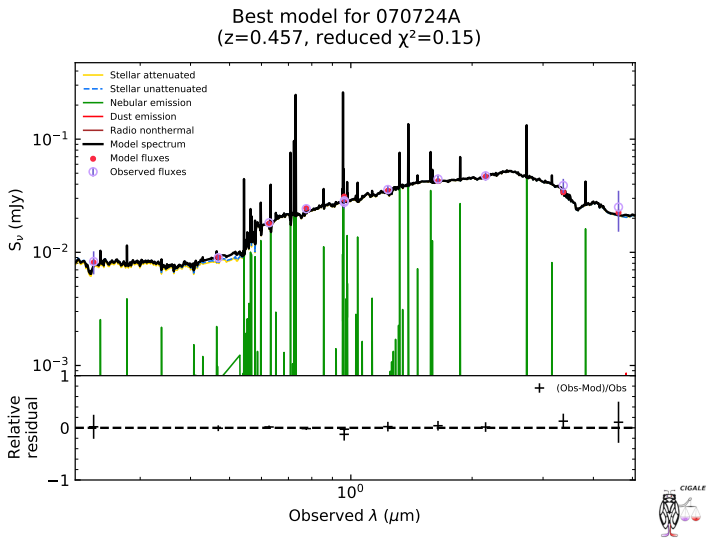

Figure 67: Best-fitted SED for GRBH 070724A. Colour and symbols convention as in Figure 54.

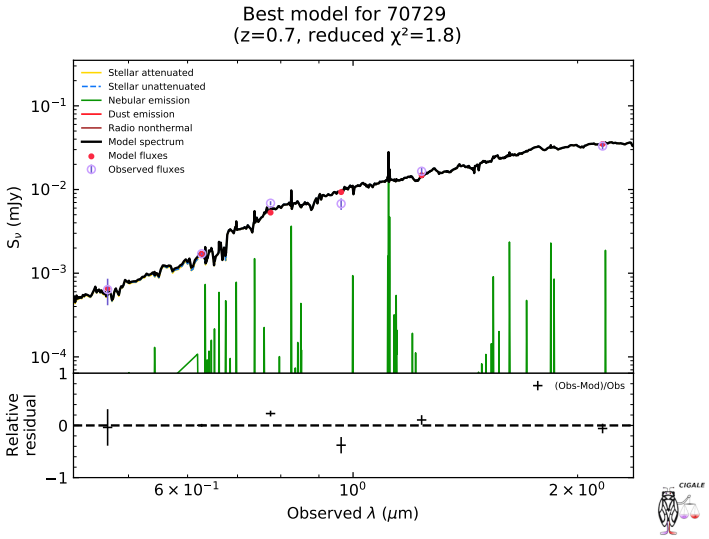

Figure 68: Best-fitted SED for GRBH 070729. Colour and symbols convention as in Figure 54.

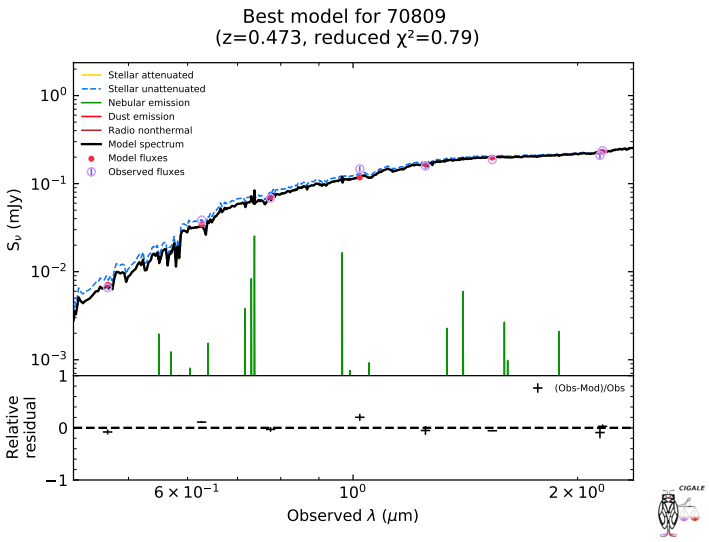

Figure 69: Best-fitted SED for GRBH 070809. Colour and symbols convention as in Figure 54.

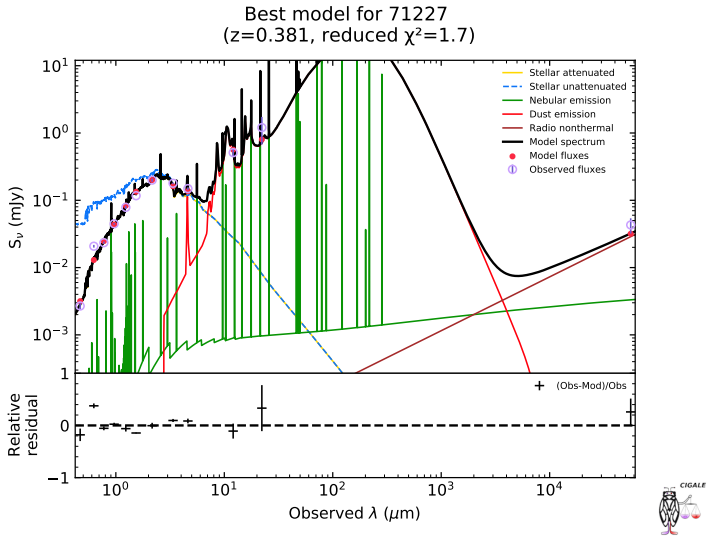

Figure 70: Best-fitted SED for GRBH 071227. Colour and symbols convention as in Figure 54.

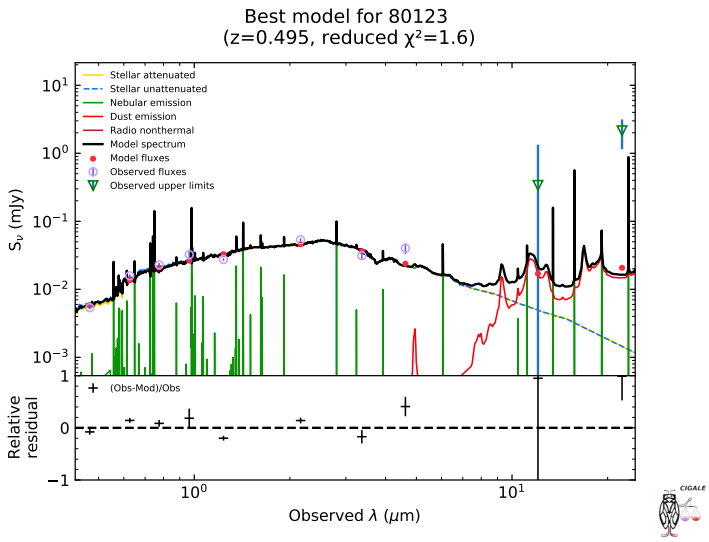

Figure 71: Best-fitted SED for GRBH 080123. Colour and symbols convention as in Figure 54.

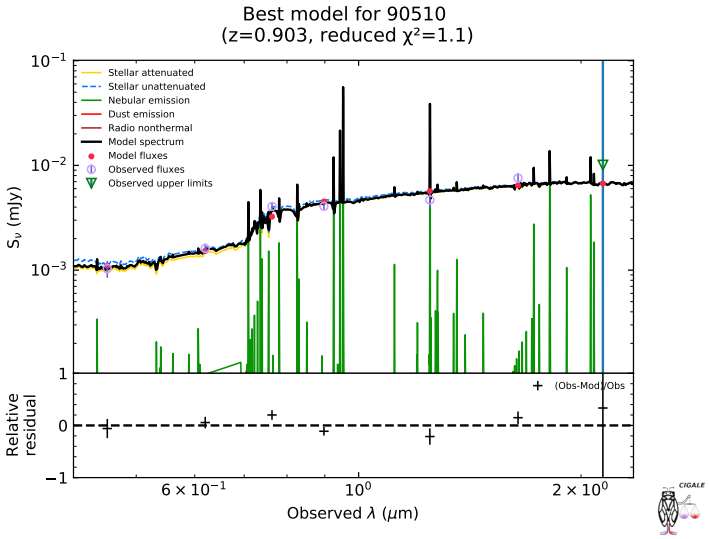

Figure 72: Best-fitted SED for GRBH 090510. Colour and symbols convention as in Figure 54.

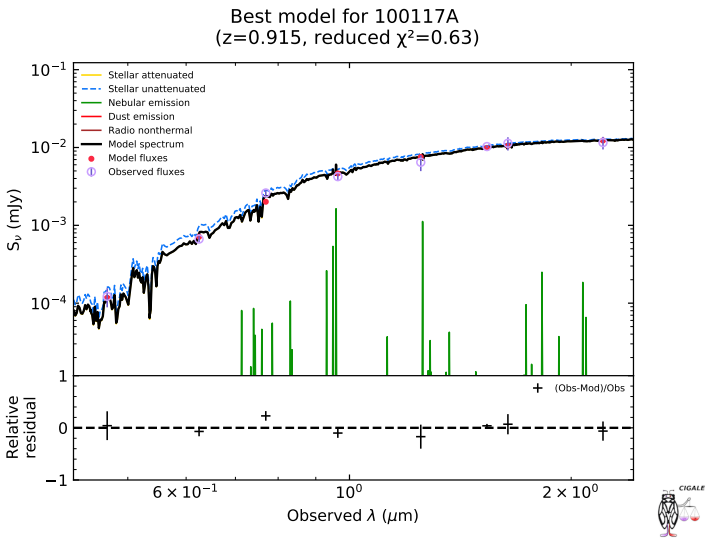

Figure 73: Best-fitted SED for GRBH 100117A. Colour and symbols convention as in Figure 54.

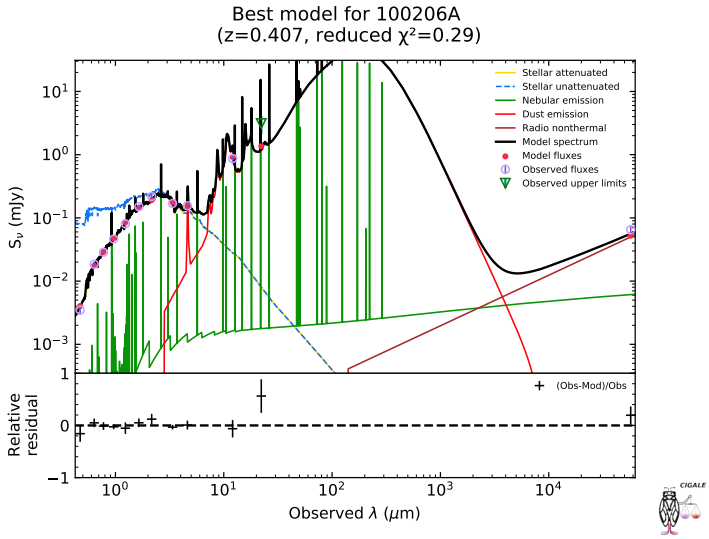

Figure 74: Best-fitted SED for GRBH 100206A. Colour and symbols convention as in Figure 54.

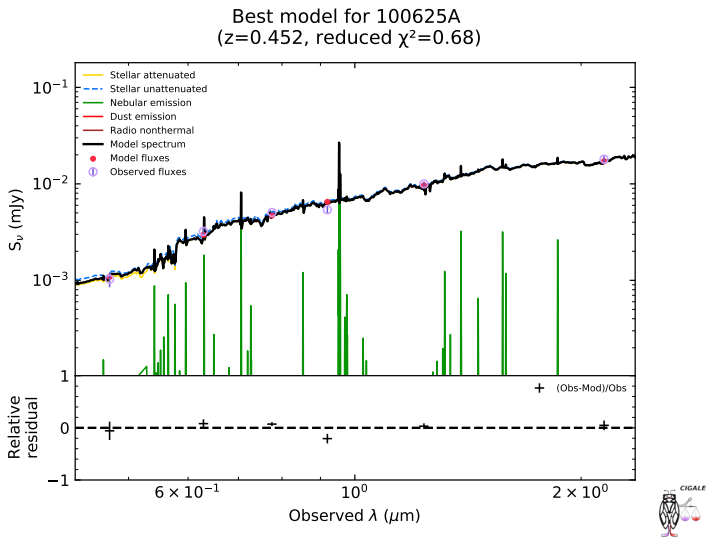

Figure 75: Best-fitted SED for GRBH 100625A. Colour and symbols convention as in Figure 54.

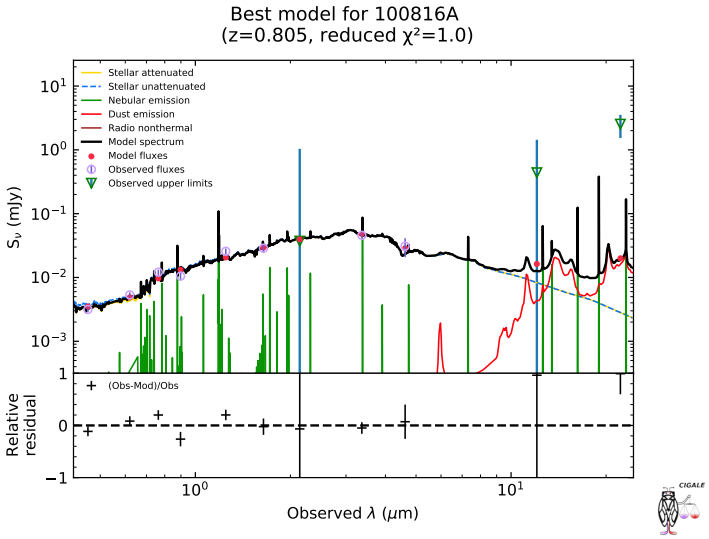

Figure 76: Best-fitted SED for GRBH 100816A. Colour and symbols convention as in Figure 54.

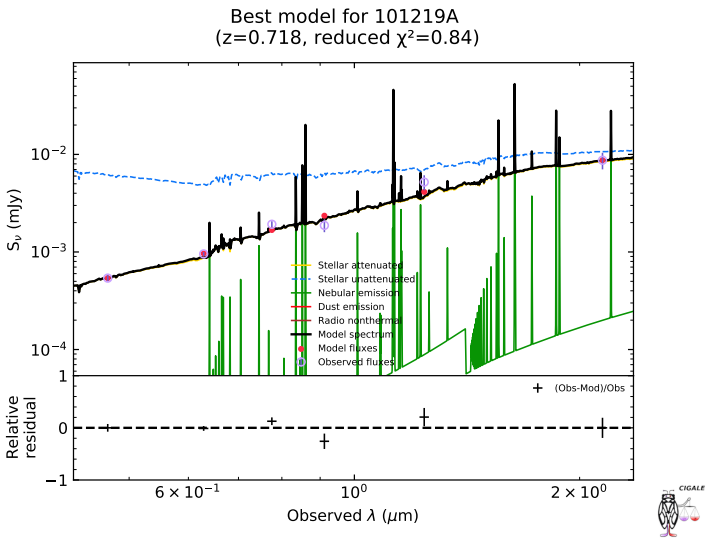

Figure 77: Best-fitted SED for GRBH 101219A. Colour and symbols convention as in Figure 54.

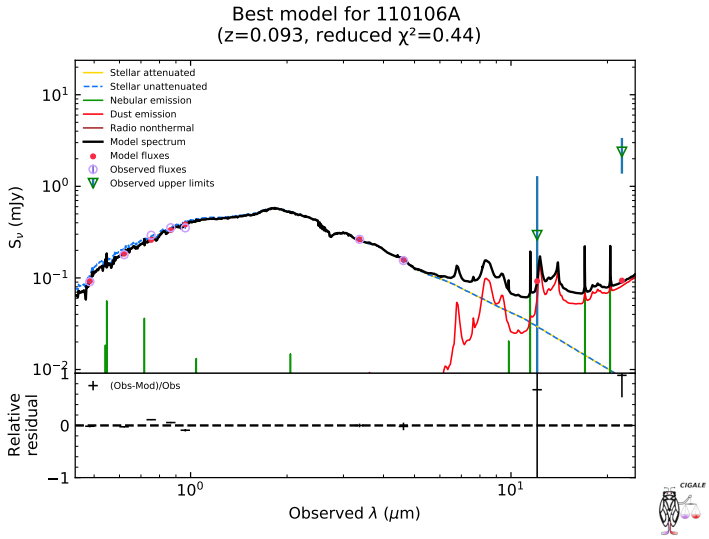

Figure 78: Best-fitted SED for GRBH 110106A. Colour and symbols convention as in Figure 54.

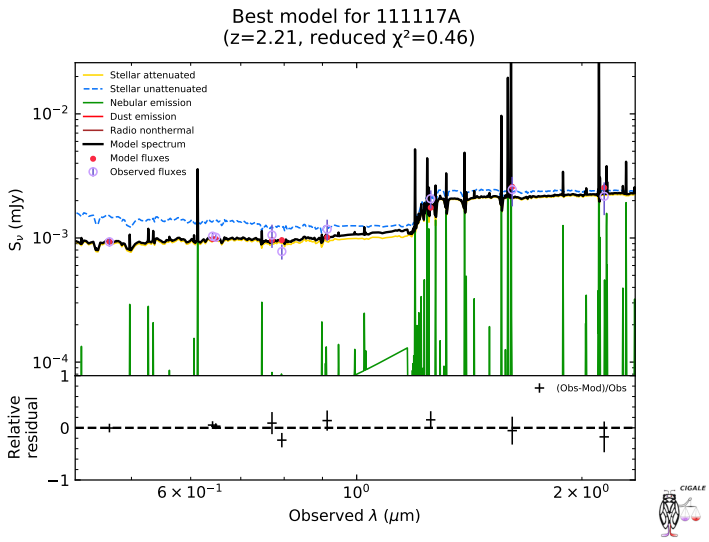

Figure 79: Best-fitted SED for GRBH 111117A. Colour and symbols convention as in Figure 54.

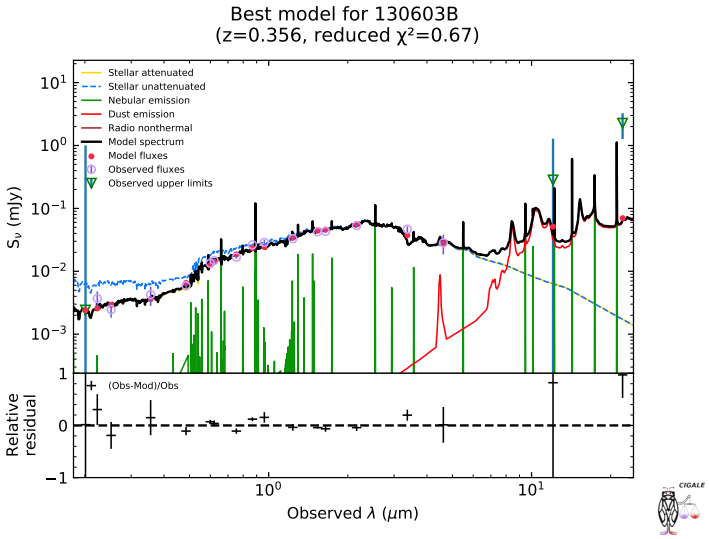

Figure 80: Best-fitted SED for GRBH 130603B. Colour and symbols convention as in Figure 54.

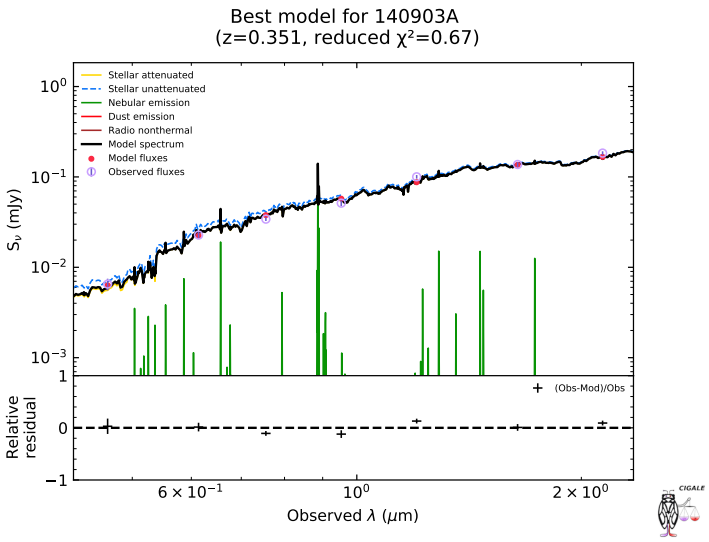

Figure 81: Best-fitted SED for GRBH 140903A. Colour and symbols convention as in Figure 54.

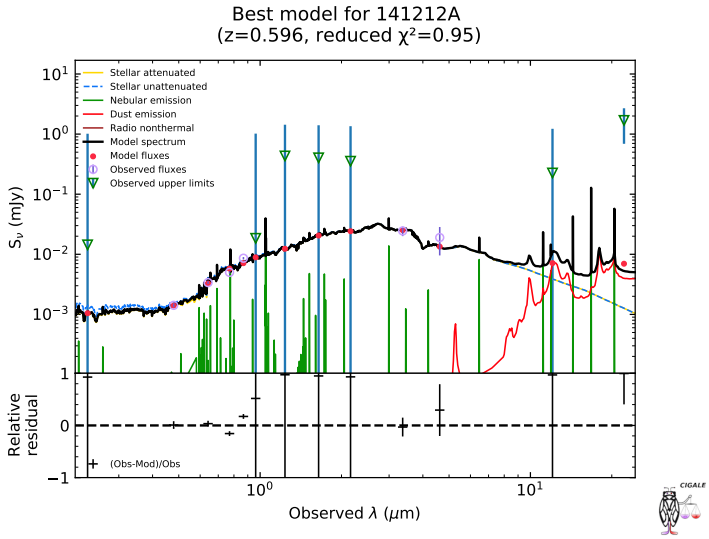

Figure 82: Best-fitted SED for GRBH 141212A. Colour and symbols convention as in Figure 54.

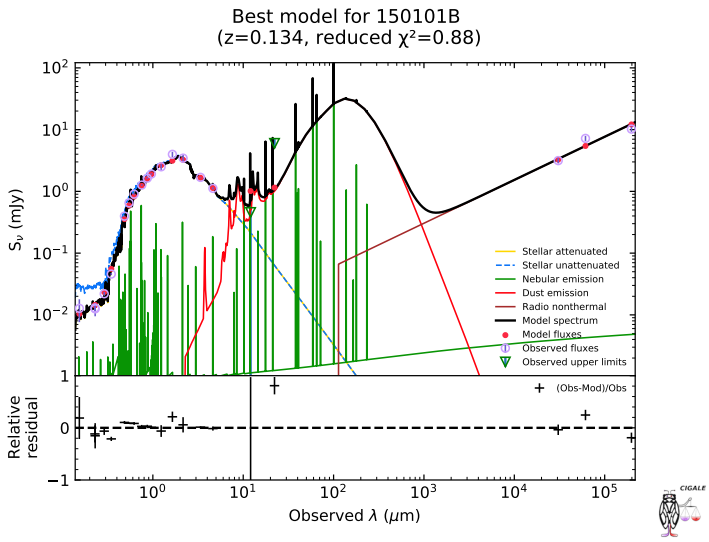

Figure 83: Best-fitted SED for GRBH 150101B. Colour and symbols convention as in Figure 54.

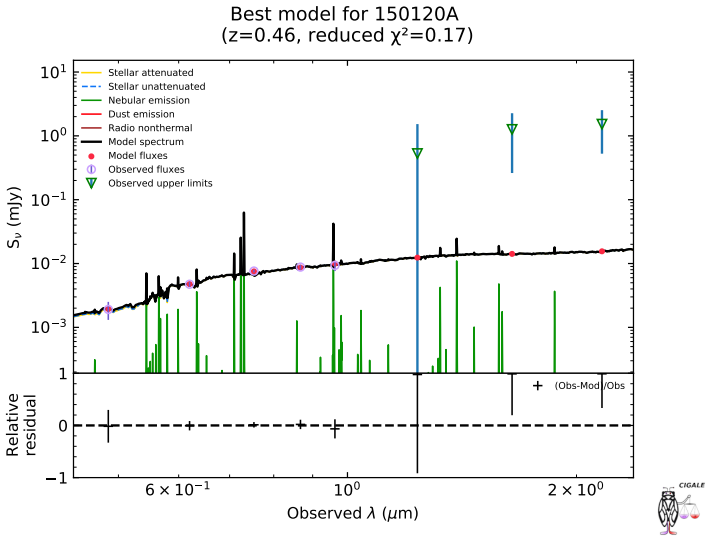

Figure 84: Best-fitted SED for GRBH 150120A. Colour and symbols convention as in Figure 54.

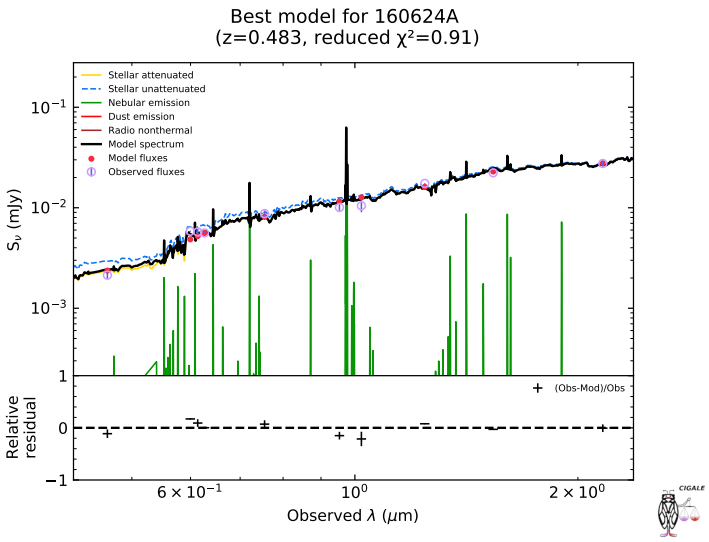

Figure 85: Best-fitted SED for GRBH 160624A. Colour and symbols convention as in Figure 54.

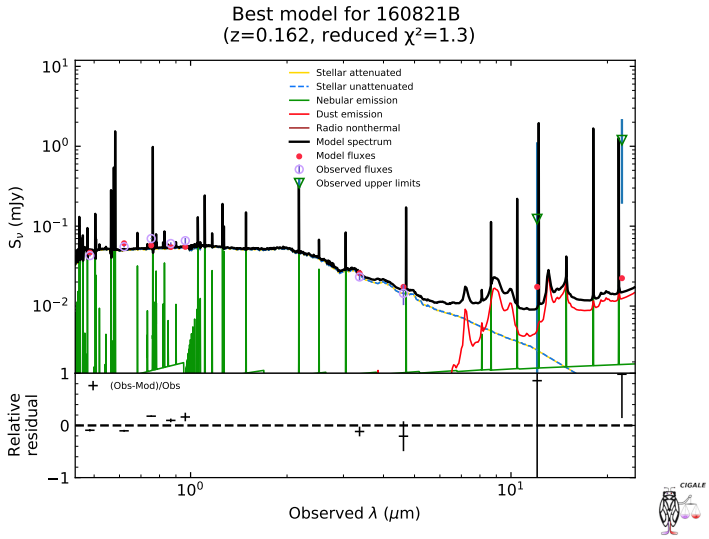

Figure 86: Best-fitted SED for GRBH 160821B. Colour and symbols convention as in Figure 54.

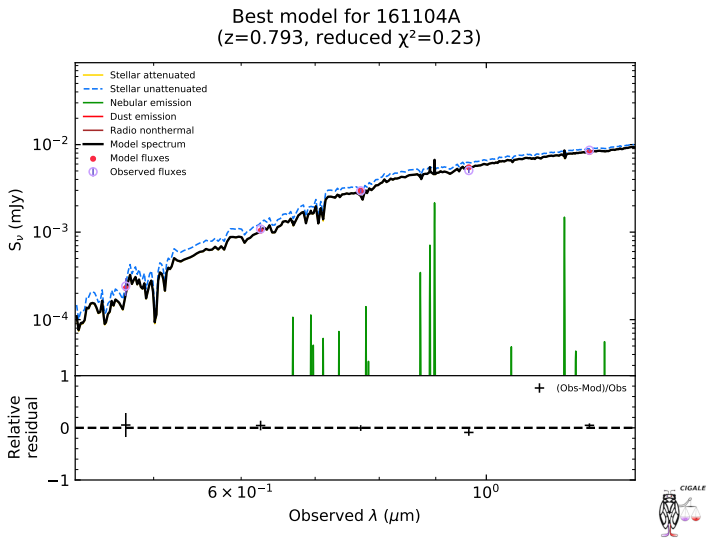

Figure 87: Best-fitted SED for GRBH 161104A. Colour and symbols convention as in Figure 54.

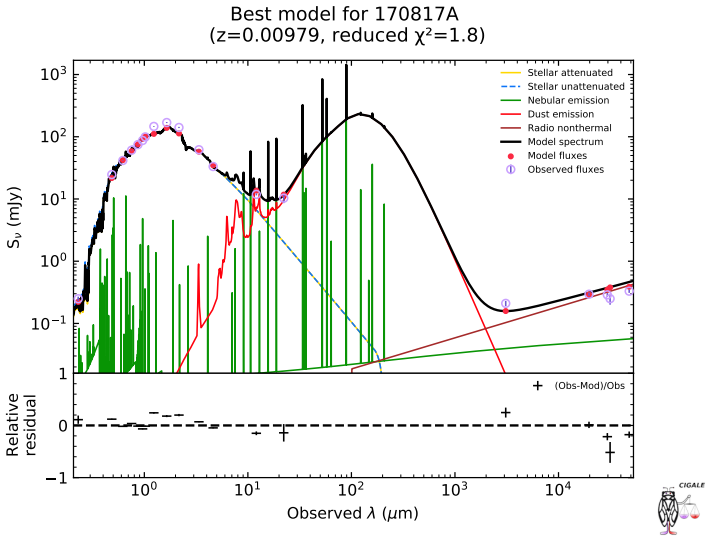

Figure 88: Best-fitted SED for GRBH 170817A. Colour and symbols convention as in Figure 54.

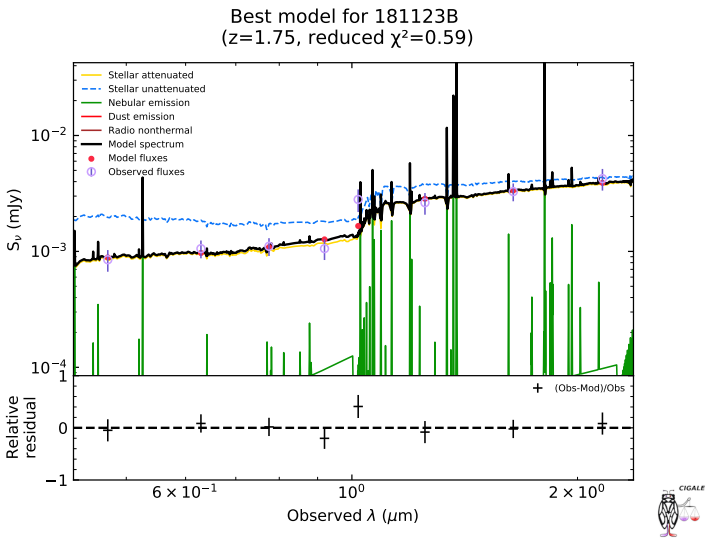

Figure 89: Best-fitted SED for GRBH 181123B. Colour and symbols convention as in Figure 54.

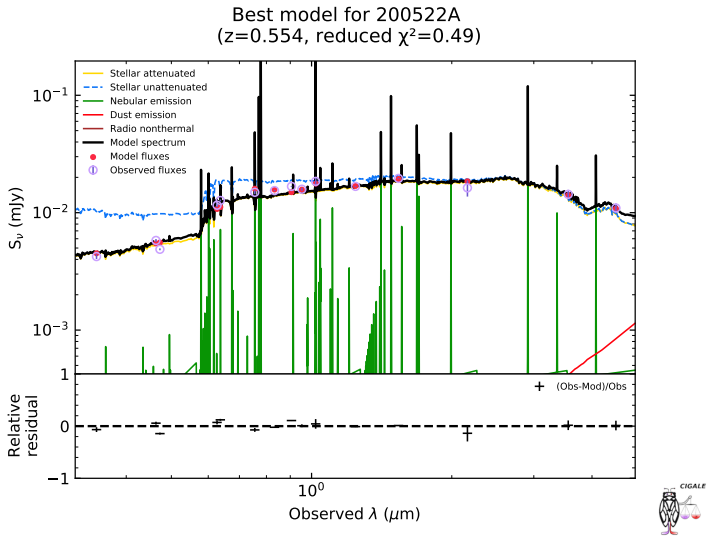

Figure 90: Best-fitted SED for GRBH 200522A. Colour and symbols convention as in Figure 54.

université PARIS-SACLAY

ÉCOLE DOCTORALE
Particules, hadrons, énergie et noyau : instrumentation, imagerie, cosmos et simulation (PHENIICS)

Titre: Astronomie multi-messagers : de l'analyse des sources transitoires d'ondes gravitationelles à la recherche de contreparties électromagnétiques.

Mots clés: astronomie multi-messagers, ciel transitoire, ondes gravitationnelles, LIGO-Virgo, SVOM, GRANDMA

Résumé: Cette thèse est dédiée à l'étude multi-messagers des ondes gravitationnelles. Dans un premier temps la thèse porte sur la validation de l'envoi des alertes ondes gravitationnelles de la collaboration LIGO-Virgo-KAGRA, en particulier en travaillant sur la caractérisation du détecteur Virgo situé à Cascina, près de Pise en Italie. Une partie du travail décrit porte sur la recherche des contreparties électromagnétiques aux événements ondes gravitationnelles, en particulier les sursauts gamma. L'analyse de données prises pendant le run O3 et les résultats sur la recherche de contreparties pour les sources détectées par les satellites Fermi et Swift sont exposés. Dans un second volet, cette thèse présente le suivi de ces alertes au sein des collaborations GRANDMA et SVOM, réseaux de télescopes terrestres et/ou spatiaux. Enfin, y est présentée l'étude de la population de galaxies hôtes de sursaut gamma courts afin d'identifier leurs propriétés et les utiliser pour optimiser le suivi des ondes gravitationnelles.

Title: Multi-messenger astronomy: from the analysis of transient sources of gravitational waves to electromagnetic counterparts searches.

Keywords: multi-messenger astronomy, transient sky, gravitational waves, LIGO-Virgo, SVOM, GRANDMA

Abstract: This thesis is dedicated to the multi-messenger study of gravitational waves. In a first step, this thesis focuses on the validation of the LIGO-Virgo-KAGRA collaboration's gravitational wave alerts, in particular by working on the characterization of the Virgo detector located in Cascina, near Pisa in Italy. Some of the work described focuses on the search for electromagnetic counterparts to gravitational wave events, in particular gamma-ray bursts. The analysis of data taken during the O3 run and the results on the search for counterparts for the sources detected by the Fermi and Swift satellites are presented. In a second part, this thesis presents the monitoring of these alerts within the GRANDMA and SVOM collaborations, networks of ground-based and/or space-based telescopes. Finally, the study of the population of short gamma-ray burst host galaxies is presented in order to identify their properties and use them to optimise the follow-up of gravitational waves.

Université Paris-Saclay
Espace Technologique / Immeuble Discovery
Route de l'Orme aux Merisiers RD 128 / 91190 Saint-Aubin, France